# TRANSIENT SIMULATION FOR MULTISCALE CHIP-PACKAGE STRUCTURES USING THE LAGUERRE-FDTD SCHEME

A Thesis
Presented to
The Academic Faculty

by

Ming Yi

In Partial Fulfillment
of the Requirements for the Degree
Doctor of Philosophy in the
School of Electrical and Computer Engineering

Georgia Institute of Technology
August 2015

# TRANSIENT SIMULATION FOR MULTISCALE CHIP-PACKAGE STRUCTURES USING THE LAGUERRE-FDTD SCHEME

Approved by:


Professor Madhavan Swaminathan,
Advisor
School of Electrical and Computer Engineering
*Georgia Institute of Technology*

Professor Ioannis Papapolymerou
School of Electrical and Computer Engineering
*Georgia Institute of Technology*

Professor Andrew F. Peterson
School of Electrical and Computer Engineering
*Georgia Institute of Technology*

Professor Suresh K. Sitaraman
School of Mechanical Engineering
*Georgia Institute of Technology*

Professor Gregory D. Durgin
School of Electrical and Computer Engineering
*Georgia Institute of Technology*



Date Approved: 21 April 2015

# DEDICATION

*To my family.*

# ACKNOWLEDGEMENTS

The completion of this dissertation would not be possible without the support, guidance and help from many individuals. I would like to express my sincere gratitude toward them.

First and foremost being my advisor Dr. Madhavan Swaminathan, who provided me with the precious opportunity to study in Georgia Tech and the guidance through my entire Ph.D. career. Being an advisor, he always shared me with his insightful ideas and deep understanding toward the research topics. All the accomplishments in research could not be possible without his continuous support. There is a Chinese saying: he who teaches me one day is the father of my lifetime, which is more close to what I saw for Professor Swaminathan. In every conversation with him, there was never correction but suggestion, never urging but encouraging, never tedious discussion but passionate sharing. He extended the meaning of advisor and made my time working with him in Georgia Tech a lifetime treasure. I also want to express my sincere gratitude to my committee members, Dr. Andrew F. Peterson, Dr. Gregory D. Durgin, Dr. Ioannis Papapolymerou, and Dr. Suresh K. Sitaraman, for their valuable time and constructive comments to improve my research.

I would like to express my gratitude to the past and current members of Mixed Signal Design Group. I am grateful to Myunghyun Ha for his insightful ideas and guidance at the early stage of my Ph.D. career. I would also like to convey my special thanks to Jianyong Xie and Biancun Xie for sharing their thoughts and discussing in detail with me about my research. I was fortunate to work with excellent colleges who are supportive and willing to share their knowledge: Myunghyun Ha, Jianyong Xie, Suzanne Huh, Jae Yong Choi, Rishik Bazaz, Nitish Natu, Stephen Dumas, Diapa

Sonogo, Sang Kyu Kim, Munmun Islam, Kyu Hwan Han, Satyan Telikepalli, Biancun Xie, David Zhang, Sung Joo Park, Colin Pardue, Huan Yu, and Chia Lin Cheng. Special thanks to Prof. Papapolymerou and his group members: Sensen Li, Wasif Khan, Cagri Ulusoy, Aida Vera, who worked on the same project with me. My thanks also extend to all the visiting scholars and students I worked with: Youkeun Han, Decao Yang, Junki Min, Sang Min Han, Antonio Astorino, Sebastian Muller, and Carmine Gianfanga.

I am always grateful to Dr. Wen-Yan Yin who is my advisor during my master study in Shanghai Jiao Tong University. Dr. Wen-Yan Yin led me into the area of electromagnetics and made me aware of what a real researcher should behave: challenge yourself, be patient and conquer the obstacles step by step. His early guidance made my research in Georgia Tech possible.

I owe my deepest heartfelt gratitude to my family. My father Mr. Xueqin Yi and my mother Ms. Ying Li have been my lifetime advisors. All my accomplishments would not be possible without their unconditional love and support. My wife Yue Zhang has been the other half of my life. Meeting her in Georgia Tech, falling in love, getting married and giving birth to our beloved son Oliver is the most beautiful memory in my life. I cannot believe this happened so fast and all happened during my Ph.D. study in Georgia Tech. Her love and support is always the source of my strength.

# TABLE OF CONTENTS

# LIST OF TABLES

# LIST OF FIGURES

# LIST OF SYMBOLS OR ABBREVIATIONS

| | |
|---|---|
| **2-D** | Two Dimensional. |
| **3-D** | Three Dimensional. |
| **ABC** | Absorbing Boundary Condition. |
| **ADI** | Alternating Direction Implicit. |
| **CFL** | Courant-Friedrichs-Lewy. |
| **CN** | Crank-Nicolson. |
| **CPW** | Coplanar Waveguide. |
| **DP** | Dual Primal. |
| **EDA** | Electronic Design Automation. |
| **EFA** | Electric Field Approximation. |
| **FDTD** | Finite-Difference Time-Domain. |
| **FETI** | Finite Element Tearing and Interconnect. |
| **FFT** | Fast Fourier Transform. |
| **IC** | Integrated Circuit. |
| **LCP** | Liquid Crystal Polymer. |
| **LOD** | Locally One Dimensional. |
| **MFA** | Magnetic Field Approximation. |
| **MOR** | Model Order Reduction. |
| **PDE** | Partial Differential Equation. |
| **PDN** | Power Delivery Network. |
| **PEC** | Perfect Electric Conductor. |
| **PEEC** | Partially Element Equivalent Circuit. |
| **PML** | Perfect Matched Layer. |
| **RCS** | Radar Cross Section. |
| **RDL** | Redistribution Layer. |

| | |
|---|---|
| **RMS** | Root Mean Square. |
| **SIBC** | Surface Impedance Boundary Condition. |
| **SIP** | System in Package. |
| **SIW** | Substrate Integrated Waveguide. |
| **SOP** | System on Package. |
| **SSN** | Simultaneous Switching Noise. |
| **TD** | Time Domain. |
| **TE** | Transverse Electric Mode. |
| **TEM** | Transverse Electromagnetic Mode. |
| **TSV** | Through Silicon Via. |

# SUMMARY

The high-density integrated circuit (IC) gives rise to geometrically complex multiscale chip-package structures whose electromagnetic performance is difficult to predict. This motivates this dissertation to work on an efficient full-wave transient solver that is capable of capturing all the electromagnetic behaviors of such structures with high accuracy and reduced computational complexity compared to the existing methods.

In this work, the unconditionally stable Laguerre-FDTD method is adopted as the core algorithm for the transient full-wave solver. As part of this research, skin-effect is rigorously incorporated into the solver which avoids dense meshing inside conductor structures and significantly increases computational efficiency. Moreover, as an alternative to typical planar interconnects for next generation high-speed ICs, substrate integrated waveguide, is investigated. Conductor surface roughness is efficiently modeled to accurately capture its high-frequency loss behavior. To further improve the computational performance of chip-package co-simulation, a novel transient non-conformal domain decomposition method has been proposed. Large-scale chip-package structure can be efficiently simulated by decomposing the computational domain into subdomains with independent meshing strategy. Numerical results demonstrate the capability, accuracy and efficiency of the proposed methods.

# CHAPTER I

# INTRODUCTION

## *1.1 Background and Motivation*

High-density integration is essential in realizing modern integrated circuits (ICs) with high performance, small size, and low cost. This has driven the complexity of the IC design to grow for the past decades. In recent years, the industrial needs have already pushed the traditional two-dimensional (2-D) integration to its limit due to transistor size, chip size and package density. Three-dimensional (3-D) integration, such as system-in-package (SIP) and system-on-package (SOP), has become a promising solution for future integration (as shown in Figure 1).

Nevertheless, the design of all these high-density integrated systems is impossible without the assistance of electronic design automation (EDA) tools. The industry has witnessed the huge demand for EDA design solutions as never before. From an electromagnetic point of view, signal propagation and interaction in modern ICs poses significant electrical simulation challenges. Therefore, the development of a full-wave electromagnetic solver that can be applied to the simulation of complex integrated applications is a necessity.

Among the main components in realizing modern electronic systems, the chip and the package play a vital role. From a geometric point of view, the chip-package structures are intrinsically multiscale structures. This implies that large scale difference in physical dimensions (as shown in Figure 2) exists in these types of structures. For instance, the dimensional difference of interconnects of chips and packages are always separated by several orders of magnitude. In practice, since full-wave solvers are developed based on discretizing Maxwell's equations, large number of unknowns will be

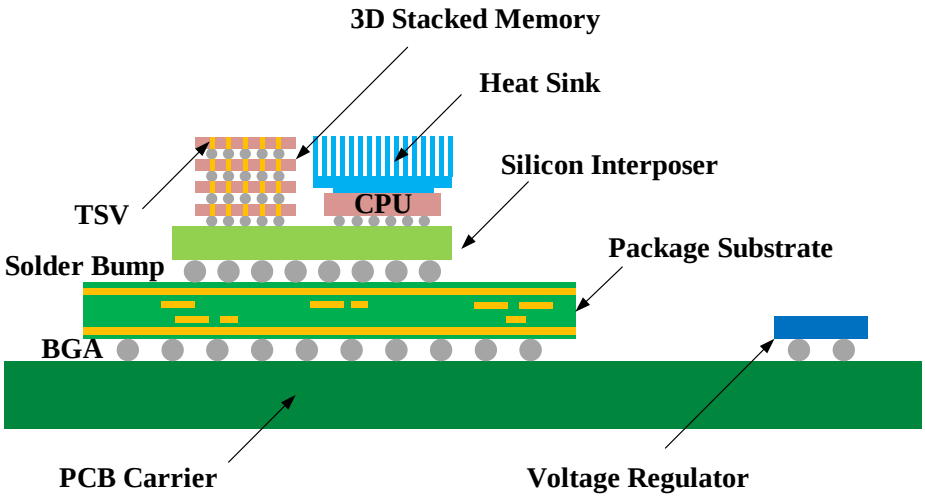


**Figure 1:** Schematic of a 3-D integration system.

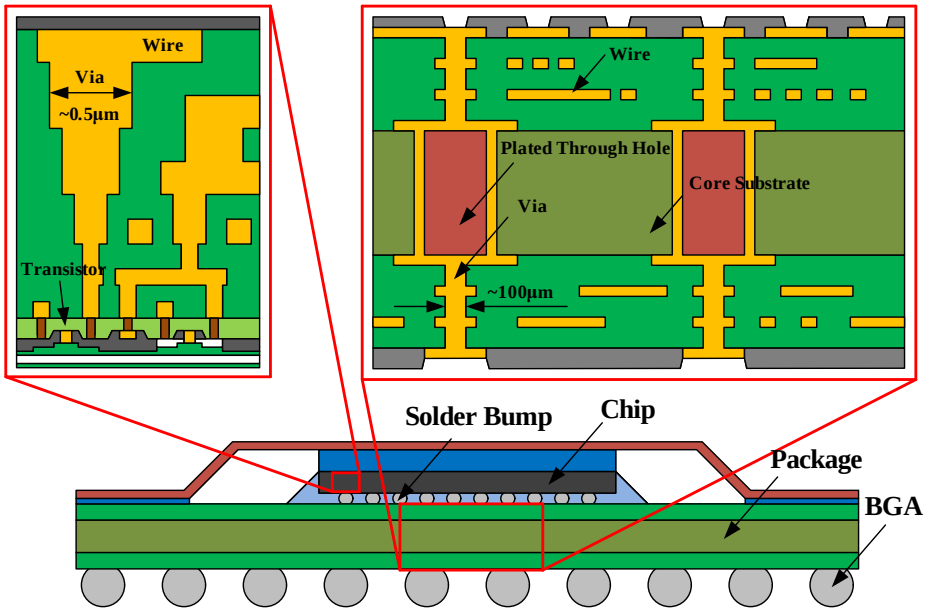


**Figure 2:** Schematic of a multi-scale chip-package structure.

generated for the multiscale structures, making the solution of such problems prohibitively expensive. Moreover, as the operating frequency reaches gigahertz range, skin-effect and conductor surface roughness need to be carefully taken into consideration. This usually adds additional computational cost to the original problems. Therefore, an accurate and efficient solution needs to be developed.

Generally, full-wave solvers can be categorized into two domains: frequency domain and time domain. The time-domain methods have the advantage of obtaining direct time-domain solution. Also, the corresponding frequency responses can be easily obtained by Fourier transforming the time domain response. However, traditional time-domain techniques, such as the finite-difference time-domain (FDTD) method, are limited by the Courant-Friedrichs-Lewy (CFL) stability condition. This stability condition makes it almost impossible to efficiently simulate multiscale structures using the traditional finite-difference-based techniques. Very fine meshes need to be applied to the physically small areas, which results in a prohibitively small time step. Moreover, it is also difficult to incorporate skin-effect and conductor surface roughness into time-domain simulations. All these challenges motivate this dissertation to work on an accurate and efficient general solution to the full-wave simulation of chip-package structures.

## *1.2 Summary of Contributions: A Broader Perspective*

To solve the problem aforementioned, an unconditionally stable time-domain scheme using Laguerre polynomials, which is known as the Laguerre-FDTD method, is used for simulating multiscale chip-package structures. The time step in the Laguerre-FDTD method is no longer confined by the smallest mesh size, and thus, multi-level meshing can be applied. The skin-effect is rigorously modeled and incorporated into the Laguerre-FDTD scheme. Moreover, a modeling method for conductor surface roughness is proposed targeting novel high-speed interconnects, namely the substrate

integrated waveguide (SIW). Although the computational complexity can be significantly reduced for multiscale simulation by using the Laguerre-FDTD scheme, the solution is still expensive for very large-scale problems. A transient non-conformal domain decomposition method based on the Laguerre-FDTD scheme is proposed, which enables the decomposed simulation of the original problem. Different meshing schemes can be applied to different domains, and the interface mesh between adjacent domains does not need to be matched. Therefore, by maintaining the accuracy, the computational complexity is further reduced for the multiscale chip-package simulation.

The goals of this dissertation are in correspondence with the contributions shown in Figure 3. In summary, the contributions of the dissertation are listed as follows:

1. The development of a skin-effect modeling method based on the Laguerre-FDTD scheme. This method rigorously captures the skin-effect of conductors in high-frequency applications. It does not require field solution inside the conductor with a fine mesh. Significant improvement of simulation speed is achieved compared to the existing standard methods.

2. The development of a transient non-conformal domain decomposition method. This method tackles large-scale multiscale problems by decomposing the computational domain into smaller problems each with its unique mesh. Field continuity at the domain interface is rigorously enforced and the solution of each domain is obtained in a parallel manner. Separate meshing strategy for the decomposed subdomains is applied, which is suitable for simulating multiscale chip-package structures.

3. The development of a conductor surface roughness modeling method. This method is designed to capture the conductor loss due to the surface roughness in the SIW, which is a promising alternative to traditional transmission lines

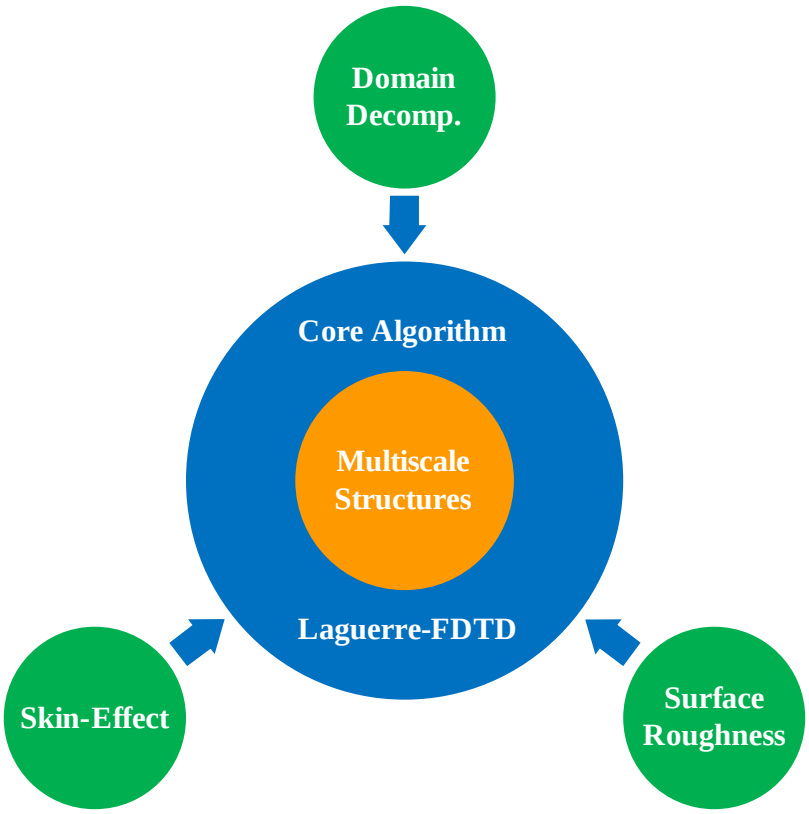


**Figure 3:** The goals and contributions of this dissertation.

at ultra-high frequencies. An analytical solution is derived which is capable of being incorporated into full-wave solvers, such as the Laguerre-FDTD solver.

## *1.3 Organization of the Dissertation*

The dissertation is organized as follows: Chapter II describes the origin and history of the problem, including a literature review and previous works. In Chapter III, the transient simulation core algorithm, the Laguerre-FDTD method, is discussed. Boundary conditions and frequency-domain result extraction schemes are also discussed in this chapter. A modeling scheme for incorporating skin-effect is investigated in Chapter IV based on the core algorithm. To be more specific, the surface impedance boundary condition (SIBC) is incorporated into the Laguerre-FDTD method using

two implementation schemes. In Chapter V, a transient non-conformal domain decomposition method is proposed for solving large multiscale problems. Chip-package structure test cases are simulated in Chapter VI based on the proposed methods. In Chapter VII, conductor surface roughness modeling for a novel type of high-speed interconnect, the substrate integrated waveguide, is investigated. An analytical solution is derived and the incorporation of the solution into the Laguerre-FDTD solver is discussed. Finally, Chapter VIII and Chapter IX present the conclusions for this work and the discussions for some future work.

# CHAPTER II

# ORIGIN AND HISTORY OF THE PROBLEM

## *2.1 Needs for Simulation of Chips and Packages*

The chips and packages are key components in realizing modern electronic systems. Early design of the chips and the packages was done manually, which results in extremely limited system performance. For modern ICs, it is impossible to design chips with billions of transistors and packages with hundreds and thousands of I/Os without the assistance of CAD tools. In recent years, the need for electrical CAD tools, especially the full-wave electromagnetic simulation tools, is increasing as the system operating frequency increases. Improper electrical design may result in system failure due to signal/power integrity problems, such as transmission loss, impedance mismatch, simultaneous switching noise (SSN), crosstalk, and jitter. Most recently, to accurately capture the electrical property of the entire system, chip-package co-simulation is desired by the industry to replace the current separate-modeling scheme of chips and packages. However, due to the geometry complexity of the chip-package structures and the simulation constraint of the current full-wave electromagnetic solvers, this problem is still challenging and solutions are limited. All the aforementioned reasons make the electromagnetic simulation of chips and packages a necessity in modern IC design.

## *2.2 Practical Concerns in Simulation of Multiscale Chip-Package Problems*

The chip-package structures are intrinsically multi-scale structures. Time domain simulation of such structures requires a method with unconditional stability. This implies that the time step can be chosen independently of the smallest mesh size.

Traditional time-domain schemes, such as the conventional FDTD method, are no longer applicable. Moreover, skin-effect is difficult to be addressed in the time domain. An efficient and accurate modeling method of skin-effect needs to be developed without compromising the simulation accuracy and stability. Moreover, for high-frequency interconnect structures, conductor surface roughness may play a vital role in signal transmission loss, leading to the challenge for efficient modeling of surface roughness. Usually, for unconditionally stable time-domain implicit methods, system matrices need to be solved. As for multiscale structures, the solution for the problem as a whole is expensive. Methods with capability of decomposing the problem, which reduces computational cost, are desirable. Apart from the existing implementation of domain decomposition in the frequency domain, for an FDTD-based scheme, non-conformal domain decomposition is still challenging, and relevant literatures are quite limited.

### 2.2.1 Time-Domain Simulation Methods

The explicit FDTD method has been widely applied to transient electromagnetic simulation problems. The marching-on-in-time scheme is efficient in field updating, and is suitable for simulating simple structures such as planar components with zero thickness strips [2]. However, the major drawback of the original explicit FDTD method proposed by Yee [3] is the CFL stability condition which is given by

$$\Delta t < \frac{1}{v_{\max}\sqrt{\left(\frac{1}{\Delta x}\right)^2 + \left(\frac{1}{\Delta y}\right)^2 + \left(\frac{1}{\Delta z}\right)^2}} \tag{1}$$

where $\Delta t$ is the time step, $v_{\max}$ is the maximum phase velocity of the propagated wave, $\Delta x$, $\Delta y$, and $\Delta z$ are the smallest cell sizes in $x$-, $y$-, and $z$-dimensions, respectively. The CFL stability condition implies that the largest time step in the simulation is restricted by the smallest cell size. In multiscale structures, a dense mesh needs to be

applied to the physically small regions, making the resulting time step prohibitively small.

To overcome the stability issue in the explicit FDTD method, semi-implicit and implicit FDTD schemes for transient electromagnetic simulation have been studied in recent decades. The alternating direction implicit (ADI) FDTD method, which was first introduced for electromagnetic simulation by Holland [4], received wide attention. Unlike the explicit FDTD method, the electric and magnetic fields are sampled at the same time, and the one time step updating leap-frog scheme is substituted by a two sub-step alternative. The ADI-FDTD method has been proved to be unconditionally stable [5], and has been extended in the followed work such that the alternation is performed in respect to mixed coordinates rather than to each respective coordinate direction [6]. Using the ADI-FDTD method, multiscale structures, such as thin wide metal strip, can be simulated efficiently with a large time step [7]. However, it is found that larger value of time step rather than the CFL limit results in a larger dispersion error [8].

Apart from the ADI-FDTD method, other implicit schemes have been proposed, such as the Crank-Nicolson (CN) scheme, which has received much attention [9]. The CN algorithm advances time by a full time step size with one marching procedure, whereas the ADI-FDTD method uses two with an intermediate time value. However, in both 2-D and 3-D cases, the system matrix is block tri-diagonal or tri-diagonal with fringes, which is very expensive to solve. Eigenvalue decomposition and approximate-decoupling methods have been proposed to further reduce the computational cost [9], [10]. Nevertheless, the CN scheme is shown to exhibit the same numerical dispersion as the ADI-FDTD method. Recently, the locally-one-dimensional (LOD) FDTD method has been proposed which is unconditionally stable [11]. The number of equations to be computed is the same as that with the ADI-FDTD method but with approximately 20% less arithmetic operations.

In recent years, the unconditionally stable Laguerre-FDTD method has been proposed using weighted Laguerre polynomials [8], [12], [13]. By applying the temporal Galerkin's testing procedure, the transient solution is made independent of time discretization, which makes it suitable for analyzing multiscale structures. The Laguerre-FDTD method is completely different from all other FDTD scheme due to its marching-on-in-order nature. A 70× to 80× speedup using this method has been reported for certain chip-package simulation cases [14]. Moreover, since for the ADI-FDTD method, the numerical dispersion error becomes larger as the time step increases, the Laguerre-FDTD method provides advantages when a larger time step is used. Since the introduction of the Laguerre-FDTD method, several modifications have been made to the algorithm. The equivalent circuit model for Laguerre-FDTD method has been presented, and simulation for multi-scale structures has been performed in [14]. A perturbation term is introduced into the matrix formation, which reduces memory consumption, and makes the simulation of large 3-D problems possible [15]. However, all these methods using the Laguerre-FDTD scheme require discretization inside of the conductor for addressing skin-effect. A considerable dense mesh must be applied to the conductor, which makes the solution very expensive. Moreover, no non-conformal domain decomposition method using the Laguerre-FDTD method exists. It is critical to resolve these problems so that large multi-scale chip-package structures can be simulated efficiently, which is also the motivation of this dissertation.

### 2.2.2 Skin-Effect Modeling

Skin effect is the tendency of an electric current to become distributed densely near the surface of the conductor as frequency increases. The current decreases exponentially between the outer surface and inside the conductor (which is illustrated in Figure 4) with the skin depth given by [16]

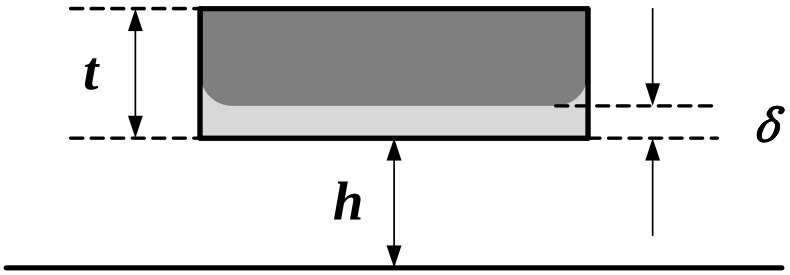


**Figure 4:** Cross section of a microstrip line operating in high-frequency. The current is concentrated on the surface of the metal strip.

$$\delta = \frac{1}{\sqrt{\pi f \mu \sigma}} \tag{2}$$

where $f$, $\mu$, and $\sigma$ are the frequency, magnetic permeability, and conductivity of the conductor, respectively. It can be inferred that for clock rates at gigahertz range, the skin depth becomes very small, which results in skin-effect loss. One straightforward way to capture skin-effect is to apply a dense mesh to the conductor structure. However, the inclusion of this method in an electromagnetic solver can be very costly in computational time and memory requirements.

Some of the early attempts in efficient modeling of the skin-effect are in the frequency domain. The vector potential method was employed to calculate the frequency-dependent resistance and inductance [17]. To improve the accuracy, a technique formulated in terms of the axial component of the vector potential was proposed. Both skin-effect and proximity effect are taken into account [18]. Other schemes, such as current density method and network approach, have also been developed [19], [20].

In the time domain, the early focus of incorporating skin-effect was to solve transmission line problems. In [21], a time-domain method based on a traveling-wave solution of the transmission line equations in the frequency domain was presented. Skin-effect has also been modeled by equivalent circuits consisting of resistors and

inductors derived from the skin-effect differential equations [22]. Other time-domain schemes based on the partial element equivalent circuit (PEEC) method have been adopted and have become a major method for the simulation of transmission lines and on-chip interconnects with skin-effect [23]. Unfortunately, very few skin-effect models using PEEC method are available which truly represent the 3-D current flow in complex structures [24].

A efficient method for modeling the skin-effect in the time domain is the surface impedance method, which has been widely used in frequency-domain simulations [25], [26]. The concept of surface impedance was first introduced by Leontovich in [27]. Using the surface impedance concept, no field components need to be calculated inside the conductor structure, which largely reduces the computational time. For FDTD schemes, the skin-effect was first modeled in [28] by applying surface impedance boundary condition (SIBC). This method was then extended by performing a rational approximation on the normalized frequency domain impedance, thus avoiding computing the exponential approximation prior to FDTD simulation [29]. To improve the accuracy of the SIBC in FDTD methods, some higher order methods have been proposed and a curved surface is able to be modeled efficiently [30], [31]. In recently years, the SIBC has been extended to unconditionally stable FDTD schemes such as the ADI-FDTD method [32]. However, no implementation of skin-effect using the SIBC based on the Laguerre-FDTD method has been reported.

### 2.2.3 Large-Scale Problem and Domain Decomposition

In mathematics, domain decomposition is a general term referring to a numerical method that solves the partial differential equation (PDE) problem by decomposing the original problem into sub-problems. Inherited from but unlike the commonly known numerical methods, the domain decomposition method does not solve the entire computational domain directly, but by dividing it into subdomains (Figure 5).

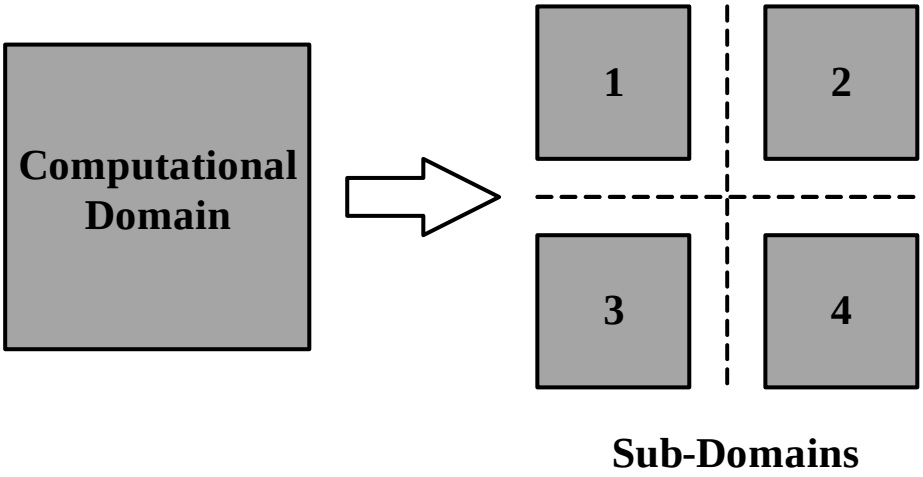


**Figure 5:** Decomposing computational domain into subdomains.

Each subdomain is solved independently, and the adjacent subdomains are coupled through interface boundaries. The entire system solution is then recovered from the solutions of all subdomains. In problems with large scale difference, such as multiscale chip-package simulation, the number of unknowns may reach several millions or above. It is inefficient to apply direct numerical methods to such problems. Therefore, a domain decomposition scheme, which saves computation time and memory storage, is desirable.

Numerous domain decomposition methods based on different decomposition schemes have been developed in applied mathematics, computational mechanics, computational fluid dynamics, and computational electromagnetics [33]. One type of the domain decomposition methods is classified as Schwartz method. The classical alternating Schwartz method is based on overlapping subdomains with Dirichlet boundaries [33]. Although the overlapping domain decomposition is still an active research topic, the non-overlapping alternatives become appealing for flexibility. An extension to the classical Schwartz method has been developed, which enables non-overlapping partitioning with replaced Robin transmission boundary conditions. The first non-overlapping domain decomposition method for Maxwell's equation was proposed by

Despres [34], and was later extended to a relaxed iteration scheme and a higher order transmission condition [35]. Another class of domain decomposition method is based on Schur complement. In the Schur complement method, internal elimination is carried out independently, which results in a reduced system relating to the interface unknowns. Using this concept, the finite element tearing and interconnect (FETI) method has been proposed, and the field continuity on the domain interface is enforced using Lagrange multipliers. The FETI method was originally developed to solve large computational mechanic problems [36], and was later extended to electromagnetic simulations such as FETI dual-primal (FETI-DP) method [37].

One of the constraints for some implementations of domain decomposition is the conformality of the interface meshing between different domains [34], [36], [37]. However, because of the different electrical properties of the decomposed domains, the meshing requirement for each domain does not need to be identical. The flexibility of non-conformal discretization across domains largely relaxes the mesh generation and adaptive mesh refinement process [38], [39], especially in multiscale structures. A popular approach, which enables geometrical non-conforming decomposition, is the mortar element method. The mortar element method was first introduced in the context of Lagrange finite element and spectral approximations for 2-D elliptic PDEs [40]. The Lagrange multipliers are chosen in a suitable subspace of the space of traces of the finite elements considered in one of the two adjacent subdomains [41]. The mortar element method has been successfully demonstrated for simulating electromagnetic problems [42]. Another approach, based on Robin or another type of transmission boundary for realizing non-conformal domain decomposition, is the cement element method [43]. The major difference between the cement method and the FETI-DP method is that the cement element method expands the dual variables on the interface explicitly instead of generating Boolean projections as in the FETI-DP method [37], [40]. This method does not require mortar and non-mortar sides,

and exhibits quick convergence [44], [45]. Recently, the non-conformal FETI-DP has been developed [46]. Both the Lagrange multiplier-based and cement element-based approaches, which are shown to be efficient in simulating periodic structures such as antenna arrays, have been studied.

In recent years, domain decomposition schemes in the time domain using the dual-field time-domain finite-element method and the discontinuous Galerkin Method have been developed [47], [48]. However, transient non-conformal domain decomposition is still very challenging, especially for the FDTD scheme. The updating equations in the FDTD method make it difficult for addressing non-conformal subdomain interface. Therefore, domain decomposition using the FDTD scheme has only been implemented for structures with conformal meshing [49].

### 2.2.4 Conductor Surface Roughness Modeling

In IC fabrication, signal traces contain rough surfaces to increase the adhesion between conductor and dielectric materials, such as in organic package substrates. This creates "tooth-like" surfaces (as shown in Figure 6) with roughness height in the order of micrometers. Most electromagnetic solvers are developed based on the assumption that the conductor surface is smooth. Although conductor loss can be captured by accurate modeling of skin-effect, this assumption begins to break down in high frequencies where the effect of surface roughness becomes dominant. At high frequencies, the surface roughness height becomes comparable to skin depth, resulting in significant increase in power loss. On one hand, accurate modeling of the surface roughness is a necessity to ensure the accuracy of the simulation result; on the other hand, surface roughness exhibits random patterns as shown in Figure 7, making it difficult to model these effects in electromagnetic solvers.

The earliest attempts generalize the rough surface into a 2-D periodic distribution of simple shapes. In [50], rough surface is modeled by 2-D rectangular and triangle

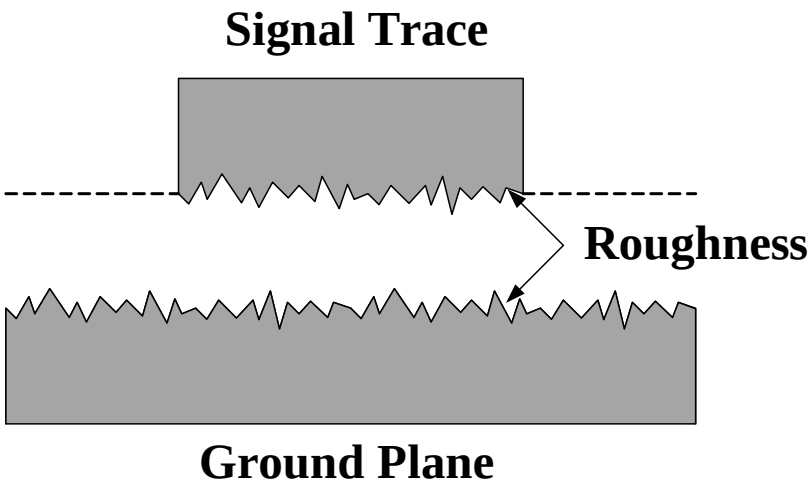


**Figure 6:** Microstrip line with surface roughness on both signal trace and ground plane.

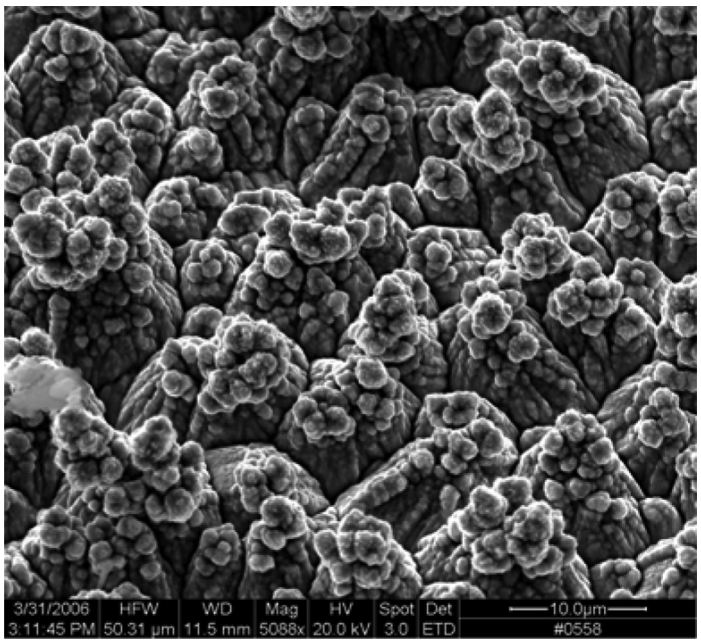


**Figure 7:** SEM photograph of rough copper surface of 5000× magnification [1].

periodic grooves. Two scenarios, namely the current flow parallel to the grooves and the current flow transverse to the grooves, are investigated. Analytical expressions are derived for easy implementation. However, the 2-D assumption is not a true representation of the real surface roughness distribution. Base on the numerical results in [50], an analytical expression with enhancement factor (or correction factor) is developed in [51] using curve fitting. The enhancement factor modifies the conductivity of the metal material, making it frequency-dependent. It has been demonstrated that this method is accurate below 10 GHz. However, the enhancement factor saturates at high frequencies, making it inapplicable for high-frequency simulation. Other methods based on the 2-D roughness distribution for different applications have also been derived [52].

To more accurately model surface roughness, methods that represent the rough surface profile with periodic 3-D simple geometries have been developed. In [1], the random roughness is modeled by conducting hemispheres sitting on the surface of the conductor. Analytical solution of the enhancement factor is derived by applying the plane wave scattering theory. This method is demonstrated to be accurate in modeling the loss of microstrip lines up to 30 GHz and later has been extended to stripline interconnects [53]. To overcome the early saturation of enhancement factor using the method in [1], the rough surface is modeled by conducting sphere bundles sitting on the conductor surfaces, creating a "pyramid-like" structure [54]. Other attempts have also been made including introducing an effective conductivity layer on the rough surfaces and the enhancement factor is extracted using electromagnetic solvers [55].

Another type of surface roughness modeling involves direct tackling of the roughness without generalizing roughness distribution into equivalent shapes or surfaces. The most straightforward way is to create 3-D structures with roughness details and

simulate using commercial full-wave solvers [56]. However, this method is computationally inefficient. Modified full-wave solutions are proposed with decreased computational time in [57]. In [58], the surface is considered as a complete random surface and a 2-D parallel waveguide problem is investigated. The second-order small perturbation method is applied to derive a closed-form expression for the coherent wave propagation and power loss. The derived result is expressed in terms of a double Sommerfeld integral. This method is then extended to 3-D problems [59]. However, the implementation of the method is still time-consuming.

It is important to note that, all the aforementioned methods have investigated the surface roughness modeling of 2-D problems or 3-D problems for transmission lines supporting a transverse electromagnetic (TEM) mode, such as microstrip lines and coaxial lines. In this dissertation, a novel interconnect, the substrate integrated waveguide (SIW), is the structure of interest. The dominant mode is the transverse electric (TE) mode with operating frequency up to 170 GHz. Unfortunately, no accurate solution of surface roughness modeling in applications with TE modes has been presented before. Moreover, modeling surface roughness in frequencies this high and integrating surface roughness modeling into full-wave solvers are extremely challenging.

## *2.3 Technical Focus of the Dissertation*

The aforementioned previous works show the advantages and limitations of the existing computational methods. These post challenges in transient simulation of multi-scale chip-package structures. New schemes need to be developed in order to overcome the limitations with significant improvement of computational capability, speed and accuracy, which is the essence of this dissertation. The technical focus of this dissertation is listed as follows:

1. The design and development of a unconditionally stable transient solver. The

Laguerre-FDTD scheme is chosen to be the core algorithm.

2. The rigorous incorporation of skin-effect into the transient solver, which reduces the computational complexity while maintaining accuracy.

3. The development of a transient non-conformal domain decomposition scheme based on Laguerre-FDTD method for the simulation of multiscale structures.

4. Simulation of multiscale chip-package problems based on the proposed schemes.

5. The investigation of an analytical solution for the conductor surface roughness modeling of SIW. The method should be easy for incorporation into full-wave solvers, such as the Laguerre-FDTD solver and other commercial solvers.

# CHAPTER III

# LAGUERRE-FDTD METHOD FOR TRANSIENT SIMULATION

## *3.1 Introduction*

In the time domain, simulating multiscale structures using the conventional FDTD method is highly inefficient due to the stability condition. The time step is confined by the smallest feature size of the simulated structure, making the simulation time prohibitively long. The Laguerre-FDTD method is introduced to overcome the stability issue associated with the conventional FDTD method. By using Laguerre basis functions to expand time, Laguerre-FDTD is no longer a marching-on-in-time scheme but a marching-on-in-order scheme. Laguerre polynomials are defined from time $t = 0$ to $t = +\infty$ and higher order terms can be generated recursively. All the Laguerre polynomials are orthogonal with respect to a weighting function in a function space defined by the inner product of two continuous functions [8]. It is important to note that the weighted Laguerre polynomials converge to zero as time $t \to \infty$, which is desired for time-domain simulation.

## *3.2 Expanding Time Using Laguerre Basis Function*

In the Laguerre-FDTD method, a time-domain waveform can be represented as a sum of infinite Laguerre basis functions $\varphi_q(\bar{t})$ scaled by Laguerre basis coefficients $\mathbf{W}^q$ as

$$\mathbf{W}(t) = \sum_{q=0}^{\infty} \mathbf{W}^q \varphi^q(\bar{t}) \tag{3}$$

where $\bar{t} = t \cdot s$, $s$ is the time scaling factor, and $t$ is time; Superscript $q$ denotes

the Laguerre coefficient of order $q$. By properly choosing the time scale factor, the simulation time scale can be increased to the order of seconds. For numerical implementation, the number of basis functions is truncated to $N$, where the optimum selection of $N$ is discussed in [14].

The Laguerre basis functions $\varphi_q(\bar{t})$ can be expressed as

$$\varphi_q(\bar{t}) = e^{-\bar{t}/2} L_q(\bar{t}) \tag{4}$$

where $L_q(\bar{t})$ is the Laguerre polynomial which is defined recursively as

$$L_0(\bar{t}) = 1 \tag{5}$$

$$L_1(\bar{t}) = 1 - \bar{t} \tag{6}$$

and for $q \geq 2$

$$qL_q(\bar{t}) = (2q - 1 - \bar{t})L_{q-1}(\bar{t}) - (q-1)L_{q-2}(\bar{t}). \tag{7}$$

The Laguerre polynomials are orthogonal with respect to the weighting function $e^{-t}$, given by

$$\int_0^\infty e^{-t} L_u(t) L_v(t) dt = \delta_{uv}. \tag{8}$$

To be noted, these basis functions are also orthogonal with respect to the scaled time variable $\bar{t}$ as

$$\int_0^\infty \varphi^p(\bar{t}) \varphi^q(\bar{t}) d\bar{t} = \delta_{pq}. \tag{9}$$

Assuming an isotropic, non-dispersive, lossy media, in Cartesian coordinates, the 3-D Maxwell's equations can be written as

$$\frac{\partial E_x}{\partial t} = \frac{1}{\varepsilon}\left(\frac{\partial H_z}{\partial y} - \frac{\partial H_y}{\partial z} - J_x - \sigma E_x\right) \tag{10}$$

$$\frac{\partial E_y}{\partial t} = \frac{1}{\varepsilon}\left(\frac{\partial H_x}{\partial z} - \frac{\partial H_z}{\partial x} - J_y - \sigma E_y\right) \tag{11}$$

$$\frac{\partial E_z}{\partial t} = \frac{1}{\varepsilon}\left(\frac{\partial H_y}{\partial x} - \frac{\partial H_x}{\partial y} - J_z - \sigma E_z\right) \tag{12}$$

$$\frac{\partial H_x}{\partial t} = \frac{1}{\mu}\left(\frac{\partial E_y}{\partial z} - \frac{\partial E_z}{\partial y}\right) \tag{13}$$

$$\frac{\partial H_y}{\partial t} = \frac{1}{\mu}\left(\frac{\partial E_z}{\partial x} - \frac{\partial E_x}{\partial z}\right) \tag{14}$$

$$\frac{\partial H_z}{\partial t} = \frac{1}{\mu}\left(\frac{\partial E_x}{\partial y} - \frac{\partial E_y}{\partial x}\right) \tag{15}$$

where $\varepsilon$ is the electric permittivity, $\mu$ is the magnetic permeability, $\sigma$ is the electric conductivity; $J_x$, $J_y$, and $J_z$ are the excitations along $x$, $y$, and $z$ axes, respectively.

For brevity, only the derivation of formulas for electric field component $E_x\,|_{i,j,k}$ in $x$-direction is discussed. Formulas for electric field components in $y$- and $z$-directions can be derived in a similar manner. Discretizing the differential equation (10) in Laguerre domain using temporal testing procedure yields

$$\begin{aligned} E_x^q\,|_{i,j,k} = {} & \bar{C}_y^E\,|_{i,j,k}\,(H_z^q\,|_{i,j,k} - H_z^q\,|_{i,j-1,k}) - \bar{C}_z^E\,|_{i,j,k}\,\left(H_y^q\,|_{i,j,k} - H_y^q\,|_{i,j,k-1}\right) \\ & - \frac{2}{s\varepsilon_{i,j,k}} J_x^q\,|_{i,j,k} - \frac{2\sigma_{i,j,k}}{s\varepsilon_{i,j,k}} E_x^q\,|_{i,j,k} - 2\sum_{n=0,q>1}^{q-1} E_x^n\,|_{i,j,k} \end{aligned} \tag{16}$$

where

$$\bar{C}_y^E\,|_{i,j,k} = \frac{2}{s\varepsilon_{i,j,k}\Delta\bar{y}_j} \tag{17}$$

$$\bar{C}_z^E\,|_{i,j,k} = \frac{2}{s\varepsilon_{i,j,k}\Delta\bar{z}_k} \tag{18}$$

where $\Delta\bar{y}_j$ and $\Delta\bar{z}_k$ are the distance between the center nodes where magnetic fields are located. Figure 8 shows the position of electric and magnetic field in the form of coefficients of order $q$ in 3-D cells in Laguerre domain.

Similarly, discretizing time derivative differential Equation (14) and (15) for magnetic fields and inserting into (16), with some manipulations, we can obtain the linear equation for electric field in $x$-direction as

$$\begin{aligned}
&\Big(1 + \bar{C}_y^E\,|_{i,j,k}\,\bar{C}_y^H\,|_{i,j,k} + \bar{C}_y^E\,|_{i,j,k}\,\bar{C}_y^H\,|_{i,j-1,k} \\
&+\bar{C}_z^E\,|_{i,j,k}\,\bar{C}_z^H\,|_{i,j,k} + \bar{C}_z^E\,|_{i,j,k}\,\bar{C}_z^H\,|_{i,j,k-1} + \frac{2\sigma_{i,j,k}}{s\varepsilon_{i,j,k}}\Big)\,E_x^q\,|_{i,j,k} \\
&- \bar{C}_y^E\,|_{i,j,k}\,\bar{C}_y^H\,|_{i,j,k}\,E_x^q\,|_{i,j+1,k} + \bar{C}_y^E\,|_{i,j,k}\,\bar{C}_x^H\,|_{i,j,k}\,E_y^q\,|_{i+1,j,k} \\
&- \bar{C}_y^E\,|_{i,j,k}\,\bar{C}_x^H\,|_{i,j,k}\,E_y^q\,|_{i,j,k} - \bar{C}_y^E\,|_{i,j,k}\,\bar{C}_y^H\,|_{i,j-1,k}\,E_x^q\,|_{i,j-1,k} \\
&- \bar{C}_y^E\,|_{i,j,k}\,\bar{C}_x^H\,|_{i,j-1,k}\,E_y^q\,|_{i+1,j-1,k} + \bar{C}_y^E\,|_{i,j,k}\,\bar{C}_x^H\,|_{i,j-1,k}\,E_y^q\,|_{i,j-1,k} \\
&+ \bar{C}_z^E\,|_{i,j,k}\,\bar{C}_x^H\,|_{i,j,k}\,E_z^q\,|_{i+1,j,k} - \bar{C}_z^E\,|_{i,j,k}\,\bar{C}_x^H\,|_{i,j,k}\,E_z^q\,|_{i,j,k} \\
&- \bar{C}_z^E\,|_{i,j,k}\,\bar{C}_z^H\,|_{i,j,k}\,E_x^q\,|_{i,j,k+1} - \bar{C}_z^E\,|_{i,j,k}\,\bar{C}_x^H\,|_{i,j,k-1}\,E_z^q\,|_{i+1,j,k-1} \\
&+ \bar{C}_z^E\,|_{i,j,k}\,\bar{C}_x^H\,|_{i,j,k-1}\,E_z^q\,|_{i,j,k-1} - \bar{C}_z^E\,|_{i,j,k}\,\bar{C}_z^H\,|_{i,j,k-1}\,E_x^q\,|_{i,j,k-1} \\
=\ & -2\bar{C}_y^E\,|_{i,j,k}\left(\sum_{n=0,q>1}^{q-1} H_z^n\,|_{i,j,k} - \sum_{n=0,q>1}^{q-1} H_z^n\,|_{i,j-1,k}\right) \\
&+ 2\bar{C}_z^E\,|_{i,j,k}\left(\sum_{n=0,q>1}^{q-1} H_y^n\,|_{i,j,k} - \sum_{n=0,q>1}^{q-1} H_y^n\,|_{i,j,k-1}\right) \\
&- \frac{2}{s\varepsilon_{i,j,k}} J_x^q\,|_{i,j,k} - 2\sum_{n=0,q>1}^{q-1} E_x^n\,|_{i,j,k}
\end{aligned} \tag{19}$$

where

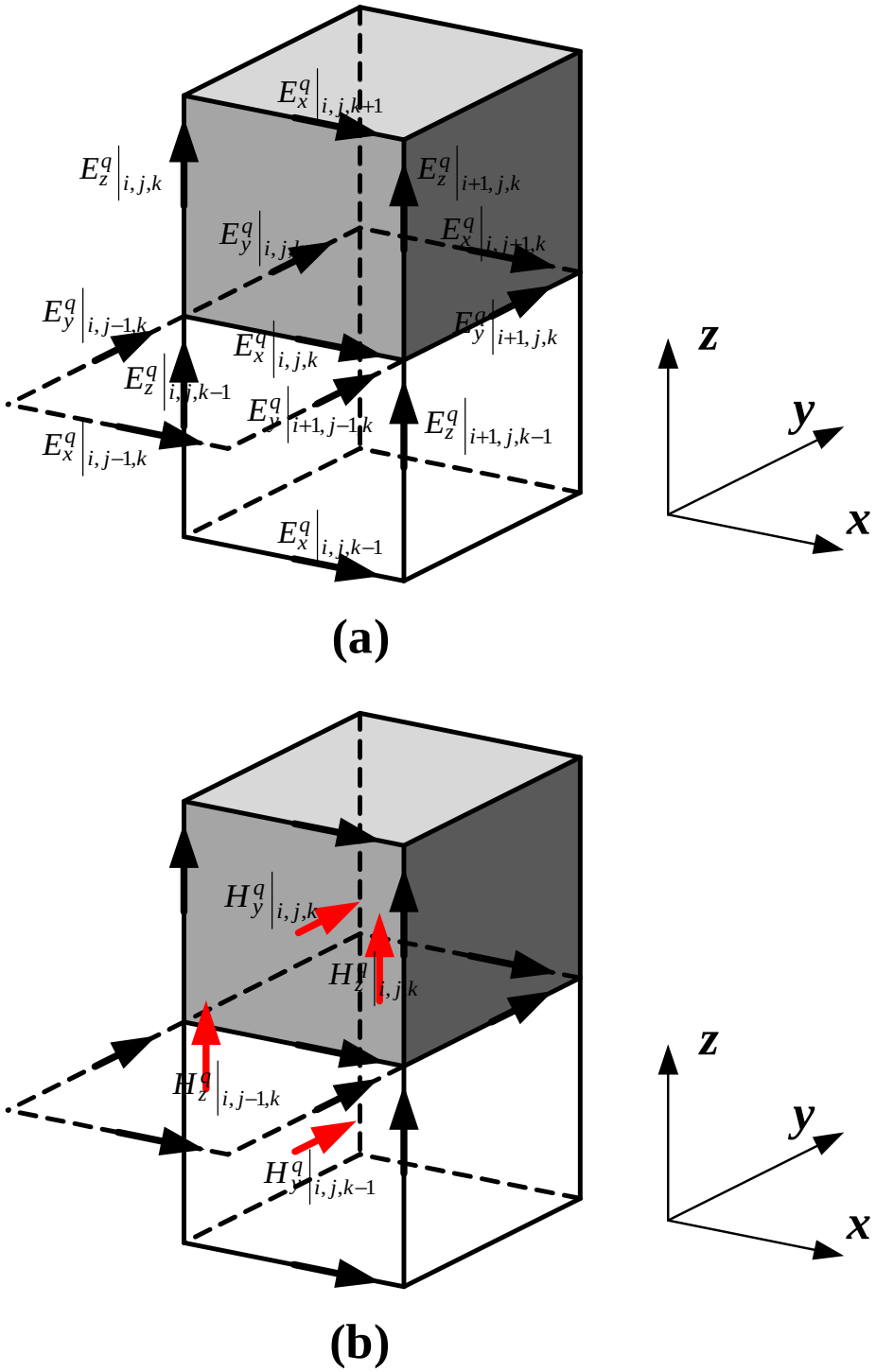


**Figure 8:** Positions of the (a) electric field (black arrow) and (b) magnetic fields (red arrow) of order $q$ in 3-D cells.

$$\bar{C}_x^H \mid_{i,j,k} = \frac{2}{s\mu_{i,j,k}\Delta x_i} \tag{20}$$

$$\bar{C}_y^H \mid_{i,j,k} = \frac{2}{s\mu_{i,j,k}\Delta y_j} \tag{21}$$

$$\bar{C}_z^H \mid_{i,j,k} = \frac{2}{s\mu_{i,j,k}\Delta z_k} \tag{22}$$

where $\Delta x_i$, $\Delta y_j$, and $\Delta z_k$ are the length of the edge where electric fields are located. The detailed derivation of the formulations can be found in Appendix A.

## *3.3 System Matrix*

It can be observed from the coefficient equation shown in (19) that the field component $E_x \mid_{i,j,k}$ is related to the adjacent twelve electric field components and four magnetic field components. The sum of magnetic field Laguerre coefficients can be considered as known since they are one order lower $(q-1)$ than the electric field counterparts. Therefore, by solving the linear system $\mathbf{Ax} = \mathbf{b}$ where each row has thirteen nonzero terms, the Laguerre basis coefficients for each field component can be determined. The time-domain waveform can therefore be recovered. The detailed solving steps are as follows

1. Initialization: $q = 0$, $\mathbf{E}^0$, $\mathbf{H}^0$;
2. Form the system matrix $\mathbf{A}$;
3. Update system right-hand-side excitation vector $\mathbf{b}$;
4. Update $\mathbf{E}^q$ by solving system matrix;
5. Update $\mathbf{E}^{q-1}$ using updated $\mathbf{E}^q$;
6. Increment $q = q + 1$ and go to step (4) if $q < q_{stop}$, otherwise go to next step;
7. Recover the time-domain waveform.

## *3.4 Boundary Conditions*

Boundary conditions define the unique solution of Maxwell's equations in a given computational domain. In time-domain simulation, some boundary conditions are often adopted.

**Perfect Electric Conductor (PEC) Boundary Condition**: The implementation of PEC boundary is most straightforward. It can be realized by setting the tangential electric field to zero at the boundary. In Laguerre-FDTD method, time-domain waveform is not directly solved but is recovered from the solution of coefficient equations. However, in Laguerre domain, the implementation of the PEC boundary is still easy. Only the Laguerre coefficients associated with the boundary electric field need to be set to zero. The PEC boundary can be used as the boundary of the air box that surrounds the structure of interest. To be noted, the radiation from the structure of interest should be low, otherwise, the PEC box will introduce simulation errors. The PEC boundary can also be adopted in simulating conductor structures. However, this will also introduce simulation errors since skin-effect is neglected at high frequencies. Surface impedance boundary condition can be used to model the skin-effect, which is one of the major topics of the dissertation.

**First-Order Absorbing Boundary Condition (ABC)**: The implementation of the first-order ABC is also straightforward. By discretizing the first-order ABC equation in Laguerre domain, relationship of the boundary electric field component and the one in the adjacent cell is establish. The ABC is widely used as the boundary of the air box which truncates the computational domain. Any radiation from the structure of interest can be absorbed at the boundary which ensures simulation accuracy. The first-order ABC is adopted for most of the simulation cases within this dissertation.

**Second-Order Absorbing Boundary Condition (ABC)**: The second-order ABC is more complex that the first-order ABC. However, the absorption quality is

usually superior than the first-order ABC. If high absorption quality is required at the boundary, the second-order ABC should be adopted. In the scope of this dissertation, the second-order ABC is usually not needed.

**Perfect Matched Layer (PML) Boundary Condition**: The absorption quality of the PML boundary condition is the best compared with the aforementioned ABC. However, the implementation of the PML boundary is complicated and requires additional boundary cells [60]. This results in additional computational cost. It is important to noted that, for simulations such as radar cross section (RCS), high quality of absorption is needed at the boundary. However, in this dissertation, for all the structure of interest, the PML boundary condition is not required and has not been implemented.

The detailed derivation and formulations related to the boundary conditions are given in Appendix A.

## *3.5 Frequency-Domain Result Extraction*

For transient computational methods such as Laguerre-FDTD method, the direct result is always in time domain (e.g. port electric field waveform). To obtain the frequency-domain results (e.g. $S$-parameters), time-domain results need to be post-processed. In this section, some techniques related to the frequency-domain result extraction are discussed.

### 3.5.1 Embedding and De-Embedding Port Resistors

When extracting frequency-domain results (e.g. $S$-parameters) from time-domain simulation results, the transient response needs to decay to zero in a finite length of time. For high-Q structures, the decay in time-domain response can be slow resulting in prohibitively long simulation time. To accelerate the simulation speed, port resistors can be used. Though incorporating resistors has been addressed before [61], [62], none of the literature considers the influence of resistors on the frequency response

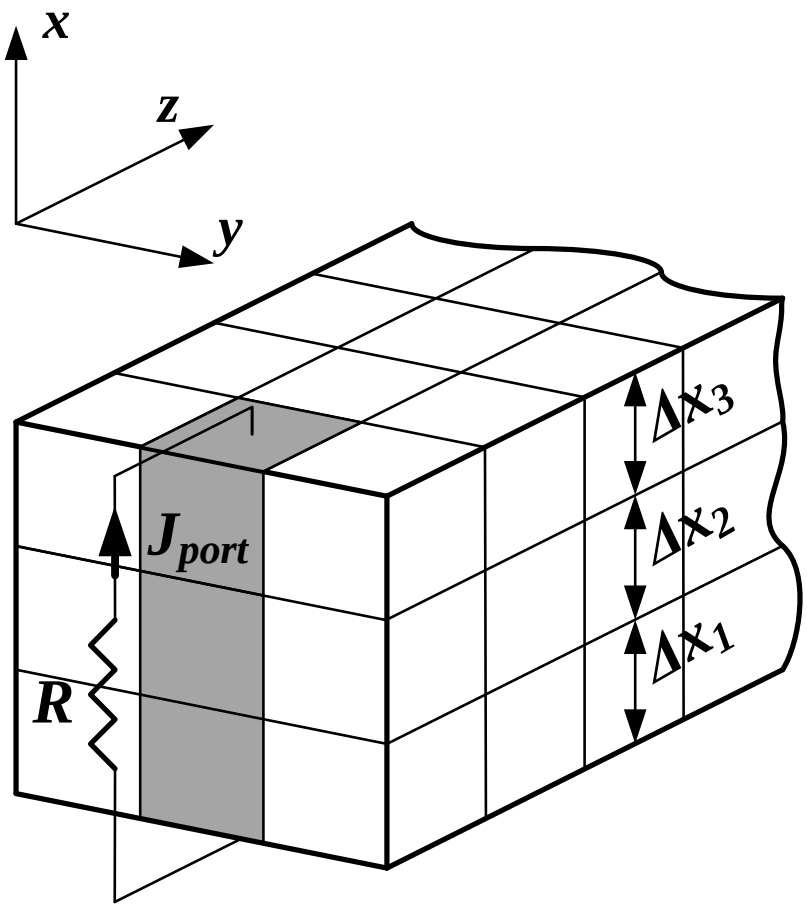


**Figure 9:** Embedded resistor for one port with three cells in the $x$-direction.

after de-embedding. In this work, port resistors are de-embedded after time-domain simulation to ensure that they do not alter the results.

For simplicity, only the implementation for a two port network is presented. The method can be extended to multi-port network as well. Figure 9 shows the attached resistor $R$ for one port with three cells in $x$-direction. An additional unknown $J_{port}$ is introduced which denotes the current flow through the shunt resistor. Therefore, (10) can be modified as

$$\frac{\partial E_x}{\partial t} = \frac{1}{\varepsilon}\left(\frac{\partial H_z}{\partial y} - \frac{\partial H_y}{\partial z} - J_x - J_{x,port} - \sigma E_x\right). \tag{23}$$

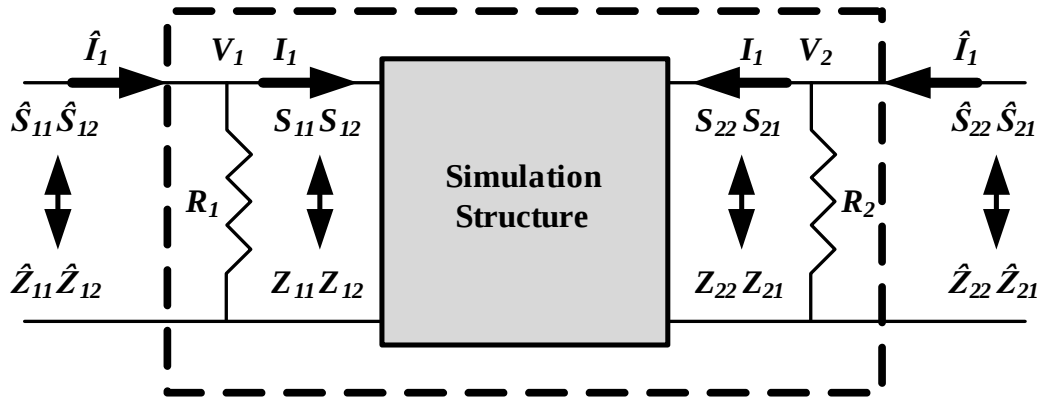


**Figure 10:** Equivalent network for the simulation structure (two ports) with embedded resistors.

Discretizing (23) in the Laguerre domain yields

$$\begin{aligned} E_x^q|_{i,j,k} = {} & \bar{C}_y^E|_{i,j,k}\left(H_z^q|_{i,j,k} - H_z^q|_{i,j-1,k}\right) \\ & - \bar{C}_z^E|_{i,j,k}\left(H_y^q|_{i,j,k} - H_y^q|_{i,j,k-1}\right) \\ & - \frac{2}{s\varepsilon_{i,j,k}} J_x^q|_{i,j,k} - \frac{2}{s\varepsilon_{i,j,k}} J_{x,port}^q|_{i,j,k} \\ & - \frac{2\sigma_{i,j,k}}{s\varepsilon_{i,j,k}} E_x^q|_{i,j,k} - 2\sum_{n=0,q>1}^{q-1} E_x^n|_{i,j,k}. \end{aligned} \tag{24}$$

In (24), it can be observed that an additional term for port current is added to the b vector as compared to (16). Suppose that the $y$-$z$ cross sectional area of the cells in Figure 9 is $A$, the port current and electric field can be related by

$$J_{x,port}^q = \frac{I^q}{A} = \frac{\sum_{i=1}^{3} \Delta x_i E_{x,i}^q}{RA}. \tag{25}$$

To de-embed the resistor after simulation, consider the same network for calculating S-parameters. Figure 10 shows the topology of the network. The network within the solid box is the original network whose $S$-parameters $[S]$ are to be determined

whereas the one with shunt resistors attached to each port inside the dashed box is the modified network with S-parameters $[\hat{S}]$. The de-embedding procedure can be implemented as follows

1. Calculate S-parameters $[\hat{S}]$ of the modified network from the time domain response;
2. Convert S-parameters $[\hat{S}]$ into Z-parameters $[\hat{Z}]$;
3. Calculate $[Z]$ from $[\hat{Z}]$ using network transformation;
4. Convert $[Z]$ into $[S]$.

To realize step 3, we have

$$[\hat{I}] = [I] + [R]^{-1}[V] \tag{26}$$

$$[\hat{Z}][\hat{I}] = [V] \tag{27}$$

$$[Z][I] = [V] \tag{28}$$

where $[I] = [I_1, I_2]^T$, $[V] = [V_1, V_2]^T$. Combining (26) to (28) results in

$$[Z] = (\mathbf{I} - [\hat{Z}][R]^{-1})^{-1}[\hat{Z}] \tag{29}$$

where $\mathbf{I}$ is the identity matrix with the same dimension of port numbers.

### 3.5.2 Voltage-Voltage Extraction Scheme

The voltage-voltage extraction of the $S$-parameters is the most straightforward frequency-domain extraction method. Since the $S$-parameter is defined as the ratio of reflected and incident port voltage, a simple fast Fourier transform (FFT) of the transient

voltage waveform is needed. Particularly, $S_{ij}$ ($i$ and $j$ are port numbers) can be calculated as

$$S_{ij} = \frac{FFT(V_{i,\text{ref}})}{FFT(V_{j,\text{inc}})} \tag{30}$$

where $V_{i,\text{ref}}$ and $V_{j,\text{inc}}$ are the reflection and incident voltage of ports $i$ and $j$, respectively.

However, in real simulations, incident and reflected wave cannot be easily distinguished. This scheme is only useful with planar structure whose feed line is relatively long. This is obviously not desired since unnecessary computational resource is wasted for the long feed line. Also, port energy needs to be completely absorbed to ensure the accuracy of the extraction. Therefore, although the calculation is straightforward, this extraction scheme is rarely used.

### 3.5.3 Voltage-Current Extraction Scheme

The voltage-current extraction scheme does not calculate the $S$-parameters directly. By recording the port voltage and current in time domain, the $Z$-parameters of the test structure can be obtained as

$$Z_{ij} = \frac{FFT(V_i)}{FFT(I_j)} \tag{31}$$

where $V_i$ and $I_j$ are the voltage and current of ports $i$ and $j$, respectively. The $Z$-parameters are then transferred into $S$-parameters. Although a transformation is needed for calculating $S$-parameters, distinguishing incident and reflected waves is avoided. It is suitable for all types of structures, including planar structures with feed line ports. To be noted, this type of extraction is especially useful for simulations with ports defined inside the structure, such as power-ground planes. Therefore, the

voltage-current extraction scheme is mostly adopted in this dissertation.

To be noted, for planar structures with feed line ports, $S$-parameters can be obtained from an energy wave point of view to reduce the magnitude of ripple generated by aforementioned method. No transformation is needed and the $S$-parameters can be calculated as

$$S_{ij} = \frac{FFT(V_i - I_i Z_0)}{FFT(V_j + I_j Z_0)} \tag{32}$$

where $Z_0$ is the port impedance. Note that this scheme is only valid if the field propagating at the measurement point behaves like a simple plane wave without any evanescent field.

## *3.6 Summary*

In this chapter, a transient full-wave solver is developed based on the unconditionally stable Laguerre-FDTD method. Unlike the marching-on-in-time schemes, the Laguerre-FDTD method eliminates the time-dependent instability by expanding the time-domain wave using Laguerre polynomials. The time step size is only dependent on the solution resolution but not the cell size. This is suitable for simulation of multiscale structures where fine structures are located in certain regions of the computational domain. A scheme for embedding and de-embedding port resistors is implemented to ensure fast convergence of the transient algorithm. Frequency domain extraction methods are also discussed.

# CHAPTER IV

# SKIN-EFFECT MODELING

## *4.1 Introduction*

In low frequency simulation, metal can be justifiably considered as perfect conductor without introducing significant error. However, in the design of high-frequency applications, accurate modeling of conductor loss due to skin-effect is critical since conductor loss cannot be neglected. To be specific, interconnect loss is related to the signal integrity of the electronic system. Failure in capturing the conductor loss may result in pre-silicon design flaws, leading to failure of post-silicon verification.

Efficient transient modeling of skin-effect has been a challenging topic for decades. Usually, a dense mesh needs to be applied to the conductor structures (e.g. interconnects) resulting in significant wastage of computational resources (Figure 11). Among the existing solutions for modeling skin-effect, the surface impedance boundary condition (SIBC) has been widely adopted. However, no implementation method exists for incorporating skin-effect into the Laguerre-FDTD method.

## *4.2 Surface Impedance Boundary Condition*

In this section, the SIBC is introduced and is used to model skin-effect. Rational fitting technique is implemented to decrease the complexity of transformation from frequency domain to Laguerre domain.

### 4.2.1 Theory

To incorporate skin-effect into the Laguerre-FDTD method, the first-order SIBC can be applied based on the assumption that skin depth is less than the smallest feature size of the conductor, which is usually satisfied at high frequencies. To be noted, for

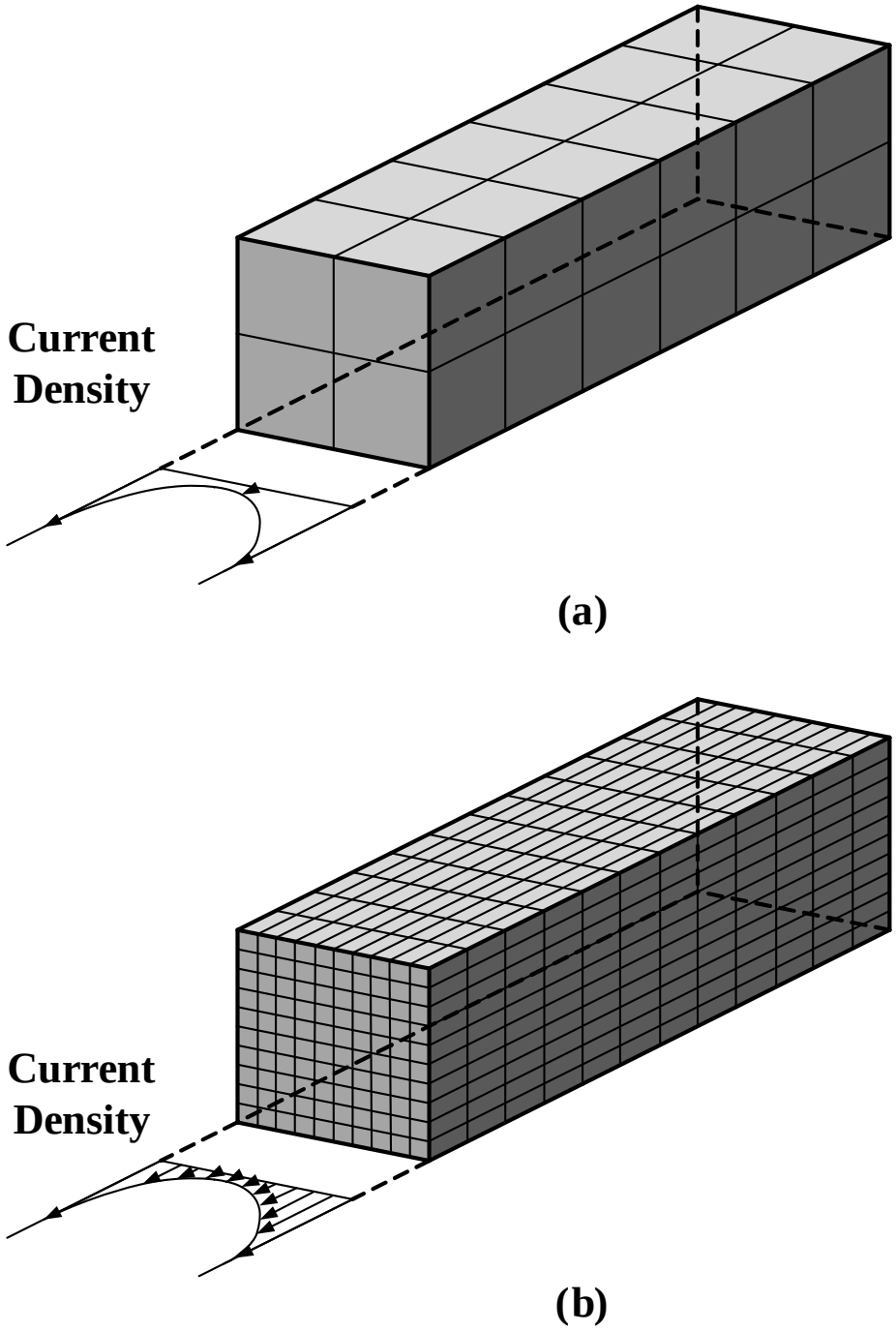


**Figure 11:** Interconnect meshing strategy: (a) coarse mesh inside conductor cannot represent the exponentially decay current which results in inaccurate simulation of the skin-effect and (b) fine mesh inside conductor results in high computational cost.

a very thin (less than the skin depth) conductor structure, this method is no longer accurate and alternatives should be considered, such as resistive boundaries [63]. In SIBC, the tangential electric and magnetic fields on the conductor surface are related by [29]

$$\mathbf{E}_{\tan}(\omega) = Z(\omega)\left[\hat{n} \times \mathbf{H}_{\tan}(\omega)\right] \tag{33}$$

where $\hat{n}$ is the unit vector normal to the conductor surface as shown in Figure 12, $\omega$ is the radian frequency, and $Z(\omega)$ is the surface impedance given by

$$Z(\omega) = \frac{1}{Y(\omega)} = \sqrt{\frac{j\omega\mu}{\sigma + j\omega\varepsilon}}. \tag{34}$$

Note that $\varepsilon$, $\mu$, and $\sigma$ are the electric permittivity, magnetic permeability, and conductivity of the conductor.

By establishing the relationship between electric field and magnetic field on the surface of the conductor, it is possible to model conductor loss without calculating the field inside the conductor. This avoids meshing inside the conductor to capture the exponentially decaying field, and thus, significantly reduces the computational complexity.

### 4.2.2 Rational Fitting

As mentioned earlier, the SIBC is expressed in the frequency domain, and it cannot be directly applied to time-domain simulations. In conventional FDTD method, one solution strategy involves direct Laplace transformation followed by Laplace domain to time domain transformation [28]. However, this results in time integral of zero-order and first-order Bessel functions which are difficult to calculate. Here, without losing accuracy, the frequency-domain expression of SIBC is first transformed into Laplace

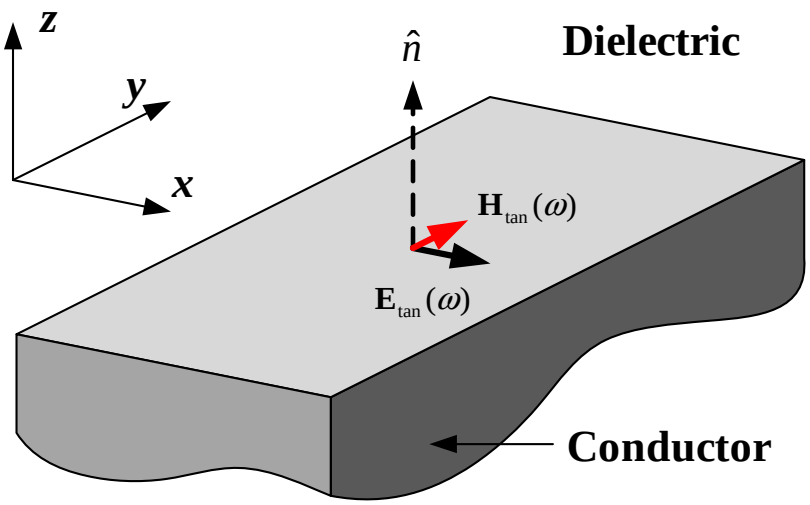


**Figure 12:** Interface of conductor and dielectric materials.

domain using rational fitting [29]. The Laplace domain expression is then transformed into time domain using summation terms which are easy to to be rewritten in the Laguerre domain.

Applying the first-order rational fitting technique to approximate the frequency domain expression of the reciprocal of the surface impedance (surface admittance) in (34), we have

$$Y(s) = \sum_{p=1}^{m} \frac{C_p}{s - A_p} + D \tag{35}$$

where $s = j\omega$, $m$ is the number of terms used in the fitting, $C_p$ and $A_p$ are the fitting coefficient and poles, and $D$ is the constant term that determines the behavior of the rational function as the frequency approaches infinity. Commonly, for infinite frequency range, $D$ can be set to zero and time domain expression of surface admittance can be written as

$$Y(t) = \sum_{p=1}^{m} C_p e^{-A_p t}. \tag{36}$$

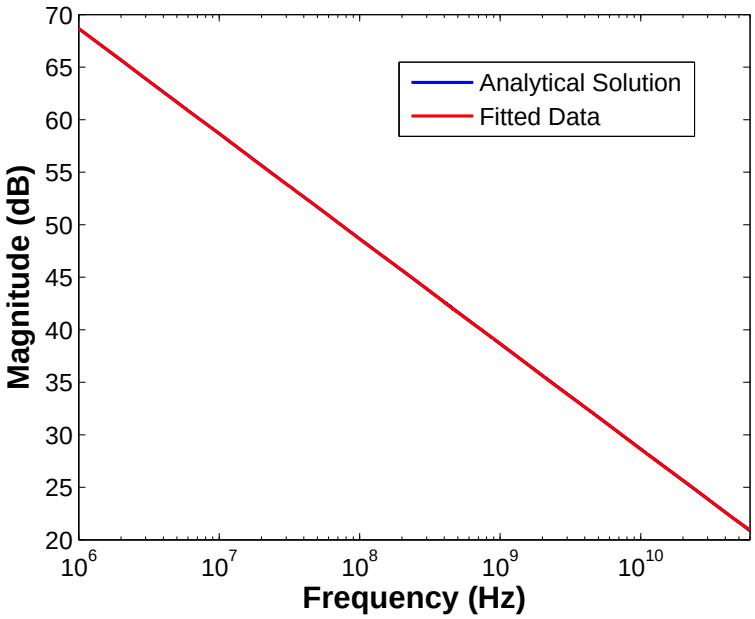


**Figure 13:** Comparison of the analytical solution and data from nine-term fitting with $D$ equal to zero.

Figure 13 shows the comparison of the analytical solution and the fitted data of the admittance term. Fine-term fitting with $D = 0$ is used for comparison. A perfect match can be observed for these two scenarios.

To better illustrate the fitting accuracy, Figure 14 shows the relative error for eight- and nine-term fitting for copper ($\sigma = 5.8 \times 10^7$ S/m) over the 0.1 GHz to 40 GHz band. It can be observed that the accuracy of nonzero constant fitting is slightly higher than zero constant fitting with the same fitting terms. Also, for both selection of $D$, the relative errors are confined within 0.5% for nine-term fitting. The accuracy level is good for the target applications considered in this dissertation.

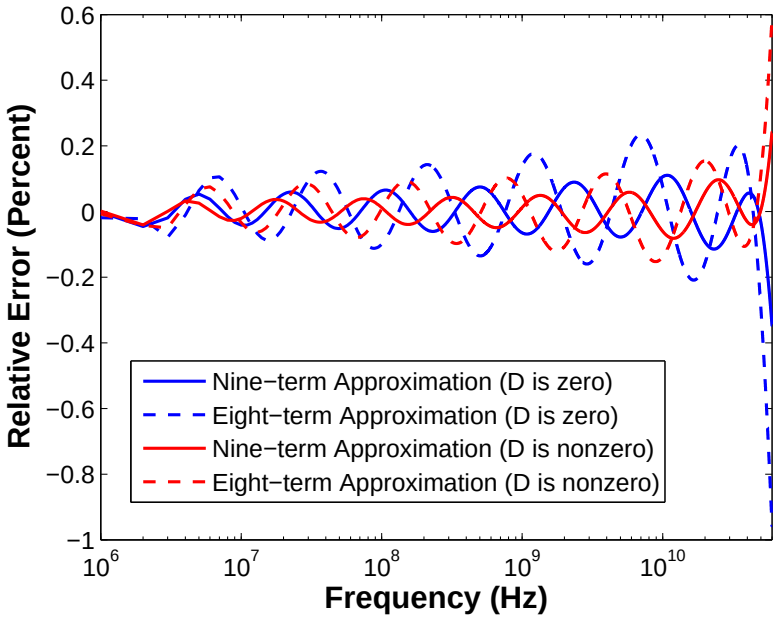


**Figure 14:** Comparison of relative error for eight- and nine-term fitting for copper with $D$ equal to zero and nonzero.

## *4.3 Skin-Effect-Incorporated Laguerre-FDTD Method*

In this section, skin-effect modeling is realized using the SIBC. The SIBC is established in the Laguerre domain and is incorporated into the existing Laguerre-FDTD method. The implementation methods are discussed and compared.

### 4.3.1 SIBC in Laguerre-Domain

It can be observed from (36) that after rational fitting, the time-domain expression of the admittance term can be written in a form that can be easily transformed into Laguerre domain. Using the definition in (3), in Laguerre domain, the coefficient for $Y$ can be written as

$$Y^q = \int_0^\infty Y(t)\varphi_q(\bar{t})dt. \tag{37}$$

In Laguerre domain, denoting

$$Y^q = \sum_{p=1}^{m} C_p G_p^q = \sum_{p=1}^{m} C_p \int_0^{\infty} e^{-A_p t} \varphi_q(\bar{t}) dt \tag{38}$$

and performing integration by parts, the final Laguerre basis coefficient expression can be written as

$$Y^q = \sum_{p=1}^{m} C_p \frac{2}{2A_p + s} \left( \frac{2A_p - s}{2A_p + s} \right)^q. \tag{39}$$

The detailed derivation is given in Appendix B.

### 4.3.2 Magnetic Field Approximation Scheme

For simplicity, consider only the electric field component in the $x$-direction, and assuming that $x$-$y$ plane shown in Figure 15 is the interface of dielectric ($z+$) and conductor ($z-$), the relationship between tangential electric and magnetic fields in the frequency domain can be written as

$$H_{y0}\,|_{i,j,k}\,(\omega) = -Y(\omega) E_x\,|_{i,j,k}\,(\omega). \tag{40}$$

Since the electric and magnetic field nodes are not collocated in the grid, the magnetic field $H_{y0}\,|_{i,j,k}$ collocated with the electric field $E_x\,|_{i,j,k}$ is unknown. This field component can be approximated using the magnetic field component $H_{y0}\,|_{i,j,k}$ above in the half cell where $E_x\,|_{i,j,k}$ is located. This translates to the Laguerre basis coefficients as

$$H_{y0}^q\,|_{i,j,k} \approx H_y^q\,|_{i,j,k} \tag{41}$$

We name this scheme the magnetic field approximation SIBC or MFA-SIBC method.

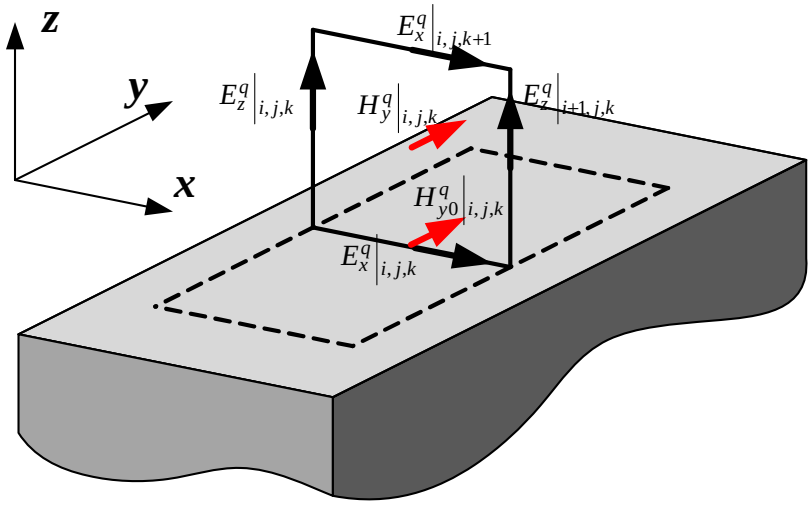


**Figure 15:** Interface cell for dielectric ($z+$ domain) and conductor ($z-$ domain) in Laguerre-FDTD method with SIBC for the magnetic field approximation scheme.

Thus, in the time domain, the relationship between the tangential electric and magnetic fields can be written in convolution form

$$H_y\,|_{i,j,k}\,(t) = -\int_0^t E_x\,|_{i,j,k}\,(t-\tau)Y(\tau)d\tau. \tag{42}$$

The convolution term can be transformed into Laguerre domain using the method in described in [64], where MFA-SIBC can be established by rewriting (42) as

$$\begin{aligned} H_y^q\,|_{i,j,k} &= -\left(\sum_{k=0,q>0}^{q} E_x^k\,|_{i,j,k}\,Y^{q-k} - \sum_{k=0,q>1}^{q-1} E_x^k\,|_{i,j,k}\,Y^{q-k-1}\right) \\ &= -\sum_{p=1}^{m} a_p\left(\sum_{k=0,q>0}^{q} E_x^k\,|_{i,j,k}\,b_p^{q-k} - \sum_{k=0,q>1}^{q-1} E_x^k\,|_{i,j,k}\,b_p^{q-k-1}\right) \\ &= -\sum_{p=1}^{m} W_p^q \end{aligned} \tag{43}$$

where

$$a_p = \frac{2C_p}{A_p + s} \tag{44}$$

$$b_p = \frac{2A_p - s}{2A_p + s}. \tag{45}$$

Here, $W_p^q$ can be expressed recursively as

$$W_p^q = b_p W_p^{q-1} + a_p \left( E_x^q \,|_{i,j,k} - E_x^{q-1} \,|_{i,j,k} \right) \tag{46}$$

$$W_p^0 = a_0 E_x^0 \,|_{i,j,k} \,. \tag{47}$$

To eliminate the intermediate term $W_p^q$, using (44) and (45), (42) can be written as

$$\begin{aligned} H_y^q \,|_{i,j,k} &= -\sum_{p=1}^{m} \left[ a_p E_x^q \,|_{i,j,k} + \left( b_p W_p^{q-1} - a_p E_x^{q-1} \,|_{i,j,k} \right) \right] \\ &= -\sum_{p=1}^{m} \left( a_p E_x^q \,|_{i,j,k} + \alpha_p^{q-1} \right) \end{aligned} \tag{48}$$

where

$$\alpha_p^q = b_p \alpha_p^{q-1} + a_p (b_p - 1) E_x^q \,|_{i,j,k} \tag{49}$$

$$\alpha_p^0 = a_p (b_p - 1) E_x^0 \,|_{i,j,k} \,. \tag{50}$$

Inserting (48) into (167) (Appendix A), the final representation of MFA-SIBC becomes

$$\begin{aligned}
&\left(\sum_{p=1}^{m} a_p + \bar{C}_z^H\,|_{i,j,k}\right) E_x^q\,|_{i,j,k} + \bar{C}_x^H\,|_{i,j,k}\; E_z^q\,|_{i+1,j,k} \\
&- \bar{C}_x^H\,|_{i,j,k}\; E_z^q\,|_{i,j,k} - \bar{C}_z^H\,|_{i,j,k}\; E_x^q\,|_{i,j,k+1} \qquad (51) \\
= &-\sum_{p=1}^{m} \alpha_p^{q-1} + 2 \sum_{n=0,q>1}^{q-1} H_y^n\,|_{i,j,k}\,.
\end{aligned}$$

Note that the left-hand side of (51) represents the nonzero Laguerre basis coefficient of electric-field components in a row of the system matrix whereas the right side corresponds to the value of the right-hand-side excitation vector in the same row.

Therefore, the skin-effect-incorporated Laguerre-FDTD using the MFA-SIBC can now be implemented as follows

1. Initialization: $q = 0$, $\mathbf{E}^0$, $\mathbf{H}^0$;
2. Form the system matrix except on the conductor surface;
3. Apply MFA-SIBC to the system matrix using the left-hand-side of (51);
4. Update system right-hand-side excitation vector except on the conductor surface;
5. Update system right-hand-side excitation vector using the right-hand-side of (51);
6. Update $\mathbf{E}^q$ by solving system matrix;
7. Update $\mathbf{E}^{q-1}$ using updated $\mathbf{E}^q$;
8. Update $\alpha_p^{q-1}$ using (49);
9. Increment $q = q + 1$ and go to step (4) if $q < q_{stop}$.

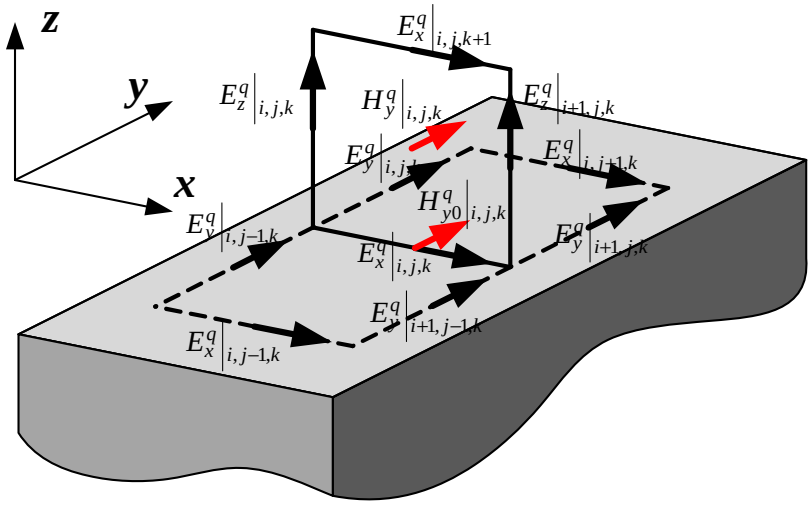


**Figure 16:** Interface cell for dielectric ($z+$ domain) and conductor ($z-$ domain) in Laguerre-FDTD method with SIBC for the electric field approximation scheme.

### 4.3.3 Electric Field Approximation Scheme

Again, considering the case in Figure 16 for electric field in the $x$-direction and making the same assumption as in MFA-SIBC, discretizing (10) in $y$- and $z$-directions with distance increments $\Delta y_j$ and $\Delta z_k/2$, respectively, results in

$$\begin{aligned} E_x^q|_{i,j,k} = {} & \bar{C}_y^E|_{i,j,k}\left(H_z^q|_{i,j,k} - H_z^q|_{i,j-1,k}\right) \\ & - 2\bar{C}_z^E|_{i,j,k}\left(H_y^q|_{i,j,k} - H_{y0}^q|_{i,j,k}\right) \\ & - \frac{2}{s\varepsilon_{i,j,k}} J_x^q|_{i,j,k} - \frac{2\sigma_{i,j,k}}{s\varepsilon_{i,j,k}} E_x^q|_{i,j,k} - 2\sum_{n=0,q>1}^{q-1} E_x^n|_{i,j,k}. \end{aligned} \tag{52}$$

Note that to avoid calculating the electric field component inside the conductor, $H_y^q|_{i,j,k-1}$ in (16) is replaced with $H_{y0}^q|_{i,j,k}$, and is discretized by half of the cell height. This is similar to shifting the surface tangential electric field in between the magnetic field components $H_y^q|_{i,j,k}$ and $H_{y0}^q|_{i,j,k}$. We name this scheme the electric field approximation SIBC or EFA-SIBC method.

As before, the surface tangential electric- and magnetic-field coefficients are related by

$$H_{y0}^{q}\,|_{i,j,k} \;= -\sum_{p=1}^{m}\left(a_p E_x^{q}\,|_{i,j,k} + \alpha_p^{q-1}\right). \tag{53}$$

Inserting (48) into (52) together with the discretization of the magnetic fields, the final expression of SIBC in Laguerre domain is

$$\begin{aligned}
&\Big(1+\bar{C}_y^{E}\,|_{i,j,k}\,\bar{C}_y^{H}\,|_{i,j,k} + \bar{C}_y^{E}\,|_{i,j,k}\,\bar{C}_y^{H}\,|_{i,j-1,k} \\
&+2\bar{C}_z^{E}\,|_{i,j,k}\,\bar{C}_z^{H}\,|_{i,j,k} + 2\bar{C}_z^{E}\,|_{i,j,k}\sum_{p=1}^{m}a_p + \frac{2\sigma_{i,j,k}}{s\varepsilon_{i,j,k}}\Big)\,E_x^{q}\,|_{i,j,k} \\
&-\bar{C}_y^{E}\,|_{i,j,k}\,\bar{C}_y^{H}\,|_{i,j,k}\,E_x^{q}\,|_{i,j+1,k} + \bar{C}_y^{E}\,|_{i,j,k}\,\bar{C}_x^{H}\,|_{i,j,k}\,E_y^{q}\,|_{i+1,j,k} \\
&-\bar{C}_y^{E}\,|_{i,j,k}\,\bar{C}_x^{H}\,|_{i,j,k}\,E_y^{q}\,|_{i,j,k} - \bar{C}_y^{E}\,|_{i,j,k}\,\bar{C}_y^{H}\,|_{i,j-1,k}\,E_x^{q}\,|_{i,j-1,k} \\
&-\bar{C}_y^{E}\,|_{i,j,k}\,\bar{C}_x^{H}\,|_{i,j-1,k}\,E_y^{q}\,|_{i+1,j-1,k} + \bar{C}_y^{E}\,|_{i,j,k}\,\bar{C}_x^{H}\,|_{i,j-1,k}\,E_y^{q}\,|_{i,j-1,k} \\
&+2\bar{C}_z^{E}\,|_{i,j,k}\,\bar{C}_x^{H}\,|_{i,j,k}\,E_z^{q}\,|_{i+1,j,k} - 2\bar{C}_z^{E}\,|_{i,j,k}\,\bar{C}_x^{H}\,|_{i,j,k}\,E_z^{q}\,|_{i,j,k} \\
&-2\bar{C}_z^{E}\,|_{i,j,k}\,\bar{C}_z^{H}\,|_{i,j,k}\,E_x^{q}\,|_{i,j,k+1} \\
=\;& -2\bar{C}_y^{E}\,|_{i,j,k}\left(\sum_{n=0,q>1}^{q-1}H_z^{n}\,|_{i,j,k} - \sum_{n=0,q>1}^{q-1}H_z^{n}\,|_{i,j-1,k}\right) \\
&+4\bar{C}_z^{E}\,|_{i,j,k}\left(\sum_{n=0,q>1}^{q-1}H_y^{n}\,|_{i,j,k} - \frac{1}{2}\sum_{p=1}^{m}\alpha_p^{q-1}\right) \\
&-\frac{2}{s\varepsilon_{i,j,k}}J_x^{q}\,|_{i,j,k} - 2\sum_{n=0,q>1}^{q-1}E_x^{n}\,|_{i,j,k}\,.
\end{aligned} \tag{54}$$

Similarly, the skin-effect-incorporated Laguerre-FDTD using the EFA-SIBC can now be implemented as follows

1. Initialization: $q=0$, $\mathbf{E}^0$, $\mathbf{H}^0$;

2. Form the system matrix except on the conductor surface;

3. Apply EFA-SIBC to the system matrix using the left-hand-side of (54);

4. Update system right-hand-side excitation vector except on the conductor surface;

5. Update system right-hand-side excitation vector using the right-hand-side of (54);

6. Update $\mathbf{E}^q$ by solving system matrix;

7. Update $\mathbf{E}^{q-1}$ using updated $\mathbf{E}^q$;

8. Update $\alpha_p^{q-1}$ using (49);

9. Increment $q = q + 1$ and go to step (4) if $q < q_{stop}$.

### 4.3.4 Stability Discussion

It is known that due to the marching-on-in-order nature, the Laguerre-FDTD method is unconditionally stable. However, by introducing SIBC, the stability of the algorithm is dependent on the conductivity of the metal structure. It can be inferred that the stability will break down when the conductivity of the metal is very low. Nevertheless, this will not affect the real world modeling since materials with very low conductivity are rarely used as metal.

To investigate the stability of the proposed method, a simple microstrip line structure shown in Figure 17 is simulated and analyzed. The structure has a dielectric substrate with width and thickness of $s = 30$ mm and $d = 0.305$ mm. The dielectric constant and loss tangent of the substrate are $\varepsilon_r = 4.5$ and $\tan\delta = 0.025$, respectively. The metal strip is considered as copper line (conductivity $\sigma = 5.8 \times 10^7$ S/m) with length, width and thickness of $l = 93.5$ mm, $w = 0.51$ mm and $t = 0.03$ mm, respectively. The simulated structure is surrounded by an ABC box with height $h = 1$ mm. Two ports are set at each end of the line and Gaussian pulse is used as the excitation.

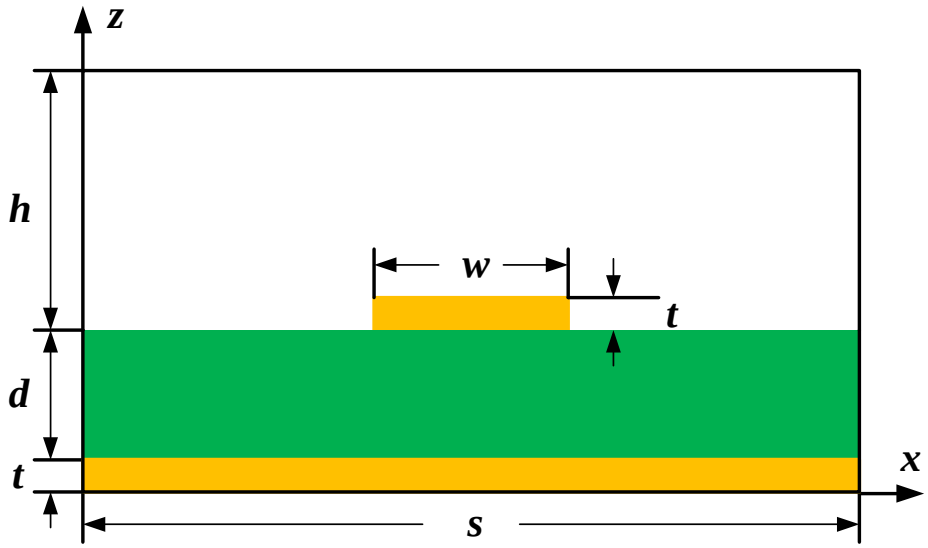


**Figure 17:** Cross-sectional view of the simulated microstrip line.

The ratio of maximum electric field at the observation point at the conductor surface ($E_2$) and the maximum electric field at the source port ($E_1$) is used as a gauge to measure the stability. The conductivity of the line varies from $1 \times 10^{-5}$ S/m to $1 \times 10^{7}$ S/m. It can be observed in Figure 18, that the MFA-SIBC method is stable for conductivity higher than $1 \times 10^{-3}$ S/m. Rapid dispersion occurs for conductivity less than $1 \times 10^{-3}$ S/m. However, EFA-SIBC method is stable across the whole conductivity range shown in Figure 19. This is because approximation (41) in MFA-SIBC uses simple shifting of the field component and is largely dependent on the cell size. To be noted, for both MFA-SIBC and EFA-SIBC methods, non-physical results are obtained as conductivity becomes less than $1 \times 10^{-3}$ S/m since the field magnitude is larger than that of the source. For high conductivity applications, MFA-SIBC is preferred due to its simpler implementation.

## *4.4 Numerical Results*

In this section, the efficiency and accuracy of the skin-effect-incorporated Laguerre-FDTD method is demonstrated with several numerical test cases.

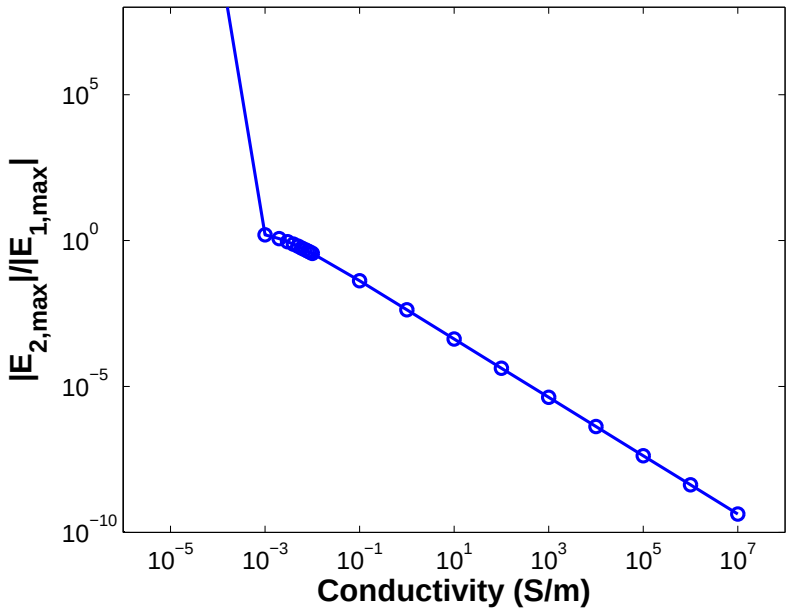


**Figure 18:** Stability analysis of the skin-effect-incorporated Laguerre-FDTD scheme using the MFA-SIBC method with test case of microstrip line.

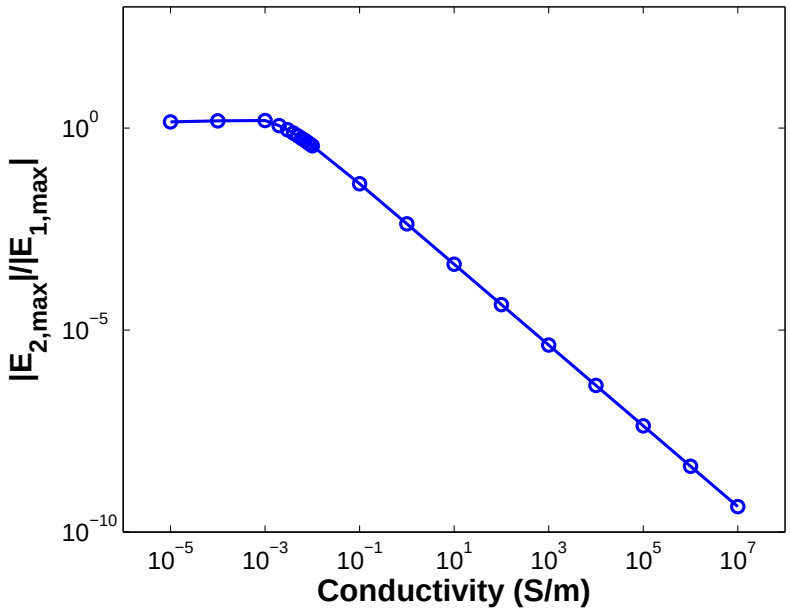


**Figure 19:** Stability analysis of the skin-effect-incorporated Laguerre-FDTD scheme using the EFA-SIBC method with test case of microstrip line.

### 4.4.1 Microstrip Line

A microstrip line that is described in the previous section shown in Figure 17 is first simulated. Note that the thickness of the line cannot be neglected since conductor loss needs to be considered. This makes the microstrip line structure intrinsically multiscale with scale difference of 3117:1 (ratio between largest and smallest feature size which are line length and thickness).

To compare between the standard Laguerre-FDTD method and the skin-effect incorporated Laguerre-FDTD method, two sets of meshing are applied. Figure 20(a) shows the mesh of the microstrip line structure for standard Laguerre-FDTD method. A dense mesh is applied inside the conductor to ensure simulation accuracy. Figure 20(b) shows the mesh for the same structure using skin-effect incorporated Laguerre-FDTD method. In this case, inside of the conductor is not meshed and thus is left blank.

Table 1 shows the mesh density of the microstrip line for different schemes. In addition, simulation using the conventional FDTD method that satisfies the CFL condition using the mesh setting shown in Figure 20(a) and simulation of the Laguerre-FDTD method using the mesh setting shown in Figure 20(b) with PEC boundary for the conductor strip are also performed. Table 1 summarizes the time interval and CPU time of each simulation case. It can be observed that under same meshing, the Laguerre-FDTD method is significantly faster than the conventional FDTD method for multiscale structures since the time step for the latter one is limited by the smallest cell dimension. In this case, the smallest cell dimension for the structure is $\Delta z = 5$ $\mu$m, which makes the time step for the conventional FDTD method $\Delta t = 6.25$ fs whereas the counterpart for the Laguerre-FDTD method is $\Delta t = 1.0$ ps. Moreover, with skin-effect incorporated Laguerre-FDTD method, a significant reduction in simulation time is observed compared to standard Laguerre-FDTD method.

Figure 21 shows the comparison of the time-domain electric field waveform ($E_z$)

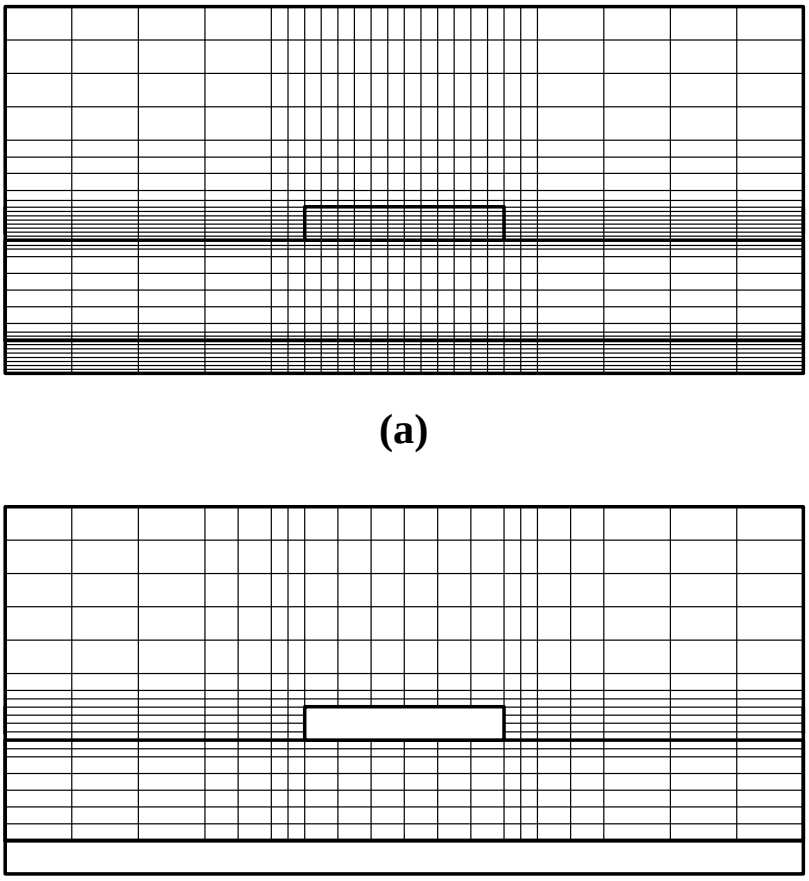


**Figure 20:** Comparison of the cross-sectional meshing grid for (a) standard Laguerre-FDTD and (b) SIBC incorporated Laguerre-FDTD.

**Table 1:** Comparison of the computational cost for different simulation methods.

| Method | $\Delta t$ | No. of Cells | CPU Time |
|---|---|---|---|
| Conventional FDTD | 6.25 fs | 26×80×35 | 10 hr |
| Laguerre-FDTD | 1.0 ps | 26×80×35 | 30 min |
| Laguerre-FDTD (PEC) | 1.0 ps | 20×80×20 | 15 min |
| Laguerre-FDTD (SIBC) | 1.0 ps | 20×80×20 | 15 min |

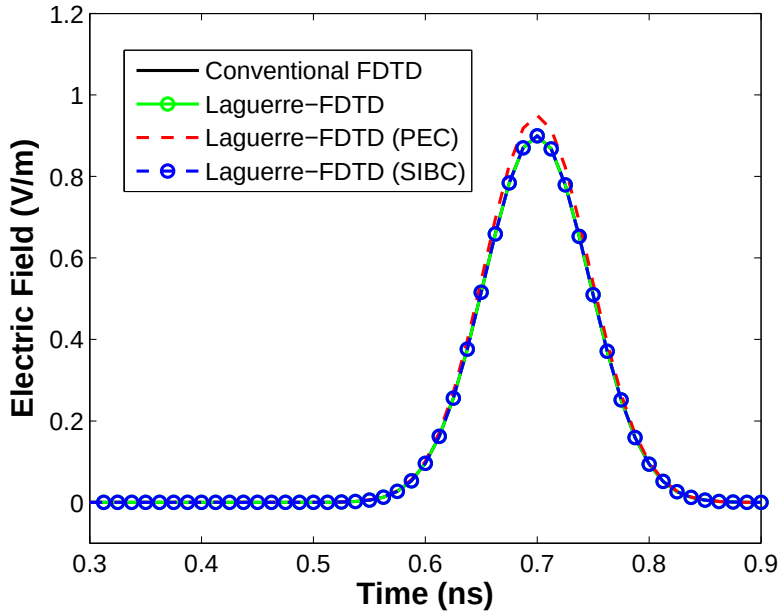


**Figure 21:** Comparison of the time domain electric field waveform at the observation point for conventional FDTD, Laguerre-FDTD, Laguerre-FDTD (PEC) and Laguerre-FDTD (SIBC) methods.

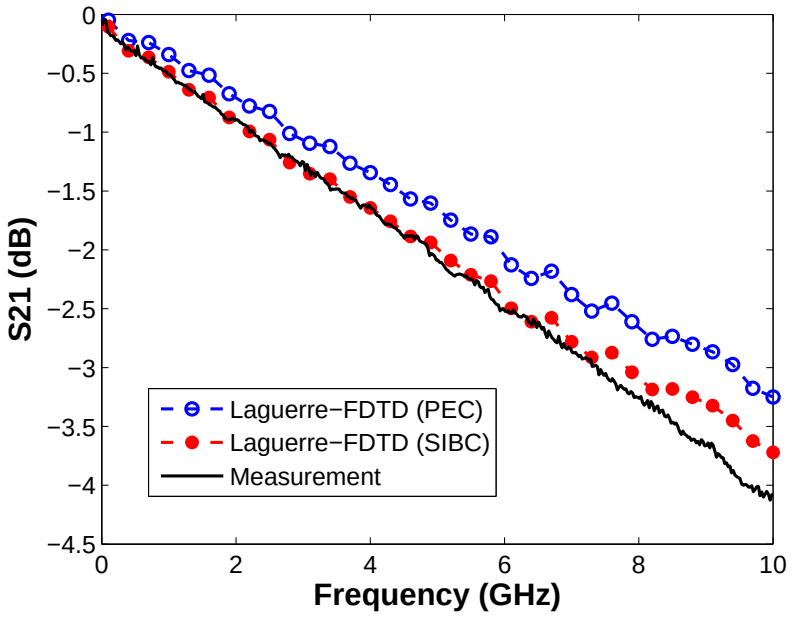


**Figure 22:** Comparison of the microstrip line insertion loss for Laguerre-FDTD (PEC), Laguerre-FDTD (SIBC) methods and measurement.

of the observation point in the middle of the microstrip line along the length direction using different FDTD schemes. The agreement of all methods is good except for Laguerre-FDTD method with PEC strip. The slightly higher magnitude of the waveform peak results from the lossless metal strip without considering skin-effect. To better illustrate this point, Figure 22 shows the insertion loss for the Laguerre-FDTD (PEC) and the Laguerre-FDTD (SIBC) cases together with the measurement. It can be observed that the result of the skin-effect incorporated Laguerre-FDTD has better correlation with the measurement.

### 4.4.2 Low Pass Filter

A microstrip low pass filter originally proposed in [65] is simulated. The structure shown in Figure 23 has a dielectric substrate with permittivity and thickness of $\varepsilon = 3.81$ and $d = 0.42$ mm, respectively. The plane symmetric filter is composed of microstrip lines with characteristic length $l_1 = 1.8$ mm, $l_2 = 1.929$ mm, $l_3 = 2.732$ mm, and $l_4 = 2.061$ mm, respectively. The width of the line segments are $w_1 = 0.85$ mm, $w_2 = 0.1$ mm, and $w_3 = 1.5$ mm. The metal strip and ground plane are made of copper (conductivity $\sigma = 5.8 \times 10^7$ S/m) with thickness $t_1 = 0.22$ mm and $t2 = 0.02$ mm. The scale difference for the structure is 1500:1 (ratio between feature sizes of structure length and ground thickness). Note the thickness of LIGA processed microstrip line is even larger than the minimum width which makes it unrealistic to model the metal strip as PEC sheet.

Figure 24 and Figure 25 show the return loss and insertion loss for the low pass filter. The comparison of the lossless case with PEC line and lossy case with skin-effect incorporated Laguerre-FDFD is shown. Also, the measurements from [65] of the insertion loss is presented (return loss is not shown in [65]). It can be observed that in Figure 24, both the Laguerre-FDTD (PEC) and Laguerre-FDTD (SIBC) correlate

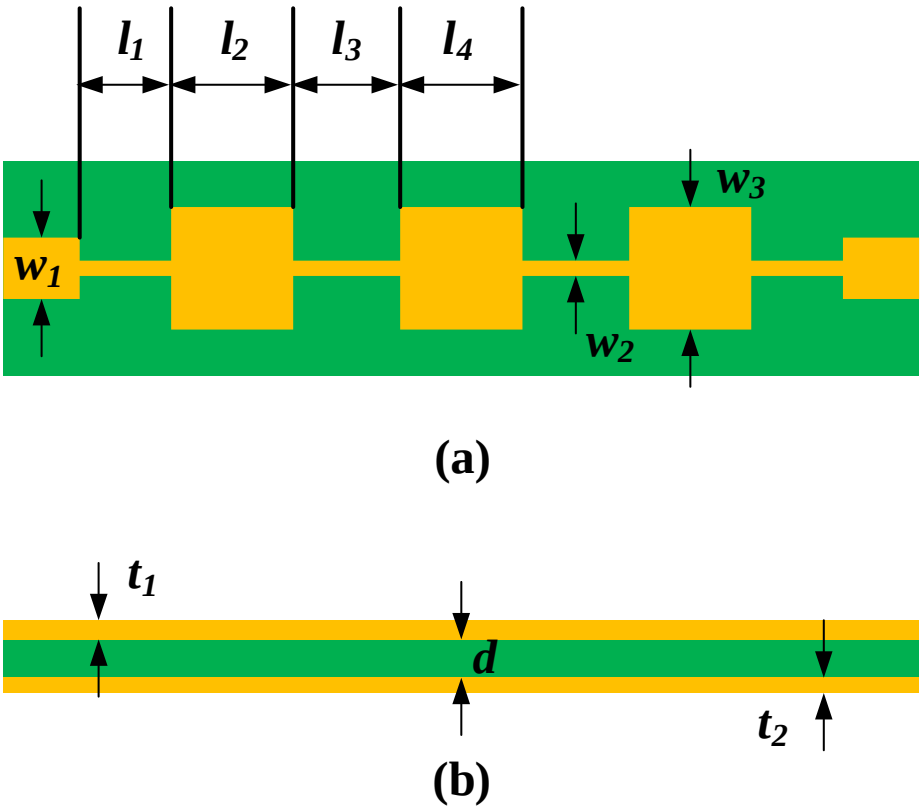


**Figure 23:** Schematic view of the LIGA micromachined microstrip low pass filter (a) top view and (b) side view.

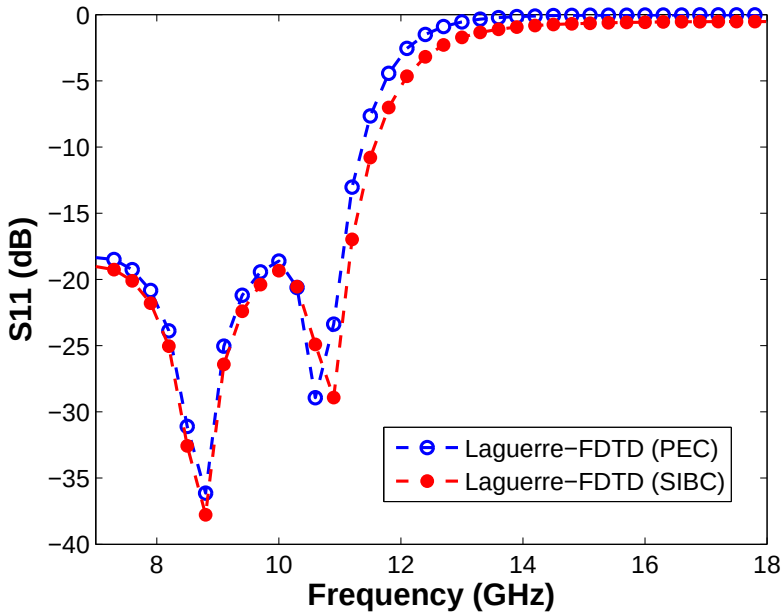


**Figure 24:** Comparison of simulated return loss of Laguerre-FDTD with PEC metal strip and skin-effect incorporated Laguerre-FDTD.

well except for 12 GHz to 18 GHz range where the loss is detected by using Laguerre-FDTD (SIBC). This can also be observed in Figure 25 where loss is modeled correctly using Laguerre-FDTD (SIBC) in 9 GHz to 12 GHz range. The good correlation with measurement also suggests that skin-effect incorporated Laguerre-FDTD yields more accurate results.

### 4.4.3 Through Silicon Via Arrays

Figure 26 shows the 3-D view of a $3 \times 3$ cylindrical through silicon via (TSV) array. Each port of the TSV array is numbered as shown in Figure 26 and the TSV array is embedded into a silicon substrate with dielectric constant and conductivity of $\varepsilon_r = 11.9$ and $\sigma = 10$ S/m, respectively. The diameter of the TSVs are identical with $d_1 = 30$ $\mu$m and the conductor is considered as copper with conductivity $\sigma = 5.8 \times 10^7$ S/m. The length of the TSV is $l = 100$ $\mu$m and the TSVs are separated from the adjacent ones by $d_2 = 30$ $\mu$m. The outer boundary has length $L_1 = L_2 = 100$ $\mu$m.

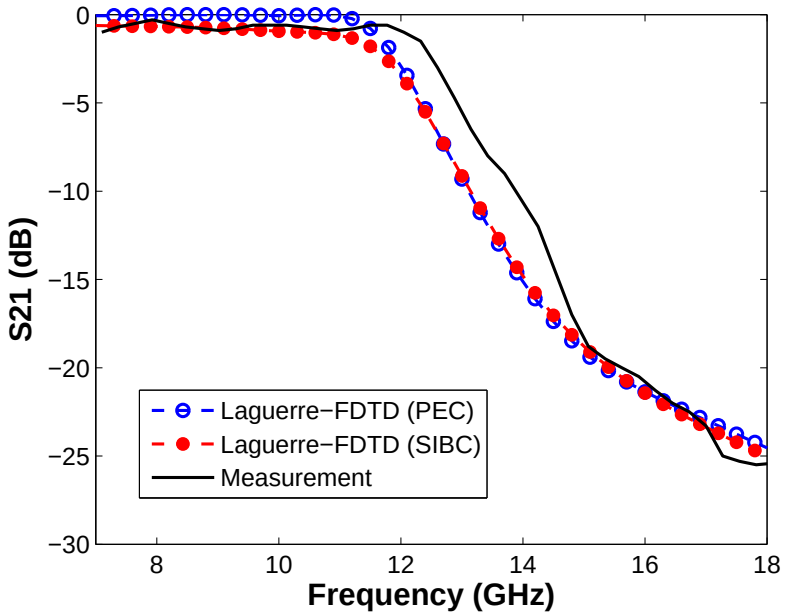


**Figure 25:** Comparison of simulated insertion loss of Laguerre-FDTD with PEC metal strip and skin-effect incorporated Laguerre-FDTD.

It is important to note that, the existence of the thin silicon dioxide layer makes the TSV array a multiscale structure that cannot be efficiently modeled by conventional FDTD method.

Figure 27 shows the simulated $S$-parameters of the TSV array using Laguerre-FDTD with skin-effect incorporated. It takes fifteen minutes for full wave simulation ($100 \times 100 \times 15$ cells). In Figure 27, good correlation of S-parameters can be observed compared with commercial software simulation results.

### 4.4.4 Spiral Inductor

To illustrate the efficiency improvement of using port resistors and the accuracy of de-embedding procedure, a spiral inductor structure originally proposed in [66] is simulated. Figure 28 shows the top view and side view of the structure. The structure has a dielectric substrate with permittivity and thickness of $\varepsilon = 9.8$ and $h_1 = 635$ $\mu$m, respectively. The feature sizes shown in Figure 28(a) and Figure 28(b) are $g = 312.5$

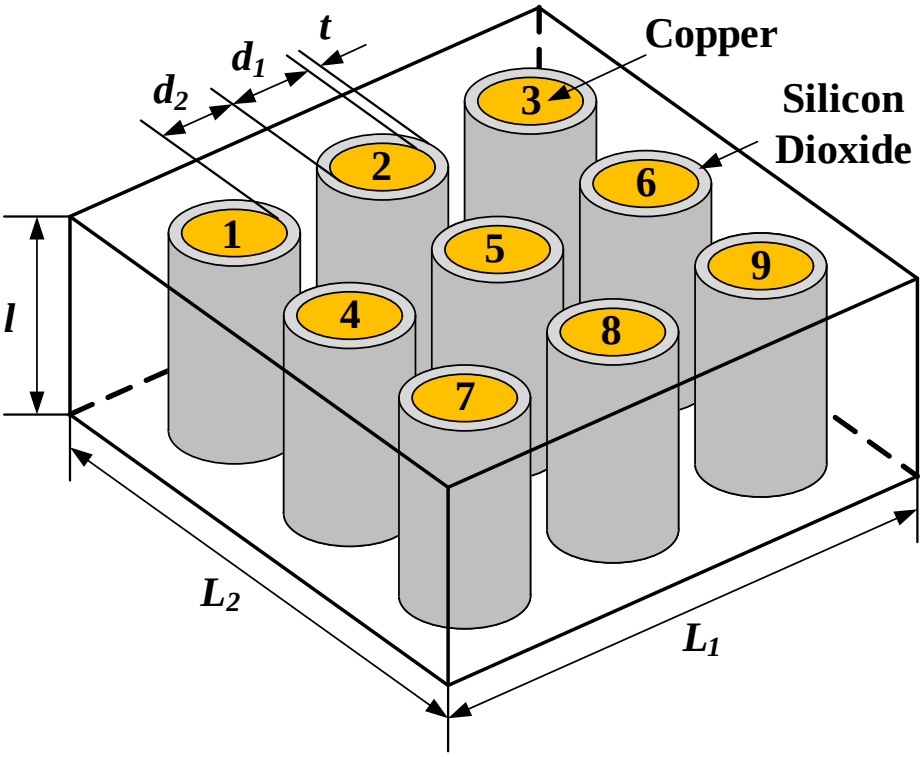


**Figure 26:** Schematic 3-D view of the $3 \times 3$ TSV array.

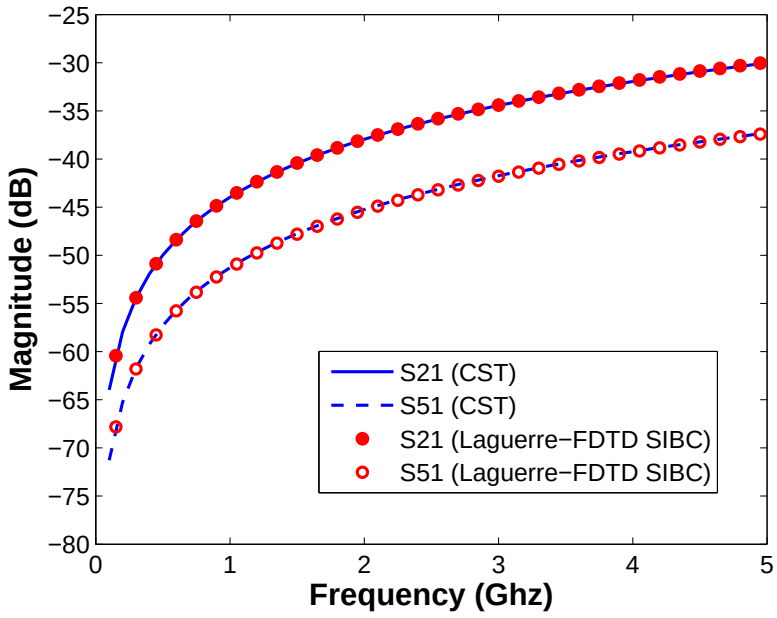


**Figure 27:** Comparison of simulated $S$-parameter of TSV array between Laguerre-FDTD (SIBC) and commercial software.

$\mu$m, $w_1 = 625$ $\mu$m, $w_2 = 312.5$ $\mu$m, and $w_3 = 312.5$ $\mu$m, and $h_2 = 317.5$ $\mu$m, respectively. The metal strip and ground plane are considered as copper (conductivity $\sigma = 5.8 \times 10^7$ S/m) with thickness $t = 10$ $\mu$m. The scale difference for the structure is 1200:1 (ratio between feature sizes of structure length and metal strip thickness).

When applying the embedded resistor, two ports are assigned at each end of the strip line. Figure 29 and Figure 30 show the time domain port voltage response of the skin-effect incorporated Laguerre-FDTD method without and with the embedding resistor, respectively. It is obvious that in Figure 29, the port voltage waveform fluctuates without damping as simulation time reaches 3 ns. This implies that simulation time duration should be increased to ensure that adequate energy is dissipated before truncating the simulation. Practically for this case, simulation duration should be at least 100 ns. In comparison, with embedded port resistors, the port voltage rapidly reduces to zero as simulation time reaches 3ns. Figure 31 and Figure 32 show the contour plot of the electric field in $z$-direction at 0.5 ns using Laguerre-FDTD (SIBC) without and with embedded resistors, respectively. It can be observed in Figure 32 that by using embedded resistors, energy is dissipated quickly as compared to Figure 31).

Figure 33 and Figure 34 show the return loss and insertion loss of the spiral inductor using both the Laguerre-FDTD (SIBC) without and with port resistors (after de-embedding procedure). Measurement extracted from [66] is also presented. The agreement of both methods is good and good correlation with the measurement is observed. Therefore, for similar accuracy, Laguerre-FDTD with port resistor scheme significantly reduces the simulation time. To be noted, this scheme is especially efficient when ports need to be defined inside the absorption boundary.

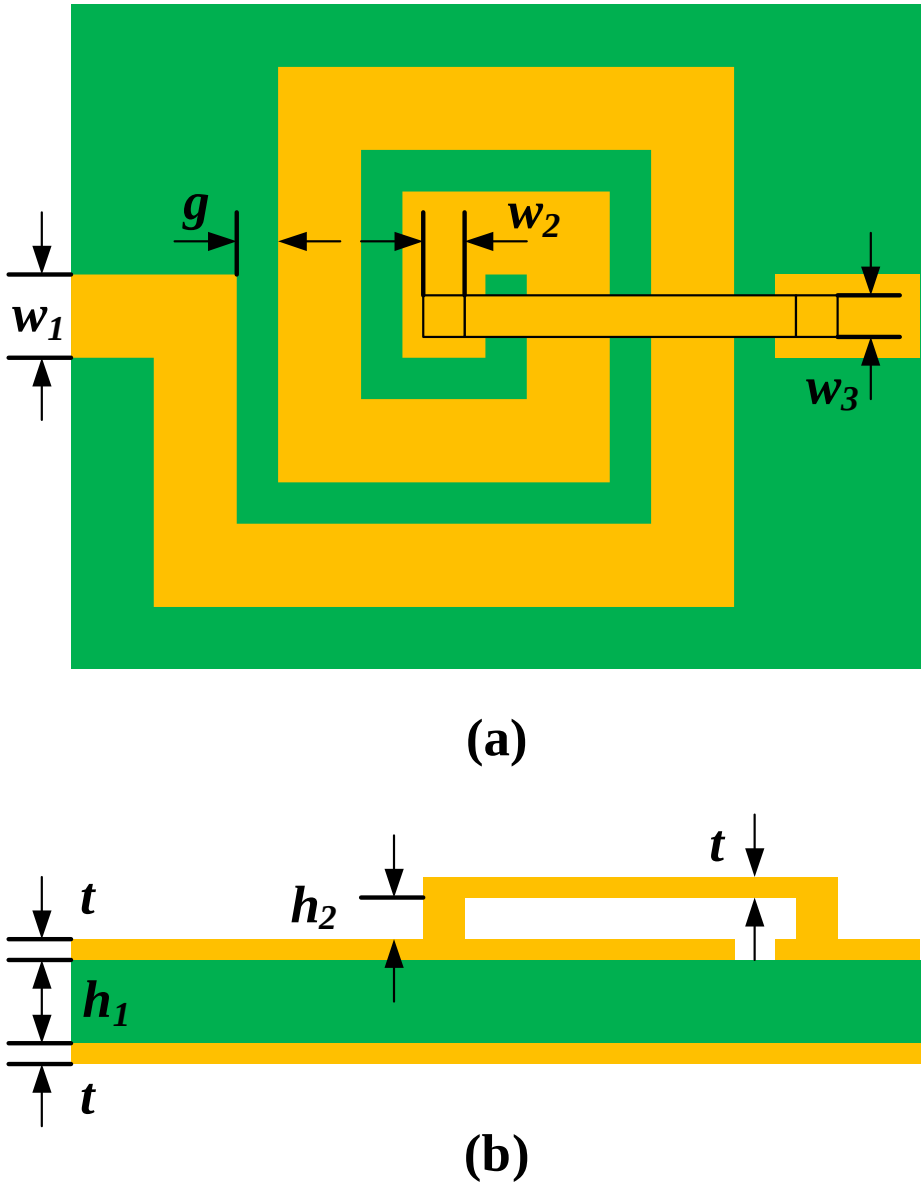


**Figure 28:** Schematic view of the spiral inductor (a) top view and (b) side view.

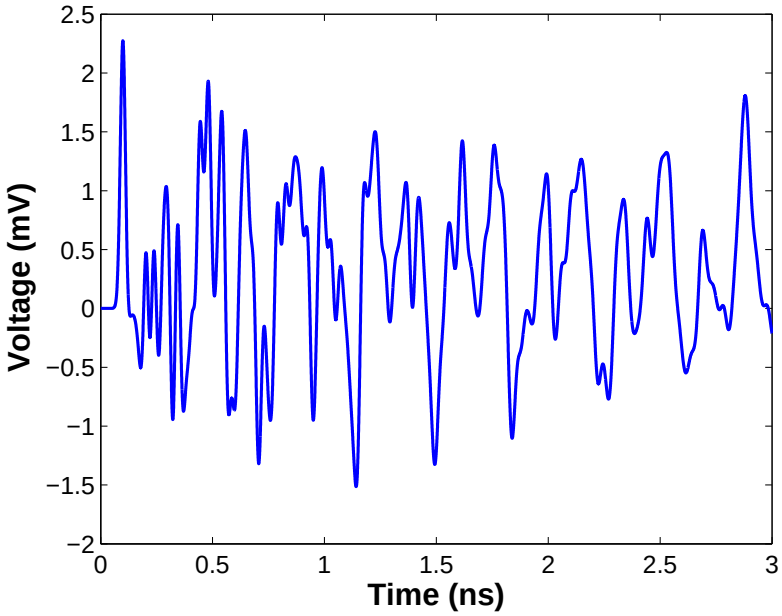


**Figure 29:** Time-domain voltage waveform at the port of the skin-effect incorporated Laguerre-FDTD without embedded port resistors.

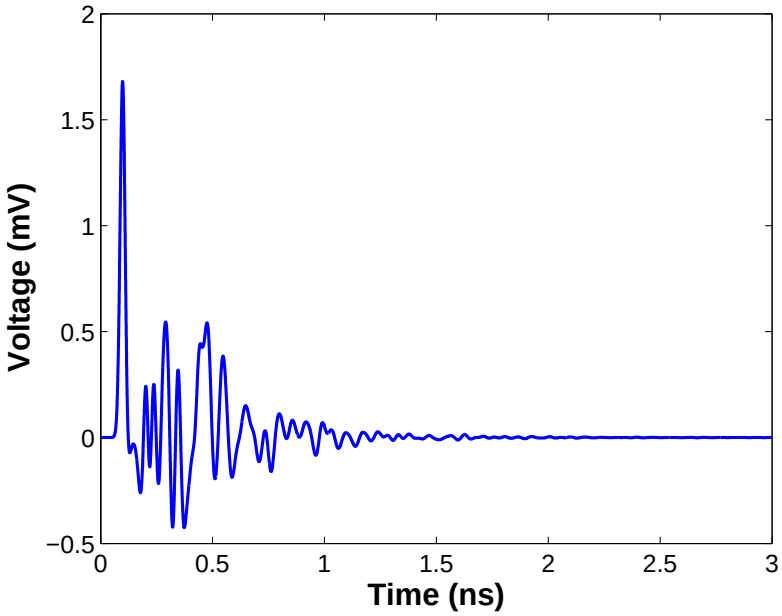


**Figure 30:** Time-domain voltage waveform at the port of the skin-effect incorporated Laguerre-FDTD with embedded port resistors.

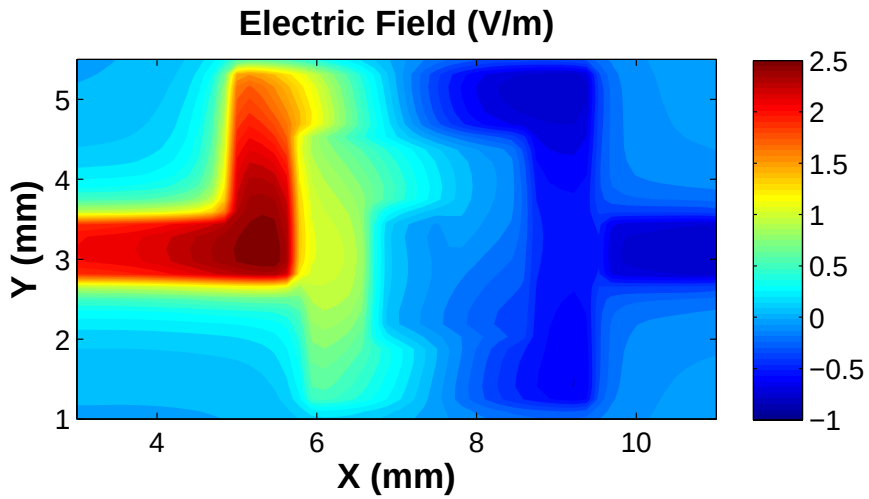


**Figure 31:** Contour plot of the electric field magnitude in $z$-direction of the spiral inductor in 0.5 ns of Laguerre-FDTD (SIBC) without port resistors.

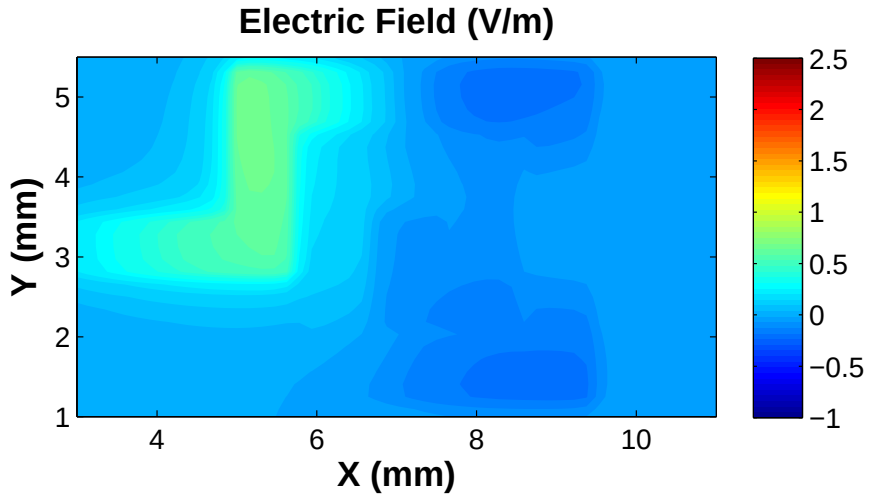


**Figure 32:** Contour plot of the electric field magnitude in $z$-direction of the spiral inductor in 0.5 ns of Laguerre-FDTD (SIBC) with port resistors.

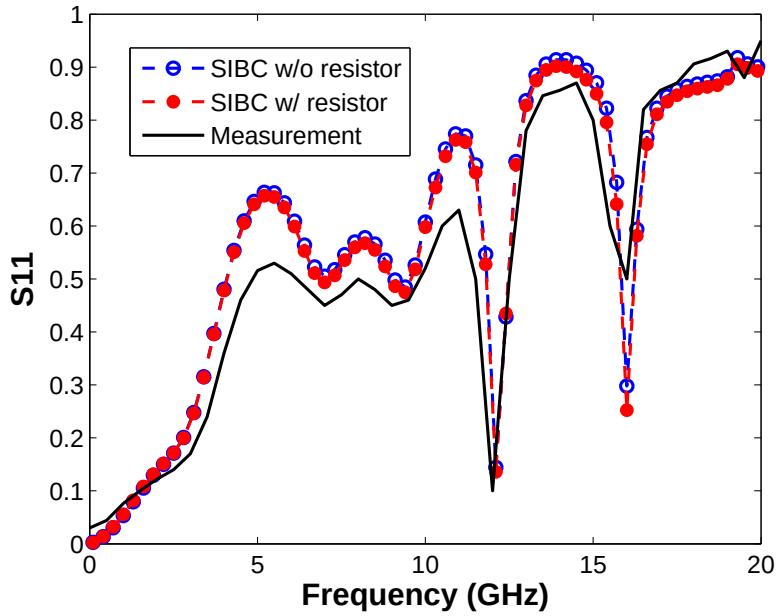


**Figure 33:** Comparison of simulated return loss of Laguerre-FDTD (SIBC) with and without port resistors.

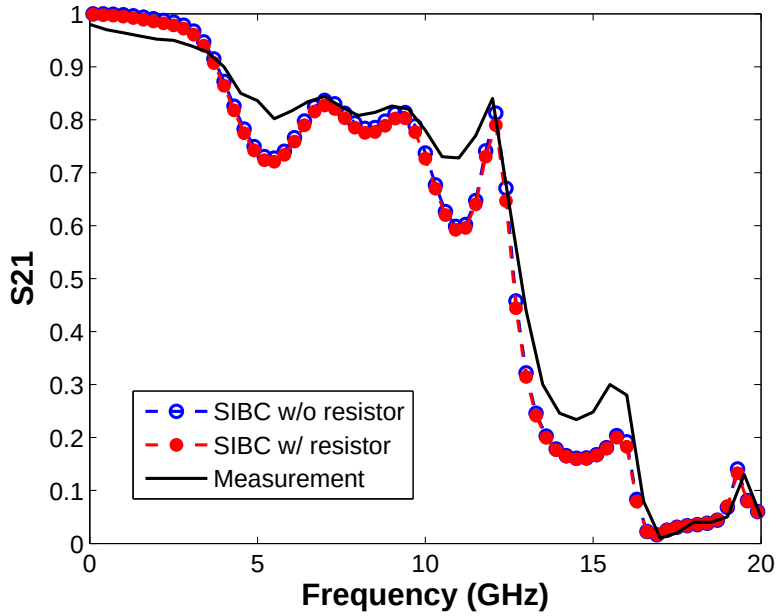


**Figure 34:** Comparison of simulated insertion loss of Laguerre-FDTD (SIBC) with and without port resistors.

## *4.5 Summary*

An efficient scheme for incorporating the skin-effect into the Laguerre-FDTD solver for multiscale structure simulation is proposed in this chapter. The skin-effect is modeled using the SIBC with two implementation methods (MFA-SIBC and EFA-SIBC). Different from standard Laguerre-FDTD method, the inside of the conductor does not have to be meshed. The numerical examples indicate that the proposed scheme shows computational accuracy with significant acceleration in simulation time compared to the standard Laguerre-FDTD method. The stability of both MFA-SIBC and EFA-SIBC is good with conductivity higher than $1 \times 10^{-3}$ S/m whereas for high conductivity case MFA-SIBC is preferred due to its simplicity. In addition, simulation results indicate that using the method of embedding and de-embedding port resistors provides rapid energy decay and accurate extraction of frequency domain parameters, which improves the computational efficiency for the Laguerre-FDTD solver.

# CHAPTER V

# TRANSIENT NON-CONFORMAL DOMAIN DECOMPOSITION SCHEME

## *5.1 Introduction*

It is known that for full-wave simulation, the number of unknowns will increase as the problem scale increases. For methods that require matrix solution, simulating large-scale problems could be very computationally expensive. This is because the complexity of algorithm for matrix solution is much larger than $O(n)$, therefore, linear growth in the number of unknowns leads to much faster growth of solution time. In fact, even to this date, some realistic problems in industry cannot be efficiently simulated. For example, the full-wave simulation of interconnects in IC package together with on-chip interconnects is considered as a problem that requires solutions.

The domain decomposition scheme is useful in simulating large-scale problems. By dividing the computational domain into several subdomains, each subdomain can be analyzed separately. This could be done in a serial or parallel manner. After each domain is evaluated, the entire solution is obtained from all the solutions of each subdomain. The problem that can be analyzed is only limited by the computational resource required by the subdomains, and thus, analyzing large-scale problems becomes possible.

However, implementing the domain decomposition scheme is challenging, especially for cases with non-conformal interface meshing. Most of the time, non-conformal domain decomposition method is desired since it significantly relaxes the mesh generation process. For example, a chip-package-board structure shown in Figure 35 is

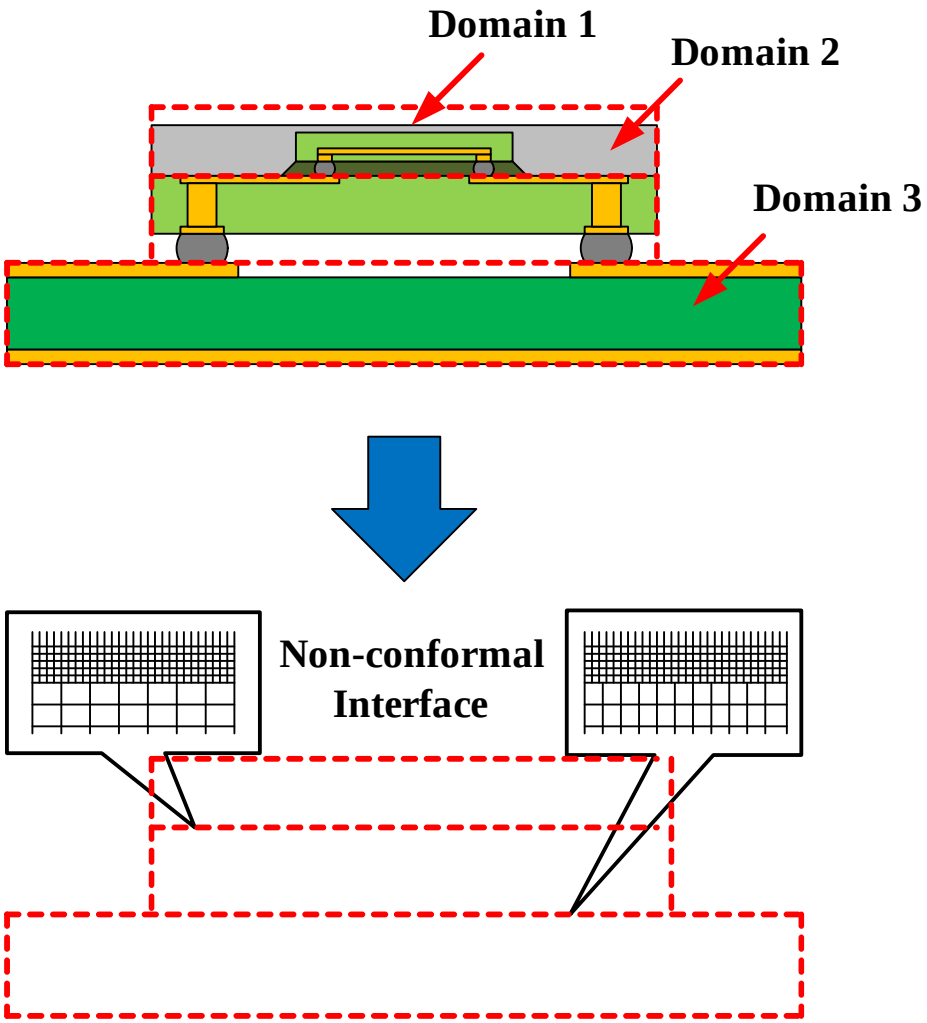


**Figure 35:** Partitioning a chip-package-board structure into three subdomains with non-conformal domain interface.

decomposed into three subdomains. Each domain is meshed according to its own feature size. In the chip domain, a fine mesh is applied whereas in the package and board domains, a coarse mesh is applied in order to reduce the total number of unknowns. Since the mesh on the domain interface does not match, this results in difficulties in enforcing interface field continuity. Up to now, no solution exists in solving this type of problem based on the Laguerre-FDTD method, which is the motivation behind the work in this chapter.

## *5.2 Preliminaries: Equivalency*

In the conventional FDTD method, a field component is related to the difference of the surrounding field components. Although the updating equation is straightforward, it is only suitable for updating within the Yee grid. In other words, the conventional FDTD method can only be implemented with conformal meshing.

If the computational domain is decomposed into several domains with non-conformal meshing, it is difficult to update the field on the domain interface using conventional FDTD due to the floating grid. Based on field interpolation, some sub-gridding schemes have been developed to deal with a non-matching grid interface [67]. However, the field interpolation requires a certain mesh difference ratio at the interface, which is not flexible and does not relax the mesh generation. This is not desired for complex multiscale structures where different domains require different meshing strategies.

A popular approach, which enables non-conformal domain decomposition, is the mortar element method. The mortar element method is based on the finite element method (FEM) that cannot be applied to the FDTD scheme directly. However, since there exists equivalency between time-domain FEM (TD-FEM) and the implicit FDTD method, a mortar-like method can be used in the Laguerre-FDTD scheme.

Assuming an isotropic, non-dispersive, lossy media, the vector wave equation in

time domain can be expressed as:

$$\nabla \times \nabla \times \mathbf{E} + \mu\varepsilon \frac{\partial^2 \mathbf{E}}{\partial t^2} + \mu\sigma \frac{\partial \mathbf{E}}{\partial t} = -\mu \frac{\partial \mathbf{J}}{\partial t}. \tag{55}$$

Discretizing the differential equation (55) in Laguerre domain using temporal testing procedure, with some manipulations, the $x$-direction electric field coefficient equation can be written as:

$$\begin{aligned}
&\Big(1 + \bar{C}_y^E\,|_{i,j,k}\,\bar{C}_y^H\,|_{i,j,k} + \bar{C}_y^E\,|_{i,j,k}\,\bar{C}_y^H\,|_{i,j-1,k} \\
&+\bar{C}_z^E\,|_{i,j,k}\,\bar{C}_z^H\,|_{i,j,k} + \bar{C}_z^E\,|_{i,j,k}\,\bar{C}_z^H\,|_{i,j,k-1} + \frac{2\sigma_{i,j,k}}{s\varepsilon_{i,j,k}}\Big)\,E_x^q\,|_{i,j,k} \\
&- \bar{C}_y^E\,|_{i,j,k}\,\bar{C}_y^H\,|_{i,j,k}\,E_x^q\,|_{i,j+1,k} + \bar{C}_y^E\,|_{i,j,k}\,\bar{C}_x^H\,|_{i,j,k}\,E_y^q\,|_{i+1,j,k} \\
&- \bar{C}_y^E\,|_{i,j,k}\,\bar{C}_x^H\,|_{i,j,k}\,E_y^q\,|_{i,j,k} - \bar{C}_y^E\,|_{i,j,k}\,\bar{C}_y^H\,|_{i,j-1,k}\,E_x^q\,|_{i,j-1,k} \\
&- \bar{C}_y^E\,|_{i,j,k}\,\bar{C}_x^H\,|_{i,j-1,k}\,E_y^q\,|_{i+1,j-1,k} + \bar{C}_y^E\,|_{i,j,k}\,\bar{C}_x^H\,|_{i,j-1,k}\,E_y^q\,|_{i,j-1,k} \\
&+ \bar{C}_z^E\,|_{i,j,k}\,\bar{C}_x^H\,|_{i,j,k}\,E_z^q\,|_{i+1,j,k} - \bar{C}_z^E\,|_{i,j,k}\,\bar{C}_x^H\,|_{i,j,k}\,E_z^q\,|_{i,j,k} \\
&- \bar{C}_z^E\,|_{i,j,k}\,\bar{C}_z^H\,|_{i,j,k}\,E_x^q\,|_{i,j,k+1} - \bar{C}_z^E\,|_{i,j,k}\,\bar{C}_x^H\,|_{i,j,k-1}\,E_z^q\,|_{i+1,j,k-1} \\
&+ \bar{C}_z^E\,|_{i,j,k}\,\bar{C}_x^H\,|_{i,j,k-1}\,E_z^q\,|_{i,j,k-1} - \bar{C}_z^E\,|_{i,j,k}\,\bar{C}_z^H\,|_{i,j,k-1}\,E_x^q\,|_{i,j,k-1} \\
= &-\frac{4}{\mu_{i,j,k}\varepsilon_{i,j,k}s^2}\sum_{n=0,q>1}^{q-1} E_x^n\,|_{i,j,k} - 4\sum_{n=0,q>1}^{q-1}\sum_{m=0}^{n} E_x^m\,|_{i,j,k} \\
&-\frac{2}{s\varepsilon_{i,j,k}}\left(J_x^q\,|_{i,j,k} + 2\sum_{n=0,q>1}^{q-1} J_x^n\,|_{i,j,k}\right).
\end{aligned} \tag{56}$$

Note that the left side of equation (56) is identical to the left side of equation (19). The detailed derivation is given in Appendix A.

In the TD-FEM method, considering fields in open space, multiplying (55) by an appropriate testing function $\mathbf{N}$, and integrating over a volume results in:

$$\int_\Omega \left[(\nabla \times \mathbf{N}) \cdot (\nabla \times \mathbf{E}) + \mu\varepsilon \mathbf{N} \cdot \frac{\partial^2 \mathbf{E}}{\partial t^2} + \mu\sigma \mathbf{N} \cdot \frac{\partial \mathbf{E}}{\partial t}\right] dV = -\int_\Omega \mu \mathbf{N} \cdot \frac{\partial \mathbf{J}}{\partial t} dV. \tag{57}$$

In the computational domain, the electric field is expanded using vector basis functions:

$$\mathbf{E} = \sum_{i=1}^{n} \mathbf{N}_i E_i \tag{58}$$

where $n$ is the total edge number, $E_i$ is the unknown expansion coefficient, and $\mathbf{N}_i$ is the vector basis function. Inserting (58) into (57) yields:

$$\mathbf{T}\frac{\partial^2 \mathbf{E}}{\partial t^2} + \mathbf{R}\frac{\partial \mathbf{E}}{\partial t} + \mathbf{S}\mathbf{E} = \mathbf{f} \tag{59}$$

where

$$T_{ij} = \int_{\Omega} \mu\varepsilon \mathbf{N}_i \cdot \mathbf{N}_j dV \tag{60}$$

$$R_{ij} = \int_{\Omega} \mu\sigma \mathbf{N}_i \cdot \mathbf{N}_j dV \tag{61}$$

$$S_{ij} = \int_{\Omega} (\nabla \times \mathbf{N}_i) \cdot (\nabla \times \mathbf{N}_j)\, dV \tag{62}$$

$$f_i = -\int_{\Omega} \mu \mathbf{N}_i \cdot \frac{\partial \mathbf{J}}{\partial t} dV. \tag{63}$$

Applying the temporal testing procedure in Laguerre domain, (59) becomes:

$$\mathbf{T}s^2 \left( \frac{1}{4}\mathbf{E}^q + \sum_{n=0,q>1}^{q-1} \sum_{j=0}^{m} \mathbf{E}^m \right) + \mathbf{R}s \left( \frac{1}{2}\mathbf{E}^q + \sum_{n=0,q>1}^{q-1} \mathbf{E}^n \right) + \mathbf{S}\mathbf{E}^q = \mathbf{f}^q \tag{64}$$

where

$$f_i^q = -\int_{\Omega} \mu s \mathbf{N}_i \cdot \left( \frac{1}{2}\mathbf{J}^q + \sum_{n=0,q>1}^{q-1} \mathbf{J}^n \right) dV. \tag{65}$$

Note here that, $\mathbf{E}^q$ denotes the Laguerre coefficient vector of electric field with order $q$ and $s$ is the time scale factor defined before.

In the Laguerre-FDTD scheme, the computational mesh is defined as rectangular brick elements. Using trapezoidal integration in (60)-(62) and (65) in the construction of the elemental matrix and extracting only the equation for electric field in $x$-direction, the resulting equation is *identical* to (56). This implies that the Laguerre-FDTD equation can be derived from TD-FEM when trapezoidal integration and Laguerre domain temporal testing procedure are used. The detailed derivation of equivalency is provided in Appendix C.

## *5.3 Direct Mortar-Element-Like Scheme*

In this section, a domain decomposition scheme using one set of Lagrange multipliers is discussed. This method is similar to the mortar element method by using the equivalency between TD-FEM and Laguerre-FDTD method. The limitations of using a direct mortar-element-like scheme is also discussed.

### 5.3.1 Lagrange Multipliers

Lagrange multipliers are widely used for solving domain decomposition problems. By introducing additional unknowns to the global system, field continuity on the domain interface is maintained. One popular scheme using Lagrange multipliers is the mortar element method and it has been successfully applied to heat transfer problems [68].

For simplicity, consider the computational domain which is decomposed into two subdomains $\Omega_1$ and $\Omega_2$ with a non-conformal sharing interface $\Gamma$, as shown in Figure 36. In the figure, $\hat{n}_1$ and $\hat{n}_2$ are the unit normal vectors pointing to the exterior region of each subdomain. By defining the Lagrange multiplier space as:

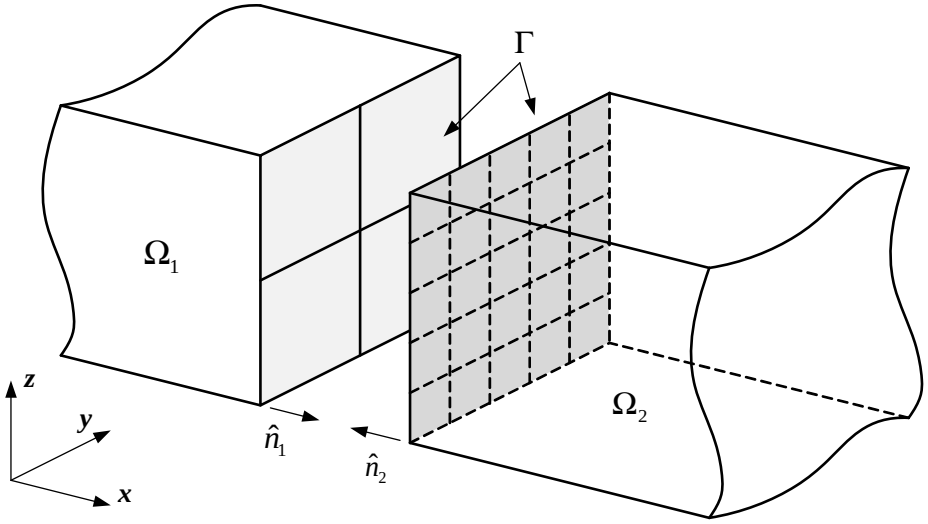


**Figure 36:** Partitioning a computational domain into two subdomains $\Omega_1$ and $\Omega_2$ with non-conformal domain interface.

$$\boldsymbol{\lambda} = \sum_{i=1}^{n} \boldsymbol{\varphi}_i \lambda_i \tag{66}$$

where $n$ is the total number of expansion terms, $\lambda_i$ is the unknown expansion coefficient, $\boldsymbol{\varphi}_i$ is the vector basis function, the following mortar-like equations are obtained

$$\begin{aligned} &\int_{\Omega_1} \left[ (\nabla \times \mathbf{N}_1) \cdot (\nabla \times \mathbf{E}_1) + \mu\varepsilon \mathbf{N}_1 \cdot \frac{\partial^2 \mathbf{E}_1}{\partial t^2} + \mu\sigma \mathbf{N}_1 \cdot \frac{\partial \mathbf{E}_1}{\partial t} \right] dV \\ &+ \int_{\Gamma} \mathbf{N}_1 \cdot \boldsymbol{\lambda} dS \qquad (67) \\ = &- \int_{\Omega_1} \mu \mathbf{N}_1 \cdot \frac{\partial \mathbf{J}_1}{\partial t} dV \\ &\int_{\Omega_2} \left[ (\nabla \times \mathbf{N}_2) \cdot (\nabla \times \mathbf{E}_2) + \mu\varepsilon \mathbf{N}_2 \cdot \frac{\partial^2 \mathbf{E}_2}{\partial t^2} + \mu\sigma \mathbf{N}_2 \cdot \frac{\partial \mathbf{E}_2}{\partial t} \right] dV \\ &- \int_{\Gamma} \mathbf{N}_2 \cdot \boldsymbol{\lambda} dS \qquad (68) \\ = &- \int_{\Omega_2} \mu \mathbf{N}_2 \cdot \frac{\partial \mathbf{J}_2}{\partial t} dV \end{aligned}$$

$$\int_{\Gamma} (\mathbf{E}_1 - \mathbf{E}_2) \cdot \boldsymbol{\varphi} dS = 0. \tag{69}$$

### 5.3.2 Implementation and Limitations

Similar to obtaining the system equation in (64), after applying the Laguerre transformation to (67)-(69), the resulting linear system for the two subdomains together with interface equations can be written as:

$$\begin{bmatrix} \mathbf{K}_1 & \mathbf{0} & \mathbf{B}_1^T \\ \mathbf{0} & \mathbf{K}_2 & -\mathbf{B}_2^T \\ \mathbf{B}_1 & -\mathbf{B}_2 & \mathbf{0} \end{bmatrix} \begin{bmatrix} \mathbf{E}_1^q \\ \mathbf{E}_2^q \\ \boldsymbol{\lambda}^q \end{bmatrix} = \begin{bmatrix} \mathbf{g}_1^q \\ \mathbf{g}_2^q \\ \mathbf{0} \end{bmatrix} \tag{70}$$

where

$$\mathbf{K}_1 = \frac{s^2}{4}\mathbf{T}_1 + \frac{s}{2}\mathbf{R}_1 + \mathbf{S}_1 \tag{71}$$

$$\mathbf{K}_2 = \frac{s^2}{4}\mathbf{T}_2 + \frac{s}{2}\mathbf{R}_2 + \mathbf{S}_2 \tag{72}$$

$$\mathbf{B}_1 = \int_\Gamma \mathbf{N}_1 \cdot \boldsymbol{\varphi} dS \tag{73}$$

$$\mathbf{B}_2 = \int_\Gamma \mathbf{N}_2 \cdot \boldsymbol{\varphi} dS \tag{74}$$

$$\mathbf{g}_1 = \mathbf{f}_1^q - \mathbf{T}_1 s^2 \sum_{n=0,q>1}^{q-1} \sum_{j=0}^{m} \mathbf{E}_1^m - \mathbf{R}_1 s \sum_{n=0,q>1}^{q-1} \mathbf{E}_1^n \tag{75}$$

$$\mathbf{g}_2 = \mathbf{f}_2^q - \mathbf{T}_2 s^2 \sum_{n=0,q>1}^{q-1} \sum_{j=0}^{m} \mathbf{E}_1^m - \mathbf{R}_1 s \sum_{n=0,q>1}^{q-1} \mathbf{E}_1^n. \tag{76}$$

By solving the system matrix (70), the Laguerre coefficients of the electric field can be obtained. The time-domain waveforms of interest can be recovered from the Laguerre basis functions and their coefficients.

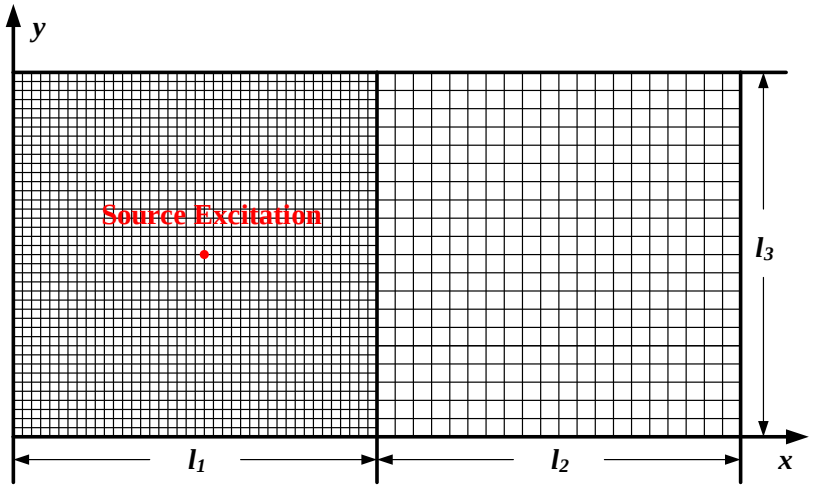


**Figure 37:** Meshing for the 2-D wave propagation problem with two subdomains.

However, direct implementation of the mortar-element-like scheme may result in field mismatch and reflection problems. Note that the mortar element method works well with the heat transfer problem because the field of interest is a scalar one. Only the temperature distribution needs to be solved with the heat transfer equation. In an electromagnetic problems, both the continuity of the electric field and the magnetic field need to be addressed. Therefore, by applying one set of Lagrange multipliers, only the electric field continuity is maintained without enforcing magnetic field continuity.

To illustrate the point, a simple wave propagation problem shown in Figure 37 in 2-D is investigated ($\text{TE}_z$ case). The length of the computational domain in $x$- and $y$-directions are 20 mm and 10 mm, respectively. The computational domain is decomposed into two equal area subdomains with feature length $l_1 = l_2 = l_3 = 10$ mm. The meshing density for these two subdomains are $40 \times 40$ and $20 \times 20$, respectively. The source excitation is located in the middle of the first domain. An ABC is used to truncate the entire computational domain.

Figure 38 shows the electric and magnetic field distribution at the time point when wave propagates from subdomain one to subdomain two. It can be observed that for

the electric fields $E_x$ and $E_y$, the field continuity at the domain interface is good. However, strong fields reflection and the distortion can be observed for the magnetic field $H_z$ at the domain interface.

Therefore, algorithm modification is needed for the direct mortar-element-like method to fully represent the continuity for both electric and magnetic field, which is the topic of the next section.

## *5.4 Domain Decomposition with Dual Sets of Lagrange Multipliers*

In this section, a non-conformal domain decomposition method using dual sets of Lagrange multipliers is discussed. This method is immune to the field mismatch problem by direct implementation of mortar-element-like method. Theory and derivations of related formulations are discussed in detail.

### 5.4.1 Formulations for Interior Fields of Subdomains

For simplicity, assuming an isotropic, non-dispersive, lossless media in three-dimensional Cartesian coordinates, the vector wave equation in the time domain can be expressed as:

$$\nabla \times \nabla \times \mathbf{E} + \mu\varepsilon \frac{\partial^2 \mathbf{E}}{\partial t^2} = -\mu \frac{\partial \mathbf{J}}{\partial t} \tag{77}$$

where $\varepsilon$ is the electric permittivity, $\mu$ is the magnetic permeability, and $\mathbf{J}$ is the source excitation.

As is known, any time-domain waveform $\mathbf{W}(t)$ can be represented as a sum of infinite Laguerre basis functions $\varphi^q(\bar{t})$ scaled by Laguerre basis coefficients $\mathbf{W}^q$ as

$$\mathbf{W}(t) = \sum_{q=0}^{\infty} \mathbf{W}^q \varphi^q(\bar{t}) \tag{78}$$

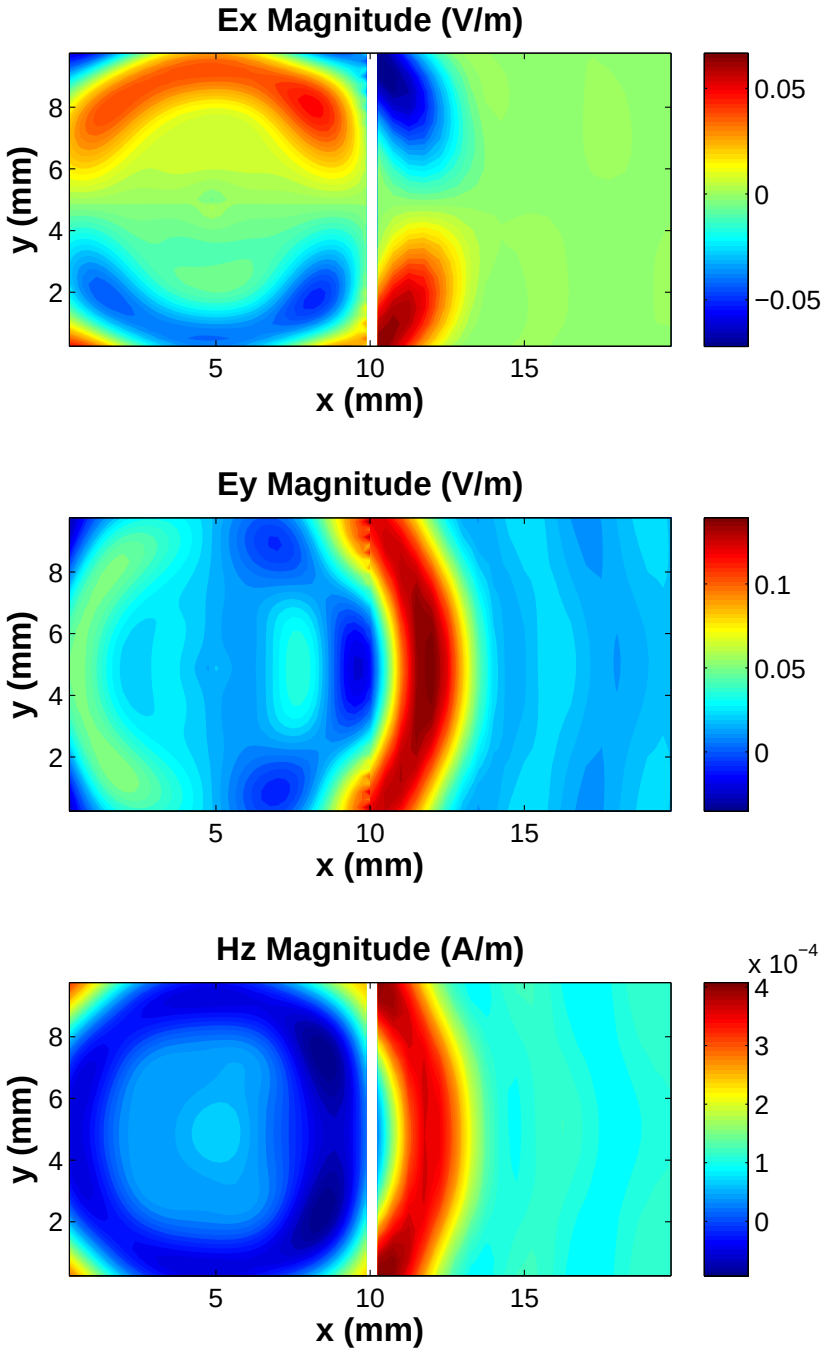


**Figure 38:** Field distribution for the 2-D wave propagation problem using the direct mortar-element-like scheme.

where $\bar{t} = t \cdot s$, $s$ is the time scaling factor, and $t$ is time. Superscript $q$ denotes the Laguerre coefficient and basis function of order $q$. The number of basis functions is truncated to $N$ in the implementation, where the optimum selection of $N$ is discussed in detail in [14]. Applying the temporal testing procedure with respect to the basis function of order $q$, in $x$-direction, the discretized vector wave equation in terms of electric field Laguerre coefficient of order $q$ can be written as:

$$
\begin{aligned}
& \left(1 + \bar{C}_y^E\,|_{i,j,k}\, \bar{C}_y^H\,|_{i,j,k} + \bar{C}_y^E\,|_{i,j,k}\, \bar{C}_y^H\,|_{i,j-1,k}\right. \\
& \left. + \bar{C}_z^E\,|_{i,j,k}\, \bar{C}_z^H\,|_{i,j,k} + \bar{C}_z^E\,|_{i,j,k}\, \bar{C}_z^H\,|_{i,j,k-1}\right) E_x^q\,|_{i,j,k} \\
& - \bar{C}_y^E\,|_{i,j,k}\, \bar{C}_y^H\,|_{i,j,k}\, E_x^q\,|_{i,j+1,k} + \bar{C}_y^E\,|_{i,j,k}\, \bar{C}_x^H\,|_{i,j,k}\, E_y^q\,|_{i+1,j,k} \\
& - \bar{C}_y^E\,|_{i,j,k}\, \bar{C}_x^H\,|_{i,j,k}\, E_y^q\,|_{i,j,k} - \bar{C}_y^E\,|_{i,j,k}\, \bar{C}_y^H\,|_{i,j-1,k}\, E_x^q\,|_{i,j-1,k} \\
& - \bar{C}_y^E\,|_{i,j,k}\, \bar{C}_x^H\,|_{i,j-1,k}\, E_y^q\,|_{i+1,j-1,k} + \bar{C}_y^E\,|_{i,j,k}\, \bar{C}_x^H\,|_{i,j-1,k}\, E_y^q\,|_{i,j-1,k} \\
& + \bar{C}_z^E\,|_{i,j,k}\, \bar{C}_x^H\,|_{i,j,k}\, E_z^q\,|_{i+1,j,k} - \bar{C}_z^E\,|_{i,j,k}\, \bar{C}_x^H\,|_{i,j,k}\, E_z^q\,|_{i,j,k} \\
& - \bar{C}_z^E\,|_{i,j,k}\, \bar{C}_z^H\,|_{i,j,k}\, E_x^q\,|_{i,j,k+1} - \bar{C}_z^E\,|_{i,j,k}\, \bar{C}_x^H\,|_{i,j,k-1}\, E_z^q\,|_{i+1,j,k-1} \\
& + \bar{C}_z^E\,|_{i,j,k}\, \bar{C}_x^H\,|_{i,j,k-1}\, E_z^q\,|_{i,j,k-1} - \bar{C}_z^E\,|_{i,j,k}\, \bar{C}_z^H\,|_{i,j,k-1}\, E_x^q\,|_{i,j,k-1} \\
= & -4 \sum_{n=0,q>1}^{q-1} \sum_{m=0}^{n} E_x^m\,|_{i,j,k} \\
& - \frac{2}{s\varepsilon_{i,j,k}} \left( J_x^q\,|_{i,j,k} + 2 \sum_{n=0,q>1}^{q-1} J_x^n\,|_{i,j,k} \right)
\end{aligned}
\tag{79}
$$

where

$$\bar{C}_y^E\,|_{i,j,k} = \frac{2}{s\varepsilon_{i,j,k}\Delta\bar{y}_j} \tag{80}$$

$$\bar{C}_z^E\,|_{i,j,k} = \frac{2}{s\varepsilon_{i,j,k}\Delta\bar{z}_k} \tag{81}$$

$$\bar{C}_x^H\,|_{i,j,k} = \frac{2}{s\mu_{i,j,k}\Delta x_i} \tag{82}$$

$$\bar{C}_y^H\,|_{i,j,k} = \frac{2}{s\mu_{i,j,k}\Delta y_j} \tag{83}$$

$$\bar{C}_z^H\,|_{i,j,k} = \frac{2}{s\mu_{i,j,k}\Delta z_k}. \tag{84}$$

in which $\Delta x_i$, $\Delta y_j$, and $\Delta z_k$ are the length of the edge where electric field components are located whereas $\Delta\bar{y}_j$ and $\Delta\bar{z}_k$ are the distance between the center nodes where magnetic fields are located.

Combining electric field coefficient equations for $y$- and $z$-directions, a system equation with Laguerre coefficient order $q$ can be obtained in matrix form and expressed as:

$$\mathbf{K}_V\mathbf{E}_V^q = \mathbf{g}_V^q. \tag{85}$$

where subscript $V$ denotes the degrees of freedom in the interior of the computational domain.

### 5.4.2 Dual Sets of Lagrange Multipliers

As is shown in Figure 36, to couple the fields between domain $\Omega_1$ and $\Omega_2$, the tangential continuity of the electric and magnetic fields at the domain interface $\Gamma$ must be satisfied, namely,

$$\mathbf{E}_{\tan,1}\,|_{\Gamma} = \mathbf{E}_{\tan,2}\,|_{\Gamma} \tag{86}$$

$$\mathbf{H}_{\tan,1}\,|_{\Gamma} = \mathbf{H}_{\tan,2}\,|_{\Gamma}\ . \tag{87}$$

For Laguerre-FDTD method with non-conformal domain interface, derivation of the field equation at the interface based on differential scheme is not straight-forward. However, because of the equivalency between FEM and FDTD method when trapezoidal integration is used in the construction of the elemental matrices with vector edge basis functions [69], field continuity can be enforced in FEM form and then rewritten in FDTD form.

The electric field continuity can be enforced by introducing Lagrange multipliers similar to those used in the mortar-element-based methods by defining the Lagrange multipliers as:

$$\boldsymbol{\lambda} = \sum_{i=1}^{n} \boldsymbol{\varphi}_i \lambda_i \tag{88}$$

where $n$ is the total number of expansion terms, $\lambda_i$ is the unknown expansion coefficient, and $\boldsymbol{\varphi}_i$ is the vector basis function. On the interface we have

$$\int_{\Gamma} (\mathbf{E}_{I,1} - \mathbf{E}_{I,2}) \cdot \boldsymbol{\varphi} dS = 0 \tag{89}$$

where subscript $I$ denotes the degrees of freedom on the domain interface.

In [68], a scalar equation is solved using a non-conformal domain decomposition method with the introduction of only one set of Lagrange multipliers. However, in

full-wave electromagnetic problems, the continuity of the magnetic field is not automatically ensured when enforcing the electric field continuity. In Laguerre-FDTD method, the straight-forward enforcement of magnetic field continuity in a similar manner is difficult since the only unknowns for the system equation are the electric field coefficients as shown in (85). Even by discretizing Maxwell's equation directly, the magnetic field coefficient is always one order lower than the electric field coefficient on the right-hand side [70]. Hence, the surface equivalent current is introduced as:

$$\mathbf{J}_m^{eq}\,|_\Gamma = \hat{n}_m \times \mathbf{H}_{\tan,m}\,|_\Gamma \tag{90}$$

where $m$ is the domain index. If an additional set of Lagrange multipliers are introduced for representing the surface equivalent current, the continuity of the magnetic field is maintained. Hence, in each domain, the time-derivative Lagrange multiplier space is defined as:

$$\frac{\partial \mathbf{J}^{eq}}{\partial t} = \frac{\partial}{\partial t}\sum_{i=1}^{n} \boldsymbol{\varphi}_i j_i^{eq} \tag{91}$$

where $n$ is the total number of expansion terms, $j_i^{eq}$ is the unknown expansion coefficient, and $\boldsymbol{\varphi}_i$ is the vector basis function. Incorporating the time-derivative Lagrange multiplier into (77) for domains $\Omega_1$ and $\Omega_2$ and multiplying by an appropriate testing function $\mathbf{N}$ with integration over the volume results in:

$$\begin{aligned}&\int_{\Omega_1}\left[(\nabla\times\mathbf{N}_1)\cdot(\nabla\times\mathbf{E}_{I,1}) + \mu\varepsilon\mathbf{N}_1\cdot\frac{\partial^2\mathbf{E}_{I,1}}{\partial t^2}\right]dV \\ &+\int_\Gamma \mathbf{N}_1\cdot\frac{\partial\mathbf{J}_1^{eq}}{\partial t}dS = 0\end{aligned} \tag{92}$$

$$\int_{\Omega_2} \left[ (\nabla \times \mathbf{N}_2) \cdot (\nabla \times \mathbf{E}_{I,2}) + \mu\varepsilon \mathbf{N}_2 \cdot \frac{\partial^2 \mathbf{E}_{I,2}}{\partial t^2} \right] dV + \int_{\Gamma} \mathbf{N}_2 \cdot \frac{\partial \mathbf{J}_2^{eq}}{\partial t} dS = 0. \tag{93}$$

Note that at the domain interface, there is no source excitation, therefore, the right-hand side of (92) and (93) equals zero. Also,

$$\mathbf{J}_1^{eq} = -\mathbf{J}_2^{eq} = \mathbf{J}^{eq}. \tag{94}$$

The last terms of the left-hand sides of (92) and (93) are the surface equivalent currents and they are of similar form as the source excitation $\mathbf{J}$. By equating the surface equivalent current in adjacent domains, magnetic field continuity is maintained.

### 5.4.3 Formulations for Fields on Domain Interface

Suppose choosing domain $\Omega_1$ as the dominant (or mortar) domain and $\Omega_2$ as the auxiliary (or slave) domain, expanding the electric field using edge vector basis functions

$$\mathbf{E} = \sum_{i=1}^{n} \mathbf{N}_i E_i \tag{95}$$

where $n$ is the total edge number, $E_i$ is the unknown expansion coefficient, and $\mathbf{N}_i$ is the vector basis function. Transferring (89), (92) and (93) into Laguerre domain yields:

$$\mathbf{B}_1 \mathbf{E}_{I,1}^q - \mathbf{B}_2 \mathbf{E}_{I,2}^q = \mathbf{0} \tag{96}$$

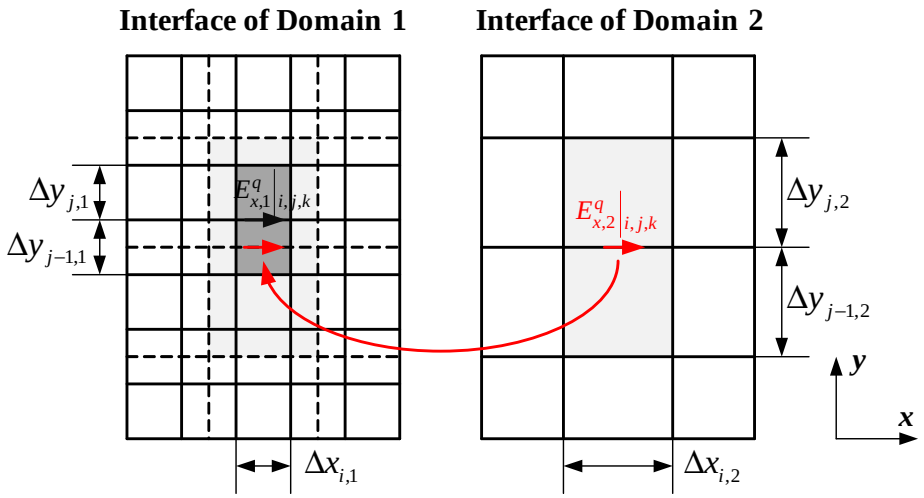


**Figure 39:** Formation of the projection matrix associated with the interface meshing.

$$\begin{aligned}
&\left(\frac{s^2}{4}\mathbf{T}_1+\mathbf{S}_1\right)\mathbf{E}^q_{I,1}+\frac{s}{2}\mathbf{B}_1^T\mathbf{j}^{eq,q}\\
&=-\mathbf{T}_1 s^2\sum_{n=1,q>0}^{q-1}\sum_{m=0}^{n}\mathbf{E}^m_{I,1}-s\mathbf{B}_1^T\sum_{n=1,q>0}^{q-1}\mathbf{j}^{eq,n}
\end{aligned}\tag{97}$$

$$\begin{aligned}
&\left(\frac{s^2}{4}\mathbf{T}_2+\mathbf{S}_2\right)\mathbf{E}^q_{I,2}-\frac{s}{2}\mathbf{B}_2^T\mathbf{j}^{eq,q}\\
&=-\mathbf{T}_2 s^2\sum_{n=1,q>0}^{q-1}\sum_{m=0}^{n}\mathbf{E}^m_{I,2}+s\mathbf{B}_2^T\sum_{n=1,q>0}^{q-1}\mathbf{j}^{eq,n}
\end{aligned}\tag{98}$$

where

$$\mathbf{B}_m=\int_\Gamma \mathbf{N}_m\boldsymbol{\varphi}_m dS \tag{99}$$

$$\mathbf{T}_m=\int_{\Omega_m}\mu\varepsilon\mathbf{N}_m\cdot\mathbf{N}_m dV \tag{100}$$

$$\mathbf{S}_m=\int_{\Omega_m}(\nabla\times\mathbf{N}_m)\cdot(\nabla\times\mathbf{N}_m)\,dV. \tag{101}$$

In grid space, two sets of Lagrange multipliers are collocated on the domain interface. To eliminate the redundant unknown vector $\mathbf{j}^{eq,q}$, a relationship between unknown vectors $\boldsymbol{\lambda}^q$ and $\mathbf{j}^{eq,q}$ are established by projection matrices which can be expressed as:

$$s\mathbf{B}_1^T\mathbf{j}^{eq,q} = s\mathbf{P}_1\mathbf{B}_1^T\boldsymbol{\lambda}^q = \mathbf{C}_1^T\boldsymbol{\lambda}^q \tag{102}$$

$$s\mathbf{B}_2^T\mathbf{j}^{eq,q} = -s\mathbf{P}_2\mathbf{B}_2^T\boldsymbol{\lambda}^q = -\mathbf{C}_2^T\boldsymbol{\lambda}^q \tag{103}$$

$$\begin{aligned} s\mathbf{B}_1^T \sum_{n=1,q>0}^{q-1} \mathbf{j}^{eq,n} &= s\mathbf{P}_1\mathbf{B}_1^T \sum_{n=1,q>0}^{q-1} \boldsymbol{\lambda}^q \\ &= \mathbf{C}_1^T \sum_{n=1,q>0}^{q-1} \boldsymbol{\lambda}^q. \end{aligned} \tag{104}$$

$$\begin{aligned} s\mathbf{B}_2^T \sum_{n=1,q>0}^{q-1} \mathbf{j}^{eq,n} &= -s\mathbf{P}_2\mathbf{B}_2^T \sum_{n=1,q>0}^{q-1} \boldsymbol{\lambda}^q \\ &= -\mathbf{C}_2^T \sum_{n=1,q>0}^{q-1} \boldsymbol{\lambda}^q. \end{aligned} \tag{105}$$

In the dominant domain $\Omega_1$, it is convenient to assume the projection matrix as

$$\mathbf{P}_1 = \mathbf{I} \tag{106}$$

where $\mathbf{I}$ is the identity matrix. In the auxiliary domain $\Omega_2$, the projection matrix $\mathbf{P}_2$ is determined by the grid ratio on the domain interface. Figure 39 shows the formation of the projection matrix associated with the interface meshing. To be specific, suppose one Lagrange multiplier $\lambda_n^q$ is collocated with the electric field component $E_{x,1}^q|_{i,j,k}$ in the dominant domain, while the interface area $(\Delta x_{i,1}\,(\Delta y_{j,1}\Delta y_{j-1,1}))$

associated with the electric field component $E^q_{x,1}|_{i,j,k}$ in domain $\Omega_1$ fully overlaps the interface area $(\Delta x_{i,2}\,(\Delta y_{j,2}\Delta y_{j-1,2}))$ associated with the electric field component $E^q_{x,2}|_{i,j,k}$ in domain $\Omega_2$. Then, the non-zero diagonal element of the projection matrix $\mathbf{P}_2$ associated with electric field component $E^q_{x,2}|_{i,j,k}$ becomes:

$$P_{2,element\rightarrow E^q_{x,2}|_{i,j,k}} = \frac{\Delta x_{i,1}\,(\Delta y_{j,1}\Delta y_{j-1,1})}{\Delta x_{i,2}\,(\Delta y_{j,2}\Delta y_{j-1,2})}. \tag{107}$$

If partial overlapping is observed, a weighted overlapping area is used to determine the non-zero diagonal element of the projection matrix. Note that the most simplified case occurs where matched meshing at the interface for both domains is observed, where the interface problem reduces to conformal domain decomposition problem with $\mathbf{P}_1 = \mathbf{P}_2$.

By inserting (102), (103), (104), and (105) into (97) and (98), the matrix representation of the electric field on the domain interface can be written in the form:

$$\mathbf{K}_{I,1}\mathbf{E}^q_{I,1} + \frac{1}{2}\mathbf{C}_1^T\boldsymbol{\lambda}^q = \mathbf{h}^q_{I,1} \tag{108}$$

$$\mathbf{K}_{I,2}\mathbf{E}^q_{I,2} + \frac{1}{2}\mathbf{C}_2^T\boldsymbol{\lambda}^q = \mathbf{h}^q_{I,2}. \tag{109}$$

Applying trapezoidal integration to (99), (100), and (101) in the interface cells, the FEM-based equations (108) and (109) can be transferred into differential form. Laguerre-FDTD formulations for the electric field on the interface can then be obtained.

To be specific, in (108) and (109), each row represents the equation for the electric field component. Suppose $\hat{z}$ is the unit normal vector pointing out of domain $\Omega_1$ as shown in Figure 40. The equation for electric field in $x$-direction on the domain interface associated with domain $\Omega_1$ can be obtained as:

$$
\begin{aligned}
&\big(1+\bar{C}_y^E\,|_{i,j,k}\,\bar{C}_y^H\,|_{i,j,k}+\bar{C}_y^E\,|_{i,j,k}\,\bar{C}_y^H\,|_{i,j-1,k}\\
&+2\bar{C}_z^E\,|_{i,j,k}\,\bar{C}_z^H\,|_{i,j,k-1}\big)\,E_x^q\,|_{i,j,k}\\
&-\bar{C}_y^E\,|_{i,j,k}\,\bar{C}_y^H\,|_{i,j,k}\,E_x^q\,|_{i,j+1,k}\\
&+\bar{C}_y^E\,|_{i,j,k}\,\bar{C}_x^H\,|_{i,j,k}\,E_y^q\,|_{i+1,j,k}\\
&-\bar{C}_y^E\,|_{i,j,k}\,\bar{C}_x^H\,|_{i,j,k}\,E_y^q\,|_{i,j,k}\\
&-\bar{C}_y^E\,|_{i,j,k}\,\bar{C}_y^H\,|_{i,j-1,k}\,E_x^q\,|_{i,j-1,k}\\
&-\bar{C}_y^E\,|_{i,j,k}\,\bar{C}_x^H\,|_{i,j-1,k}\,E_y^q\,|_{i+1,j-1,k}\\
&+\bar{C}_y^E\,|_{i,j,k}\,\bar{C}_x^H\,|_{i,j-1,k}\,E_y^q\,|_{i,j-1,k}\\
&-2\bar{C}_z^E\,|_{i,j,k}\,\bar{C}_x^H\,|_{i,j,k-1}\,E_z^q\,|_{i+1,j,k-1}\\
&+2\bar{C}_z^E\,|_{i,j,k}\,\bar{C}_x^H\,|_{i,j,k-1}\,E_z^q\,|_{i,j,k-1}\\
&-2\bar{C}_z^E\,|_{i,j,k}\,\bar{C}_z^H\,|_{i,j,k-1}\,E_x^q\,|_{i,j,k-1}\\
&+\frac{1}{2}\mathbf{v}\mathbf{C}_1^T\cdot\boldsymbol{\lambda}^q\\
=\;&-4\sum_{n=0,q>1}^{q-1}\sum_{m=0}^{n}E_x^m\,|_{i,j,k}
\end{aligned}
\tag{110}
$$

where $\mathbf{v}=[v_1,v_2,\ldots,v_n]$ is the vector for extracting a specific row of the coupling matrix where the elements satisfy:

$$
v_i=\begin{cases}1, & i=l\\ 0, & i\neq l\end{cases}
\tag{111}
$$

where $l$ is the row number associated with the electric field component $E_x^q\,|_{i,j,k}$.

Similarly, suppose $-\hat{z}$ is the unit normal vector pointing out of domain $\Omega_2$. The equation for electric field in $x$-direction on the domain interface associated with domain $\Omega_2$ can be written as:

$$
\begin{aligned}
&\big(1+\bar{C}_y^E\,|_{i,j,k}\,\bar{C}_y^H\,|_{i,j,k}+\bar{C}_y^E\,|_{i,j,k}\,\bar{C}_y^H\,|_{i,j-1,k}\\
&+2\bar{C}_z^E\,|_{i,j,k}\,\bar{C}_z^H\,|_{i,j,k}\big)\,E_x^q\,|_{i,j,k}\\
&-\bar{C}_y^E\,|_{i,j,k}\,\bar{C}_y^H\,|_{i,j,k}\,E_x^q\,|_{i,j+1,k}\\
&+\bar{C}_y^E\,|_{i,j,k}\,\bar{C}_x^H\,|_{i,j,k}\,E_y^q\,|_{i+1,j,k}\\
&-\bar{C}_y^E\,|_{i,j,k}\,\bar{C}_x^H\,|_{i,j,k}\,E_y^q\,|_{i,j,k}\\
&-\bar{C}_y^E\,|_{i,j,k}\,\bar{C}_y^H\,|_{i,j-1,k}\,E_x^q\,|_{i,j-1,k}\\
&-\bar{C}_y^E\,|_{i,j,k}\,\bar{C}_x^H\,|_{i,j-1,k}\,E_y^q\,|_{i+1,j-1,k}\\
&+\bar{C}_y^E\,|_{i,j,k}\,\bar{C}_x^H\,|_{i,j-1,k}\,E_y^q\,|_{i,j-1,k}\\
&+2\bar{C}_z^E\,|_{i,j,k}\,\bar{C}_x^H\,|_{i,j,k}\,E_z^q\,|_{i+1,j,k}\\
&-2\bar{C}_z^E\,|_{i,j,k}\,\bar{C}_x^H\,|_{i,j,k}\,E_z^q\,|_{i,j,k}\\
&-2\bar{C}_z^E\,|_{i,j,k}\,\bar{C}_z^H\,|_{i,j,k}\,E_x^q\,|_{i,j,k+1}\\
&+\frac{1}{2}\mathbf{v}\mathbf{C}_2^T\cdot\boldsymbol{\lambda}^q\\
=\;&-4\sum_{n=0,q>1}^{q-1}\sum_{m=0}^{n}E_x^m\,|_{i,j,k}\,.
\end{aligned}
\tag{112}
$$

The equations for electric field component in any direction on the domain interface can be derived in a similar manner.

Note that for (110) and (112), the equations for the electric field components on the domain boundary are in simple differential form similar to those on the interior of each domain. The only additional part that needs to be calculated are matrices $\mathbf{B}_m^T$ and $\mathbf{C}_m^T$ which can be easily derived from (99), (102)–(105) with negligible computational cost.

### 5.4.4 Global System

After obtaining the equations for interior field and field on the domain interface, the system equation can be expressed in matrix form as:

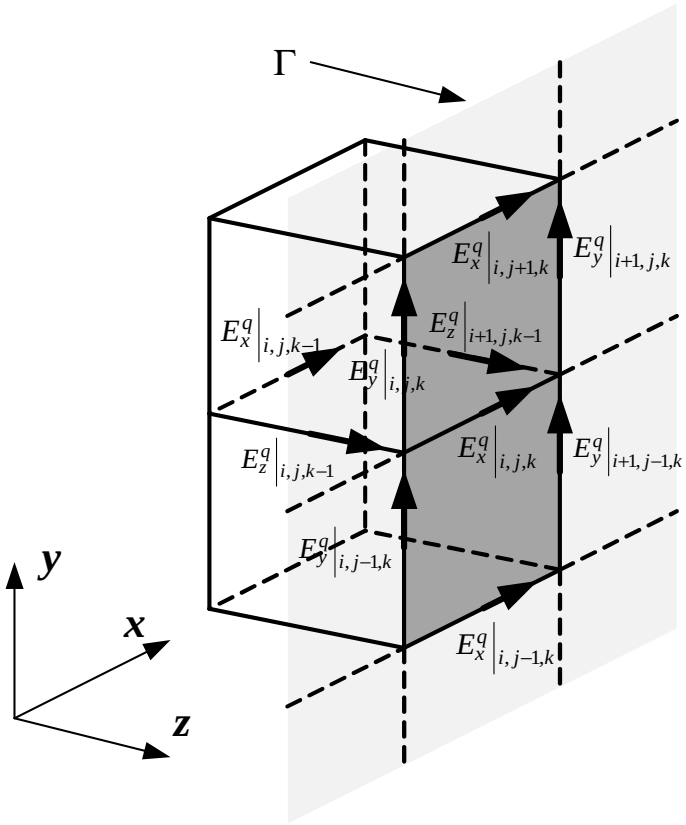


**Figure 40:** Positions of electric field components of order $q$ associated with field component $E_x^q\,|_{i,j,k}$.

$$\begin{bmatrix} \mathbf{K}_1 & & \mathbf{F}_1 \\ & \mathbf{K}_2 & \mathbf{F}_2 \\ \mathbf{D}_1 & \mathbf{D}_2 & \end{bmatrix} \begin{bmatrix} \mathbf{E}_1^q \\ \mathbf{E}_2^q \\ \boldsymbol{\lambda}^q \end{bmatrix} = \begin{bmatrix} \mathbf{f}_1^q \\ \mathbf{f}_1^q \\ \mathbf{0} \end{bmatrix} \tag{113}$$

where

$$\mathbf{K}_m = \begin{bmatrix} \mathbf{K}_{V,m} & \\ & \mathbf{K}_{I,m} \end{bmatrix} \tag{114}$$

$$\mathbf{f}_m^q = \begin{bmatrix} \mathbf{g}_{V,m}^q & \mathbf{h}_{I,m}^q \end{bmatrix}^T \tag{115}$$

$$\mathbf{D}_m = \begin{bmatrix} \mathbf{0} & \mathbf{B}_m \end{bmatrix} \tag{116}$$

$$\mathbf{F}_m = \begin{bmatrix} \mathbf{0} & \frac{1}{2}\mathbf{C}_m^T \end{bmatrix}^T. \tag{117}$$

Similarly, for $N$ domains, the system equation can be derived as:

$$\begin{bmatrix} \mathbf{K}_1 & & & & \mathbf{F}_1 \\ & \mathbf{K}_2 & & & \mathbf{F}_2 \\ & & \ddots & & \vdots \\ & & & \mathbf{K}_N & \mathbf{F}_N \\ \mathbf{D}_1 & \mathbf{D}_2 & \cdots & \mathbf{D}_N & \mathbf{0} \end{bmatrix} \begin{bmatrix} \mathbf{E}_1^q \\ \mathbf{E}_2^q \\ \vdots \\ \mathbf{E}_N^q \\ \boldsymbol{\lambda}^q \end{bmatrix} = \begin{bmatrix} \mathbf{f}_1^q \\ \mathbf{f}_2^q \\ \vdots \\ \mathbf{f}_N^q \\ \mathbf{0} \end{bmatrix} \tag{118}$$

where $\mathbf{D}_m$ and $\mathbf{F}_m$ denote the interface coupling between domain $m$ and all adjacent domains.

Using the Schur complement, the interface problem can be extracted and each individual domain can be evaluated separately. To be specific, by eliminating $\mathbf{E}_m^q$ from (118), the interface equation can be extracted as:

$$\left(\sum_{m=1}^{N} \mathbf{D}_m \mathbf{K}_m^{-1} \mathbf{F}_m\right) \boldsymbol{\lambda}^q = \sum_{m=1}^{N} \mathbf{D}_m \mathbf{K}_m^{-1} \mathbf{f}_m^q. \tag{119}$$

After $\boldsymbol{\lambda}^q$ is determined, the electric field coefficient for each domain can be obtained using

$$\mathbf{E}_m^q = \mathbf{K}_m^{-1} \left(\mathbf{f}_m^q - \mathbf{F}_m \boldsymbol{\lambda}^q\right). \tag{120}$$

Previously, all derivations were based on the assumption of an isotropic, non-dispersive and lossless media for simplicity. However, in real-world applications, material dispersion and conductor loss cannot be neglected. Material dispersion is incorporated using the method discussed in [64] and conductor loss is incorporated using the method discussed in [70].

Here, the simple 2-D wave propagation problem shown in Figure 37 is simulated again using the proposed method. Figure 41 shows the electric and magnetic field distribution at the same time point as the simulation using the direct mortar-element-like method. It can be observed that both the electric and magnetic field continuity is maintained at the domain interface without significant reflection and field distortion.

### 5.4.5 Solution Procedure and Parallel Computing

The solution procedure using the proposed domain decomposition scheme is shown in Figure 42. First, the system matrix is formed. In some cases when the total number of unknowns is small, the system matrix can be solved with direct solvers without using Schur complement. For large-scale problems, direct solution of the system matrix is not possible since direct solvers require a large amount of memory storage. Instead,

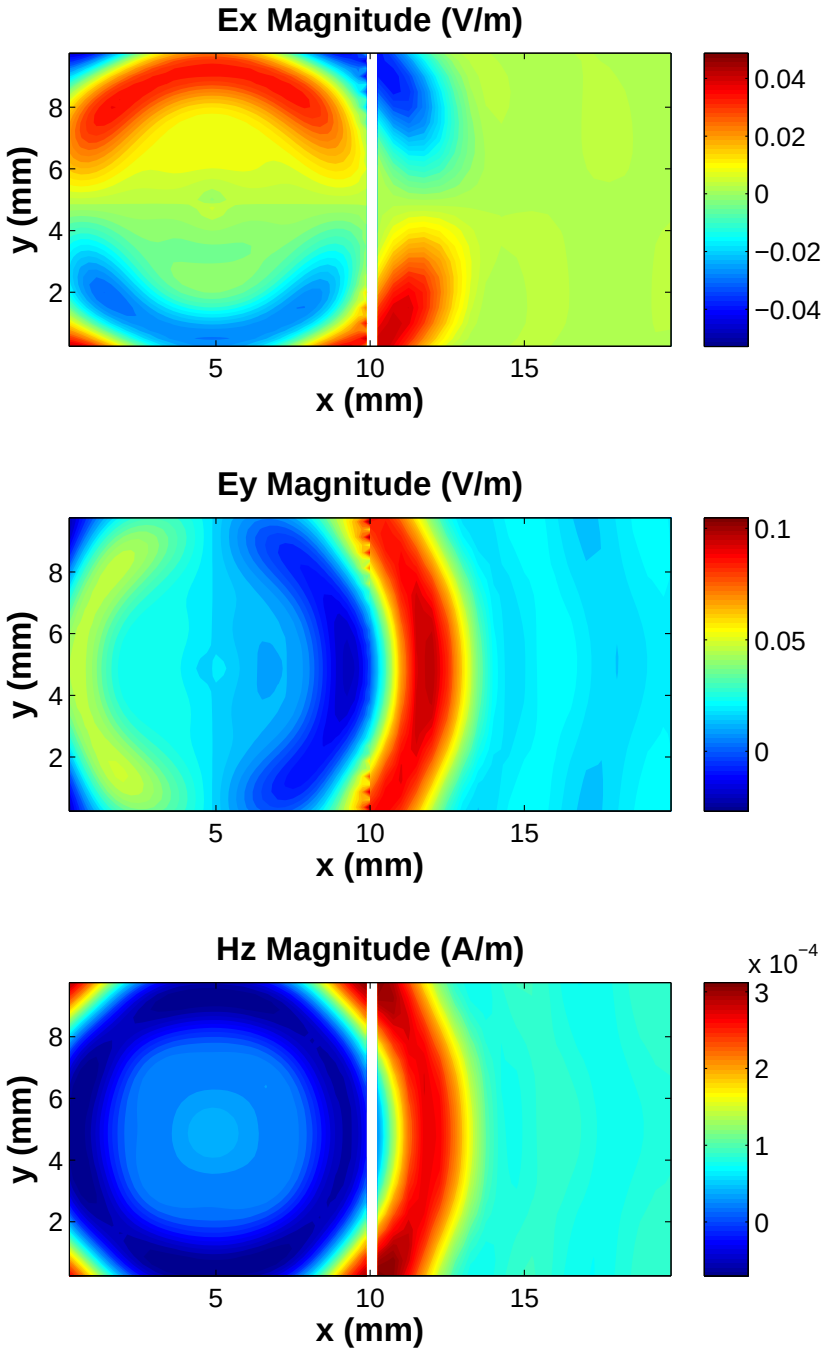


**Figure 41:** Field distribution for the 2-D wave propagation problem using dual sets of Lagrange multipliers.

the interface problem is extracted using the Schur complement. Therefore, the sub-system for each domain can be solved independently. After the solution for each domain is obtained, the solution for the entire computational domain can be derived.

It is obvious that the solution of the sub-system corresponding to each domain can be obtained in a parallel manner which will significantly reduce the computational time. Parallel computing can be realized by using a multi-core feature of the processor or GPU computing. Another approach is to utilize distributed computing using a cluster of computers. This approach involves more complex algorithm design, including the communication between different computers, which is preferred for ultra-large problems. In the scope of this work, only the first approach is adopted.

It is important to note that, the solution of each domain can also be calculated in a series manner if parallel computing is not available. The simulation speed can also be enhanced by the domain decomposition scheme due to the reduction of total unknowns. The speedup dependents on the meshing in each domain and the meshing at the interface.

### 5.4.6 Stability Analysis

When implementing non-conformal domain decomposition schemes, artificial error can be generated due to the non-matching grid interface, which often shows up as spurious reflection. A simple microstrip line structure is tested to gauge the reflection introduced by the proposed method. The width, length and thickness of the metal strip are 0.4 mm, 50 mm and 0.02 mm, respectively. The thickness and dielectric constant of the substrate are 0.2 mm and 4.3. The simulated structure is decomposed into three subdomains, as shown in Figure 43. Domain two is densely meshed with metal strip length of 10 mm. Two ports are defined at each end of the microstrip line. A Gaussian pulse is excited at one port and artificial reflection is recorded. The reflection is normalized by the result simulated by Laguerre-FDTD with only one

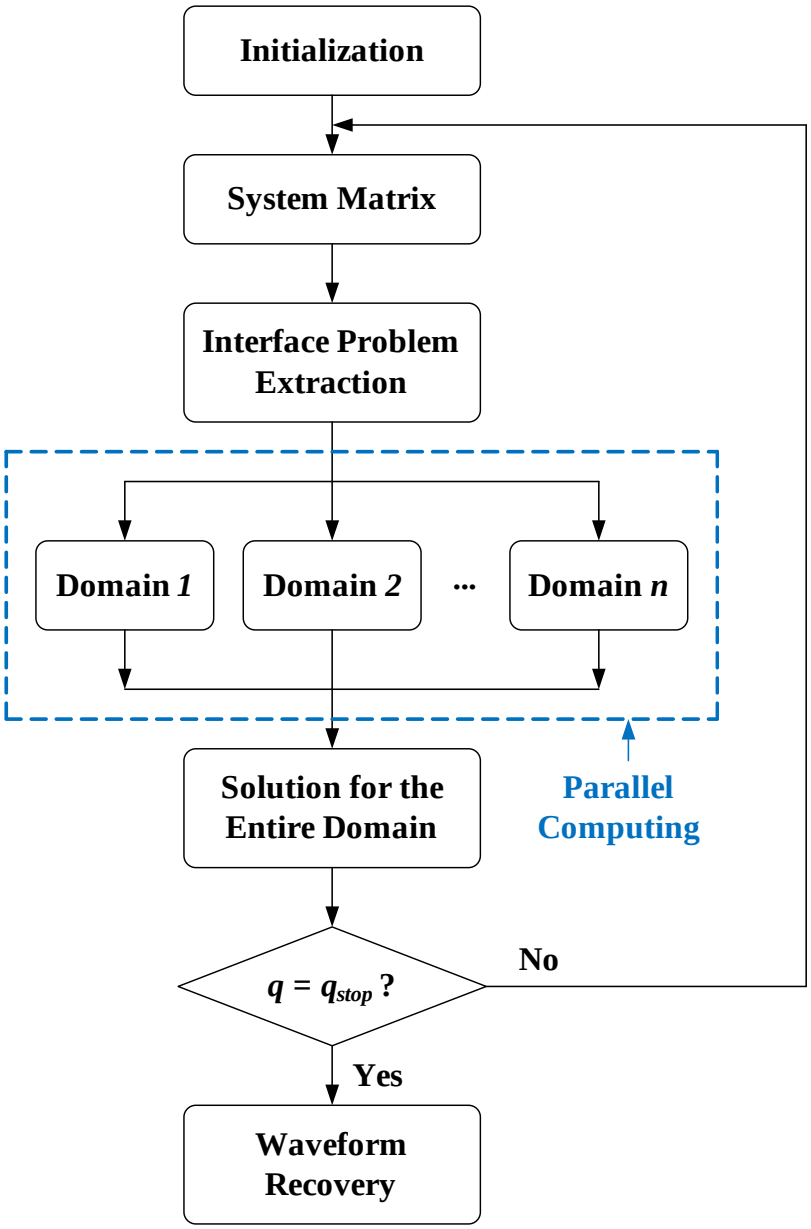


**Figure 42:** Flow chat for the non-conformal domain decomposition scheme with parallel computing

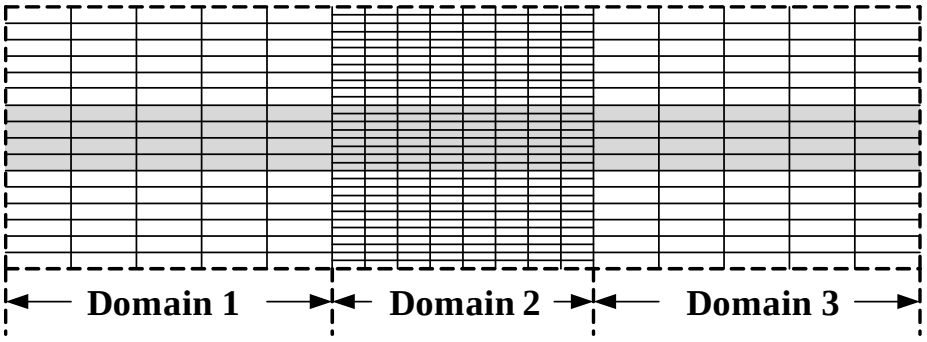


**Figure 43:** Schematic top view of decomposed microstrip line with mesh. The microstrip line is partitioned into three subdomains

domain.

Figure 44 shows the artificial reflection magnitude with respect to time. Two scenarios are investigated, namely interface grid ratio of 2 : 1 and 10 : 1. It can be observed that the maximum reflection of the time period for these two cases are $-50.7$ dB and $-43.6$ dB, respectively. The reflection of the latter case is larger due to the larger mismatch of dispersion behavior of the densely meshed and coarsely meshed regions. This level of reflection is maximum and is therefore acceptable for the structures of interest.

### 5.4.7 Selection of Dominant Face

The proposed domain decomposition uses a mortar-element-like scheme with dual sets of Lagrange unknowns. By interface problem extraction, a 3-D problem is reduced to a 2-D problem with fewer degrees of freedom. For implementation, a practical concern is the selection of the dominant face.

Consider the domain interface between domain two and domain three for the microstrip line shown in Figure 43. At the interface, the face belonging to domain two is densely meshed whereas the one belonging to domain three is coarsely meshed (Figure 45). From (119) it can be concluded that the complexity of the interface problem extraction is dependent on the dominant face selection. Selecting the face

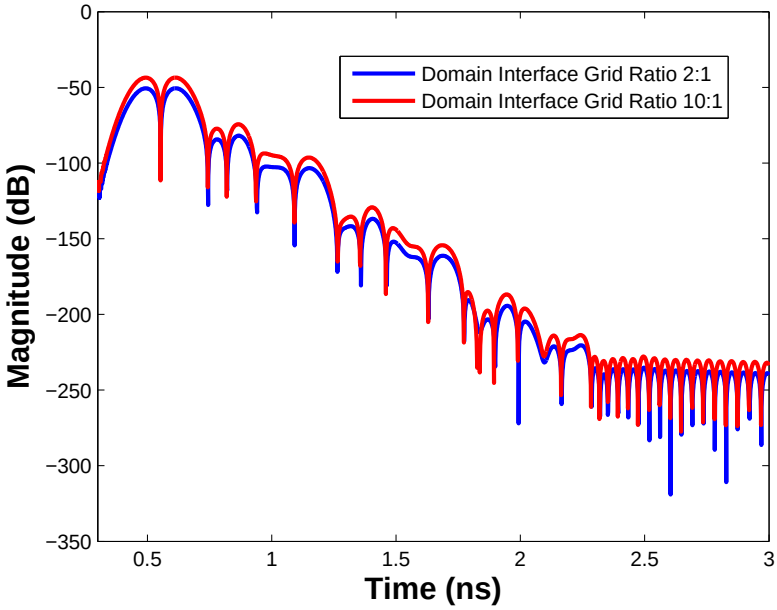


**Figure 44:** Time domain normalized artificial reflection waveform for the simulated microstrip line with domain interface grid ratio of $2:1$ and $10:1$.

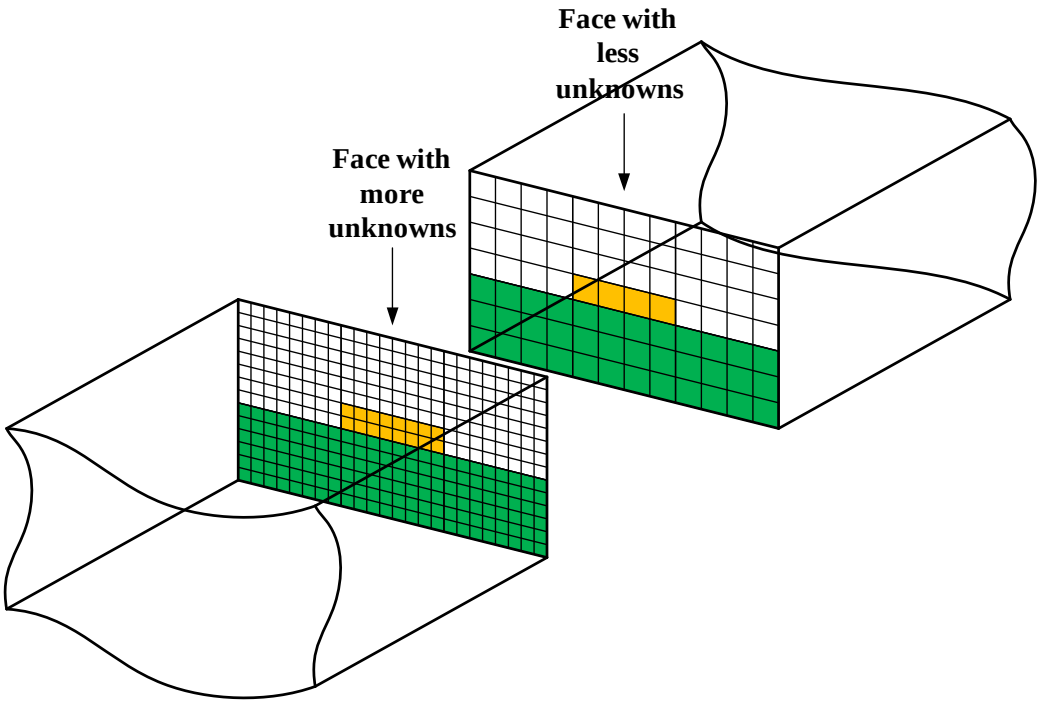


**Figure 45:** Domain interface of the microstrip line.

with dense mesh as the dominant face will result in more interface unknowns, which is not desired. In the previous microstrip line test case, all the faces with coarse mesh are selected as the dominant face. This guideline is also used for all other simulation cases.

## *5.5 Numerical Results*

In this section, some test cases are simulated which validate the proposed non-conformal domain decomposition method. It is important to note that, the non-conformal domain decomposition method shows significant advantages only when multiscale structures, such as chip-package structures, are simulated. These examples are discussed in detail in the next chapter.

### 5.5.1 Cavity Resonator

To validate the proposed domain decomposition method, a simple air-filled rectangular cavity resonator shown in Figure 46 is simulated and analyzed. The side length of the structure along the $x$, $y$, and $z$ coordinates are $l = 20$ mm, $w = 10$ mm, and $h = 2$ mm, respectively. For the domain decomposition method, the cavity is divided into two equal domains. Table 2 shows the meshing details of these two subdomains. For comparison, the meshing for the Laguerre-FDTD method without domain decomposition is also created. The excitation is located in the center of subdomain one along the $z$-direction and the entire computational domain is truncated using a PEC boundary.

Figure 47 shows the comparison of the time-domain electric field waveform at the observation point for the Laguerre-FDTD method and domain decomposition. The observation point is located in the center of subdomain two. Good correlation can be observed for these two methods. Table 2 summarizes the CPU time using different simulation schemes. It can be observed that the CPU time of domain decomposition

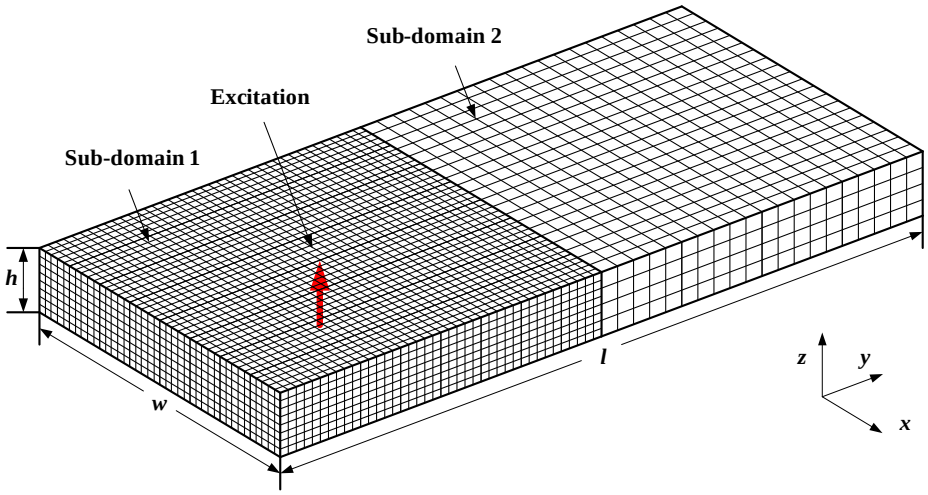


**Figure 46:** Meshing of the simulated cavity structure with two subdomains.

**Table 2:** Comparison of the computational cost for the standard Laguerre-FDTD method and the Laguerre-FDTD method with domain decomposition.

| Method | $\Delta t$ | No. of Cells | CPU Time |
|---|---|---|---|
| Laguerre-FDTD | 0.4 ps | 80×40×8 | 15 min |
| Domain decomposition | 0.4 ps | 40×40×8 (Sub-domain 1) | 8 min |
| | | 20×20×4 (Sub-domain 2) | |

method is almost half of the standard Laguerre-FDTD method. This is because non-conformal domain decomposition allows coarse meshing for subdomain two, which significantly reduces the computational time.

To be noted, this test case is just a demonstration of non-conformal domain decomposition method. The cavity resonator in this case does not necessarily need to be decomposed with different meshing schemes in different subdomains. However, for complex cases such as chip-package or package-board application, the mesh ratio between two adjacent subdomains can easily exceed 10:1. In such cases, a direct solution is highly inefficient, and the non-conformal domain decomposition method is required.

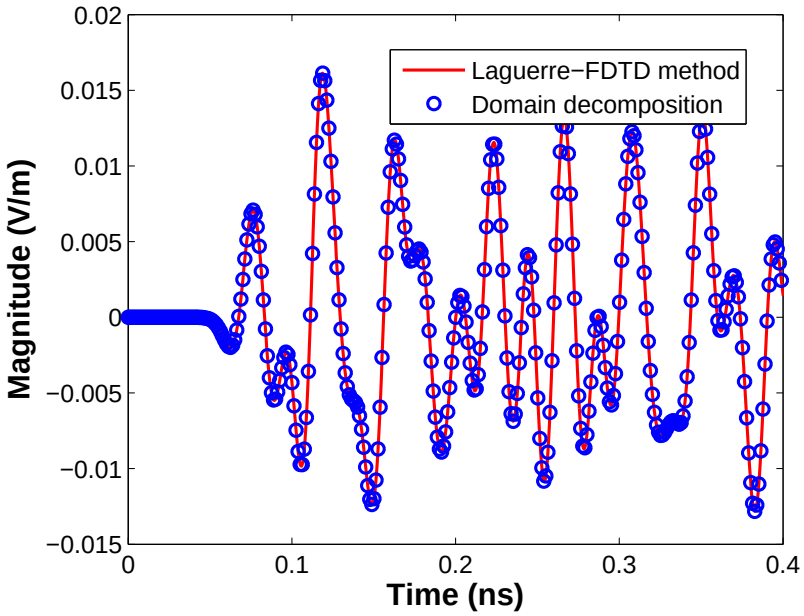


**Figure 47:** Comparison of the time domain electric field waveform at the observation point for the Laguerre-FDTD method without and with domain decomposition.

### 5.5.2 Via Transition

To further validate the accuracy of the proposed method, a simple via structure originally proposed in [71] is simulated. Figure 48 shows the cross-sectional view of the via structure with all the feature sizes marked. The dielectric constant of the substrate is $\varepsilon_r = 3.4$ and the conductivity of the metal strip is $\sigma = 5.8 \times 10^7$ S/m. Note that in [71], the metal strip and ground plane are considered as zero thickness PEC sheets. Here, the thickness of the metal strip and ground is considered as $t = 20$ $\mu$m which makes the structure multiscale. Two ports are defined at each end of the metal strip. The scale difference for the structure is 1500:1 (ratio between feature sizes of length and metal thickness). The structure is decomposed into two subdomains. Figure 49 shows portion of the enlarged top view of the domain interface. Coarse mesh is applied to the microstrip line region whereas dense mesh is applied to the via transition. The non-matching interface can be clearly seen.

Figure 50 shows the return loss and insertion loss of the simulated structure. For

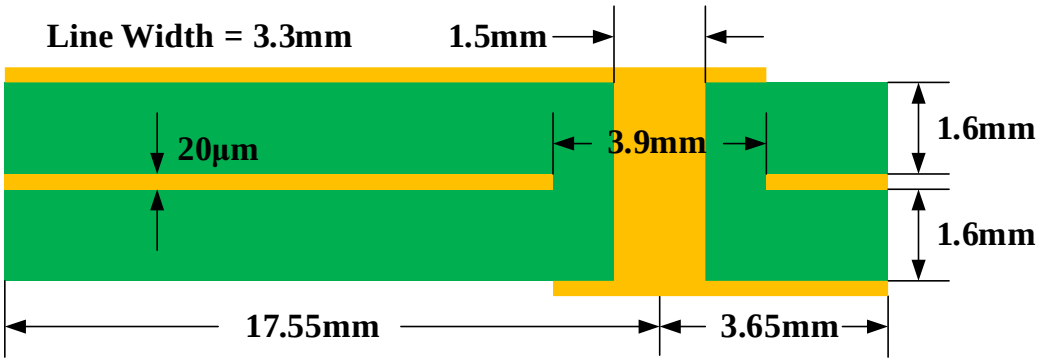


**Figure 48:** Cross-sectional view of the via transition.

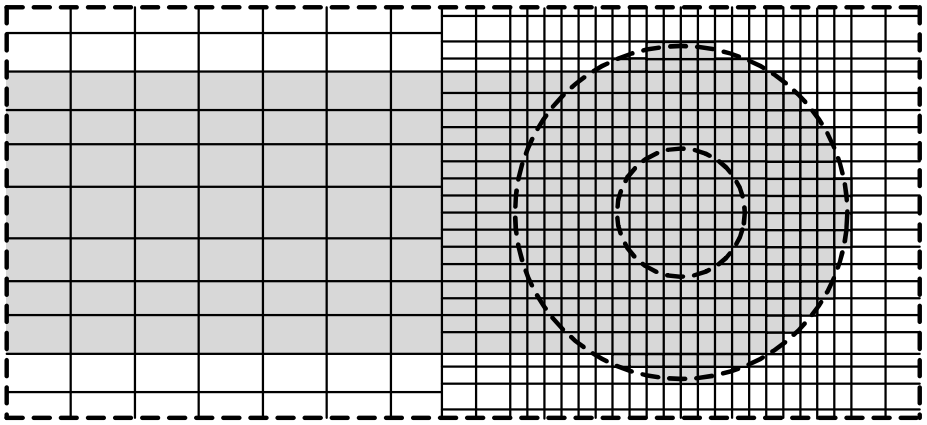

**Figure 49:** Top view of the decomposed via transition with mesh. The via transition is partitioned into two subdomains.

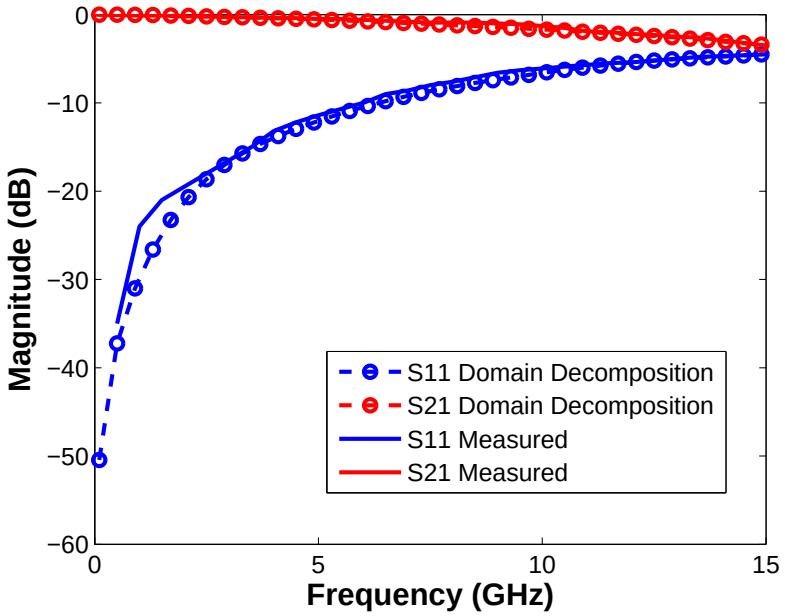


**Figure 50:** Return loss and insertion loss of the simulated via transition.

comparison, a measurement from [71] is also shown. It can be observed that the simulation results correlate well with the measurement and no non-physical phenomenon can be identified.

## *5.6 Summary*

A full-wave transient non-conformal domain decomposition scheme based on the Laguerre-FDTD method is proposed in this chapter. Unlike the traditional computational methods which compute the entire domain in a single run, the computational domain is decomposed into several subdomains with independent meshing strategies. In this chapter, electric and magnetic field continuity at the interface is enforced by introducing dual sets of Lagrange multipliers. This implies that dense mesh and coarse mesh can be applied separately in the physically small and large regions which is suitable for multiscale structure simulation. The interface problem can be solve first using Schur complement and each subdomain can be calculated in a parallel manner. The final solution is obtained by the combination of results of all subdomains. Several

multiscale structures are investigated using the proposed method. Comparison of the results of the proposed method with the results simulated by commercial transient solver and measurement has also been carried out. The examples demonstrate that the proposed method is accurate and efficient for multiscale structure simulation.

# CHAPTER VI

# MULTISCALE CHIP-PACKAGE CO-SIMULATION

## *6.1 Introduction*

The design and simulation of chips and packages have been considered as disjoint tasks in semiconductor industry for several decades. However, as the integration density and operating frequency increases, the electromagnetic interaction between chip and package becomes non-negligible, posing problems in signal/power integrity. These interactions are difficult to be modeled using circuit type of schemes. Therefore, a full-wave chip-package co-simulation solution that rigorously captures the system behavior is required for simulating on-chip and on-package interconnects. For example, if a signal trace starts from a package, passes through a solder bump and ends in the chip, a typical modeling strategy would be first extracting the $S$-parameters of these three parts and then cascading them together (Figure 51(a)). However, this does not account for the mutual coupling among these three parts. A straightforward and more accurate way would be to analyze the entire system at once (Figure 51(b)).

One critical problem in chip-package co-simulation is the multiscale dimension. The typical feature sizes for chip and package are nanometer and micrometer, resulting in a scale ratio around 1:1000. Such structures are difficult to simulate efficiently especially for time-domain solvers. Very fine mesh needs to be applied to the on-chip area, resulting in prohibitively long simulation time due to stability conditions arising in the conventional FDTD method. Even with unconditionally stable schemes, the memory usage will become a significant problem as system complexity grows.

The problems mentioned can be solved efficiently using the proposed non-conformal

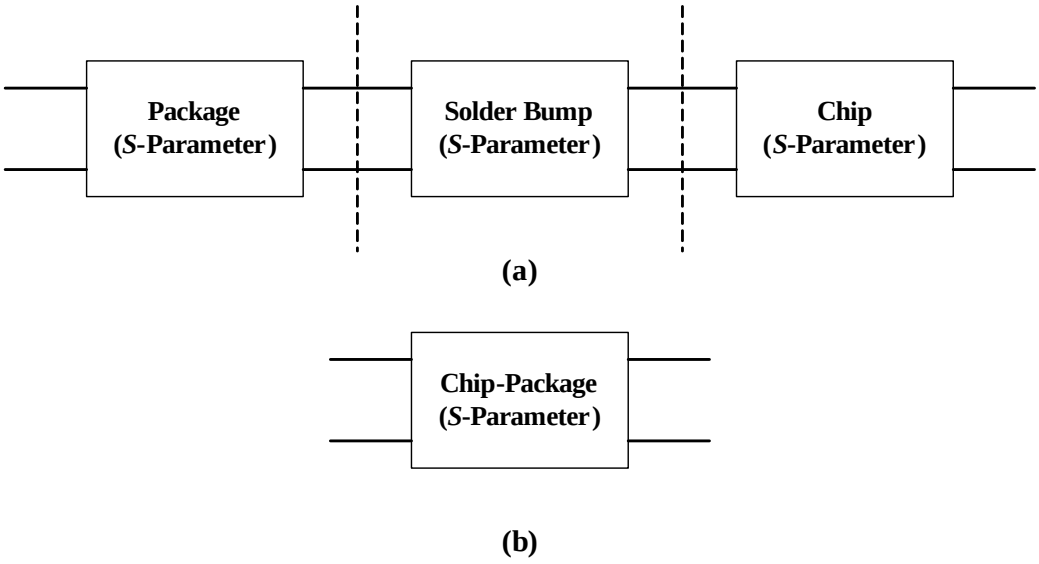


**Figure 51:** Chip-package structure simulation strategy (a) cascading models of package, solder bump and chip and (b) chip-package co-simulation.

domain decomposition method applied to the Laguerre-FDTD scheme. First, the simulation time using the Laguerre-FDTD method is no longer constrained by the time step but by the required simulation resolution. The key idea of the non-conformal domain decomposition scheme is that the simulation is performed by decomposing the structure into subdomains with non-matching mesh interface. Each domain is evaluated separately and the system solution is obtained by combining the solutions of all subdomains. This implies that the chip and package can be meshed separately and less peak memory will be consumed. The field continuity between adjacent subdomains is guaranteed by introducing the Lagrange multipliers. In this chapter, several typical chip-package co-simulation problems are investigated. The simulation results indicate that the proposed method is accurate and computationally efficient compared to the existing schemes.

## *6.2 Multiscale Interconnects in Chip-Package Structure*

In this section, interconnects in a chip-package structure are investigated with the proposed non-conformal domain decomposition scheme. Numerical results show the

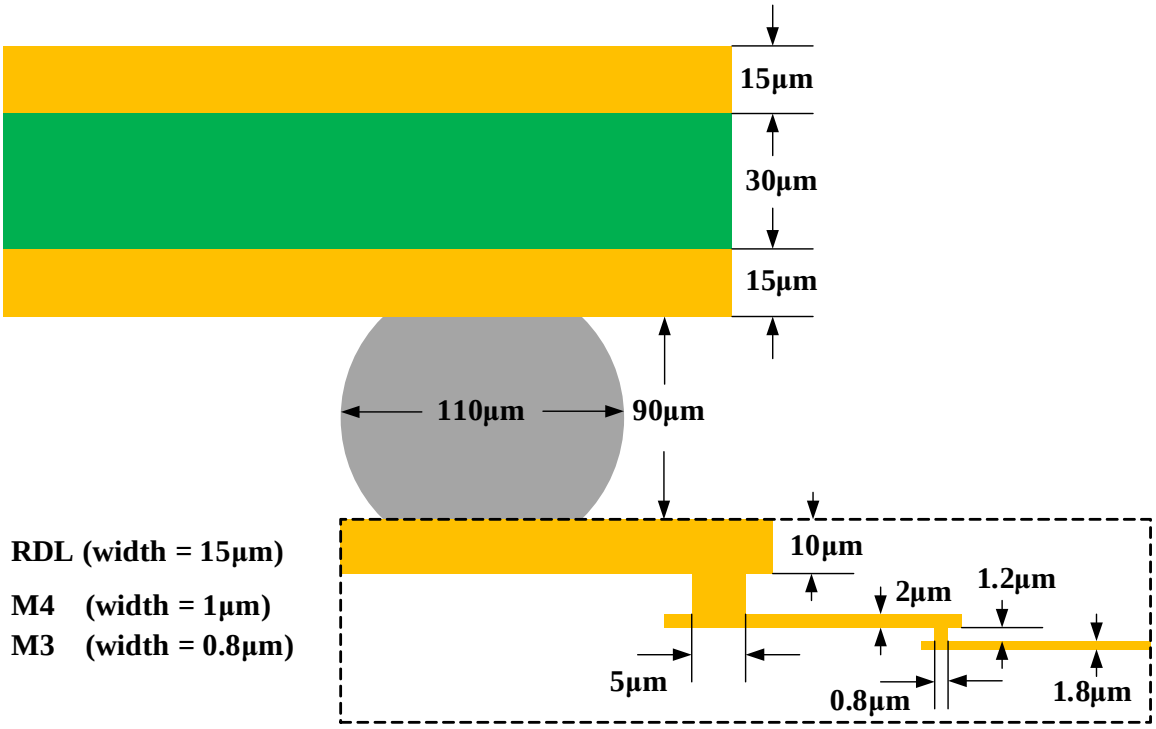


**Figure 52:** Schematic cross-sectional view of the interconnects in chip-package structure.

efficiency and accuracy of the proposed method.

### 6.2.1 Test Case: Signal Traces Connecting Package to Chip with Four Coupled Lines

Multiscale interconnects in a chip-package structure are simulated. Figure 52 shows the hierarchical cross-sectional view of the multiscale interconnect structure. For on-package area, one signal layer and one ground layer with thickness of 15 $\mu$m are considered. A substrate with thickness of 30 $\mu$m and dielectric constant of 4.3 is used. For on-chip area, the width of the redistribution layer (RDL), the fourth metal layer (M4) and the third metal layer (M3) are 15 $\mu$m, 1 $\mu$m and 0.8 $\mu$m, respectively. The thickness and via size of each on-chip layer are marked in Figure 52. The chip is mounted on package with solder bumps. The diameter and the height of the solder bumps are 110 $\mu$m and 90 $\mu$m.

Figure 53 shows the top view of the entire simulated structure. Four signal lines

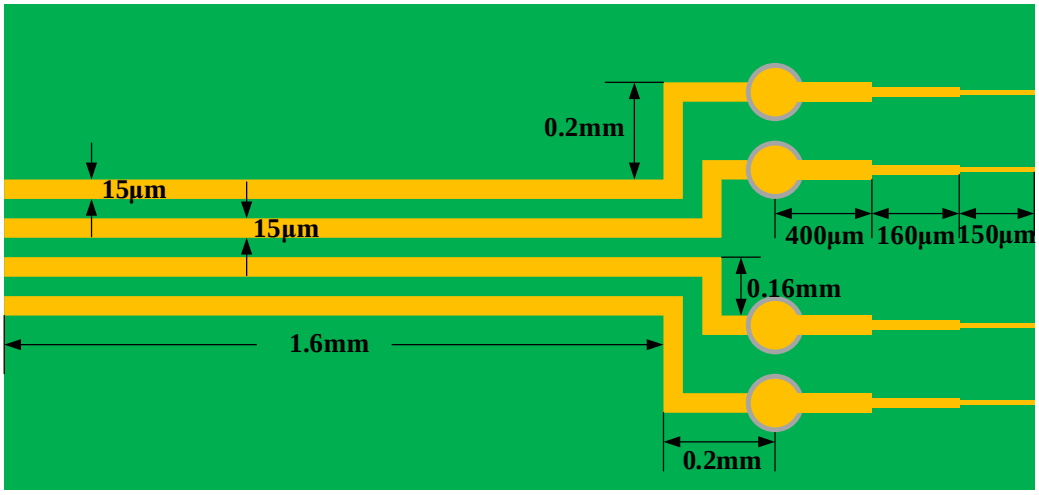


**Figure 53:** Top view of the four coupled line structure.

are simulated with eight ports defined at the left side of the package substrate (port 1, 2, 3 and 4) and the right side of the chip cross section (port 5, 6, 7 and 8). The signal is excited at the port on the package, passes through the solder bump and enters into the on-chip area. All the feature sizes are marked on Figure 53 and the 3-D view of the structure is shown in Figure 54. The scale difference for the structure is 2500:1 (ratio between feature sizes of the total length of the signal line and minimum on-chip interconnect thickness).

Two scenarios are investigated. First, the computational domain is discretized with only one domain, namely discretizing using the standard Laguerre-FDTD method. The meshing of the structure is shown in Figure 55. Comparatively, to implement the domain decomposition, the computational domain is discretized into three sub-domains with cell sizes corresponding to the feature size within each domain. The meshing of the structure using the domain decomposition is shown in Figure 56. It can be observed that an unnecessarily dense mesh is applied to the coupled line structure using the standard Laguerre-FDTD method. In contrast, a reduced mesh density is achieved by the separate meshing strategy.

Figure 57 shows the simulated $S$-parameters using the domain decomposition

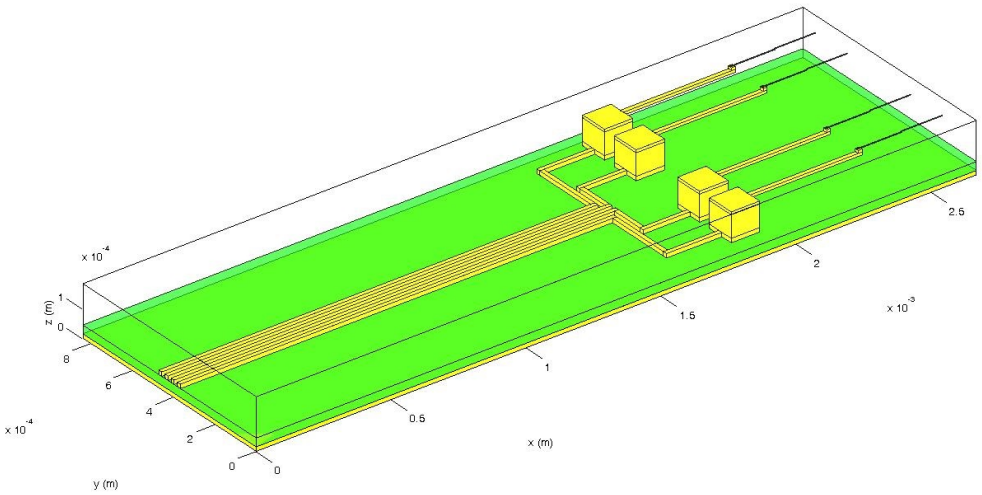


**Figure 54:** 3-D view of the four coupled line structure.

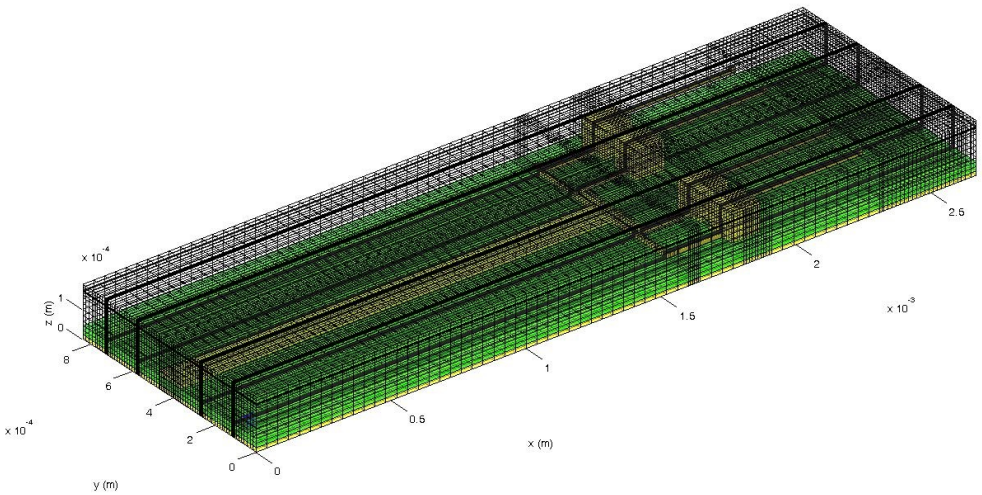


**Figure 55:** Conformal meshing with one computational domain for the test structure.

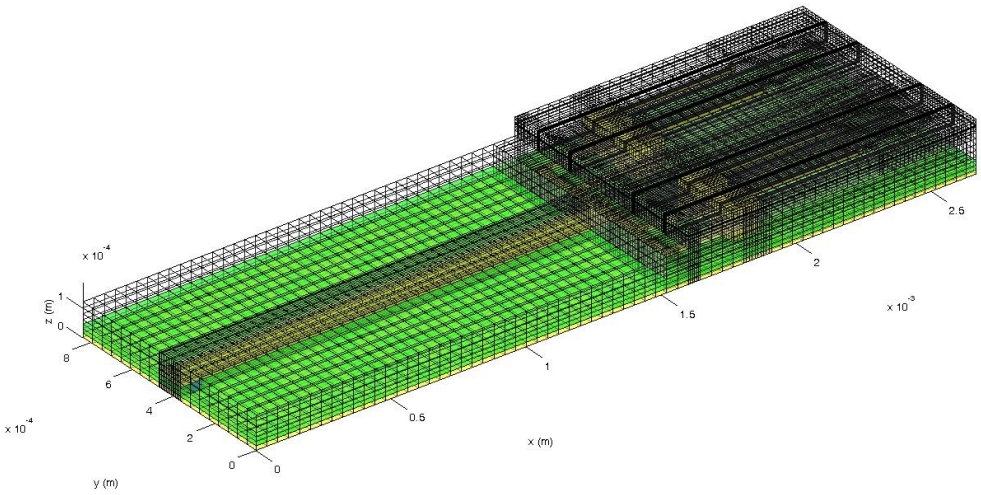


**Figure 56:** Non-conformal meshing with three subdomains for the test structure.

method. For comparison, the structure is simulated using the standard Laguerre-FDTD method with only one domain, as shown in Figure 55. It can be observed from Figure 57 that these two methods correlate well with each other.

### 6.2.2 Test Case: Package-Chip-Package Signal Traces with Three Coupled Lines

The signal integrity problem for interconnects in a chip-package structure is of vital importance to system performance. By applying the domain decomposition method, the $S$-parameters of the entire interconnect system can be extracted. Time domain performance, such as crosstalk and eye diagrams, can be easily investigated.

Figure 58 shows the top view of the entire simulated structure. Three signal lines are simulated with six ports defined at the left (port 1, 2, and 3) and right (port 4, 5, and 6) side of the package substrate. The signal is excited at the port on one side, passes through the solder bump into the on-chip area interconnect and finally ends at the corresponding port on the other side. All the feature sizes are marked on Figure 58. The scale difference for the structure is 5000:1 (ratio between feature sizes

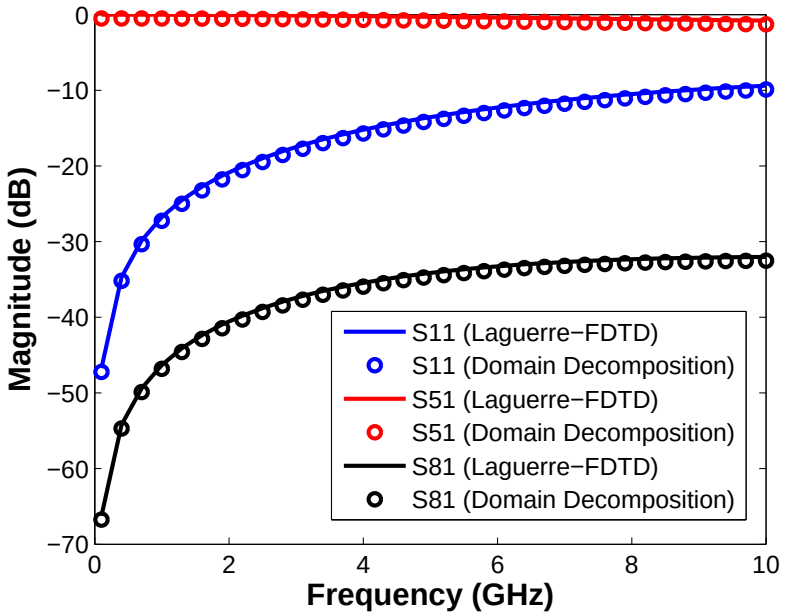


**Figure 57:** *S*-parameters for the four coupled line structure.

of the total length of the signal line and minimum on-chip interconnect thickness). The entire structure is decomposed into two domains (on-package area and on-chip area) with separate meshing strategies.

For comparison, the structure is also simulated with a conventional FDTD method and Laguerre-FDTD method with only one domain. Simulation results from a commercial time-domain electromagnetic full-wave solver (Computer Simulation Technolgy, (CST)) is used for correlation. For a fair comparison, the grid resolution on chip is kept constant for all simulation schemes. Figure 59 shows the S-parameters of the simulated structure. It can be observed that the simulated results correlate well with the results from the commercial solver. Table 3 summarizes the comparison of simulation parameters for different simulation methods. Note that for conventional FDTD method, the maximum time step is constrained by the minimum feature size. Thus, for multiscale chip-package structure, the time step is much smaller than that

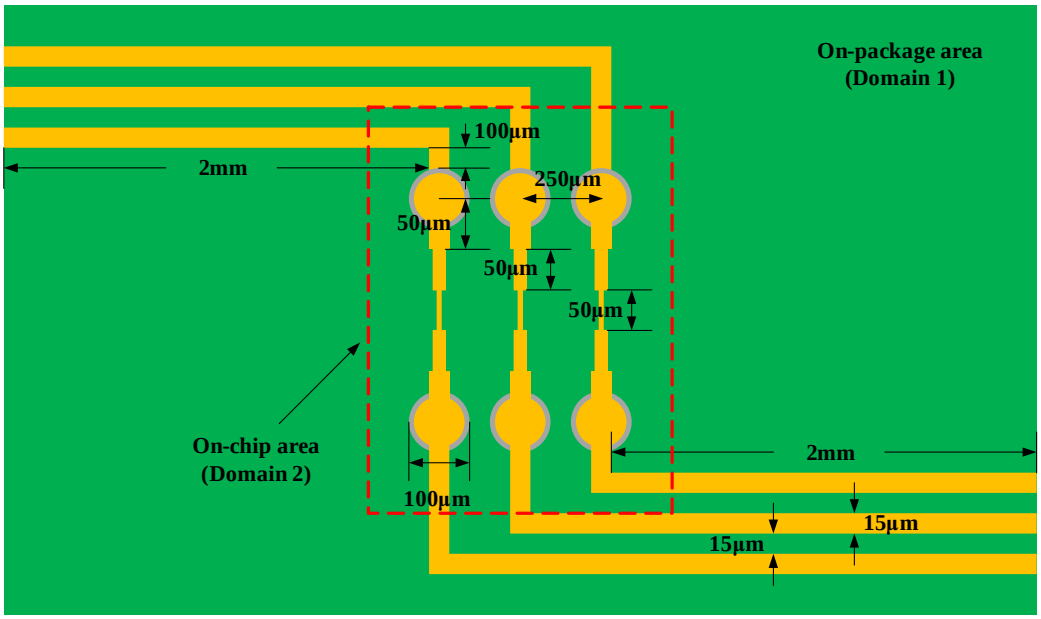


**Figure 58:** Schematic top view of the simulated multiscale interconnect structure with two subdomains (package domain and chip domain).

**Table 3:** Comparison of the simulation parameters for chip-package interconnects.

| Method | Cells | $\Delta t$ | CPU Time |
|---|---|---|---|
| FDTD | 70.4 K | 1.2 fs | >24 hr |
| Laguerre-FDTD | 70.4 K | 1.0 ps | 3.5 hr |
| Domain Decomposition | 34.6 K | 1.0 ps | 2 hr |
| Commercial Transient Solver | 64.4 K | - | 5 hr |

of Laguerre-FDTD method which results in a prohibitively long simulation time. Since a separate meshing strategy is applied for the domain decomposition method, the dense mesh of the chip area will not affect the meshing density of the package area. This results in a reduced total number of cells and faster simulation speed with domain decomposition scheme compared to standard Laguerre-FDTD method. Also, the simulation speed of the proposed method is faster than the commercial solver for this specific structure.

Using the simulated $S$-parameters, time-domain crosstalk is investigated using the Advance Design System (ADS). Line 1 with ports 1 and 4 is designated as the

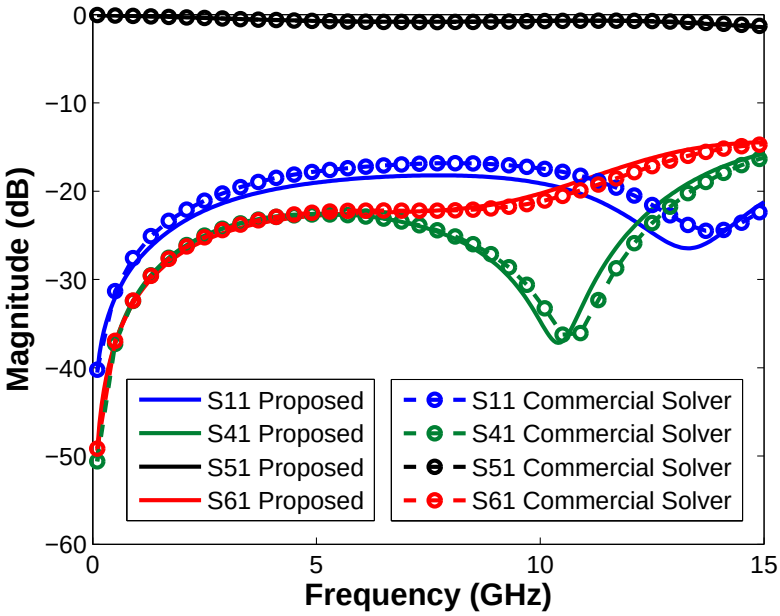


**Figure 59:** S-parameters of the simulated multiscale interconnect structure.

attacking line whereas the other two lines are considered as victim lines. Figure 60 and Figure 61 show the far end and near end crosstalk of the system, respectively. It can be observed that the far end crosstalk for the victim lines are comparable whereas the near end crosstalk of the victim line located near the aggressive line is higher than the one located further away. It is clear that by using the proposed method, the signal integrity problem can be investigated at the chip-package level for early stage chip/package design, which will help to eliminate any design flaws.

## *6.3 Multiscale Power Delivery Networks in Chip-Package Structure*

In this section, multiscale power delivery networks (PDN) in a chip-package structure are simulated with the proposed non-conformal domain decomposition method. Numerical results show the efficiency and accuracy of the proposed method.

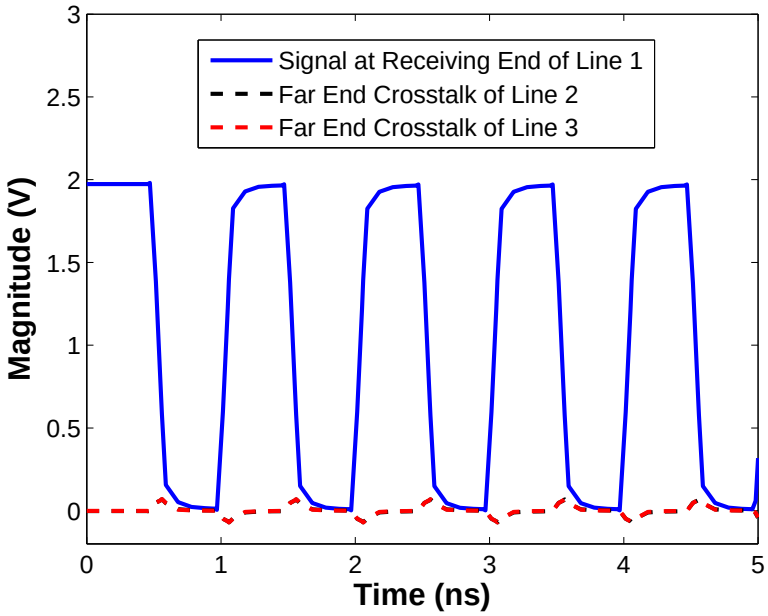


**Figure 60:** Far end crosstalk of the three coupled line structure (line 1 is the attacking line whereas line 2 and line 3 are the victim lines).

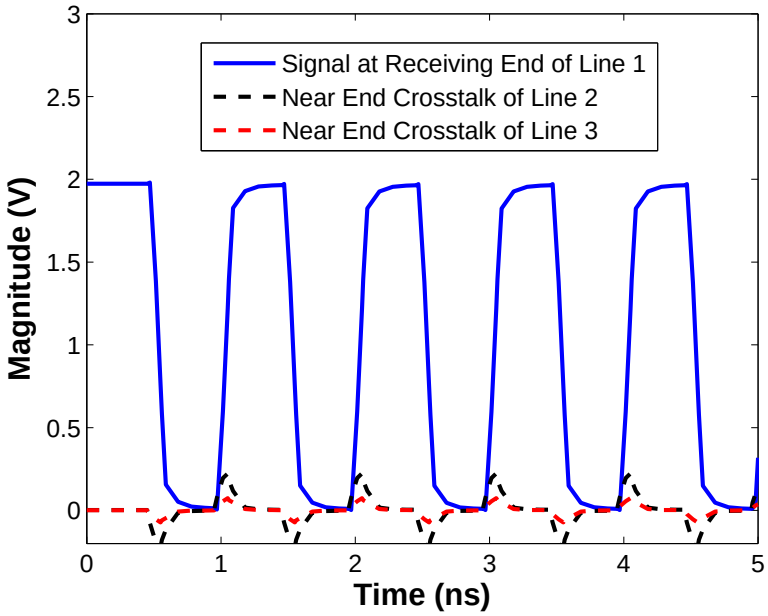


**Figure 61:** Near end crosstalk of the three coupled line structure (line 1 is the attacking line whereas line 2 and line 3 are the victim lines).

### 6.3.1 Test Case: Multilayer On-Chip Power Grid

The design of the PDN is critical in modern chip design since the system signal integrity is dependent on constant and stable voltage supply. It is known that simultaneous switching noise (SSN) generated in a PDN is the major cause of signal degradation. The design goal of the PDN is to lower its impedance to meet the target impedance requirement, and therefore minimize the influence of the SSN on system signal integrity is important. This involves efficient and accurate simulation of the impedance of the PDN.

A typical PDN in a chip-package structure is the on-chip power grid. Unlike the on-package power-ground plane pair PDN design, the on-chip PDN is commonly realized using multilayer orthogonal lines. Figure 62 shows a portion of the on-chip multilayer power grid. On a certain layer, the power and ground interconnects are distributed in a parallel manner whereas inter-layer grids are weaved vertically with respect to each other.

The on-chip power grid is intrinsically multiscale. The total area of the power grid is significantly larger compared to the width and thickness of each power interconnect. In addition, the grid density of each metal layer is different. This structure can be efficiently simulated using the domain decomposition scheme by discretizing the computational domain by metal layer with different feature size.

A four metal layer on-chip power grid is simulated as shown in Figure 63. The line width and spacing in each layer are marked in Figure 63. The total length and width of the first two grid layers with large line spacing are 500 $\mu$m and 500 $\mu$m, respectively. The total length and width of the other two grid layers with small line spacing are 250 $\mu$m and 250 $\mu$m, respectively. The coarse and fine grid share one quarter of the on-chip space.

Figure 64 shows the meshing for the simulation structure. The computational domain is decomposed into two subdomains. Coarse mesh is applied to the first two

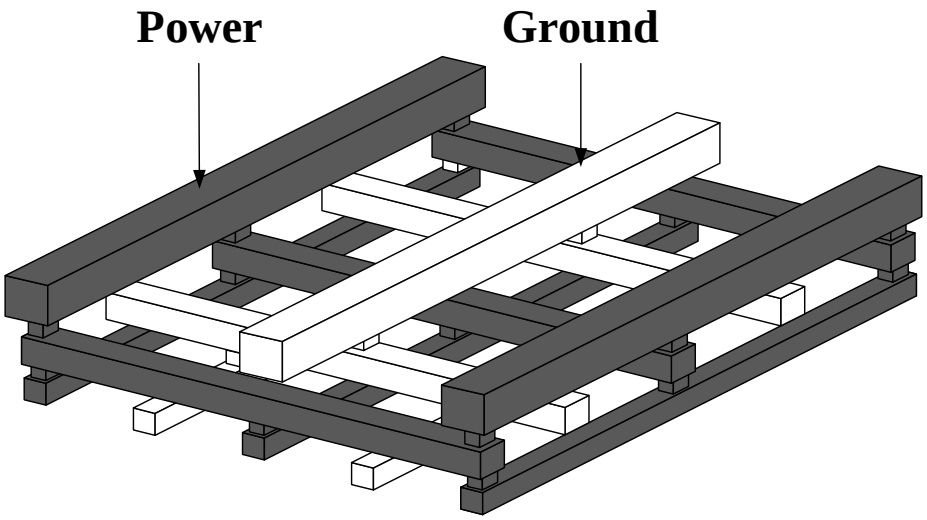


**Figure 62:** Multilayer on-chip power grid (dark gray: power interconnect, white: ground interconnect).

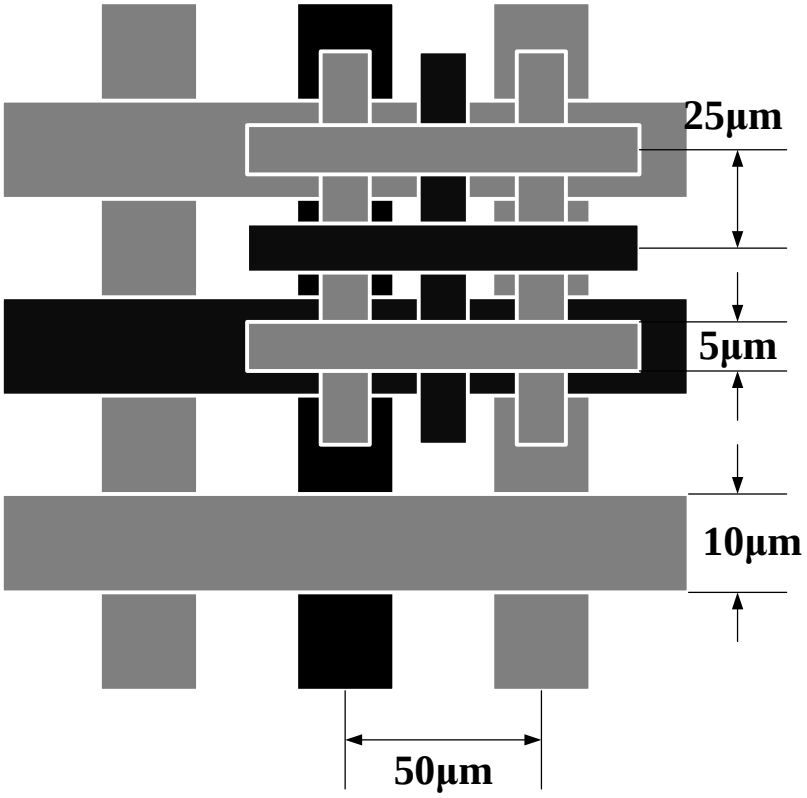


**Figure 63:** On-chip power grid of four metal layers.

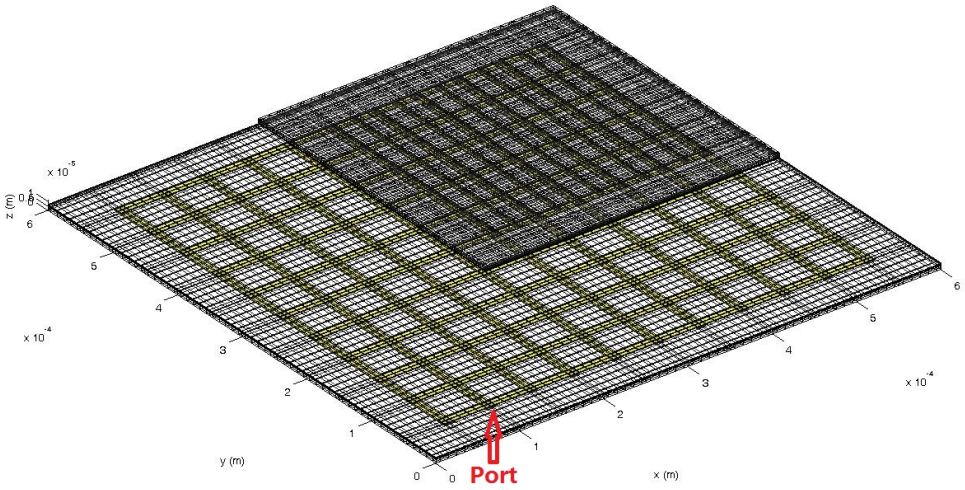


**Figure 64:** Meshing of the four layer power grid with two subdomains

grid layers with large line spacing whereas fine mesh is applied to the other two grid layers with small line spacing. The port is defined at the corner of the grid structure between the power and grid interconnects, as shown in Figure 64.

Figure 65 shows the self-impedance of the on-chip power grid. To make comparison, the simulation result from the commercial solver is also presented. It can be observed that the result of the proposed non-conformal domain decomposition matches well with that of the commercial solver. To be noted, the simulation time of the proposed method is much shorter.

### 6.3.2 Test Case: Chip-Package PDN Co-Simulation

A more challenging simulation scenario is the chip-package PDN co-simulation, meaning that the on-package power-ground plane pairs and the on-chip power grid together with the connecting solder bumps are simulated in a single run. The scale difference of the on-package structure and on-chip structure can be significant, making it difficult or even impossible to simulate using the conventional schemes.

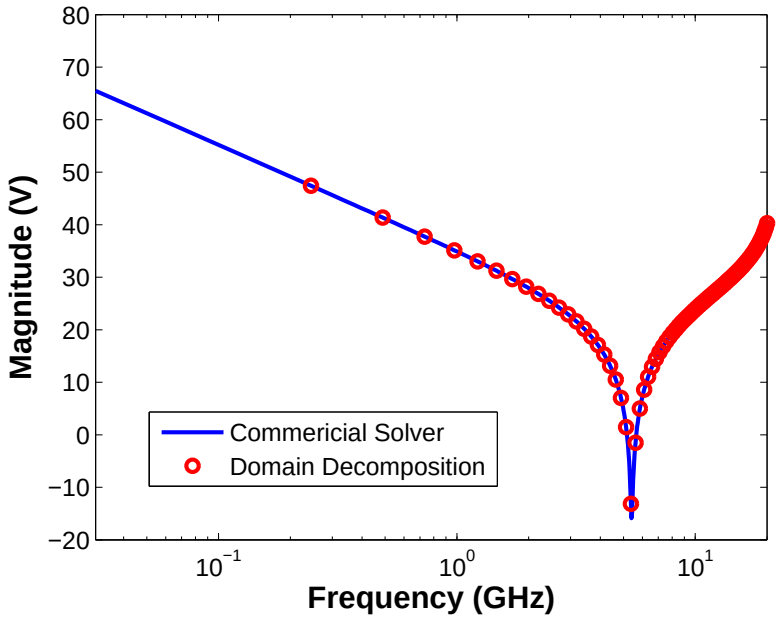


**Figure 65:** Simulated impedance profile of the multilayer on-chip power grid.

A chip-package power distribution network (PDN) is simulated. Figure 66 shows the cross-sectional view and top view of the simulated structure. The chip level PDN is mounted on the package level PDN connected by solder bumps. The size of the package level PDN is 10 mm×10 mm. The package level PDN is considered as power-ground plane pairs filled with dielectric substrate. The thickness and dielectric constant of the substrate are 30 $\mu$m and 3.4, respectively. The height, diameter and pitch of the solder bump are 90 $\mu$m, 100 $\mu$m and 250 $\mu$m, respectively. The chip level PDN is simulated with size 1000 $\mu$m×1000 $\mu$m which is the portion of the entire chip level PDN inside a die with size 4 mm×4 mm. The dielectric constant of the on-chip substrate is 2.2. The chip level PDN is considered as two layers of copper grid with line width, pitch and thickness of 10 $\mu$m, 50 $\mu$m and 0.8 $\mu$m, respectively. One on-package port and one on-chip port are defined with locations shown in Figure 66. The scale difference for the structure is 12500:1 (ratio between feature sizes of the width of the package and minimum on-chip interconnect thickness). Similarly, the

**Table 4:** Comparison of the simulation parameters for chip-package PDN.

| Method | $\delta_{\min}$ | Cells | CPU Time |
|---|---|---|---|
| Domain Decomposition | 0.4 $\mu$m | 45.6 K | 4.5 hr |
| | 0.2 $\mu$m | 87.4 K | 9.5 hr |
| Commercial Transient Solver | 0.4 $\mu$m | 97.2 K | 10.5 hr |
| | 0.2 $\mu$m | 181.5 K | NA |

entire structure is decomposed into two domains (on-package area and on-chip area) with separate meshing strategies.

Similar to the previous example, the grid resolution on chip is kept constant for the proposed method and the commercial solver. Table 4 summarizes the comparison of simulation parameters for different simulation methods, where $\delta_{\min}$ is the minimum grid increment. Two scenarios are considered, namely coarse grid and fine grid resolution for the on chip area. It can be observed that the proposed method is significant faster and the commercial solver cannot solve the problem if fine grid resolution is used for on chip structures. Figure 67 shows the self impedance of port located on the package. It can be observed that the magnitude and resonant peaks of the proposed method correlates well with the results of commercial solver. Figure 68 shows the self impedance of port located on the chip. Good correlation of results from the proposed method and the commercial solver is also observed.

## *6.4 Summary*

In this chapter, chip-package co-simulation problems are investigated. Solutions are obtained based on the Laguerre-FDTD solver. The non-conformal domain decomposition scheme is applied to efficiently tackle the multiscale structures. Chips and packages are conveniently decomposed into subdomains with separate meshing strategies. Skin-effect is considered by applying the proposed method discussed in Chapter IV. Also, material dispersion is modeled. Several multiscale structures, including

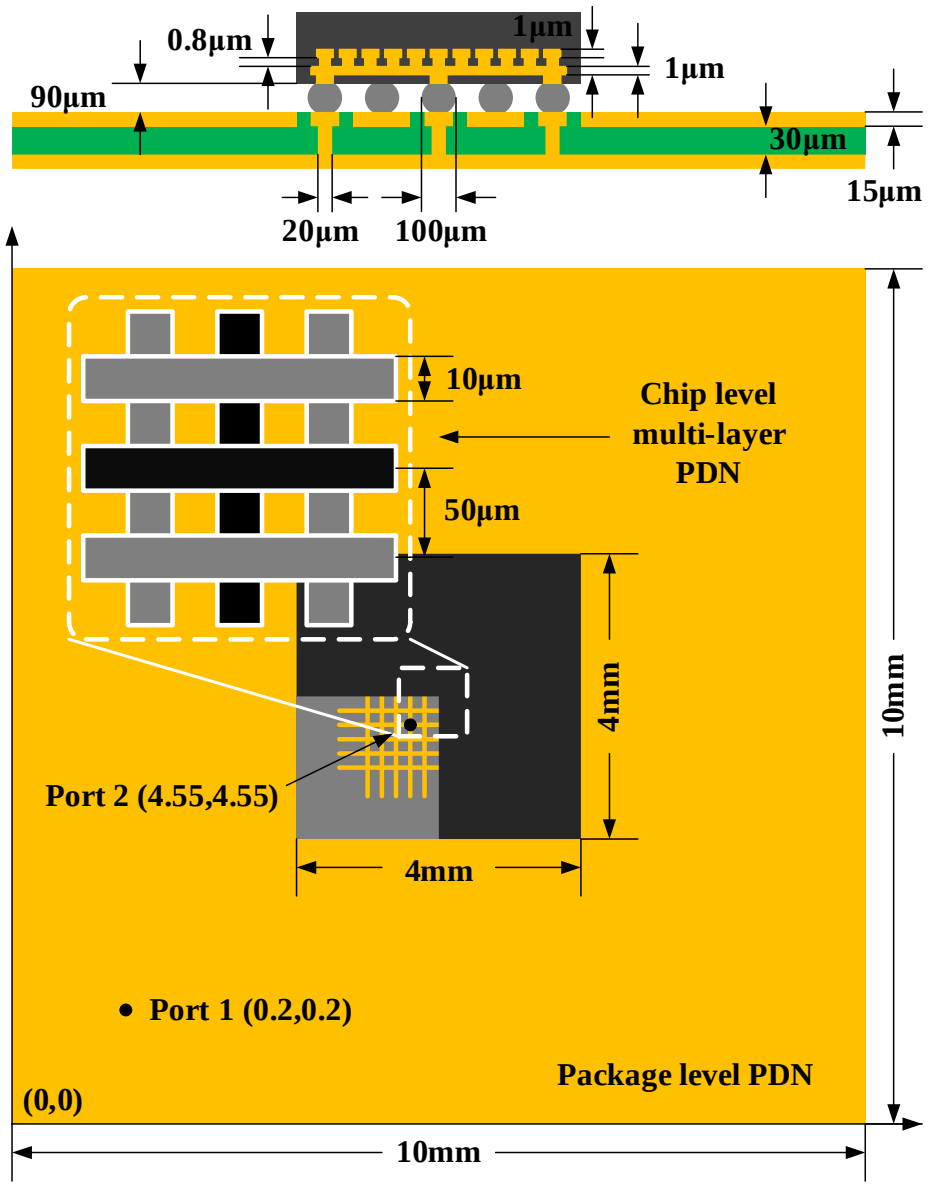


**Figure 66:** Schematic cross-sectional and top view of the chip-package PDN.

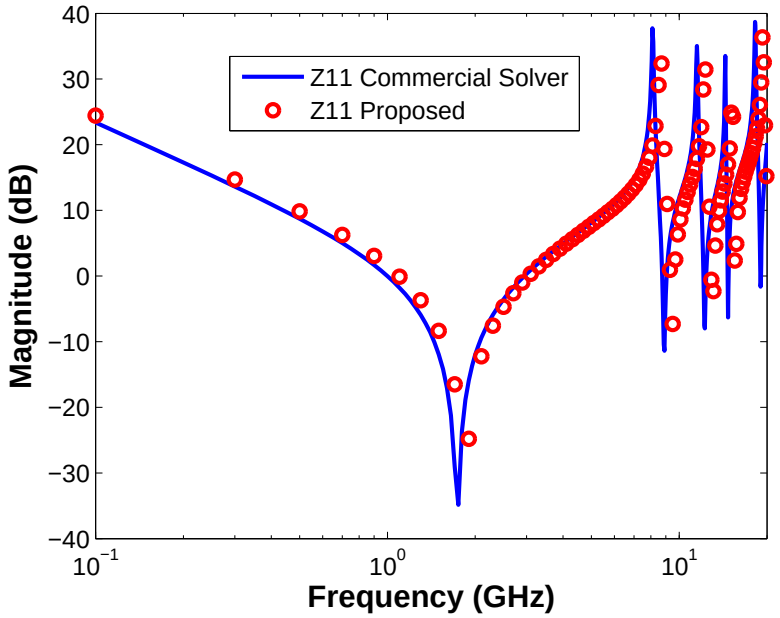


**Figure 67:** Self impedance ($Z_{11}$) of the chip-package PDN at on-package port.

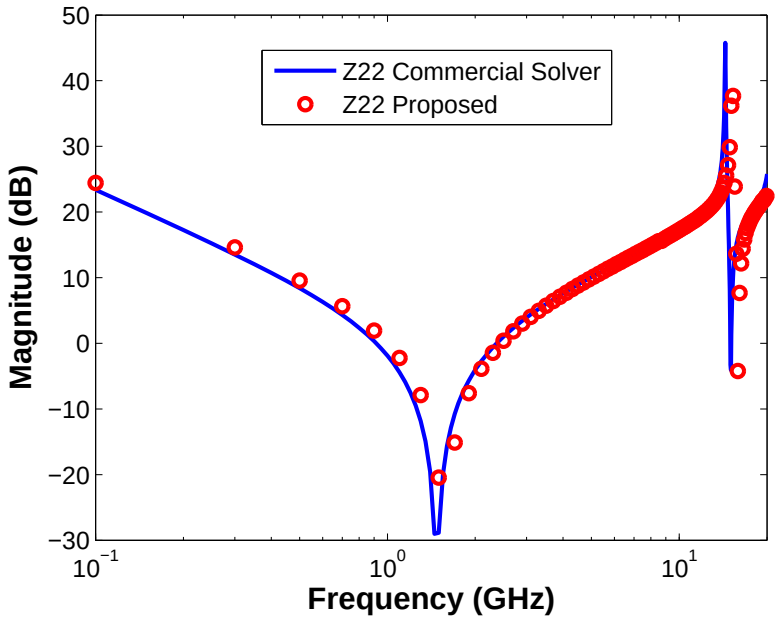


**Figure 68:** Self impedance ($Z_{22}$) of the chip-package PDN at on-chip port.

interconnects in chip-package structure and chip-package PDN, are investigated using the proposed method. Comparison of the results of the proposed method with the results simulated by commercial transient solver and measurement is also carried out. The examples demonstrate that the proposed method is accurate and efficient for multiscale structure simulation.

# CHAPTER VII

# SURFACE ROUGHNESS MODELING FOR HIGH-SPEED INTERCONNECTS

## *7.1 Introduction*

In most high-frequency simulations, a conductor surface can be treated as a smooth surface without losing simulation accuracy. Conductor loss can be accurately modeled by taking into account skin-effect, as discussed earlier. However, as frequency increases, the simulation error associated with the smooth surface assumption also increases. This is because the loss due to the conductor surface roughness is neglected. Theoretically, surface roughness creates a larger surface area compared to the smooth counterpart which makes the current path longer, resulting in more conductor loss. At the same time, the surface roughness is not easy to model due to its random distributed nature. This is especially true for full-wave methods which require spacial discretization. Direct modeling of the roughness detail with cell elements is computationally inefficient or not possible. Therefore, a model that is accurate in capturing the surface roughness loss and is simple to be incorporated into full-wave solvers is critical in high-frequency simulation.

## *7.2 Substrate Integrated Waveguide for High-Speed interconnections*

As operating frequency reaches hundreds of gigahertz, traditional planar transmission lines, such as microstrip line and stripline, begin to show disadvantages in loss, crosstalk and power capacity. Moreover, due to machining precision, the quality of the traditional planar transmission in mass production is difficult to be controlled for high frequency applications.

To solve this problem, a new type of transmission line, the substrate integrated waveguide (SIW), is proposed [72]. Unlike the rectangular waveguide, via fences are used in the SIW to replace the side walls of the rectangular waveguide whereas two metal planes serve as the top and bottom metal walls (Figure 69). This makes the SIW easy to be integrated into planar circuits. Also, it can be connected to microstrip and coplanar circuits using simple transitions [73]. Since the amount of metal that carries the signal in the SIW is far greater than it would for microstrip or stripline, the conductor loss is expected to be low. Little crosstalk is involved due to the shielding effect of the via fences. Moreover, for waveguide type of structure, the power capacity is high, making it suitable for high power applications.

The SIW is already proven to be useful in the design of transmission lines, filters, resonators and antennas, especially in millimeter wave applications [74], [75]. The miniaturization of the SIW in such applications makes it a promising alternative as compared to traditional planar structures. However, since a large conductor surface is used to carry the signal, conductor surface roughness will play an important role in conductor loss. In some circumstances, the conductor loss is even larger than the microstrip and stripline operating in the same frequency. Therefore, to accurately capture the loss mechanism of surface roughness is critical in SIW design. Although many surface roughness models have been developed for TEM type of transmission lines [1], [50]–[57], [76], models for TE type of transmission line are limited. This motivates the investigation of surface roughness modeling of SIW.

## *7.3 Design and Fabrication of Substrate Integrated Waveguide*

In this section, a D-band (110 GHz to 170 GHz) SIW is designed and fabricated. The transmission mode is the $TE_{10}$ mode, namely no other modes exist within the band of interest.

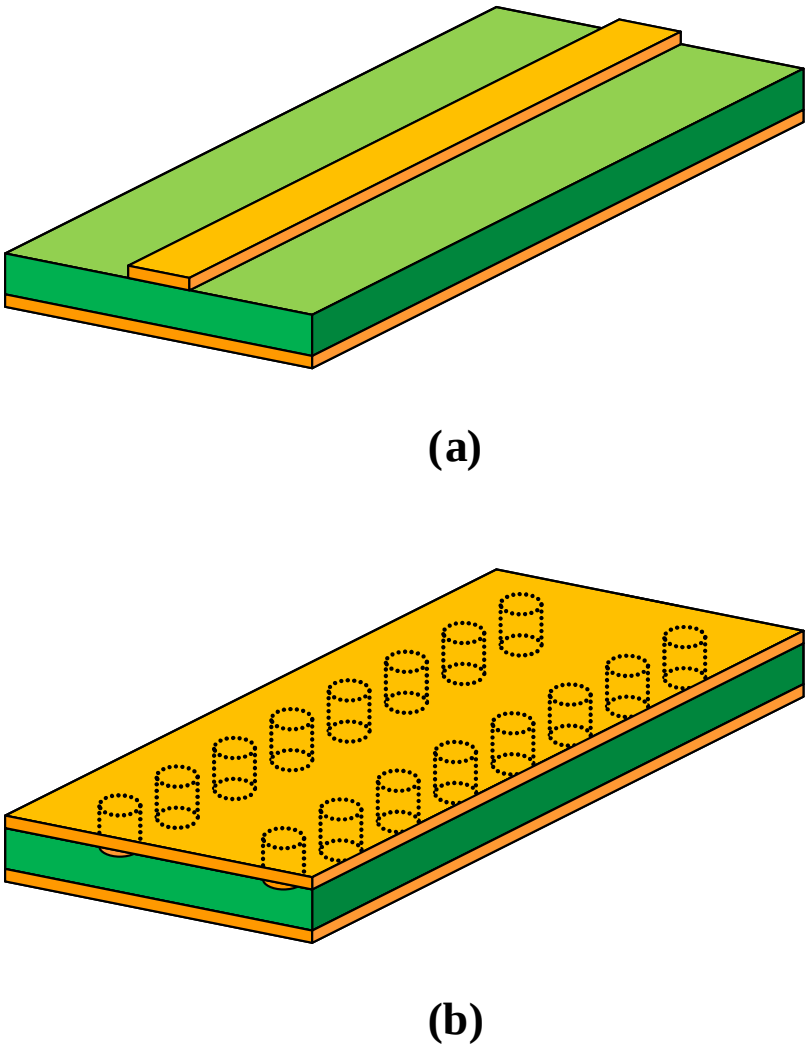


**Figure 69:** Two types of planar interconnects: (a) microstrip line and (b) substrate integrated waveguide (SIW).

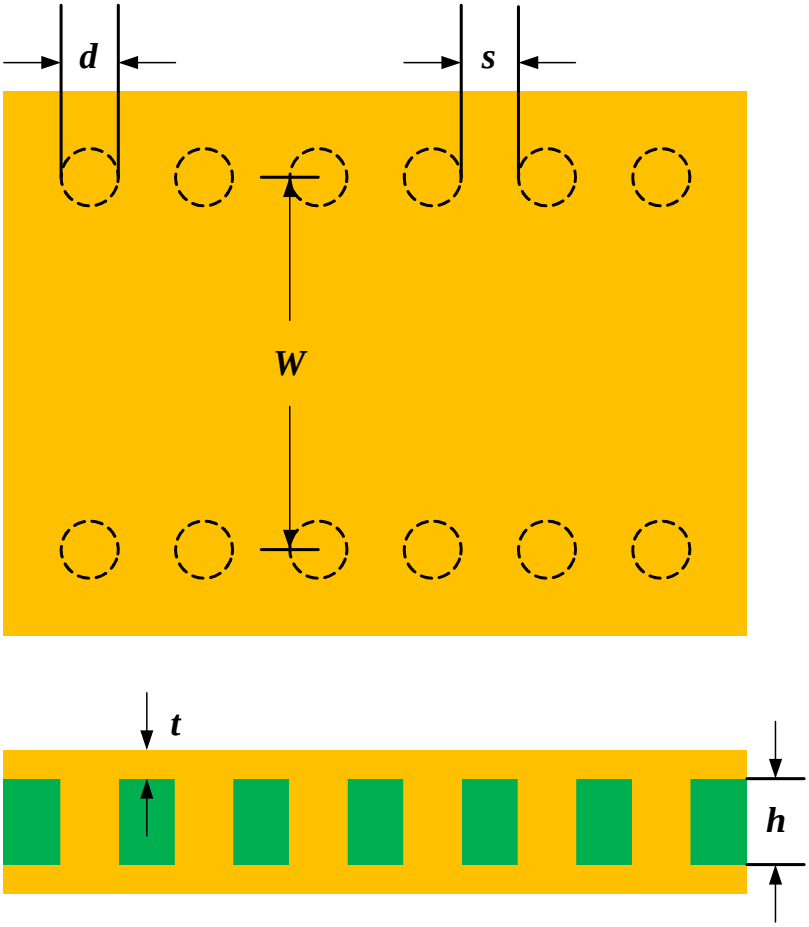


**Figure 70:** Two view and side view of the SIW

### 7.3.1 Physical Design of the SIW

Figure 70 shows the schematic of the SIW. $W$ is the width of the SIW defined as the distance between the center of the vias on two sides. $d$ and $s$ are the diameter of the via and spacing between two vias, respectively. $t$ and $h$ are the thickness of the copper layer and the substrate, respectively.

For a rectangular waveguide, the cut-off frequency for the $TE_{10}$ mode is given by

$$f_c = \frac{1}{2a\sqrt{\mu\varepsilon}} \tag{121}$$

where $a$ is the width of the waveguide ($>$ height of the waveguide), $\varepsilon$ and $\mu$ are the

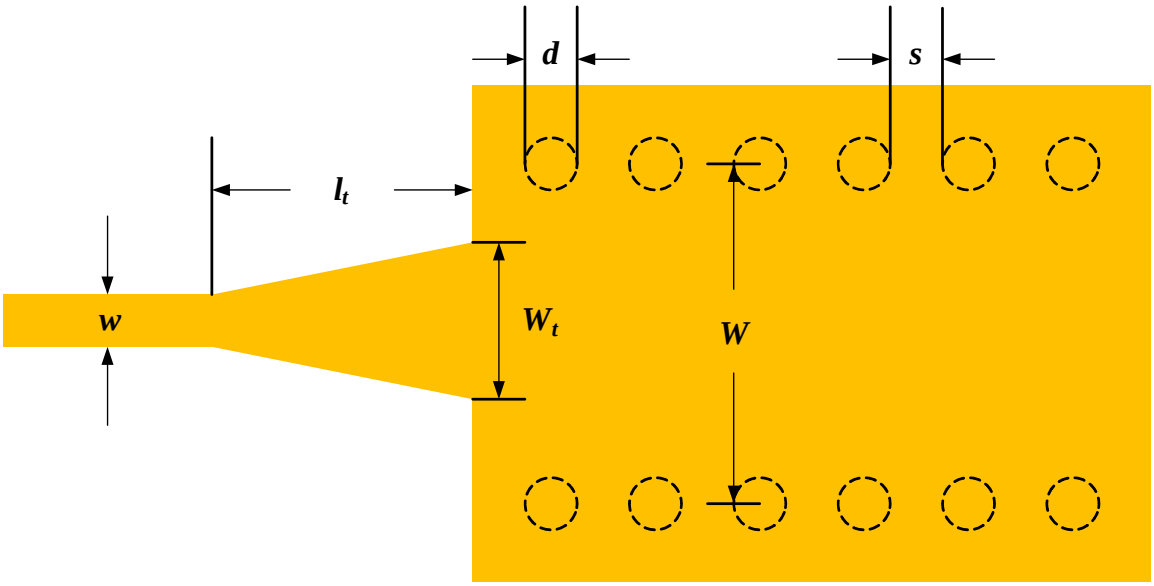


**Figure 71:** Microstrip line to SIW tapered transition

permittivity and permeability of the filled dielectric. Since the side wall of the SIW is a via-fence structure but not a flat conductor surface, the width $W$ of the SIW which exhibits the same propagation characteristic as a rectangular waveguide of width $a$ is given by [77]

$$W = a + \frac{d^2}{0.95(s+d)}. \tag{122}$$

Following the design rule, the SIW is designed with the following parameters: $W = 0.925$ mm, $d = 0.0508$ mm, $s = 0.075$ mm, $t = 0.009$ mm, and $h = 0.0508$ mm.

### 7.3.2 Microstrip to SIW Transition

The $S$-parameters of the SIW are not easy to be directly measured using a probe station. A microstrip to SIW transition is designed to facilitate the measurement (Figure 71). Low reflection is desired. Multiple transition designs have been proposed [74], [77], [78] among which the tapered line transition shows advantages for simple implementation with low transition loss.

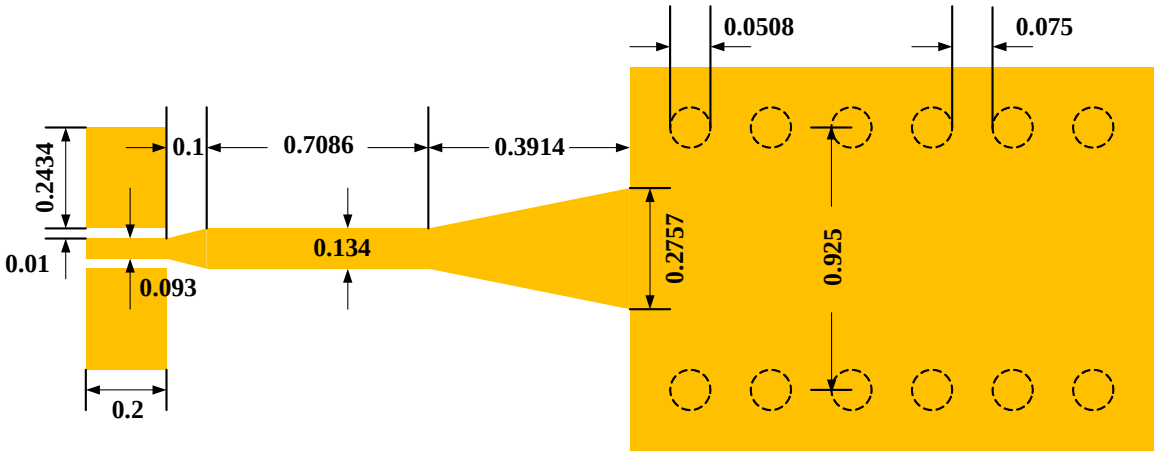


**Figure 72:** Mask design of the SIW (unit: mm)

In this work, the tapered line transition is adopted. While there is no strict design rule of the microstrip to SIW transition, a commercial full-wave solver (HFSS) is used to optimize the width $W_t$ and length $l_t$ of the SIW, yielding minimum return loss. The final optimized results are $W_t = 0.26$ mm, $l_t = 0.39$ mm and $w = 0.124$ mm, respectively.

### 7.3.3 Fabrication Process

The SIW is fabricated based using the liquid crystal polymer (LCP) substrate. The LCP is widely used in high-frequency applications due to its low loss property (loss tangent $\tan\delta = 0.005$) and commercial availability of laminates. The dielectric constant of the LCP is $\varepsilon_r = 3.1$. A Mask is designed for the fabrication of the SIW. The detailed mask design of one SIW is shown in Figure 72. The mask for other auxiliary structures is not shown here. To make proper probing, a coplanar waveguide (CPW) to microstrip line transition is also designed. Note that the feature size of the mask is not identical to the feature size obtained from the full-wave solver. Over etching is considered and the typical over etching width is 9 $\mu$m.

The D-band SIW is fabricated based on the liquid-crystal polymer (LCP) technology. The fabrication process is as follows.

1. First, the LCP sample is cut into square with copper on both sides. A square area smaller than the top side is covered with blue tape, leaving space for alignment vias (Figure 73(a)). The tape is firmly attached to the top side, otherwise under-etch will oxidize or etch the copper from the edges.

2. The sample is etched with Nitric acid and water with 1:2 composition. After the copper is etched out completely from the bottom and edges of the top side, rinse the sample with water and then remove the blue tape (Figure 73(b)).

3. The sample is processed with micron laser drill for forming the alignment vias at each edge of the sample. The vias for the SIW side wall are also drilled through the LCP and stop at the top side copper (Figure 74(c)).

4. A 9 $\mu$m copper layer is sputtered on the bottom side of the sample where the copper is originally etch out at the second step. The 25 min sputtering is followed by 15 min of cooling step. To get the desired thickness of the copper, this process loops (Figure 74(d)).

5. The SIW and all the other related structures are patterned on the top side. Fine feature of the CPW pads for probing is realized by careful etching (Figure 75(e)).

6. The SIW and all the other related structures are patterned on the bottom side with the similar procedure as in step 5.(Figure 75(f)).

Figure 76 shows a portion of the fabricated SIW. Auxiliary open and through lines are also fabricated for de-embedding the $S$-parameters of the SIW. Figure 77 shows the cross-sectional view of the fabricated SIW. Roughness can be observed at the interface of copper and LCP substrate. Figure 78 shows the top view of the copper surface near a via. Spherical-like roughness can be observed on the surface.

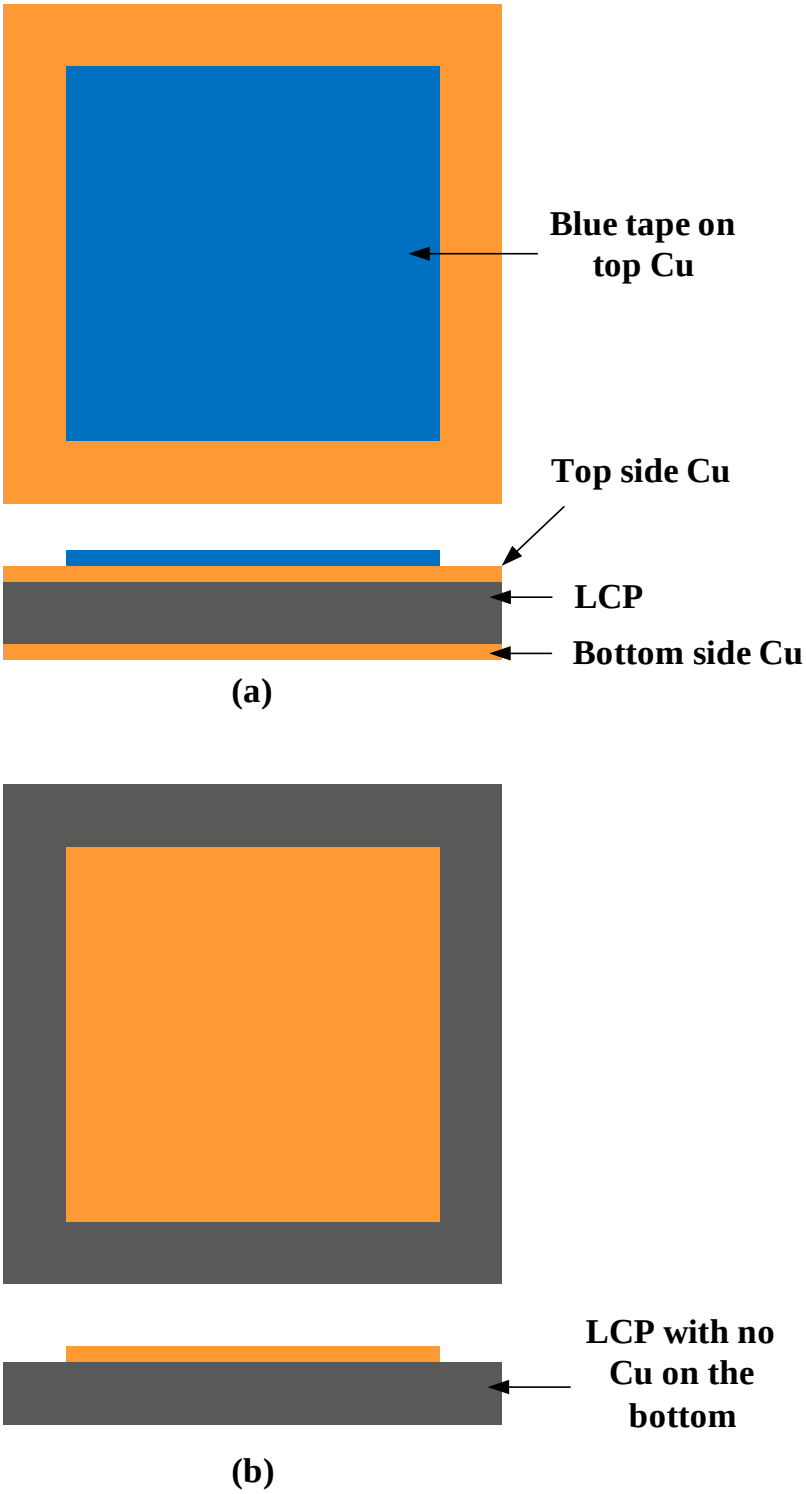


**Figure 73:** Fabrication process of the SIW (part 1)

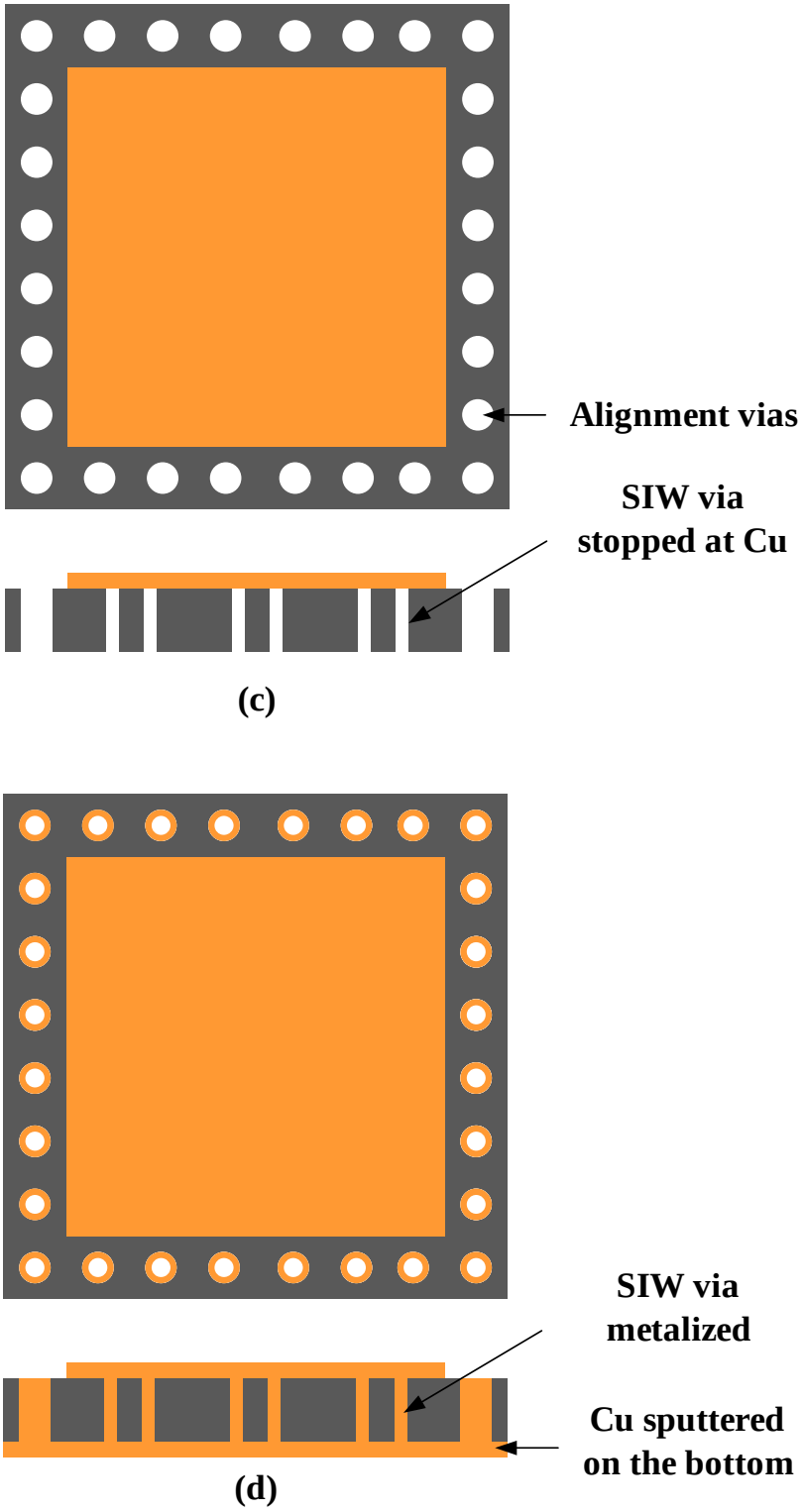


**Figure 74:** Fabrication process of the SIW (continued, part 2)

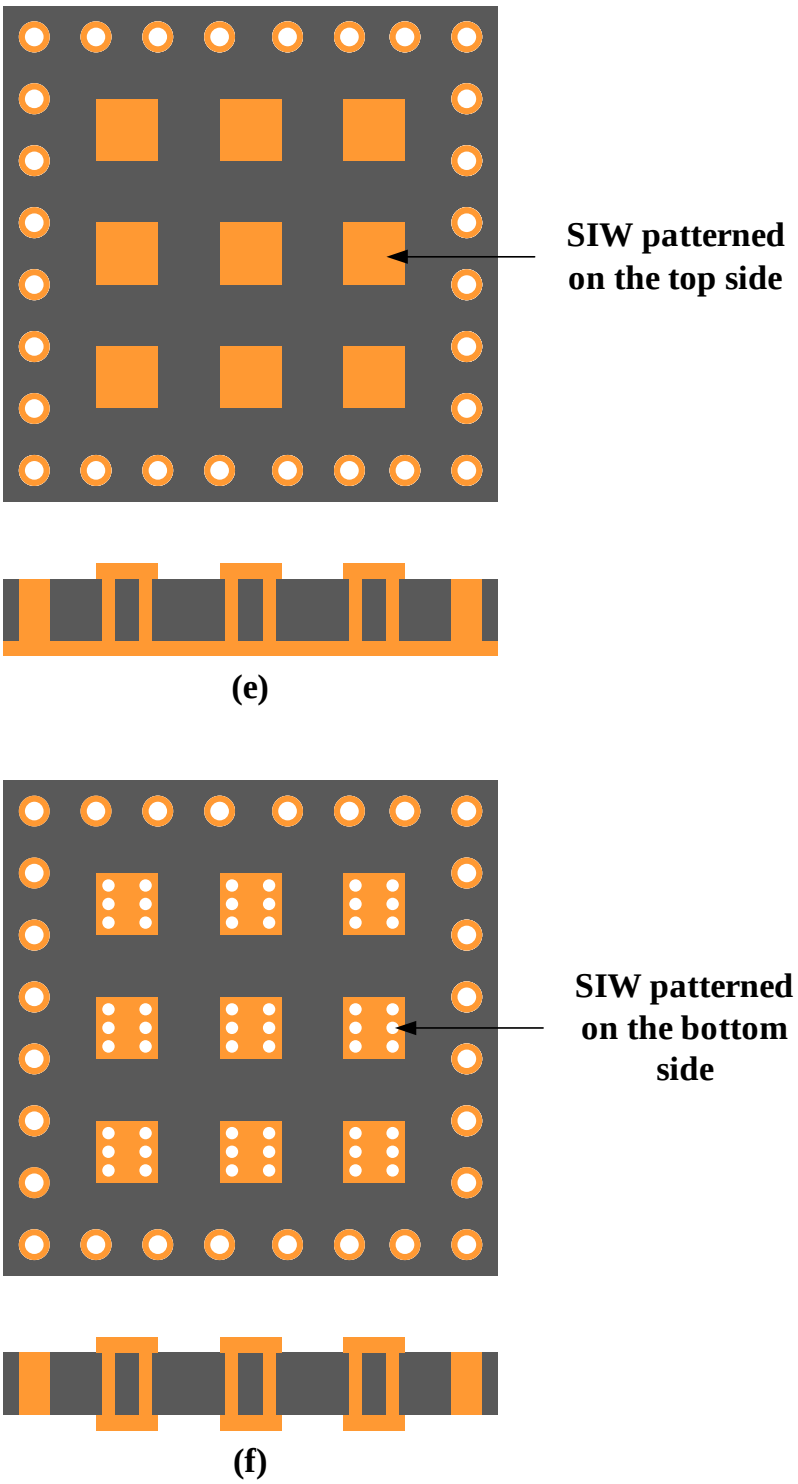


**Figure 75:** Fabrication process of the SIW (continued, part 3)

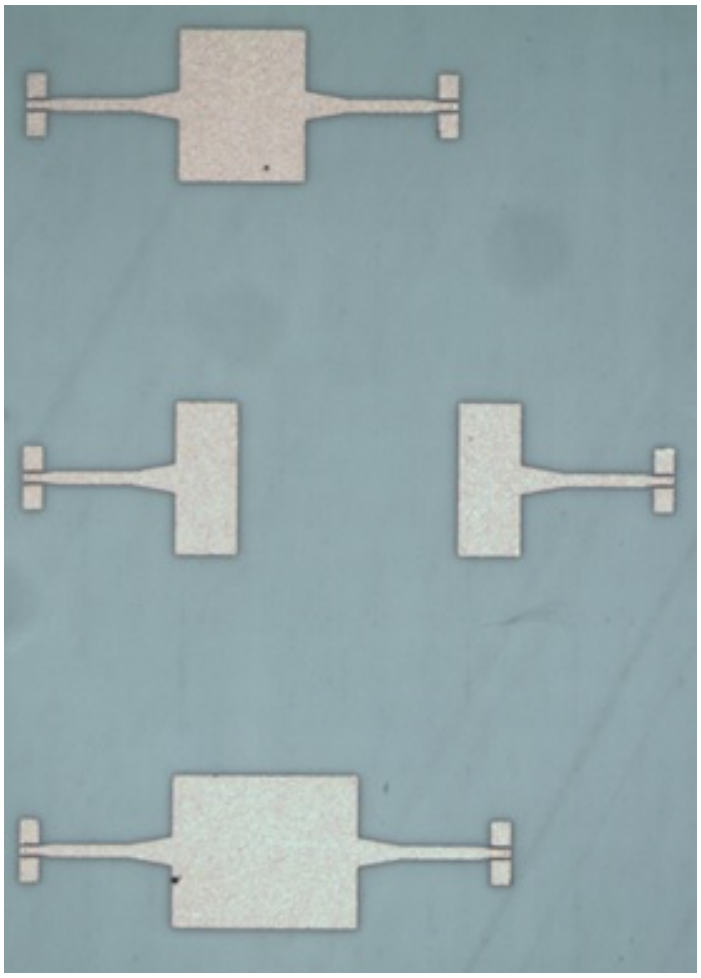

**Figure 76:** Fabricated D-band SIW (bottom). Short (top) and open (middle) lines are also fabricated for de-embedding $S$-parameters of the SIW.

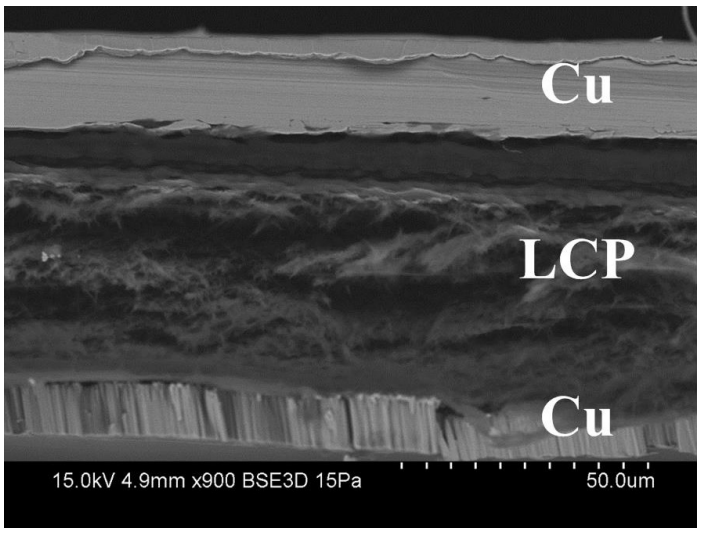


**Figure 77:** Cross-sectional view of the SIW (captured by Hitachi 3700 Variable-Pressure SEM).

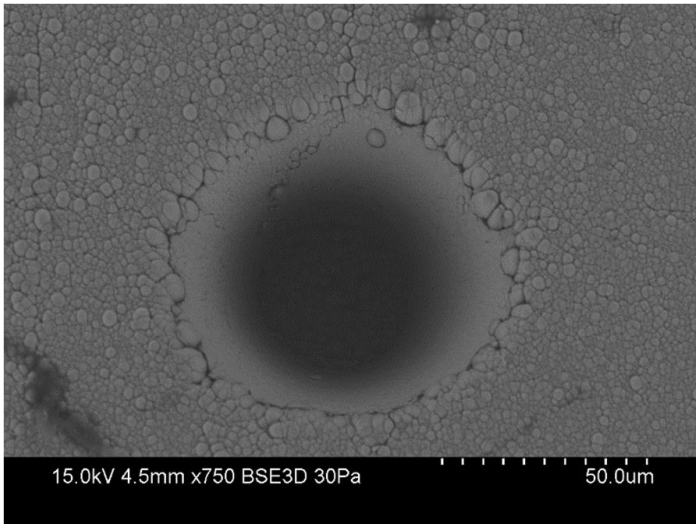


**Figure 78:** Top view of the copper surface near a via (captured by Hitachi 3700 Variable-Pressure SEM).

## *7.4 Surface Roughness Models for SIW*

In this section, analytical models for surface roughness of the SIW are discussed and compared. All the models are based on the surface approximation strategy, namely transferring the random roughness into a equivalent surface with simple shapes from which analytical models can be derived.

### 7.4.1 Enhancement Factor and Loss Mechanism

Consider a straight transmission line without discontinuities. Due to the surface roughness of the conductor, the difference between the conductor loss with smooth surface and rough surface will increase as frequency increases. This is equivalent to the scenario that the conductivity of the conducting metal decreases as frequency increases. Therefore, it is convenient to introduce a frequency-dependent conductivity as

$$\sigma'(\omega) = \frac{\sigma}{K_s(\omega)^2} \tag{123}$$

where $K_s(\omega)$ is the frequency dependent enhancement factor. The enhancement factor should be greater than one across all the frequencies of interest since a rough surface is always more lossy than a smooth surface. For a fixed design, the enhancement factor can be expressed as follows

$$K_s = \frac{P_{\text{roughn}}}{P_{\text{flat}}} \tag{124}$$

where $P_{\text{rough}}$ is the power loss due to the rough surface and $P_{\text{flat}}$ is the power loss due to the smooth surface.

Normally speaking, the power loss due to the rough surface mainly consists of two parts: First, since the surface roughness can be considered as protrusions out of a

smooth surface, energy will be reflected back to the power source; Second, since the equivalent surface area of a rough surface is larger than a smooth surface, the time-average power absorbed by the conducting surface is larger, and is a major source of power loss. To be noted, radiation loss is associated with the SIW because of the non-complete-shielding via fence structure. However, the radiation loss at high frequency is negligible compared to conductor loss, and thus, is not discussed here. For a SIW, any power that is not transmitted is considered as power loss, which satisfies

$$|\Gamma|^2 + |\mathrm{T}|^2 = 1 - \frac{P_{\text{loss}}}{P_{\text{incident}}} \tag{125}$$

where $\Gamma$ and T are the reflection and transmission coefficient respectively. $|\Gamma|^2 P_{\text{incident}}$ and $P_{\text{loss}}$ correspond to the aforementioned two parts of power loss.

### 7.4.2 Surface Approximation

Random roughness is difficult to be modeled. Although there are some attempts dealing with the random roughness directly, most of them are computationally inefficient. The best way is to develop an analytical solution that can be easily incorporated into full-wave solvers. To be specific, an analytical solution for the enhancement factor should be derived to obtain the equivalent frequency-dependent conductivity. To achieve this, random roughness is often represented by some equivalent surface with simple shapes from which the derivation of analytical solution is possible.

One approach is to model the rough surface as repeated periodic triangles sitting on a smooth surface (Figure 79(a)). This model is a 2-D model which is not a good representation of a 3-D rough surface. Another approach is to model the rough surface as repeated hemispheres sitting on a smooth surface (Figure 79(b)). This model is demonstrated to be accurate in modeling microstrip lines with surface roughness up to 30 GHz [1]. However, this type of model has a drawback. At low frequency, the

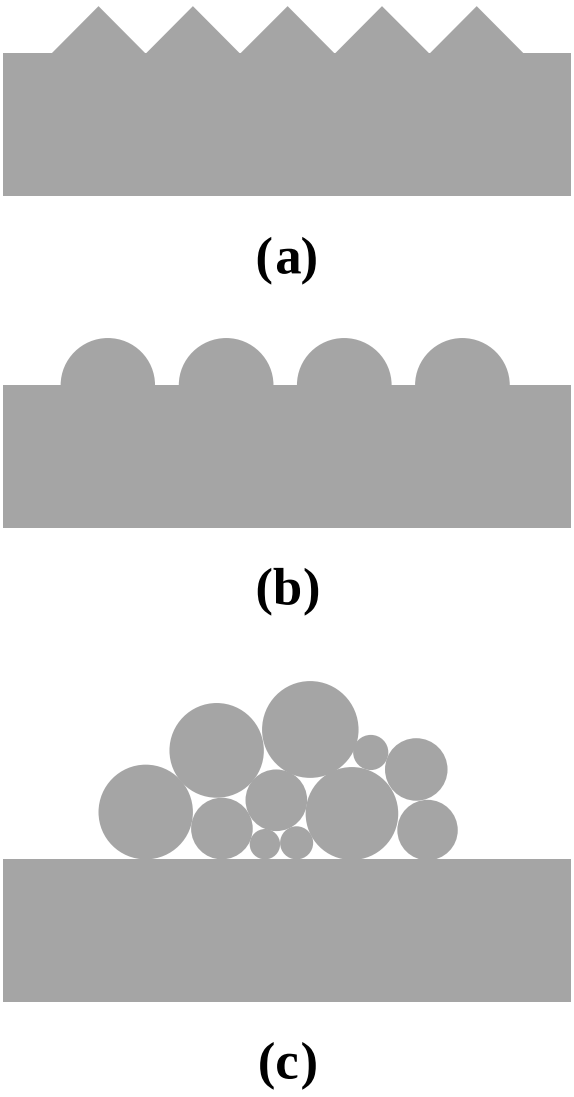


**Figure 79:** Different models for surface roughness (a) periodic triangle (b) periodic hemisphere (c) Huray model.

enhancement factor could be less than 1, which is physically incorrect. Manual cut-off frequency is needed and the enhancement factor suffers from early saturation.

A more realistic representation of the surface roughness is proposed by Huray [54] as shown in Figure 79(c). By inspecting the real surface distribution of the roughness (Figure 7), it is more reasonable to model the roughness as conducting sphere bundles sitting on the smooth surface. The enhancement factor generated by this model is always greater than 1 and early saturation is eliminated.

An important item to be mentioned is that the Huray model cannot be directly applied to the SIW case since it is only correct for TEM type of transmission line.

### 7.4.3 Modified Huray Model

In actual calculation of the enhancement factor, a conductor surface will be discretized into rectangular cells or "tiles", which will be explained in detail in later sections. Using the Huray model, the rough surface can be generalized with one conducting sphere sitting on a smooth conducting surface as shown in Figure 80.

Consider that a wave is incident from the left to right as shown in Figure 80. The total power scattered and absorbed from a sphere divided by the incident flux can be calculated as [1]

$$\sigma_{\text{tot}} = -\frac{3\pi}{2k^2}\text{Re}\left[\alpha(1) + \beta(1)\right] \tag{126}$$

where $k = 2\pi/\lambda$ and

$$\alpha(1) = -\frac{2j}{3}(kr)^3\left[\frac{1 - \frac{\delta}{r}(1+j)}{1 + \frac{\delta}{2r}(1+j)}\right] \tag{127}$$

$$\beta(1) = -\frac{2j}{3}(kr)^3\left[\frac{1 - \left(\frac{4j}{k^2 r\delta}\right)\left(\frac{1}{1-j}\right)}{1 + \left(\frac{2j}{k^2 r\delta}\right)\left(\frac{1}{1-j}\right)}\right] \tag{128}$$

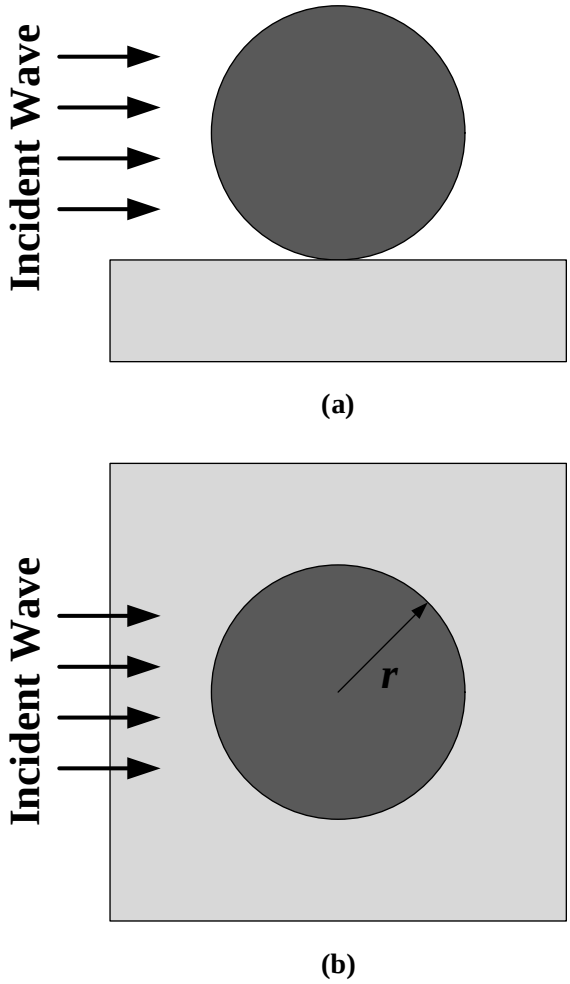


**Figure 80:** A conducting sphere sitting on a conducting plane with (a) top view and (b) side view.

where $\delta$ is the skin depth and $r$ is the radius of the sphere.

Consider a rectangular waveguide whose width and height are $a$ and $b$, respectively as shown in Figure 81. The TE wave is propagating in the $z$-direction. The field components for $TE_{10}$ can be written as:

$$H_z = A_{10} \cos \frac{\pi x}{a} e^{-j\beta z} \tag{129}$$

$$E_y = \frac{-j\omega\mu a}{\pi} A_{10} \sin \frac{\pi x}{a} e^{-j\beta z} \tag{130}$$

$$H_x = \frac{j\beta a}{\pi} A_{10} \sin \frac{\pi x}{a} e^{-j\beta z} \tag{131}$$

where $\beta$ is the propagating constant and $A_{10}$ is the magnitude constant for $TE_{10}$ mode. The Poynting vector associated with the $TE_{10}$ mode is given by:

$$\begin{aligned} |\mathbf{S}| &= \left| \frac{1}{2} \mathrm{Re} \left( \mathbf{E} \times \mathbf{H}^* \right) \right| \\ &= \left| \frac{1}{2} \mathrm{Re} \left( E_y H_x^* \right) \right| \\ &= \left| \frac{1}{2} \mathrm{Re} \left[ |A_{10}|^2 \frac{\omega\mu\beta a^2}{\pi^2} \sin^2 \frac{\pi x}{a} \right] \right| \end{aligned} \tag{132}$$

Therefore, the total power absorbed and reflected by the conducting sphere can be calculated as:

$$P_{\text{sphere}} = |\mathbf{S}| \, \sigma_{\text{tot}} \tag{133}$$

Note that $P_{\text{sphere}}$ takes into account both power loss from reflection and absorption of the conducting sphere. The conductor loss due to the smooth surface is

$$P_{\text{flat}} = \frac{\mu\omega\delta}{4} |H_{\tan}|^2 A_{\text{tile}} \tag{134}$$

where $A_{\text{tile}}$ is the surface area of the smooth surface tile and

$$|H_{\tan}|^2 = |H_x|^2 + |H_z|^2 \tag{135}$$

Therefore, the enhancement factor (124) can be calculated as:

$$\begin{aligned} K_s &= \frac{\sum_{n=1}^{N} mP_{\text{sphere}} + \sum_{n=1}^{N} P_{\text{flat}}}{\sum_{n=1}^{N} P_{\text{flat}}} \\ &= \frac{\sum_{n=1}^{N} m\text{Re}\left||A_{10}|^2 \frac{3\omega\mu\beta a^2}{4\pi k^2} \sin^2 \frac{\pi x(n)}{a} \cdot [\alpha(1) + \beta(1)]\right| + \sum_{n=1}^{N} \frac{\mu\omega\delta}{4} |H_{\tan}|^2 A_{tile}}{\sum_{n=1}^{N} \frac{\mu\omega\delta}{4} |H_{\tan}|^2 A_{tile}} \end{aligned} \tag{136}$$

where $N$ is the total number of the discretized cells and $m$ is the total number of spheres sitting on one tile.

### 7.4.4 Rigorous Waveguide Model

The modified Huray model discussed in the previous section improves the original model by considering the Poynting vector inside a rectangular waveguide instead of a TEM transmission line. However, the scattering term $\sigma_{\text{tot}}$ is still derived from a plane-wave-incident scenario. In the SIW, this assumption is not valid since no TEM mode is supported. It is obvious that the loss is mode-dependent since the conducting sphere interacts with the field inside the waveguide which is determined by the propagating mode. Directly using the scattering term might lead to reasonable loss results, but it is not physically rigorous. Therefore, a strict TE-mode-based model needs to be developed.

A rigorous scenario involves considering a conducting sphere sitting on the bottom of a rectangular waveguide, as shown in Figure 81. Recall that in (125), the loss due

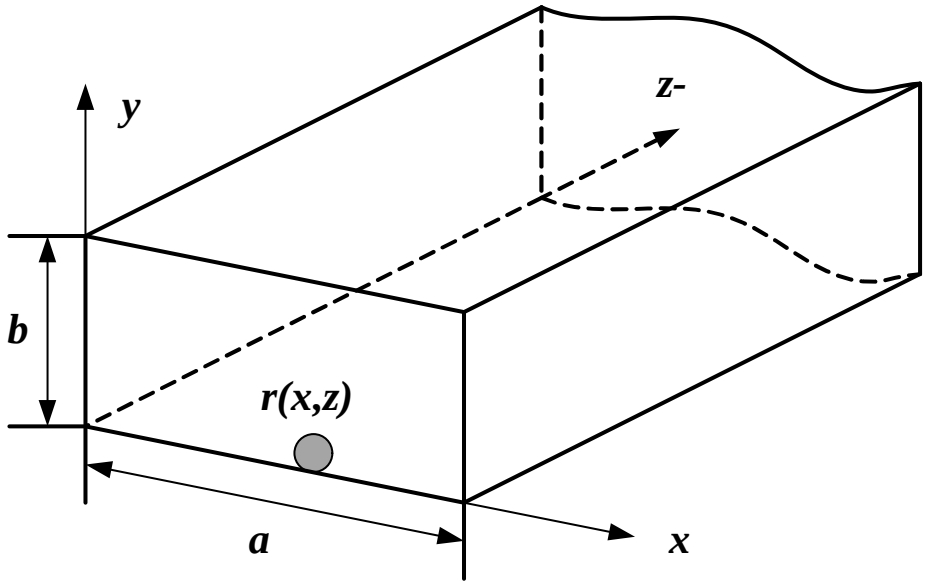


**Figure 81:** A conducting sphere sitting on the bottom of a waveguide.

to the surface roughness consists of reflection loss and absorption loss. By calculating these two power-loss components under the TE mode, the total loss can be recovered. The reflection coefficient of a conducting sphere sitting in the middle of the bottom of a rectangular waveguide has been investigated in [79], and can be expressed as

$$\Gamma_{\text{sphere}} = \left(\frac{2r}{b}\right)^3 \left(\frac{\pi b}{2a}\right)^2 \frac{k}{k_c} \left[\frac{5.44}{\sqrt{1-(k_c/k)^2}} + \sqrt{1-(k_c/k)^2}\right] \tag{137}$$

where $k_c = \pi/a$. The power flux of a rectangular waveguide can be calculated from:

$$\begin{aligned} P_{10} &= \frac{1}{2}\text{Re}\int_{x=0}^{a}\int_{y=0}^{b} \mathbf{E}\times\mathbf{H}^*\cdot\hat{z}dydx \\ &= \frac{1}{2}\text{Re}\int_{x=0}^{a}\int_{y=0}^{b} E_y H_x^* dydx \\ &= \frac{\omega\mu a^3|A_{10}|^2 b}{4\pi^2}\text{Re}\,(\beta) \end{aligned} \tag{138}$$

Note that in [79], the reflection factor is calculated for a conducting sphere sitting in the middle of the bottom wall of the waveguide. However, in a waveguide with

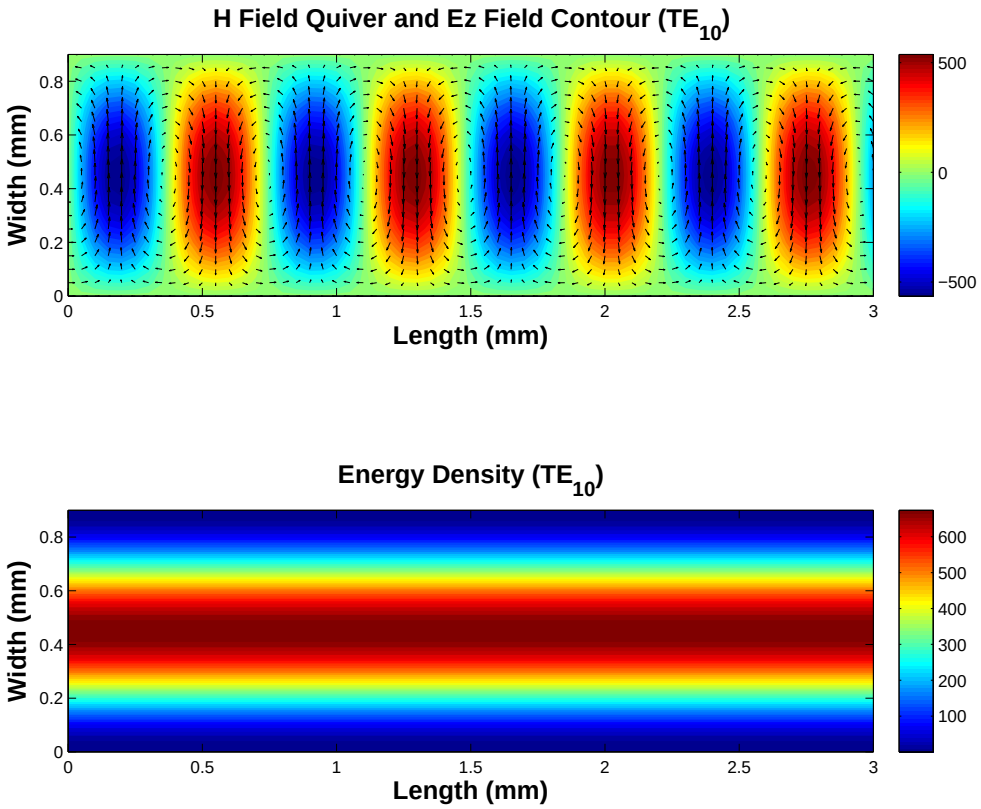


**Figure 82:** Field distribution and energy density of a rectangular waveguide for $TE_{10}$ mode.

a propagation mode, the energy density inside the waveguide is position-dependent. Figure 82 shows the field distribution and energy density of a rectangular waveguide for $TE_{10}$ mode. As can be seen that the highest energy density is observed in the center of the waveguide. Thus, energy being reflected by a conducting sphere sitting in the middle of a waveguide is larger than that being reflected by the same sphere sitting near the side wall.

To account for this effect, the power loss due to the reflection can be calculated using:

$$P_{\text{ref}} = |\Gamma_{\text{sphere}}|^2 \sin^2 \frac{\pi x}{a} P_{10} \tag{139}$$

where the $\sin^2(\pi x/a)$ term is used to represent the position-dependent reflection energy of the conducting sphere.

For a conducting sphere sitting on the bottom of a waveguide, the field strength will be low in the "shade region" between the sphere and the smooth plane [79]. This negligible field region makes the equivalent surface area increment of a conducting sphere approximately half the sphere surface area, namely $2\pi r^2$. The relationship of the skin depth and the radius of the sphere should also be taken into consideration, which results in the power loss due to the energy absorption taking the form

$$P_{\text{loss}} = \frac{\mu\omega\delta}{4} |H_{\tan}|^2 2\pi r^2 \gamma(r) \tag{140}$$

where $\gamma(r)$ is a correction factor taking into account the ratio between skin depth and radius of the sphere, which can be expressed as:

$$\gamma(r) = \begin{cases} 0 & r \leq \delta \\ 1 - e^{-\frac{r}{\delta}+1} & r > \delta \end{cases} \tag{141}$$

It is obvious from (140) that for surface roughness height less than the skin depth of the conductor, the energy loss due to the increment of current path can be neglected. For surface roughness height much larger than the skin depth, the correction factor is approximately 1, making the equivalent surface area equal to half of a sphere surface.

Therefore, the enhancement factor can be calculated as:

$$K_s = \frac{\sum_{n=1}^{N} mP_{\text{ref}} + \sum_{n=1}^{N} mP_{\text{loss}} + \sum_{n=1}^{N} P_{\text{flat}}}{\sum_{n=1}^{N} P_{\text{flat}}}$$
$$= \frac{\sum_{n=1}^{N} m|\Gamma_{\text{sphere}}|^2 \sin^2\frac{\pi x}{a} P_{10} + \sum_{n=1}^{N} m\frac{\mu\omega\delta}{4}|H_{\tan}|^2 2\pi r^2\gamma(r) + \sum_{n=1}^{N} \frac{\mu\omega\delta}{4}|H_{\tan}|^2 A_{\text{tile}}}{\sum_{n=1}^{N} \frac{\mu\omega\delta}{4}|H_{\tan}|^2 A_{\text{tile}}} \tag{142}$$

where $N$ is the total number of the discretized cells and $m$ is the total number of spheres sitting on one tile.

### 7.4.5 Solution Strategy and Roughness Parameter Extraction

The loss due to a single protrusion can be calculated analytically as mentioned before. Based on the loss of a signal protrusion, the enhancement factor is calculated by taking account the loss for all the protrusions, as shown in (136) and (142). In practice, this requires the rough surface of the copper to be discretized by rectangular cells. Figure 83 shows the discretization of the copper surface of the SIW. The cell size is determined by the measured profile of the surface roughness. It is convenient to make cell size in accordance with the root mean square (RMS) value of the distance between the peak of the protrusions ($d_{\text{peak,RMS}}$) as shown in Figure 84.

The method of determining the number of spheres used to represent the protrusion profile is discussed in detail in [80] and can be expressed as:

$$m = \frac{A_{\text{lat}}}{A_{\text{sphere}}} \tag{143}$$

where $A_{\text{sphere}}$ is the surface area of a single sphere and $A_{\text{lat}}$ is the lateral surface area of a hemispheroid which is given by:

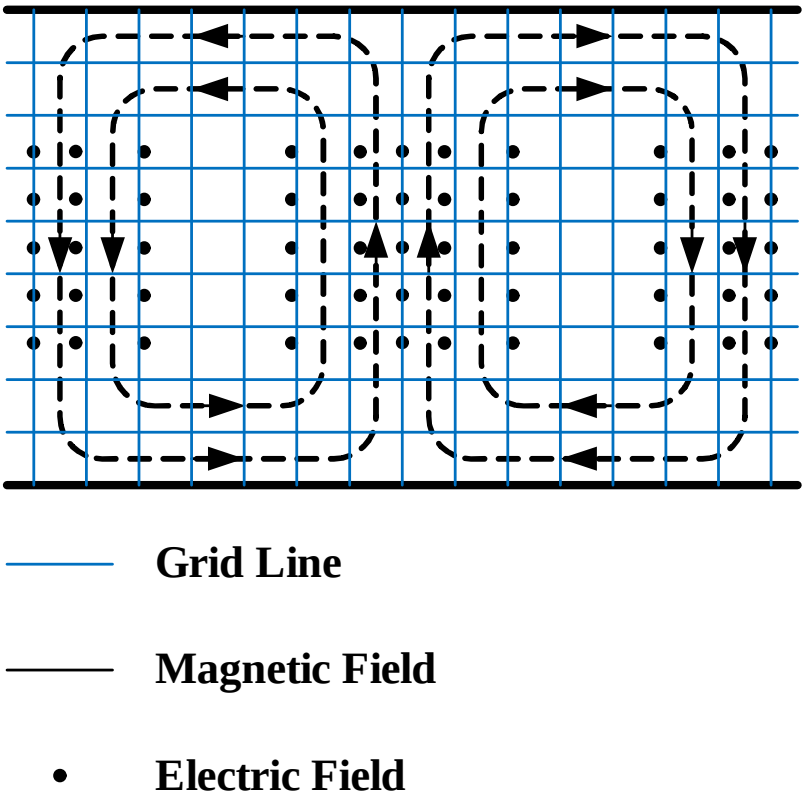


**Figure 83:** Discretization of the copper surface of the SIW.

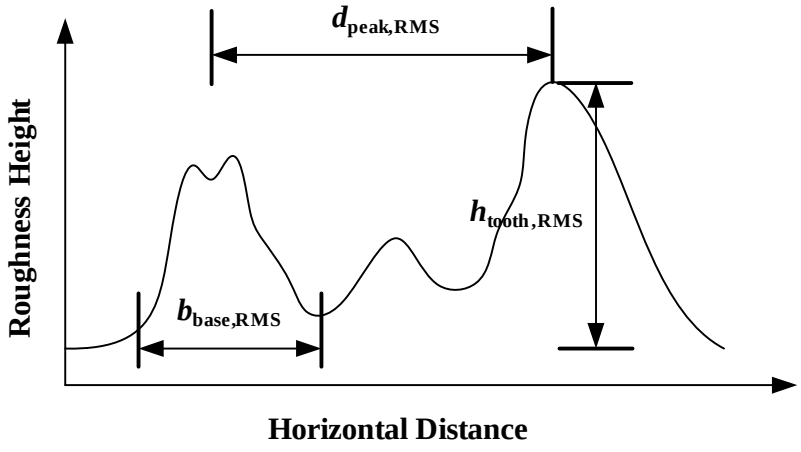


**Figure 84:** Conductor surface roughness profile and key parameters.

$$A_{\text{lat}} = \pi h_{\text{tooth}} \frac{b_{\text{base}}}{2} \left[ h_{\text{tooth}} \frac{\arcsin\left(\sqrt{1 - \frac{b_{\text{base}}^2}{4h_{\text{tooth}}^2}}\right)}{\sqrt{1 - \frac{b_{\text{base}}^2}{4h_{\text{tooth}}^2}}} + \frac{b_{\text{base}}}{2} \right] \tag{144}$$

where $h_{\text{tooth}}$ and $b_{\text{base}}$ are the feature length marked in Figure 84. Note that this method calculates the number of spheres using a equivalent surface concept. The number of sphere can also be calculated using a equivalent volume concept which is expressed as

$$m = \frac{V_{\text{hemispheroid}}}{V_{\text{sphere}}} \tag{145}$$

where $V_{\text{hemispheroid}}$ is the volume of the hemispheroid which is calculated by

$$V_{\text{hemispheroid}} = \frac{2}{3}\pi \left(\frac{b_{\text{base}}}{2}\right)^2 h_{\text{tooth}} \tag{146}$$

Note that the determination of the number of spheres can be extracted from a 2-D measured profile. More rigorously, a 3-D profile should be measured and the number of spheres for each discretized cell can be calculated from these measurement results.

### 7.4.6 Incorporation with the Laguerre-FDTD Method

Recall that in Chapter IV, conductor loss is modeled by incorporating the skin-effect in the Laguerre-FDTD solver. Skin-effect is modeled by introducing the SIBC. For smooth surface, the conductivity is always constant. To model the conductor surface roughness, methods of obtaining the frequency-dependent conductivity was proposed in the previous sections. Therefore, to incorporate the surface roughness into the Laguerre-FDTD solver, it is convenient to transform (34) into

$$Z(\omega) = \frac{1}{Y(\omega)} = \sqrt{\frac{j\omega\mu}{\sigma'(\omega) + j\omega\varepsilon}} \tag{147}$$

where $\sigma'(\omega)$ is the frequency-dependent conductivity adjusted by the enhancement factor. Since fitting techniques are used to derive the Laguerre-domain expression of the SIBC, the only change needed is the replacement of constant conductivity with the frequency-dependent conductivity.

## *7.5 Numerical Results*

The SIW structure has been simulated using the proposed methods. The frequency-dependent conductivity was imported into the commercial full-wave solver (HFSS). It is important to note that, the frequency-dependent conductivity can be easily incorporated into the Laguerre-FDTD solver which is capable of handling conductor loss. The detailed feature size of the structure can be found in Figure 72. To extract the model parameters, the roughness profile was measured. Figure 85 shows the 2-D measurement result of the copper surface of the SIW. The root mean square (RMS) of the roughness height is approximately 0.5 $\mu$m.

Figure 86 shows the enhancement factor calculated from the modified Huray model and the rigorous waveguide model. The result from the modified Huray model indicates that the enhancement factor is lower than that calculated from the rigorous waveguide model at low frequencies.

Figure 87 and Figure 88 show the simulated and measured $S$-parameters of the SIW structure. For comparison, the same SIW with a smooth conductor surface is also simulated. It can be observed from Figure 87 that surface roughness does not have a major impact on the return loss of the SIW. However, it is observed from Figure 88 that the surface roughness has a significant influence on the insertion loss of the SIW. The magnitude difference of the insertion loss between a simulated SIW

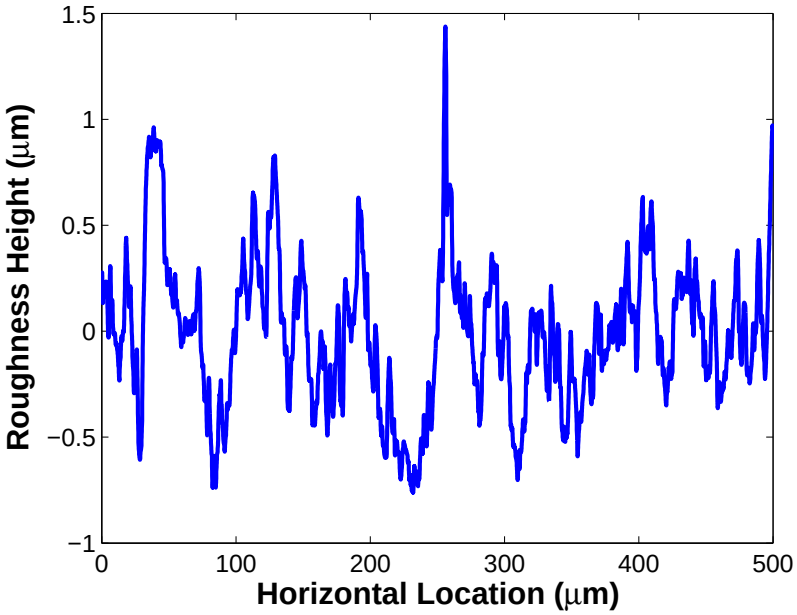


**Figure 85:** Measured surface roughness of the top copper wall of the SIW.

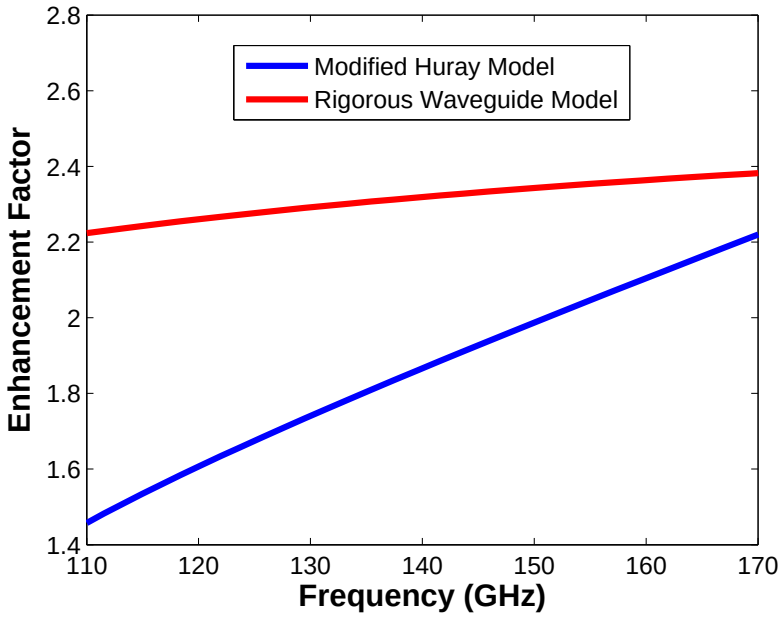


**Figure 86:** Enhancement factor of the SIW.

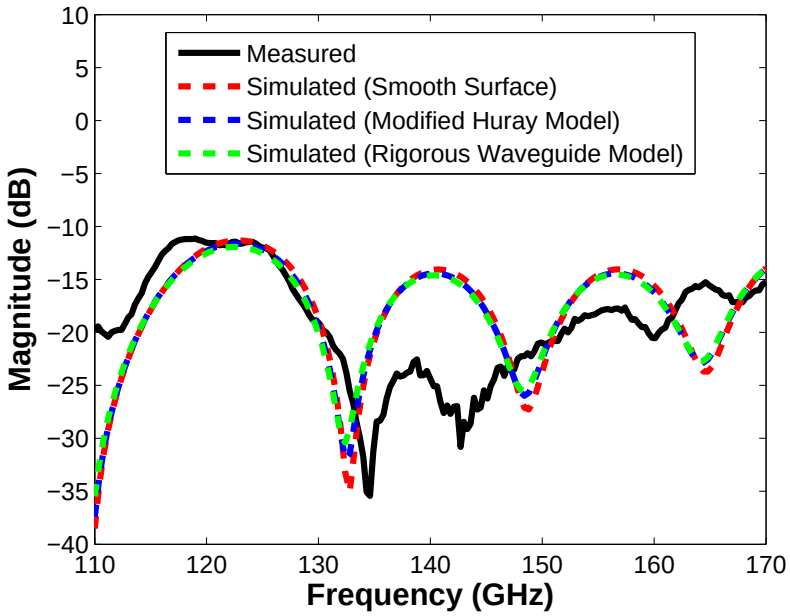


**Figure 87:** Simulated and measured return loss of the SIW.

with a smooth conductor surface and the measurement indicates that the loss effect cannot be simply modeled by a smooth surface. It is obvious that by modeling the surface roughness using the proposed methods, the loss in SIW is more accurately captured. Moreover, although for 170 GHz, the loss is accurately modeled by both the modified Huray model and rigorous waveguide model, at lower frequencies, the rigorous waveguide model is more accurate.

SIWs with different RMS heights of the surface roughness are investigated using both models. Figure 89 and Figure 90 show the return loss and insertion loss of the SIW with different surface roughness heights using the modified Huray model. Four scenarios are considered, namely the RMS of the surface roughness height of 0.05 $\mu$m, 0.1 $\mu$m, 0.25 $\mu$m, and 0.5 $\mu$m, respectively. Similarly, Figure 91 and Figure 92 show the return loss and insertion loss of the SIW with different surface roughness heights using the rigorous waveguide model. The same four scenarios are considered. It can be observed from the results that higher roughness height results in higher loss. This

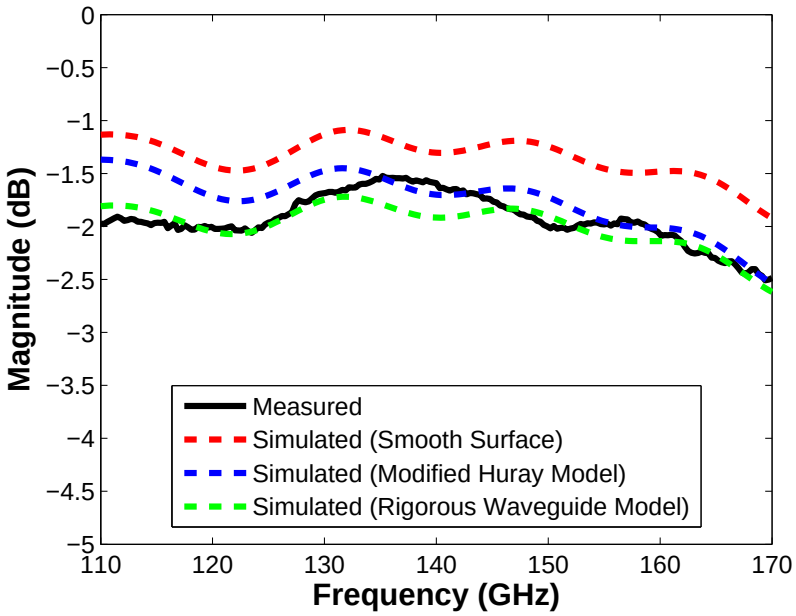


**Figure 88:** Simulated and measured insertion loss of the SIW.

is because the equivalent length of current path is longer for higher roughness cases. To be noted, roughness height RMS of 0.1 $\mu$m or below has little impact on the overall insertion loss of the SIW. This is because the roughness height is close to the skin depth at the frequency of interest, resulting in limited increment of equivalent length of current path as frequency increases.

The loss behavior of the SIW and the microstrip line are compared. For fair comparison, SIW is simulated without any transitions. The SIW and the microstrip line share the same LCP substrate for which the RMS roughness height of the copper is 0.5 $\mu$m. The roughness of the SIW is modeled using the rigorous waveguide model. Four scenarios are considered for the SIW, namely 2 mil substrate with smooth surface, 4 mil substrate with smooth surface, 2 mil substrate with rough surface and 4 mil substrate with rough surface.

Figure 93 shows the comparison of attenuation of the SIW and the microstrip line. It can be observed that surface roughness has larger impact on the insertion loss of

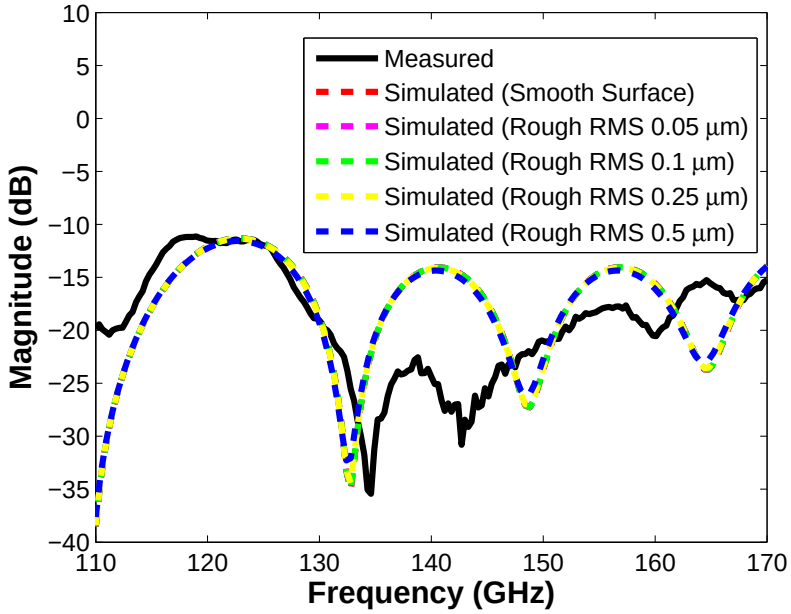


**Figure 89:** Simulated and measured return loss of the SIW with different surface roughness height using the modified Huray model.

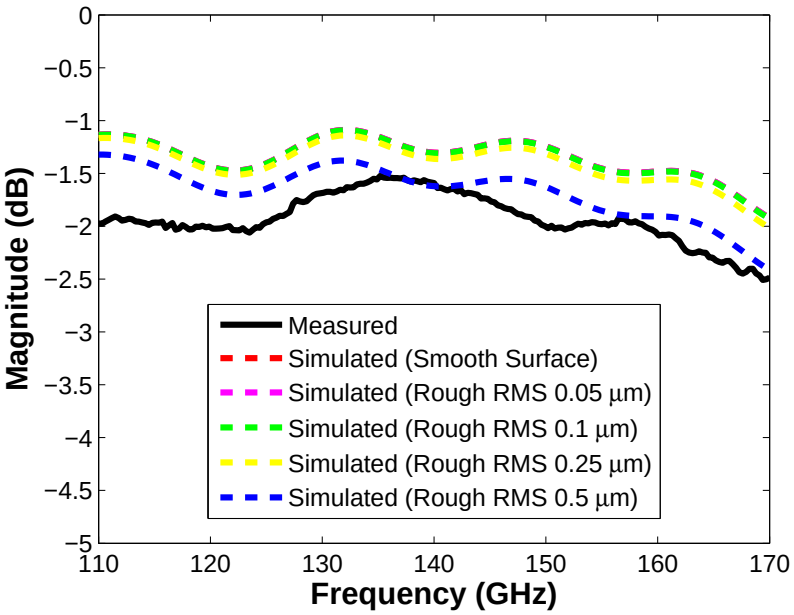


**Figure 90:** Simulated and measured insertion loss of the SIW with different surface roughness height using the modified Huray model.

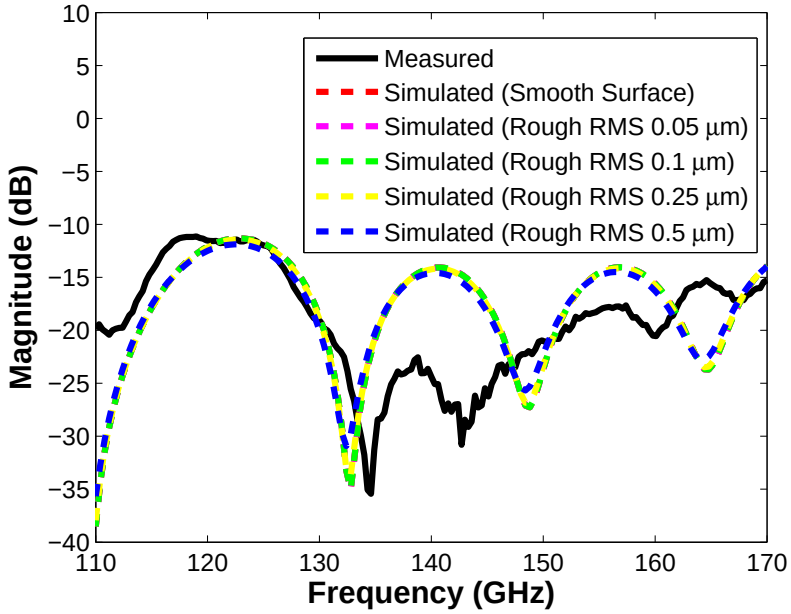


**Figure 91:** Simulated and measured return loss of the SIW with different surface roughness height using the rigorous waveguide model.

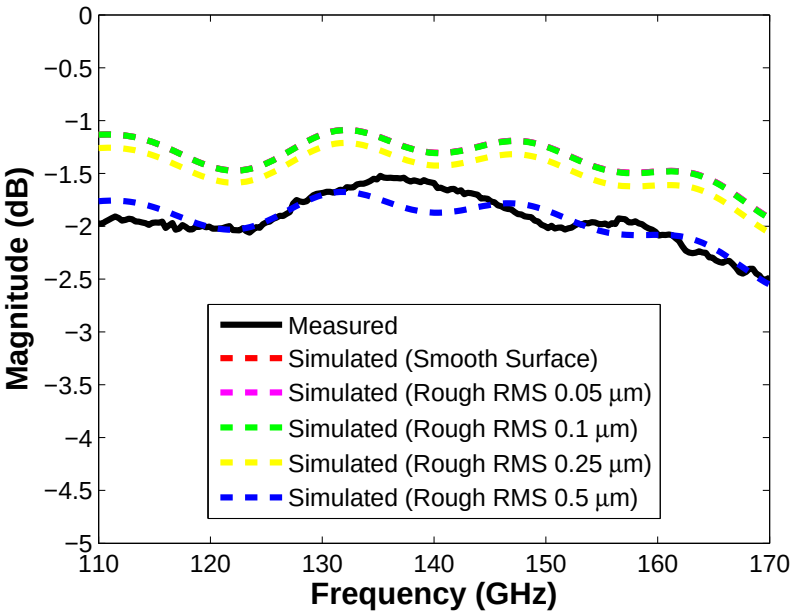


**Figure 92:** Simulated and measured insertion loss of the SIW with different surface roughness height using the rigorous waveguide model.

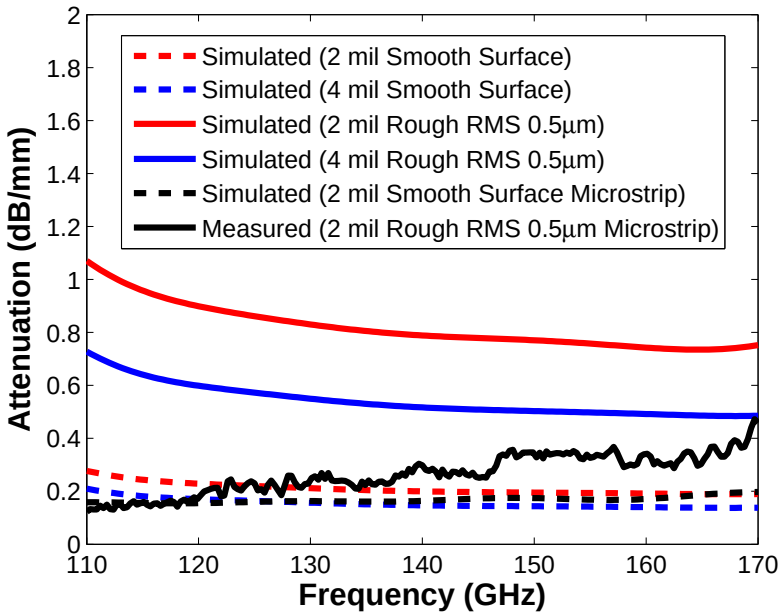


**Figure 93:** Attenuation of the SIW and the microstrip line.

the SIW than that of the microstrip line. This is because in SIW, large amount of metal carries the current. If the roughness height is high, the larger surface area of the roughness may exhibit larger influence on the transmission loss. It can also be observed from Figure 93 that the thicker the substrate, the lower the loss. This is the same as what is expected since conductor loss of a waveguide is geometry-dependent. For the smooth surface case, the attenuation due to the conductor can be expressed as [74]

$$\alpha_c = \frac{R_s}{\sqrt{1-\left(\frac{f_c}{f}\right)^2}}\sqrt{\frac{\varepsilon}{\mu}}\left[\frac{1}{b}+\frac{2}{a}\left(\frac{f_c}{f}\right)^2\right] \tag{148}$$

where $b$ is the substrate thickness. It can be concluded from the discussions above that to lower the loss of an SIW at millimeter wave frequencies, increasing the substrate thickness and polishing the conductor surface are good solutions.

## *7.6 Summary*

In this chapter, conductor surface roughness is modeled for the SIW. Enhancement factor has been introduced to generate the equivalent frequency-dependent conductivity of the conductor. The conductor loss due to the surface roughness is therefore captured by the frequency-dependent conductivity. The enhancement factor is expressed analytically, thus, it is convenient to incorporate the frequency-dependent conductivity into the existing full-wave solvers, including the Laguerre-FDTD solver. To tackle the TE transmission mode of the SIW, two modeling schemes are adopted, namely the modified Huray model and rigorous waveguide model. Both models use equivalent surfaces with protrusions of some simple geometries to approximate the random surface roughness. Loss is calculated by considering both the reflection and absorption of energy due to the protrusions. The numerical results show that the rigorous waveguide model is more accurate and loss due to the surface roughness is properly modeled.

# CHAPTER VIII

# CONCLUSIONS

The increasing need for consumer electronic products with high performance, small size and low cost requires modern ICs with high-density integration. As a result, the complexity of the IC design has witnessed a significant ramp-up in the past decades. In recent years, the switching of 2-D integration to 3-D integration has accelerated this trend. Hence, efficient EDA solutions become a necessity for modern IC design.

Among all the EDA solutions, the full-wave electromagnetic EDA solution is a critical component since it addresses the electromagnetic simulation of the products without compromising simulation accuracy. This is of vital importance in analyzing signal/power integrity, electromagnetic compatibility and signal interaction of structures of interest. However, the simulation of high-density integrated systems is challenging, especially for simulation of chip-package structures. Up to date, there is no transient full-wave solver that is capable of balancing simulation accuracy and efficiency.

As discussed in Chapter I and Chapter II, the challenges lie in the following aspects: First, a transient solver that is capable of solving multiscale structures with good efficiency is required. Second, skin-effect needs to be addressed for high-frequency simulations in order to accurately capture the conductor loss. Third, for ultra-high-frequency interconnects, a rigorous model for conductor surface roughness needs to be developed. The model should be easy for incorporation into the solver. Fourth, simulation schemes for large multiscale problems need to be developed, enabling simulation of chip-package structures. To address these challenges, several numerical methods are developed and presented in Chapter IV to Chapter VI. To be specific,

the solver developed for this work is based on an unconditionally stable transient method, the Laguerre-FDTD method. This method is suitable for simulating multiscale structures. A scheme for accurate modeling of the skin-effect is proposed and incorporated into the full-wave solver. An analytical solution for capturing the loss mechanism of the surface roughness is presented. Finally, a transient non-conformal domain decomposition method, which improves efficiency of simulation of large multiscale structures, is proposed and tested. All the proposed schemes are verified using numerical test cases. The simulation results indicate that the proposed schemes are accurate and more efficient compared to existing methods in simulating multiscale chip-package problems.

## *8.1 Contributions*

The contributions of the dissertation are summarized as follows.

1. **Development of an unconditionally stable transient full-wave solver for multiscale structures.**

   A transient solver is developed based on the Laguerre-FDTD method. Unlike the marching-on-in-time schemes such as the conventional FDTD method, the Laguerre-FDTD method is a marching-on-in-order scheme. Physical quantities that are time-variant are spanned by the Laguerre basis functions. Hence the method is unconditionally stable because the Laguerre basis functions are absolutely convergent as time goes to infinity. In other words, the time term is eliminated. To accurately and efficiently extract the frequency domain results, a scheme for embedding and de-embedding port resistors is proposed. The proposed embedding scheme allows the energy to decay significantly faster within the simulation structure whereas the de-embedding scheme ensures extraction accuracy. $S$-parameter extraction schemes are investigated and compared. A proper extraction method is chosen based on the analysis type of the problem.

2. **Rigorous implementation of the skin-effect.**

   The skin-effect is incorporated into the transient solver based on the Laguerre-FDTD method. By applying the SIBC, the relationship between electric field and magnetic field on the conductor surface is established. This avoids a fine mesh inside the conductor, which is typically adopted by conventional methods to capture the exponential decaying field. Despite the reduced unknowns due to non-meshing the interior of the conductor, the conductor surface meshing density can be reduced at the same time. This method is proved to be accurate with significant improvement of simulation speed compared to the standard Laguerre-FDTD method. Two implementation approaches, namely the MFA-SIBC and the EFA-SIBC methods are proposed and compared. Both approaches show good numerical stability with large variation of the conductor conductivity. The proposed method is very useful for simulating chip-package structures with dense interconnects at high frequencies with high efficiency.

3. **Development of a transient non-conformal domain decomposition method based on the Laguerre-FDTD scheme.**

   A transient non-conformal domain decomposition scheme is developed. By using the domain decomposition scheme, the demand for computational resources is reduced because of fewer total unknowns and the potential for parallel computing. Therefore, large-scale problems can be solved using a divide-and-conquer strategy. The proposed scheme outperforms the conformal domain decomposition schemes for the simulation of multiscale structures. Since the interface mesh does not need to be matched, meshing complexity for different domains can be significantly relaxed. Different domains can be meshed independently based on the feature size without the need for mesh conformality. For multiscale

structures, regions with physically small structures can be meshed finely whereas regions with physically large structures can be meshed coarsely. This reduces the total number of unknowns by eliminating unnecessary finely meshed regions. To maintain field continuity at the domain interface, two sets of Lagrange multipliers are introduced which account for continuity of tangential electric and magnetic fields. This scheme results in reduced field distortion and reflection performance than the direct implementation of the mortar-element-like scheme. Moreover, the solution of each domain can be calculated in a parallel manner using Schur complement, which further increases the simulation speed.

4. **Investigation on the multiscale chip-package structure simulation.**

   Multiscale chip-package problems are investigated based on all the proposed schemes. To be more specific, the skin-effect loss is accurately modeled using the proposed SIBC-based scheme. To deal with the large multiscale nature of the chip-package problems, the non-conformal domain decomposition method is used with separate meshing strategy for chip and package regions. Several typical chip-package structures, including a multi-port interconnect network and a multiscale chip-package PDN, are simulated. The results indicate that the proposed methods are accurate and computationally efficient. Significant improvement of the simulation speed for chip-package structures is achieved. Most importantly, the proposed methods are capable of solving problems that cannot be efficiently analyzed by existing commercial solvers.

5. **Development of a conductor surface roughness modeling scheme for the SIW.**

   The conductor surface roughness is modeled for SIW. As an alternate interconnect structure, SIW exhibits better performance in ultra-high frequency applications due to its immunity to crosstalk, large power capacity and low

transmission loss. Although the loss due to the surface roughness is investigated for the TEM type of transmission lines, the surface roughness loss of the SIW is still unexplored. This work models the surface roughness based on the enhancement factor concept. Analytical expressions for the enhancement factor are developed to create an equivalent frequency-dependent conductivity of the conductor. The equivalent conductivity can then be easily incorporated into commercial solvers or the Laguerre-FDTD solver. To be specific, the random roughness of the conductor surface is modeled by an equivalent surface with protrusions of simple geometries. Loss due to a signal protrusion is obtained analytically and the total loss is derived using the summation of loss of all protrusions. In implementation, two models are developed to capture the loss due to protrusions, namely the modified Huray model and the rigorous waveguide model. Measurement data is used to gauge the accuracy of the proposed models. Both models are accurate by considering the transmission mode of the SIW whereas the rigorous waveguide model shows better results in low frequencies.

## *8.2 Publications*

This work results in the following publications.

**List of Journal Publications**

1. **Ming Yi**, Myunghyun Ha, Zhiguo Qian, Alaeddin Aydiner, and Madhavan Swaminathan, "Skin-effect-incorporated transient simulation using the Laguerre-FDTD scheme," *IEEE Trans. Microwave Theory and Techniques*, vol. 61, no. 52, pp. 4029-4039, Dec. 2013

2. **Ming Yi**, Zhiguo Qian, Alaeddin Aydiner, and Madhavan Swaminathan, "Transient simulation of multiscale structures using the non-conformal domain decomposition Laguerre-FDTD method," *IEEE Trans. Components, Packaging and Manufacturing Technology*, vol. 5, no. 4, pp. 532-540, Apr. 2015

3. **Ming Yi**, Sensen Li, Wasif Khan, Cagri Ulusoy, Aida Vera, Henning Braunisch, Adel Elsherbini, Telesphor Kamgaing, Ioannis Papapolymerou, and Madhavan Swaminathan, "Surface roughness modeling of the D-band substrate integrated waveguide", *IEEE Trans. Microwave Theory and Techniques*, 2015 (to be submitted)

**List of Conference Publications**

1. **Ming Yi**, and Madhavan Swaminathan, "Transient non-conformal domain decomposition using the Laguerre-FDTD method," in Proc. *IEEE International Conference for Computational Electromagnetics (ICCEM)*, Feb. 2015

2. **Ming Yi**,and Madhavan Swaminathan, "Transient simulation of interconnects in chip-package structure using the non-conformal domain decomposition scheme," in Proc. *Semiconductor Research Corporation (SRC) TECHCON*, Sept. 2014

3. **Ming Yi**, Madhavan Swaminathan, Zhiguo Qian, and Alaeddin Aydiner, "2-D non-conformal domain decomposition using the Laguerre-FDTD scheme," in Proc. *IEEE Antennas Propagation Society International Symposium(APS/URSI)*, July 2014

4. **Ming Yi**, Madhavan Swaminathan, Myunghyun Ha, Zhiguo Qian, and Alaeddin Aydiner, "Memory efficient Laguerre-FDTD scheme for dispersive media," in Proc. *IEEE Electrical Performance of Electronic Packaging and Systems (EPEPS)*, Oct. 2013, pp. 51-54

5. **Ming Yi**, Madhavan Swaminathan, Zhiguo Qian, and Alaeddin Aydiner, "Skin effect modeling of interconnects using the Laguerre-FDTD scheme," in Proc. *IEEE Electrical Performance of Electronic Packaging and Systems (EPEPS)*, Oct. 2012, pp. 51-54

# CHAPTER IX

# FUTURE WORK

This dissertation addressed multiscale chip-package simulation problems. However, there are still some fields related to this topic that are challenging and require further exploration. They are categorized as future work in this chapter.

## *9.1 High-Efficiency Parallel Domain Decomposition*

The domain decomposition method discussed in this work is efficient in simulating multiscale chip-package structures. By introducing the dual sets of Lagrange multipliers and choosing dominant-auxiliary domain pairs, the field continuity on the domain interface is maintained while each domain can be meshed separately (Figure 94). Using the Schur complement scheme, the interface problem is extracted with less degrees of freedom, and therefore the system solution can be performed in a parallel manner which significantly reduces the computational time.

However, the current domain decomposition scheme has its limitations. Since field continuity is enforced by applying the Lagrange multipliers, additional unknowns are introduced into the system solution. The number of unknowns depends on the domain

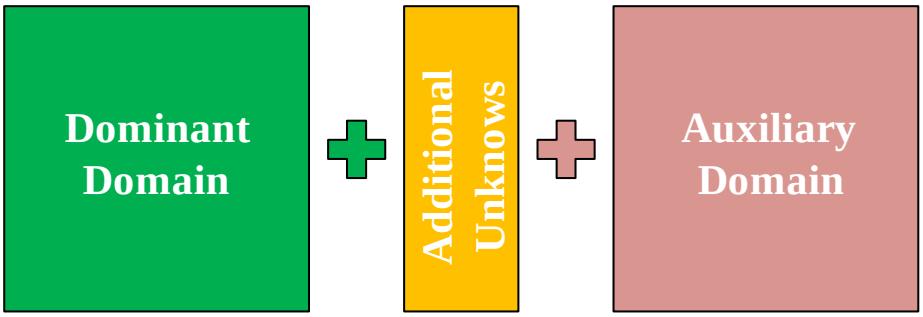


**Figure 94:** Non-conformal domain decomposition method in this work.

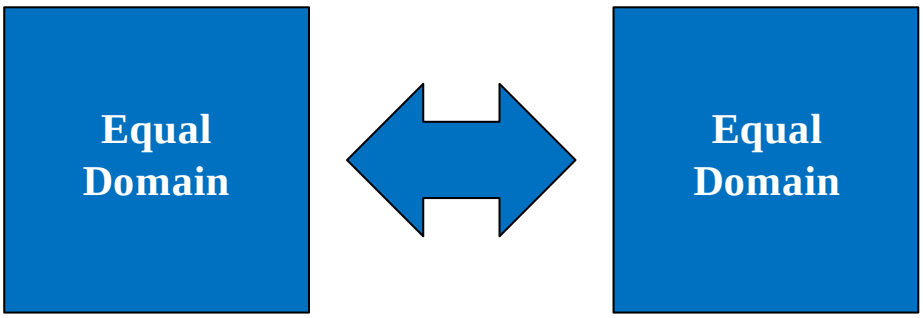


**Figure 95:** Non-conformal domain decomposition using domain-by-domain iteration scheme.

partition and dominant interface selection. It is obvious that computational cost will increase as the number of interface unknowns increases, which is very common for decomposed structures with many domains.

One of the solution methods is the domain-by-domain iteration scheme as shown in Figure 95. Instead of introducing additional unknowns, this method considers domain interfaces as mutual excitation sources [44]. In a certain time step or frequency point, each domain is solved recursively until convergence is reached. Fast convergence methods are important in realizing the domain-by-domain iteration scheme.

## *9.2 Model Order Reduction*

It is known that the most accurate method of solving electromagnetic problems is the full-wave method. By discretizing the computational space with elements (e.g., hexahedral, tetrahedron), the field information at any point of the computational domain can be solved. However, the full-wave methods suffer from large computational cost which makes the simulation of large-scale problems (e.g. entire package layout) computationally inefficient. To overcome the speed limit, circuit methods using lumped elements are developed. By extracting the equivalent circuit models based on the actual physics of the problems, some electromagnetic problems can be analyzed in a significantly faster manner. This type of method has been successfully

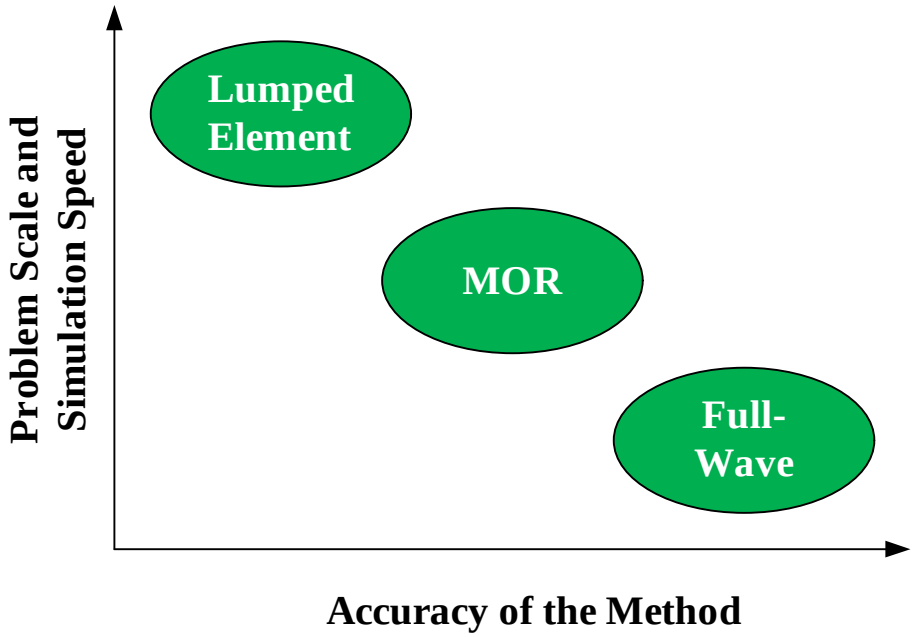


**Figure 96:** Problem complexity and simulation accuracy of various computational methods.

demonstrated in simulating structures such as power grids and PDNs [81]. One of the critical drawbacks is the simulating accuracy. Moreover, equivalent circuits for complex structures are difficult to be derived.

One solution is the model order reduction (MOR) method as shown in Figure 96. The basic idea of MOR method is to create a reduced linear system such that the transfer function of the system is approximated with acceptable tolerance [82]. The solution will be much faster than the full-wave method with acceptable accuracy. Since the linear system expression using the Laguerre-FDTD method has already been developed in [70], it is promising that large-scale problems can be solved much more efficiently based on the Laguerre-FDTD method.

## *9.3 Algorithm Hybridization*

The Laguerre-FDTD method shows significant speed-up compared to the conventional FDTD method when multiscale structures are simulated. However, compared to

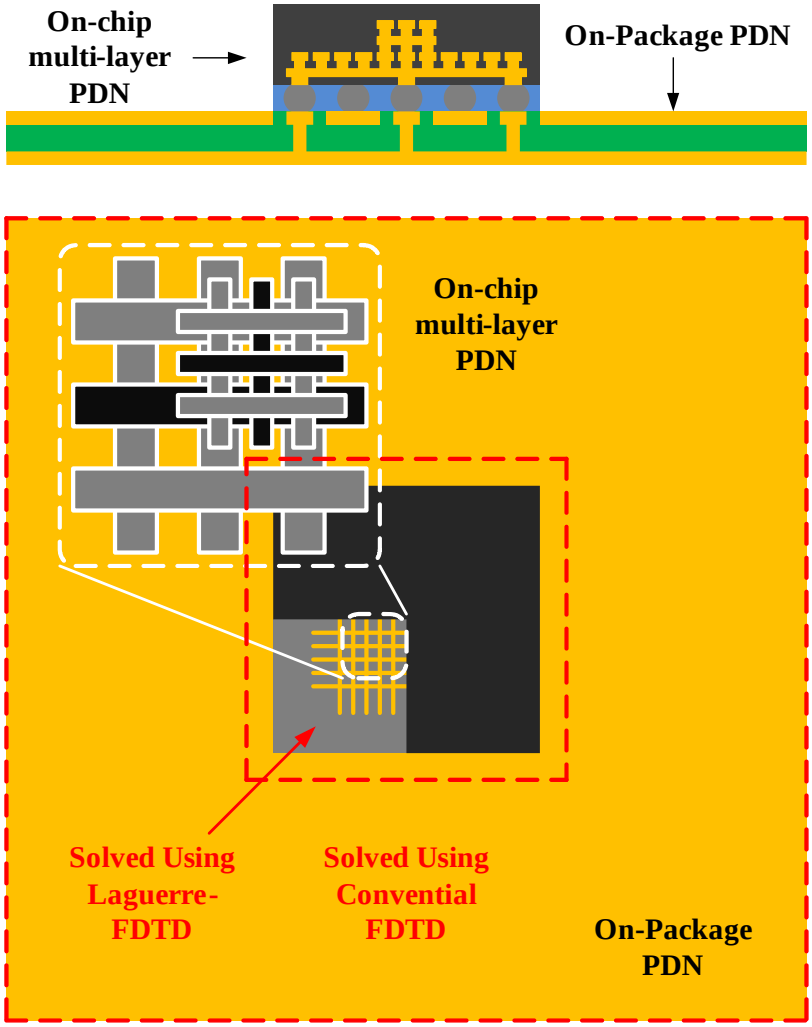


**Figure 97:** The hybridization of the Laguerre-FDTD method and the conventional FDTD method in solving chip-package PDN problem.

conventional FDTD method, Laguerre-FDTD method requires a matrix solution at each order step. This is computationally expensive if the structure of interest is not multiscale or the mesh resolution requirement is not high. There are certain types of structure for which some regions require multiscale dense mesh whereas other regions require coarse mesh. Considering the chip-package PDN problem shown in Figure 97, the on-chip multi-level power grid is multiscale whereas the on-package power-ground-plane-pairs can be justifiably considered as structures requiring a coarse mesh resolution.

By applying algorithm hybridization, it is possible to utilized the advantages of both conventional FDTD method and Laguerre-FDTD method. Conventional FDTD is applied to the low mesh resolution regions whereas the Laguerre-FDTD method is applied to the multiscale regions. The key of this solution is to find the method for hybridizing the marching-on-in-time scheme and marching-on-in order scheme. The solution speed is expected to be much faster than using a single time-domain method.

# APPENDIX A

# FORMULATIONS FOR THE LAGUERRE-FDTD METHOD

## *A.1 Formulations Based Upon the Two First-Order Equations*

Considering an isotropic, non-dispersive, lossy media, in Cartesian coordinates, two first-order Maxwell's equations can be expressed as

$$\nabla \times \mathbf{E} = -\mu \frac{\partial \mathbf{H}}{\partial t} \tag{149}$$

$$\nabla \times \mathbf{H} = \varepsilon \frac{\partial \mathbf{E}}{\partial t} + \mathbf{J} \tag{150}$$

Rewriting (149) and (150) into 3-D form, we have

$$\frac{\partial E_x}{\partial t} = \frac{1}{\varepsilon}\left(\frac{\partial H_z}{\partial y} - \frac{\partial H_y}{\partial z} - J_x - \sigma E_x\right) \tag{151}$$

$$\frac{\partial E_y}{\partial t} = \frac{1}{\varepsilon}\left(\frac{\partial H_x}{\partial z} - \frac{\partial H_z}{\partial x} - J_y - \sigma E_y\right) \tag{152}$$

$$\frac{\partial E_z}{\partial t} = \frac{1}{\varepsilon}\left(\frac{\partial H_y}{\partial x} - \frac{\partial H_x}{\partial y} - J_z - \sigma E_z\right) \tag{153}$$

$$\frac{\partial H_x}{\partial t} = \frac{1}{\mu}\left(\frac{\partial E_y}{\partial z} - \frac{\partial E_z}{\partial y}\right) \tag{154}$$

$$\frac{\partial H_y}{\partial t} = \frac{1}{\mu}\left(\frac{\partial E_z}{\partial x} - \frac{\partial E_x}{\partial z}\right) \tag{155}$$

$$\frac{\partial H_z}{\partial t} = \frac{1}{\mu}\left(\frac{\partial E_x}{\partial y} - \frac{\partial E_y}{\partial x}\right) \tag{156}$$

where $\varepsilon$ is the electric permittivity, $\mu$ is the magnetic permeability, $\sigma$ is the electric

conductivity; $J_x$, $J_y$, and $J_z$ are the excitations along $x$, $y$, and $z$ axes, respectively.

First, consider the equations related to the electric field in $x$-direction. Using the Laguerre basis functions, the temporal coefficients in (151) can be expanded as

$$E_x = \sum_{p=0}^{\infty} E_x^p \varphi^p(\bar{t}) \tag{157}$$

$$H_y = \sum_{p=0}^{\infty} H_y^p \varphi^p(\bar{t}) \tag{158}$$

$$H_z = \sum_{p=0}^{\infty} H_z^p \varphi^p(\bar{t}). \tag{159}$$

For any given time-domain waveform $W$, the first derivative with respect to time $t$ is

$$\frac{\partial W}{\partial t} = s \sum_{p=0}^{\infty} \left( \frac{1}{2} W^p + \sum_{n=0,p>1}^{p-1} W^n \right) \varphi^p(\bar{t}). \tag{160}$$

Therefore, applying (160) into (151) results in

$$\begin{aligned} & s \sum_{p=0}^{\infty} \left( \frac{1}{2} E_x^p + \sum_{n=0,p>1}^{p-1} E_x^n \right) \varphi^p(\bar{t}) \\ = & \frac{1}{\varepsilon} \left( \sum_{p=0}^{\infty} \frac{\partial H_z^p}{\partial y} \varphi^p(\bar{t}) - \sum_{p=0}^{\infty} \frac{\partial H_y^p}{\partial z} \varphi^p(\bar{t}) - J_x - \sigma \sum_{p=0}^{\infty} E_x^p \varphi^p(\bar{t}) \right). \end{aligned} \tag{161}$$

To eliminate the time-dependent terms $\varphi^p(\bar{t})$, introducing a temporal Galerkins testing procedure of (161) by using the orthogonal property of the weighted Laguerre functions. Multiply both sides of (161) by $\varphi^q(\bar{t})$ and integrate over time, we have

$$\begin{aligned} & s \left( \frac{1}{2} E_x^q + \sum_{q=0,p>1}^{q-1} E_x^n \right) \\ = & \frac{1}{\varepsilon} \left( \frac{\partial H_z^q}{\partial y} - \frac{\partial H_y^q}{\partial z} - J_x^q - \sigma E_x^q \right) \end{aligned} \tag{162}$$

where

$$J_x^q = \int_0^{T_f} J_x \varphi^q(\bar{t}) d\bar{t}. \tag{163}$$

The upper limit of the time interval is finite length time period of $T_f$. Discretizing (162) using the Yee grid shown in Figure 8 yields

$$\begin{aligned} E_x^q|_{i,j,k} = \bar{C}_y^E|_{i,j,k} \left(H_z^q|_{i,j,k} - H_z^q|_{i,j-1,k}\right) - \bar{C}_z^E|_{i,j,k} \left(H_y^q|_{i,j,k} - H_y^q|_{i,j,k-1}\right) \\ - \frac{2}{s\varepsilon_{i,j,k}} J_x^q|_{i,j,k} - \frac{2\sigma_{i,j,k}}{s\varepsilon_{i,j,k}} E_x^q|_{i,j,k} - 2 \sum_{n=0,q>1}^{q-1} E_x^n|_{i,j,k} \end{aligned} \tag{164}$$

where

$$\bar{C}_y^E|_{i,j,k} = \frac{2}{s\varepsilon_{i,j,k}\Delta\bar{y}_j} \tag{165}$$

$$\bar{C}_z^E|_{i,j,k} = \frac{2}{s\varepsilon_{i,j,k}\Delta\bar{z}_k} \tag{166}$$

where $\Delta\bar{y}_j$ and $\Delta\bar{z}_k$ are the distance between the center nodes where magnetic fields are located.

Similarly, discretizing time derivative differential equations (155) and (156) for magnetic fields in three cells shown in Figure 8, the Laguerre coefficient expressions of the related magnetic fields are

$$\begin{aligned} H_y^q|_{i,j,k} = \bar{C}_x^H|_{i,j,k} \left(E_z^q|_{i+1,j,k} - E_z^q|_{i,j,k}\right) \\ - \bar{C}_z^H|_{i,j,k} \left(E_x^q|_{i,j,k+1} - E_x^q|_{i,j,k}\right) - 2 \sum_{n=0,q>1}^{q-1} H_y^n|_{i,j,k} \end{aligned} \tag{167}$$

$$\begin{aligned} H_y^q|_{i,j,k-1} = \bar{C}_x^H|_{i,j,k-1} \left(E_z^q|_{i+1,j,k-1} - E_z^q|_{i,j,k-1}\right) \\ - \bar{C}_z^H|_{i,j,k-1} \left(E_x^q|_{i,j,k} - E_x^q|_{i,j,k-1}\right) - 2 \sum_{n=0,q>1}^{q-1} H_y^n|_{i,j,k-1} \end{aligned} \tag{168}$$

$$H_z^q\,|_{i,j,k} = \bar{C}_y^H\,|_{i,j,k}\,(E_x^q\,|_{i,j+1,k} - E_x^q\,|_{i,j,k}) - \bar{C}_x^H\,|_{i,j,k}\,\left(E_y^q\,|_{i+1,j,k} - E_y^q\,|_{i,j,k}\right) - 2\sum_{n=0,q>1}^{q-1} H_z^n\,|_{i,j,k} \tag{169}$$

$$H_z^q\,|_{i,j-1,k} = \bar{C}_y^H\,|_{i,j-1,k}\,(E_x^q\,|_{i,j,k} - E_x^q\,|_{i,j-1,k}) - \bar{C}_x^H\,|_{i,j-1,k}\,\left(E_y^q\,|_{i+1,j-1,k} - E_y^q\,|_{i,j-1,k}\right) - 2\sum_{n=0,q>1}^{q-1} H_z^n\,|_{i,j-1,k} \tag{170}$$

where

$$\bar{C}_x^H\,|_{i,j,k} = \frac{2}{s\mu_{i,j,k}\Delta x_i} \tag{171}$$

$$\bar{C}_y^H\,|_{i,j,k} = \frac{2}{s\mu_{i,j,k}\Delta y_j} \tag{172}$$

$$\bar{C}_z^H\,|_{i,j,k} = \frac{2}{s\mu_{i,j,k}\Delta z_k}. \tag{173}$$

in which $\Delta x_i$, $\Delta y_j$, and $\Delta z_k$ are the length of the edge where electric fields are located.

Inserting (167)-(170) into (164), with some manipulations, the equation for electric field in $x$-direction associated with cell $(i, j, k)$ can be obtained as

$$
\begin{aligned}
&\Big(1+\bar{C}_y^E\,|_{i,j,k}\,\bar{C}_y^H\,|_{i,j,k}+\bar{C}_y^E\,|_{i,j,k}\,\bar{C}_y^H\,|_{i,j-1,k}\\
&+\bar{C}_z^E\,|_{i,j,k}\,\bar{C}_z^H\,|_{i,j,k}+\bar{C}_z^E\,|_{i,j,k}\,\bar{C}_z^H\,|_{i,j,k-1}+\frac{2\sigma_{i,j,k}}{s\varepsilon_{i,j,k}}\Big)\,E_x^q\,|_{i,j,k}\\
&-\bar{C}_y^E\,|_{i,j,k}\,\bar{C}_y^H\,|_{i,j,k}\,E_x^q\,|_{i,j+1,k}+\bar{C}_y^E\,|_{i,j,k}\,\bar{C}_x^H\,|_{i,j,k}\,E_y^q\,|_{i+1,j,k}\\
&-\bar{C}_y^E\,|_{i,j,k}\,\bar{C}_x^H\,|_{i,j,k}\,E_y^q\,|_{i,j,k}-\bar{C}_y^E\,|_{i,j,k}\,\bar{C}_y^H\,|_{i,j-1,k}\,E_x^q\,|_{i,j-1,k}\\
&-\bar{C}_y^E\,|_{i,j,k}\,\bar{C}_x^H\,|_{i,j-1,k}\,E_y^q\,|_{i+1,j-1,k}+\bar{C}_y^E\,|_{i,j,k}\,\bar{C}_x^H\,|_{i,j-1,k}\,E_y^q\,|_{i,j-1,k}\\
&+\bar{C}_z^E\,|_{i,j,k}\,\bar{C}_x^H\,|_{i,j,k}\,E_z^q\,|_{i+1,j,k}-\bar{C}_z^E\,|_{i,j,k}\,\bar{C}_x^H\,|_{i,j,k}\,E_z^q\,|_{i,j,k}\\
&-\bar{C}_z^E\,|_{i,j,k}\,\bar{C}_z^H\,|_{i,j,k}\,E_x^q\,|_{i,j,k+1}-\bar{C}_z^E\,|_{i,j,k}\,\bar{C}_x^H\,|_{i,j,k-1}\,E_z^q\,|_{i+1,j,k-1}\\
&+\bar{C}_z^E\,|_{i,j,k}\,\bar{C}_x^H\,|_{i,j,k-1}\,E_z^q\,|_{i,j,k-1}-\bar{C}_z^E\,|_{i,j,k}\,\bar{C}_z^H\,|_{i,j,k-1}\,E_x^q\,|_{i,j,k-1}\\
=\;&-2\bar{C}_y^E\,|_{i,j,k}\left(\sum_{n=0,q>1}^{q-1}H_z^n\,|_{i,j,k}-\sum_{n=0,q>1}^{q-1}H_z^n\,|_{i,j-1,k}\right)\\
&+2\bar{C}_z^E\,|_{i,j,k}\left(\sum_{n=0,q>1}^{q-1}H_y^n\,|_{i,j,k}-\sum_{n=0,q>1}^{q-1}H_y^n\,|_{i,j,k-1}\right)\\
&-\frac{2}{s\varepsilon_{i,j,k}}J_x^q\,|_{i,j,k}-2\sum_{n=0,q>1}^{q-1}E_x^n\,|_{i,j,k}
\end{aligned}
\tag{174}
$$

Similarly, for electric field associated with cell $(i,j,k)$ in $y$- and $z$-direction, (151) and (152) can be written into the coefficient equations in Laguerre domain as

$$
\begin{aligned}
E_y^q\,|_{i,j,k}=\;&\bar{C}_z^E\,|_{i,j,k}\,(H_x^q\,|_{i,j,k}-H_x^q\,|_{i,j,k-1})-\bar{C}_x^E\,|_{i,j,k}\,(H_z^q\,|_{i,j,k}-H_z^q\,|_{i-1,j,k})\\
&-\frac{2}{s\varepsilon_{i,j,k}}J_y^q\,|_{i,j,k}-\frac{2\sigma_{i,j,k}}{s\varepsilon_{i,j,k}}E_y^q\,|_{i,j,k}-2\sum_{n=0,q>1}^{q-1}E_y^n\,|_{i,j,k}
\end{aligned}
\tag{175}
$$

and

$$
\begin{aligned}
E_z^q\,|_{i,j,k}=\;&\bar{C}_x^E\,|_{i,j,k}\left(H_y^q\,|_{i,j,k}-H_y^q\,|_{i-1,j,k}\right)-\bar{C}_y^E\,|_{i,j,k}\,(H_x^q\,|_{i,j,k}-H_x^q\,|_{i,j-1,k})\\
&-\frac{2}{s\varepsilon_{i,j,k}}J_z^q\,|_{i,j,k}-\frac{2\sigma_{i,j,k}}{s\varepsilon_{i,j,k}}E_z^q\,|_{i,j,k}-2\sum_{n=0,q>1}^{q-1}E_z^n\,|_{i,j,k}\,.
\end{aligned}
\tag{176}
$$

The coefficient equations for magnetic field associated with electric field are

$$H_x^q\,|_{i,j,k} = \bar{C}_z^H\,|_{i,j,k}\left(E_y^q\,|_{i,j,k+1} - E_y^q\,|_{i,j,k}\right) - \bar{C}_y^H\,|_{i,j,k}\left(E_z^q\,|_{i,j+1,k} - E_z^q\,|_{i,j,k}\right) - 2\sum_{n=0,q>1}^{q-1} H_x^n\,|_{i,j,k} \tag{177}$$

$$H_x^q\,|_{i,j,k-1} = \bar{C}_z^H\,|_{i,j,k-1}\left(E_y^q\,|_{i,j,k} - E_y^q\,|_{i,j,k-1}\right) - \bar{C}_y^H\,|_{i,j,k-1}\left(E_z^q\,|_{i,j+1,k-1} - E_z^q\,|_{i,j,k-1}\right) - 2\sum_{n=0,q>1}^{q-1} H_x^n\,|_{i,j,k-1} \tag{178}$$

$$H_z^q\,|_{i,j,k} = \bar{C}_y^H\,|_{i,j,k}\left(E_x^q\,|_{i,j+1,k} - E_x^q\,|_{i,j,k}\right) - \bar{C}_x^H\,|_{i,j,k}\left(E_y^q\,|_{i+1,j,k} - E_y^q\,|_{i,j,k}\right) - 2\sum_{n=0,q>1}^{q-1} H_z^n\,|_{i,j,k} \tag{179}$$

$$H_z^q\,|_{i-1,j,k} = \bar{C}_y^H\,|_{i-1,j,k}\left(E_x^q\,|_{i-1,j+1,k} - E_x^q\,|_{i-1,j,k}\right) - \bar{C}_x^H\,|_{i-1,j,k}\left(E_y^q\,|_{i,j,k} - E_y^q\,|_{i-1,j,k}\right) - 2\sum_{n=0,q>1}^{q-1} H_z^n\,|_{i-1,j,k} \tag{180}$$

and

$$H_y^q\,|_{i,j,k} = \bar{C}_x^H\,|_{i,j,k}\left(E_z^q\,|_{i+1,j,k} - E_z^q\,|_{i,j,k}\right) - \bar{C}_z^H\,|_{i,j,k}\left(E_x^q\,|_{i,j,k+1} - E_x^q\,|_{i,j,k}\right) - 2\sum_{n=0,q>1}^{q-1} H_y^n\,|_{i,j,k} \tag{181}$$

$$H_y^q\,|_{i-1,j,k} = \bar{C}_x^H\,|_{i-1,j,k}\left(E_z^q\,|_{i,j,k} - E_z^q\,|_{i-1,j,k}\right) - \bar{C}_z^H\,|_{i-1,j,k}\left(E_x^q\,|_{i-1,j,k+1} - E_x^q\,|_{i-1,j,k}\right) - 2\sum_{n=0,q>1}^{q-1} H_y^n\,|_{i-1,j,k} \tag{182}$$

$$H_x^q\,|_{i,j,k} = \bar{C}_z^H\,|_{i,j,k}\left(E_y^q\,|_{i,j,k+1} - E_y^q\,|_{i,j,k}\right) - \bar{C}_y^H\,|_{i,j,k}\left(E_z^q\,|_{i,j+1,k} - E_z^q\,|_{i,j,k}\right) - 2\sum_{n=0,q>1}^{q-1} H_x^n\,|_{i,j,k} \tag{183}$$

$$
\begin{aligned}
H_x^q\,|_{i,j-1,k} = \bar{C}_z^H\,|_{i,j-1,k}\,\left(E_y^q\,|_{i,j-1,k+1} - E_y^q\,|_{i,j-1,k}\right) \\
- \bar{C}_y^H\,|_{i,j-1,k}\,(E_z^q\,|_{i,j,k} - E_z^q\,|_{i,j-1,k}) - 2\sum_{n=0,q>1}^{q-1} H_x^n\,|_{i,j-1,k}
\end{aligned}
\tag{184}
$$

Following the same procedure as is used deriving the coefficient equation for electric field in $x$-direction, the coefficient equations for electric field in $y$- and $z$-direction can be obtained as

$$
\begin{aligned}
&\Big(1 + \bar{C}_z^E\,|_{i,j,k}\,\bar{C}_z^H\,|_{i,j,k} + \bar{C}_z^E\,|_{i,j,k}\,\bar{C}_z^H\,|_{i,j,k-1} \\
&+\bar{C}_x^E\,|_{i,j,k}\,\bar{C}_x^H\,|_{i,j,k} + \bar{C}_x^E\,|_{i,j,k}\,\bar{C}_x^H\,|_{i-1,j,k} + \frac{2\sigma_{i,j,k}}{s\varepsilon_{i,j,k}}\Big)\,E_y^q\,|_{i,j,k} \\
&- \bar{C}_z^E\,|_{i,j,k}\,\bar{C}_z^H\,|_{i,j,k}\,E_y^q\,|_{i,j,k+1} + \bar{C}_z^E\,|_{i,j,k}\,\bar{C}_y^H\,|_{i,j,k}\,E_z^q\,|_{i,j+1,k} \\
&- \bar{C}_z^E\,|_{i,j,k}\,\bar{C}_y^H\,|_{i,j,k}\,E_z^q\,|_{i,j,k} - \bar{C}_z^E\,|_{i,j,k}\,\bar{C}_z^H\,|_{i,j,k-1}\,E_y^q\,|_{i,j,k-1} \\
&- \bar{C}_z^E\,|_{i,j,k}\,\bar{C}_y^H\,|_{i,j,k-1}\,E_z^q\,|_{i,j+1,k-1} + \bar{C}_z^E\,|_{i,j,k}\,\bar{C}_y^H\,|_{i,j,k-1}\,E_z^q\,|_{i,j,k-1} \\
&+ \bar{C}_x^E\,|_{i,j,k}\,\bar{C}_y^H\,|_{i,j,k}\,E_x^q\,|_{i,j+1,k} - \bar{C}_x^E\,|_{i,j,k}\,\bar{C}_y^H\,|_{i,j,k}\,E_x^q\,|_{i,j,k} \\
&- \bar{C}_x^E\,|_{i,j,k}\,\bar{C}_x^H\,|_{i,j,k}\,E_y^q\,|_{i+1,j,k} - \bar{C}_x^E\,|_{i,j,k}\,\bar{C}_y^H\,|_{i-1,j,k}\,E_x^q\,|_{i-1,j+1,k} \\
&+ \bar{C}_x^E\,|_{i,j,k}\,\bar{C}_y^H\,|_{i-1,j,k}\,E_x^q\,|_{i-1,j,k} - \bar{C}_x^E\,|_{i,j,k}\,\bar{C}_x^H\,|_{i-1,j,k}\,E_y^q\,|_{i-1,j,k} \\
=\ &- 2\bar{C}_z^E\,|_{i,j,k}\left(\sum_{n=0,q>1}^{q-1} H_x^n\,|_{i,j,k} - \sum_{n=0,q>1}^{q-1} H_x^n\,|_{i,j,k-1}\right) \\
&+ 2\bar{C}_x^E\,|_{i,j,k}\left(\sum_{n=0,q>1}^{q-1} H_z^n\,|_{i,j,k} - \sum_{n=0,q>1}^{q-1} H_z^n\,|_{i-1,j,k}\right) \\
&- \frac{2}{s\varepsilon_{i,j,k}} J_y^q\,|_{i,j,k} - 2\sum_{n=0,q>1}^{q-1} E_y^n\,|_{i,j,k}
\end{aligned}
\tag{185}
$$

and

$$
\begin{aligned}
&\big(1+\bar{C}_x^E\,|_{i,j,k}\,\bar{C}_x^H\,|_{i,j,k}+\bar{C}_x^E\,|_{i,j,k}\,\bar{C}_x^H\,|_{i-1,j,k}\\
&+\bar{C}_y^E\,|_{i,j,k}\,\bar{C}_y^H\,|_{i,j,k}+\bar{C}_y^E\,|_{i,j,k}\,\bar{C}_y^H\,|_{i,j-1,k}+\frac{2\sigma_{i,j,k}}{s\varepsilon_{i,j,k}}\Big)\,E_z^q\,|_{i,j,k}\\
&-\bar{C}_x^E\,|_{i,j,k}\,\bar{C}_x^H\,|_{i,j,k}\,E_z^q\,|_{i+1,j,k}+\bar{C}_x^E\,|_{i,j,k}\,\bar{C}_z^H\,|_{i,j,k}\,E_x^q\,|_{i,j,k+1}\\
&-\bar{C}_x^E\,|_{i,j,k}\,\bar{C}_z^H\,|_{i,j,k}\,E_x^q\,|_{i,j,k}-\bar{C}_x^E\,|_{i,j,k}\,\bar{C}_x^H\,|_{i-1,j,k}\,E_z^q\,|_{i-1,j,k}\\
&-\bar{C}_x^E\,|_{i,j,k}\,\bar{C}_z^H\,|_{i-1,j,k}\,E_x^q\,|_{i-1,j,k+1}+\bar{C}_x^E\,|_{i,j,k}\,\bar{C}_z^H\,|_{i-1,j,k}\,E_x^q\,|_{i-1,j,k}\\
&+\bar{C}_y^E\,|_{i,j,k}\,\bar{C}_z^H\,|_{i,j,k}\,E_y^q\,|_{i,j,k+1}-\bar{C}_y^E\,|_{i,j,k}\,\bar{C}_z^H\,|_{i,j,k}\,E_y^q\,|_{i,j,k}\\
&-\bar{C}_y^E\,|_{i,j,k}\,\bar{C}_y^H\,|_{i,j,k}\,E_z^q\,|_{i,j+1,k}-\bar{C}_y^E\,|_{i,j,k}\,\bar{C}_z^H\,|_{i,j-1,k}\,E_y^q\,|_{i,j-1,k+1}\\
&+\bar{C}_y^E\,|_{i,j,k}\,\bar{C}_z^H\,|_{i,j-1,k}\,E_y^q\,|_{i,j-1,k}-\bar{C}_y^E\,|_{i,j,k}\,\bar{C}_y^H\,|_{i,j-1,k}\,E_z^q\,|_{i,j-1,k}\\
=\;&-2\bar{C}_x^E\,|_{i,j,k}\left(\sum_{n=0,q>1}^{q-1}H_y^n\,|_{i,j,k}-\sum_{n=0,q>1}^{q-1}H_y^n\,|_{i-1,j,k}\right)\\
&+2\bar{C}_y^E\,|_{i,j,k}\left(\sum_{n=0,q>1}^{q-1}H_x^n\,|_{i,j,k}-\sum_{n=0,q>1}^{q-1}H_x^n\,|_{i,j-1,k}\right)\\
&-\frac{2}{s\varepsilon_{i,j,k}}J_z^q\,|_{i,j,k}-2\sum_{n=0,q>1}^{q-1}E_z^n\,|_{i,j,k}
\end{aligned}
\tag{186}
$$

## *A.2 Formulations Based Upon the One Second-Order Equations*

Again, considering an isotropic, non-dispersive, lossy media, in Cartesian coordinates, the one second-order wave vector equation can be expressed as

$$
\nabla\times\nabla\times\mathbf{E}+\mu\varepsilon\frac{\partial^2\mathbf{E}}{\partial t^2}+\mu\sigma\frac{\partial\mathbf{E}}{\partial t}=-\mu\frac{\partial\mathbf{J}}{\partial t}. \tag{187}
$$

Rewriting (187) into 3-D form, we have

$$\frac{\partial^2 E_y}{\partial x \partial y} - \frac{\partial^2 E_x}{\partial y^2} - \frac{\partial^2 E_x}{\partial z^2} + \frac{\partial^2 E_z}{\partial x \partial z} + \mu\varepsilon \frac{\partial^2 E_x}{\partial t^2} + \mu\sigma \frac{\partial E_x}{\partial t} = -\mu \frac{\partial J_x}{\partial t} \tag{188}$$

$$\frac{\partial^2 E_z}{\partial y \partial z} - \frac{\partial^2 E_y}{\partial z^2} - \frac{\partial^2 E_y}{\partial x^2} + \frac{\partial^2 E_x}{\partial x \partial y} + \mu\varepsilon \frac{\partial^2 E_y}{\partial t^2} + \mu\sigma \frac{\partial E_y}{\partial t} = -\mu \frac{\partial J_y}{\partial t} \tag{189}$$

$$\frac{\partial^2 E_x}{\partial x \partial z} - \frac{\partial^2 E_z}{\partial x^2} - \frac{\partial^2 E_z}{\partial y^2} + \frac{\partial^2 E_y}{\partial y \partial z} + \mu\varepsilon \frac{\partial^2 E_z}{\partial t^2} + \mu\sigma \frac{\partial E_z}{\partial t} = -\mu \frac{\partial J_z}{\partial t}. \tag{190}$$

For any given time-domain waveform $W$, the second derivative with respect to time $t$ is

$$\begin{aligned} \frac{\partial^2 W}{\partial t^2} &= s^2 \sum_{p=0}^{\infty} \left[ \frac{1}{4} W^p + \sum_{n=0,p>1}^{p-1} (p-n)\, W^n \right] \varphi^p(\bar{t}) \\ &= s^2 \sum_{p=0}^{\infty} \left( \frac{1}{4} W^p + \sum_{n=0,p>1}^{p-1} \sum_{n=0}^{n} W^m \right) \varphi^p(\bar{t}). \end{aligned} \tag{191}$$

First, consider the equations related to the electric field in $x$-direction. Discretizing (189) in the Yee's cells in the Laguerre domain, the coefficient equation associated with electric component $E_x\,|_{i,j,k}$ becomes

$$
\begin{aligned}
&\Big(1+\bar{C}_y^E\,|_{i,j,k}\,\bar{C}_y^H\,|_{i,j,k}+\bar{C}_y^E\,|_{i,j,k}\,\bar{C}_y^H\,|_{i,j-1,k}\\
&+\bar{C}_z^E\,|_{i,j,k}\,\bar{C}_z^H\,|_{i,j,k}+\bar{C}_z^E\,|_{i,j,k}\,\bar{C}_z^H\,|_{i,j,k-1}+\frac{2\sigma_{i,j,k}}{s\varepsilon_{i,j,k}}\Big)\,E_x^q\,|_{i,j,k}\\
&-\bar{C}_y^E\,|_{i,j,k}\,\bar{C}_y^H\,|_{i,j,k}\,E_x^q\,|_{i,j+1,k}+\bar{C}_y^E\,|_{i,j,k}\,\bar{C}_x^H\,|_{i,j,k}\,E_y^q\,|_{i+1,j,k}\\
&-\bar{C}_y^E\,|_{i,j,k}\,\bar{C}_x^H\,|_{i,j,k}\,E_y^q\,|_{i,j,k}-\bar{C}_y^E\,|_{i,j,k}\,\bar{C}_y^H\,|_{i,j-1,k}\,E_x^q\,|_{i,j-1,k}\\
&-\bar{C}_y^E\,|_{i,j,k}\,\bar{C}_x^H\,|_{i,j-1,k}\,E_y^q\,|_{i+1,j-1,k}+\bar{C}_y^E\,|_{i,j,k}\,\bar{C}_x^H\,|_{i,j-1,k}\,E_y^q\,|_{i,j-1,k}\\
&+\bar{C}_z^E\,|_{i,j,k}\,\bar{C}_x^H\,|_{i,j,k}\,E_z^q\,|_{i+1,j,k}-\bar{C}_z^E\,|_{i,j,k}\,\bar{C}_x^H\,|_{i,j,k}\,E_z^q\,|_{i,j,k}\\
&-\bar{C}_z^E\,|_{i,j,k}\,\bar{C}_z^H\,|_{i,j,k}\,E_x^q\,|_{i,j,k+1}-\bar{C}_z^E\,|_{i,j,k}\,\bar{C}_x^H\,|_{i,j,k-1}\,E_z^q\,|_{i+1,j,k-1}\\
&+\bar{C}_z^E\,|_{i,j,k}\,\bar{C}_x^H\,|_{i,j,k-1}\,E_z^q\,|_{i,j,k-1}-\bar{C}_z^E\,|_{i,j,k}\,\bar{C}_z^H\,|_{i,j,k-1}\,E_x^q\,|_{i,j,k-1}\\
=\;&-\frac{4}{\mu_{i,j,k}\varepsilon_{i,j,k}s^2}\sum_{n=0,q>1}^{q-1}E_x^n\,|_{i,j,k}-4\sum_{n=0,q>1}^{q-1}\sum_{m=0}^{n}E_x^m\,|_{i,j,k}\\
&-\frac{2}{s\varepsilon_{i,j,k}}\left(J_x^q\,|_{i,j,k}+2\sum_{n=0,q>1}^{q-1}J_x^n\,|_{i,j,k}\right).
\end{aligned}
\tag{192}
$$

Similarly, consider the equations related to the electric field in $y$- and $z$-direction, the coefficient equation associated with electric component $E_y\,|_{i,j,k}$ and $E_z\,|_{i,j,k}$ becomes

$$
\begin{aligned}
&\big(1+\bar{C}_z^E\,|_{i,j,k}\,\bar{C}_z^H\,|_{i,j,k}+\bar{C}_z^E\,|_{i,j,k}\,\bar{C}_z^H\,|_{i,j,k-1}\\
&+\bar{C}_x^E\,|_{i,j,k}\,\bar{C}_x^H\,|_{i,j,k}+\bar{C}_x^E\,|_{i,j,k}\,\bar{C}_x^H\,|_{i-1,j,k}+\frac{2\sigma_{i,j,k}}{s\varepsilon_{i,j,k}}\Big)\,E_y^q\,|_{i,j,k}\\
&-\bar{C}_z^E\,|_{i,j,k}\,\bar{C}_z^H\,|_{i,j,k}\,E_y^q\,|_{i,j,k+1}+\bar{C}_z^E\,|_{i,j,k}\,\bar{C}_y^H\,|_{i,j,k}\,E_z^q\,|_{i,j+1,k}\\
&-\bar{C}_z^E\,|_{i,j,k}\,\bar{C}_y^H\,|_{i,j,k}\,E_z^q\,|_{i,j,k}-\bar{C}_z^E\,|_{i,j,k}\,\bar{C}_z^H\,|_{i,j,k-1}\,E_y^q\,|_{i,j,k-1}\\
&-\bar{C}_z^E\,|_{i,j,k}\,\bar{C}_y^H\,|_{i,j,k-1}\,E_z^q\,|_{i,j+1,k-1}+\bar{C}_z^E\,|_{i,j,k}\,\bar{C}_y^H\,|_{i,j,k-1}\,E_z^q\,|_{i,j,k-1}\\
&+\bar{C}_x^E\,|_{i,j,k}\,\bar{C}_y^H\,|_{i,j,k}\,E_x^q\,|_{i,j+1,k}-\bar{C}_x^E\,|_{i,j,k}\,\bar{C}_y^H\,|_{i,j,k}\,E_x^q\,|_{i,j,k}\\
&-\bar{C}_x^E\,|_{i,j,k}\,\bar{C}_x^H\,|_{i,j,k}\,E_y^q\,|_{i+1,j,k}-\bar{C}_x^E\,|_{i,j,k}\,\bar{C}_y^H\,|_{i-1,j,k}\,E_x^q\,|_{i-1,j+1,k}\\
&+\bar{C}_x^E\,|_{i,j,k}\,\bar{C}_y^H\,|_{i-1,j,k}\,E_x^q\,|_{i-1,j,k}-\bar{C}_x^E\,|_{i,j,k}\,\bar{C}_x^H\,|_{i-1,j,k}\,E_y^q\,|_{i-1,j,k}\\
=\;&-\frac{4}{\mu_{i,j,k}\varepsilon_{i,j,k}s^2}\sum_{n=0,q>1}^{q-1}E_y^n\,|_{i,j,k}-4\sum_{n=0,q>1}^{q-1}\sum_{m=0}^{n}E_y^m\,|_{i,j,k}\\
&-\frac{2}{s\varepsilon_{i,j,k}}\left(J_y^q\,|_{i,j,k}+2\sum_{n=0,q>1}^{q-1}J_y^n\,|_{i,j,k}\right).
\end{aligned}
\tag{193}
$$

and

$$
\begin{aligned}
&\Big(1+\bar{C}_x^E\,|_{i,j,k}\,\bar{C}_x^H\,|_{i,j,k}+\bar{C}_x^E\,|_{i,j,k}\,\bar{C}_x^H\,|_{i-1,j,k}\\
&+\bar{C}_y^E\,|_{i,j,k}\,\bar{C}_y^H\,|_{i,j,k}+\bar{C}_y^E\,|_{i,j,k}\,\bar{C}_y^H\,|_{i,j-1,k}+\frac{2\sigma_{i,j,k}}{s\varepsilon_{i,j,k}}\Big)\,E_z^q\,|_{i,j,k}\\
&-\bar{C}_x^E\,|_{i,j,k}\,\bar{C}_x^H\,|_{i,j,k}\,E_z^q\,|_{i+1,j,k}+\bar{C}_x^E\,|_{i,j,k}\,\bar{C}_z^H\,|_{i,j,k}\,E_x^q\,|_{i,j,k+1}\\
&-\bar{C}_x^E\,|_{i,j,k}\,\bar{C}_z^H\,|_{i,j,k}\,E_x^q\,|_{i,j,k}-\bar{C}_x^E\,|_{i,j,k}\,\bar{C}_x^H\,|_{i-1,j,k}\,E_z^q\,|_{i-1,j,k}\\
&-\bar{C}_x^E\,|_{i,j,k}\,\bar{C}_z^H\,|_{i-1,j,k}\,E_x^q\,|_{i-1,j,k+1}+\bar{C}_x^E\,|_{i,j,k}\,\bar{C}_z^H\,|_{i-1,j,k}\,E_x^q\,|_{i-1,j,k}\\
&+\bar{C}_y^E\,|_{i,j,k}\,\bar{C}_z^H\,|_{i,j,k}\,E_y^q\,|_{i,j,k+1}-\bar{C}_y^E\,|_{i,j,k}\,\bar{C}_z^H\,|_{i,j,k}\,E_y^q\,|_{i,j,k}\\
&-\bar{C}_y^E\,|_{i,j,k}\,\bar{C}_y^H\,|_{i,j,k}\,E_z^q\,|_{i,j+1,k}-\bar{C}_y^E\,|_{i,j,k}\,\bar{C}_z^H\,|_{i,j-1,k}\,E_y^q\,|_{i,j-1,k+1}\\
&+\bar{C}_y^E\,|_{i,j,k}\,\bar{C}_z^H\,|_{i,j-1,k}\,E_y^q\,|_{i,j-1,k}-\bar{C}_y^E\,|_{i,j,k}\,\bar{C}_y^H\,|_{i,j-1,k}\,E_z^q\,|_{i,j-1,k}\\
=\;&-\frac{4}{\mu_{i,j,k}\varepsilon_{i,j,k}s^2}\sum_{n=0,q>1}^{q-1}E_z^n\,|_{i,j,k}-4\sum_{n=0,q>1}^{q-1}\sum_{m=0}^{n}E_z^m\,|_{i,j,k}\\
&-\frac{2}{s\varepsilon_{i,j,k}}\left(J_z^q\,|_{i,j,k}+2\sum_{n=0,q>1}^{q-1}J_z^n\,|_{i,j,k}\right).
\end{aligned}
\tag{194}
$$

## *A.3 Absorbing Boundary Conditions*

First, considering the first-order absorbing boundary condition (ABC) is used to truncate the simulation space. For electric field in $x$-direction, the ABC at boundary face $z=0$ in time domain is given by

$$
\left(\frac{\partial}{\partial z}-\frac{1}{v_0}\frac{\partial}{\partial t}\right)E_x=0 \tag{195}
$$

where $v_0$ is the velocity of light in vacuum. Discretizing (195) in Laguerre domain yields

$$\begin{aligned}
&\left(\frac{1}{\Delta z_1}+\frac{s}{4v_0}\right)E_x^q\,|_{i,j,1}+\left(-\frac{1}{\Delta y_1}+\frac{s}{4v_0}\right)E_x^q\,|_{i,j,2}\\
=&-\frac{s}{2v_0}\sum_{n=0,q>0}^{q-1}(E_x^n\,|_{i,j,2}+E_x^n\,|_{i,j,1}).
\end{aligned}\tag{196}$$

At the edge boundaries, for instance $y = 0$ and $z = 0$, coordinate rotation is performed to discretize (195) to ensure computational stability and accuracy which results in

$$\begin{aligned}
&\left(\frac{1}{\sqrt{(\Delta y_1)^2+(\Delta z_1)^2}}+\frac{s}{4v_0}\right)E_x^q\,|_{i,1,1}\\
&+\left(-\frac{1}{\sqrt{(\Delta y_1)^2+(\Delta z_1)^2}}+\frac{s}{4v_0}\right)E_x^q\,|_{i,2,2}\\
=&-\frac{s}{2v_0}\sum_{n=0,q>0}^{q-1}(E_x^n\,|_{i,2,2}+E_x^n\,|_{i,1,1})
\end{aligned}\tag{197}$$

The first-order ABC at other arbitrary boundary faces and edges can be derived in a similar manner.

Considering the second-order absorbing boundary condition (ABC) is used to truncate the simulation space. For electric field in $x$-direction, the ABC at boundary face $z = 0$ in time domain is given by

$$\left[\frac{1}{v_0}\frac{\partial^2}{\partial z\partial t}-\frac{1}{v_0^2}\frac{\partial^2}{\partial t^2}+\frac{1}{2}\left(\frac{\partial^2}{\partial x^2}+\frac{\partial^2}{\partial y^2}\right)\right]E_x=0.\tag{198}$$

Discretizing (198) in Laguerre domain yields

$$
\begin{aligned}
&\left(\frac{-s}{2v_0\Delta z_1}-\frac{s^2}{4v_0^2}-\frac{1}{2\Delta x_{i-1}\Delta x_i}-\frac{1}{2\Delta y_{j-1}\Delta y_j}\right)E_x^q\,|_{i,j,1}\\
&+\left(\frac{s}{2v_0\Delta z_1}-\frac{s^2}{4v_0^2}-\frac{1}{2\Delta x_{i-1}\Delta x_i}-\frac{1}{2\Delta y_{j-1}\Delta y_j}\right)E_x^q\,|_{i,j,2}\\
&+\frac{E_x^q\,|_{i-1,j,1}+E_x^q\,|_{i-1,j,2}}{2\Delta x_{i-1}\left(\Delta x_{i-1}+\Delta x_i\right)}+\frac{E_x^q\,|_{i+1,j,1}+E_x^q\,|_{i+1,j,2}}{2\Delta x_i\left(\Delta x_{i-1}+\Delta x_i\right)}\\
&+\frac{E_x^q\,|_{i,j-1,1}+E_x^q\,|_{i,j-1,2}}{2\Delta y_{j-1}\left(\Delta y_{j-1}+\Delta y_j\right)}+\frac{E_x^q\,|_{i,j+1,1}+E_x^q\,|_{i,j+1,2}}{2\Delta y_j\left(\Delta y_{j-1}+\Delta y_j\right)}\\
=&\frac{-s}{v_0\Delta z_1}\sum_{n=0,q>1}^{q-1}\left(E_x^n\,|_{i,j,2}-E_x^n\,|_{i,j,1}\right)\\
&+\frac{s^2}{2v_0}\sum_{n=0,q>1}^{q-1}\sum_{m=0}^{n}\left(E_y^m\,|_{i,j,1}+E_y^m\,|_{i,j,2}\right)
\end{aligned}
\tag{199}
$$

The second-order ABC at other arbitrary boundary faces and edges can be derived in a similar manner.

# APPENDIX B

# FORMULATIONS FOR SKIN-EFFECT MODELING

After implementing the rational fitting, the time-domain expression for surface admittance can be written as

$$Y(t) = \sum_{p=1}^{m} C_p e^{-A_p t} \tag{200}$$

By definition, the corresponding Laguerre coefficient for the time-domain admittance term is

$$Y^q = \int_0^\infty Y(t)\varphi(\bar{t})dt. \tag{201}$$

Denoting

$$Y^q = \sum_{p=1}^{m} C_p G_p^q = \sum_{p=1}^{m} C_p \int_0^\infty e^{-A_p t}\varphi_q(\bar{t})dt \tag{202}$$

and performing integral by part results in

$$\begin{aligned} G_p^q = & -\frac{1}{A_p}\varphi_q(\bar{t})e^{-A_p t}\,|_0^\infty \\ & -\int_0^\infty \frac{s}{2A_p}\left[\varphi_q(\bar{t}) + 2\sum_{n=0,q>0}^{n-1}\varphi_n(\bar{t})\right]e^{-A_p t}dt. \end{aligned} \tag{203}$$

By inspection, we have

$$
\begin{aligned}
G_p^q &= \frac{1}{A_p} - \frac{s}{2A_p} G_p^q - \frac{s}{A_p} \sum_{n=0,q>0}^{q-1} G_p^n \\
&= \frac{2}{2A_p + s} \left( \frac{2A_p - s}{2A_p + s} \right)^q
\end{aligned}
\tag{204}
$$

Therefore, the final Laguerre basis coefficient expression can be written as

$$
Y^q = \sum_{p=1}^{m} C_p \frac{2}{2A_p + s} \left( \frac{2A_p - s}{2A_p + s} \right)^q \tag{205}
$$

# APPENDIX C

# FORMULATIONS FOR THE NON-CONFORMAL DOMAIN DECOMPOSITION METHOD

## *C.1 Derivation of Equivalency Between the TD-FEM and the Laguerre-FDTD Method*

Assuming the computational domain is descretized using hexahedral unit cell as shown in Figure 98, vector basis functions associated with the unit cell can be constructed as

$$\mathbf{E} = \sum_{i=1}^{n} \mathbf{N}_i E_i \tag{206}$$

where $n$ is the total edge number, $E_i$ is the unknown expansion coefficient, $\mathbf{N}_i$ is the vector basis function. In the hexahedral element, the total edge number is 12. The field component in the element can be written as

$$E_x = \sum_{i=1}^{4} N_{xi} E_{xi} \tag{207}$$

$$E_y = \sum_{i=1}^{4} N_{yi} E_{yi} \tag{208}$$

$$E_z = \sum_{i=1}^{4} N_{zi} E_{zi} \tag{209}$$

where

$$N_{x1} = \frac{1}{\Delta y \Delta z}\left(y_c + \frac{\Delta y}{2} - y\right)\left(z_c + \frac{\Delta z}{2} - z\right) \tag{210}$$

$$N_{x2} = \frac{1}{\Delta y \Delta z}\left(-y_c + \frac{\Delta y}{2} + y\right)\left(z_c + \frac{\Delta z}{2} - z\right) \tag{211}$$

$$N_{x3} = \frac{1}{\Delta y \Delta z}\left(y_c + \frac{\Delta y}{2} - y\right)\left(-z_c + \frac{\Delta z}{2} + z\right) \tag{212}$$

$$N_{x4} = \frac{1}{\Delta y \Delta z}\left(-y_c + \frac{\Delta y}{2} + y\right)\left(-z_c + \frac{\Delta z}{2} + z\right) \tag{213}$$

$$N_{y1} = \frac{1}{\Delta z \Delta x}\left(z_c + \frac{\Delta z}{2} - z\right)\left(x_c + \frac{\Delta x}{2} - x\right) \tag{214}$$

$$N_{y2} = \frac{1}{\Delta z \Delta x}\left(-z_c + \frac{\Delta z}{2} + z\right)\left(x_c + \frac{\Delta x}{2} - x\right) \tag{215}$$

$$N_{y3} = \frac{1}{\Delta z \Delta x}\left(z_c + \frac{\Delta z}{2} - z\right)\left(-x_c + \frac{\Delta x}{2} + x\right) \tag{216}$$

$$N_{y4} = \frac{1}{\Delta z \Delta x}\left(-z_c + \frac{\Delta z}{2} + z\right)\left(-x_c + \frac{\Delta x}{2} + x\right) \tag{217}$$

$$N_{z1} = \frac{1}{\Delta x \Delta y}\left(x_c + \frac{\Delta x}{2} - x\right)\left(y_c + \frac{\Delta y}{2} - y\right) \tag{218}$$

$$N_{z2} = \frac{1}{\Delta x \Delta y}\left(-x_c + \frac{\Delta x}{2} + x\right)\left(y_c + \frac{\Delta y}{2} - y\right) \tag{219}$$

$$N_{z3} = \frac{1}{\Delta x \Delta y}\left(x_c + \frac{\Delta x}{2} - x\right)\left(-y_c + \frac{\Delta y}{2} + y\right) \tag{220}$$

$$N_{z4} = \frac{1}{\Delta x \Delta y}\left(-x_c + \frac{\Delta x}{2} + x\right)\left(-y_c + \frac{\Delta y}{2} + y\right) \tag{221}$$

in which $\Delta_x$, $\Delta_y$ and $\Delta_z$ are the length of the edge in $x$-, $y$- and $z$-direction, $x_c$, $y_c$ and $z_c$ are the coordinates of the central point inside the element.

Assuming an isotropic, non-dispersive, lossy media, the vector wave equation in time domain can be expressed as

$$\nabla \times \nabla \times \mathbf{E} + \mu\varepsilon\frac{\partial^2 \mathbf{E}}{\partial t^2} + \mu\sigma\frac{\partial \mathbf{E}}{\partial t} = -\mu\frac{\partial \mathbf{J}}{\partial t}. \tag{222}$$

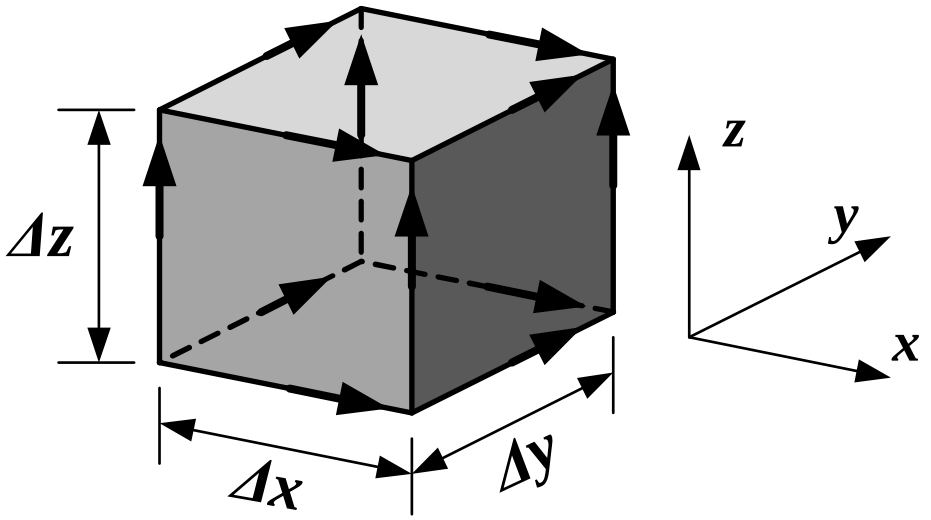


**Figure 98:** 3-D hexahedral unit cell.

Multiply (222) by an appropriate testing function $\mathbf{N}$, and integrate over volume results in

$$\int_{\Omega} \left[ (\nabla \times \mathbf{N}) \cdot (\nabla \times \mathbf{E}) + \mu\varepsilon \mathbf{N} \cdot \frac{\partial^2 \mathbf{E}}{\partial t^2} + \mu\sigma \mathbf{N} \cdot \frac{\partial \mathbf{E}}{\partial t} \right] dV = -\int_{\Omega} \mu \mathbf{N} \cdot \frac{\partial \mathbf{J}}{\partial t} dV. \quad (223)$$

Expanding the electric field using the aforementioned vector basis function by inserting (206) into (223), we have

$$\mathbf{T}\frac{\partial^2 \mathbf{E}}{\partial t^2} + \mathbf{R}\frac{\partial \mathbf{E}}{\partial t} + \mathbf{S}\mathbf{E} = \mathbf{f} \quad (224)$$

where

$$T_{ij} = \int_{\Omega} \mu\varepsilon \mathbf{N}_i \cdot \mathbf{N}_j dV \tag{225}$$

$$R_{ij} = \int_{\Omega} \mu\sigma \mathbf{N}_i \cdot \mathbf{N}_j dV \tag{226}$$

$$S_{ij} = \int_{\Omega} (\nabla \times \mathbf{N}_i) \cdot (\nabla \times \mathbf{N}_j) \, dV \tag{227}$$

$$f_i = -\int_{\Omega} \mu \mathbf{N}_i \cdot \frac{\partial \mathbf{J}}{\partial t} dV. \tag{228}$$

Using the trapezoidal integration, (225) to (227) can be rewritten into

$$\mathbf{T} = \mu\varepsilon \frac{\Delta x_i \Delta y_j \Delta z_k}{4} \begin{bmatrix} \mathbf{I} & & \\ & \mathbf{I} & \\ & & \mathbf{I} \end{bmatrix} \tag{229}$$

$$\mathbf{R} = \mu\sigma \frac{\Delta x_i \Delta y_j \Delta z_k}{4} \begin{bmatrix} \mathbf{I} & & \\ & \mathbf{I} & \\ & & \mathbf{I} \end{bmatrix} \tag{230}$$

$$\mathbf{S} = \begin{bmatrix} \mathbf{S}_{xx} & \mathbf{S}_{xy} & \mathbf{S}_{xz} \\ \mathbf{S}_{yx} & \mathbf{S}_{yy} & \mathbf{S}_{yz} \\ \mathbf{S}_{zx} & \mathbf{S}_{zy} & \mathbf{S}_{zz} \end{bmatrix} \tag{231}$$

in which $\mathbf{S}_{\xi\xi} = \frac{\Delta\xi}{2}\left[\frac{\Delta\eta}{\Delta\zeta}\mathbf{K}_1 + \frac{\Delta\zeta}{\Delta\eta}\mathbf{K}_2\right]$, $\mathbf{S}_{\xi\eta} = -\frac{\Delta\zeta}{2}\mathbf{K}_3$, and

$$\mathbf{K}_1 = \begin{bmatrix} 1 & 0 & -1 & 0 \\ 0 & 1 & 0 & -1 \\ -1 & 0 & 1 & 0 \\ 0 & -1 & 0 & 1 \end{bmatrix} \tag{232}$$

$$\mathbf{K}_2 = \begin{bmatrix} 1 & -1 & 0 & 0 \\ -1 & 1 & 0 & 0 \\ 0 & 0 & 1 & -1 \\ 0 & 0 & -1 & 1 \end{bmatrix} \tag{233}$$

$$\mathbf{K}_3 = \begin{bmatrix} 1 & 0 & -1 & 0 \\ -1 & 0 & 1 & 0 \\ 0 & 1 & 0 & 1 \\ 0 & -1 & 0 & -1 \end{bmatrix} \tag{234}$$

Applying the temporal testing procedure in Laguerre domain, (224) becomes

$$\mathbf{T}s^2 \left( \frac{1}{4}\mathbf{E}^q + \sum_{n=0,q>1}^{q-1} \sum_{j=0}^{m} \mathbf{E}^m \right) + \mathbf{R}s \left( \frac{1}{2}\mathbf{E}^q + \sum_{n=0,q>1}^{q-1} \mathbf{E}^n \right) + \mathbf{S}\mathbf{E}^q = \mathbf{f}^q \tag{235}$$

where

$$f_i^q = -\int_\Omega \mu s \mathbf{N}_i \cdot \left( \frac{1}{2}\mathbf{J}^q + \sum_{n=0,q>1}^{q-1} \mathbf{J}^n \right) dV. \tag{236}$$

To derive the coefficient equation associated with the electric field component $E_x\,|_{i,j,k}$, (235) needs to be discretized within four adjacent elements, namely element cell $(i,j,k)$, $(i,j-1,k)$, $(i,j,k-1)$, and $(i,j-1,k-1)$. By adding the equations associated with electric field component $E_x\,|_{i,j,k}$ in the four cells, the coefficient equation can be derived as

$$
\begin{aligned}
&\Big(1+\bar{C}_y^E\,|_{i,j,k}\,\bar{C}_y^H\,|_{i,j,k}+\bar{C}_y^E\,|_{i,j,k}\,\bar{C}_y^H\,|_{i,j-1,k}\\
&+\bar{C}_z^E\,|_{i,j,k}\,\bar{C}_z^H\,|_{i,j,k}+\bar{C}_z^E\,|_{i,j,k}\,\bar{C}_z^H\,|_{i,j,k-1}+\frac{2\sigma_{i,j,k}}{s\varepsilon_{i,j,k}}\Big)\,E_x^q\,|_{i,j,k}\\
&-\bar{C}_y^E\,|_{i,j,k}\,\bar{C}_y^H\,|_{i,j,k}\,E_x^q\,|_{i,j+1,k}+\bar{C}_y^E\,|_{i,j,k}\,\bar{C}_x^H\,|_{i,j,k}\,E_y^q\,|_{i+1,j,k}\\
&-\bar{C}_y^E\,|_{i,j,k}\,\bar{C}_x^H\,|_{i,j,k}\,E_y^q\,|_{i,j,k}-\bar{C}_y^E\,|_{i,j,k}\,\bar{C}_y^H\,|_{i,j-1,k}\,E_x^q\,|_{i,j-1,k}\\
&-\bar{C}_y^E\,|_{i,j,k}\,\bar{C}_x^H\,|_{i,j-1,k}\,E_y^q\,|_{i+1,j-1,k}+\bar{C}_y^E\,|_{i,j,k}\,\bar{C}_x^H\,|_{i,j-1,k}\,E_y^q\,|_{i,j-1,k}\\
&+\bar{C}_z^E\,|_{i,j,k}\,\bar{C}_x^H\,|_{i,j,k}\,E_z^q\,|_{i+1,j,k}-\bar{C}_z^E\,|_{i,j,k}\,\bar{C}_x^H\,|_{i,j,k}\,E_z^q\,|_{i,j,k}\\
&-\bar{C}_z^E\,|_{i,j,k}\,\bar{C}_z^H\,|_{i,j,k}\,E_x^q\,|_{i,j,k+1}-\bar{C}_z^E\,|_{i,j,k}\,\bar{C}_x^H\,|_{i,j,k-1}\,E_z^q\,|_{i+1,j,k-1}\\
&+\bar{C}_z^E\,|_{i,j,k}\,\bar{C}_x^H\,|_{i,j,k-1}\,E_z^q\,|_{i,j,k-1}-\bar{C}_z^E\,|_{i,j,k}\,\bar{C}_z^H\,|_{i,j,k-1}\,E_x^q\,|_{i,j,k-1}\\
=\;&-\frac{4}{\mu_{i,j,k}\varepsilon_{i,j,k}s^2}\sum_{n=0,q>1}^{q-1}E_x^n\,|_{i,j,k}-4\sum_{n=0,q>1}^{q-1}\sum_{m=0}^{n}E_x^m\,|_{i,j,k}\\
&-\frac{2}{s\varepsilon_{i,j,k}}\left(J_x^q\,|_{i,j,k}+2\sum_{n=0,q>1}^{q-1}J_x^n\,|_{i,j,k}\right).
\end{aligned}
\tag{237}
$$

# REFERENCES


[1] S. Hall, S. Pytel, P. Huray, D. Hua, A. Moonshiram, G. Brist, and E. Sijercic, "Multigigahertz causal transmission line modeling methodology using a 3-D hemispherical surface roughness approach," *IEEE Trans. Microw. Theory Tech.*, vol. 55, no. 12, pp. 2614–2624, May 2007.

[2] D. Sheen, S. Ali, M. Abouzahra, and J.-A. Kong, "Application of the three-dimensional finite-difference time-domain method to the analysis of planar microstrip circuits," *IEEE Trans. Microw. Theory Tech.*, vol. 38, no. 7, pp. 849–857, July 1990.

[3] K. Yee, "Numerical solution of initial boundary value problems involving Maxwell's equations in isotropic media," *IEEE Trans. Antennas Propag.*, vol. 14, no. 3, pp. 302–307, May 1966.

[4] R. Holland, "Implicit three-dimensional finite differencing of Maxwell's equations," *IEEE Trans. Nucl. Sci.*, vol. 31, no. 6, pp. 1322–1326, Dec. 1984.

[5] T. Namiki, "A new FDTD algorithm based on alternating-direction implicit method," *IEEE Trans. Microw. Theory Tech.*, vol. 47, no. 10, pp. 2003–2007, Oct. 1999.

[6] F. Zhen, Z. Chen, and J. Zhang, "Toward the development of a three-dimensional unconditionally stable finite-difference time-domain method," *IEEE Trans. Microw. Theory Tech.*, vol. 48, no. 9, pp. 1550–1558, Sept. 2000.

[7] T. Namiki and K. Ito, "Numerical simulation of microstrip resonators and filters using the ADI-FDTD method," *IEEE Trans. Microw. Theory Tech.*, vol. 49, no. 4, pp. 665–670, Apr. 2001.

[8] Y. Chung, T. Sarkar, B. H. Jung, and M. Salazar-Palma, "An unconditionally stable scheme for the finite-difference time-domain method," *IEEE Trans. Microw. Theory Tech.*, vol. 51, no. 3, pp. 697–704, Mar. 2003.

[9] G. Sun and C. Trueman, "Approximate Crank-Nicolson schemes for the 2-D finite-difference time-domain method for TEz waves," *IEEE Trans. Antennas Propag.*, vol. 52, no. 11, pp. 2963–2972, Nov. 2004.

[10] A. Fijany, M. Jensen, Y. Rahmat-Samii, and J. Barhen, "A massively parallel computation strategy for FDTD: time and space parallelism applied to electromagnetics problems," *IEEE Trans. Antennas Propag.*, vol. 43, no. 12, pp. 1441–1449, Dec. 1995.

[11] I. Ahmed, E.-K. Chua, E.-P. Li, and Z. Chen, "Development of the three-dimensional unconditionally stable LOD-FDTD method," *IEEE Trans. Antennas Propag.*, vol. 56, no. 11, pp. 3596–3600, Nov. 2008.

[12] K. Srinivasan, "Multiscale EM and circuit simulation using the Laguerre-FDTD scheme for package-aware integrated-circuit design," *Ph.D. Dissertation*, 2008.

[13] H. Myunghyun, "EM simulation using the Laguerre-FDTD scheme for multiscale 3-D interconnections," *Ph.D. Dissertation*, 2011.

[14] M. Ha, K. Srinivasan, and M. Swaminathan, "Transient chip-package cosimulation of multiscale structures using the Laguerre-FDTD scheme," *IEEE Trans. Adv. Packag.*, vol. 32, no. 4, pp. 816–830, Nov. 2009.

[15] Y.-T. Duan, B. Chen, D.-G. Fang, and B.-H. Zhou, "Efficient implementation for 3-D Laguerre-based finite-difference time-domain method," *IEEE Trans. Microw. Theory Tech.*, vol. 59, no. 1, pp. 56–64, Jan. 2011.

[16] L.-T. Hwang and I. Turlik, "A review of the skin effect as applied to thin film interconnections," *IEEE Trans. Compon., Hybrids, Manuf. Technol.*, vol. 15, no. 1, pp. 43–55, Feb. 1992.

[17] P. Waldow and I. Wolff, "The skin-effect at high frequencies," *IEEE Trans. Microw. Theory Tech.*, vol. 33, no. 10, pp. 1076–1082, Oct. 1985.

[18] R.-B. Wu and J.-C. Yang, "Boundary integral equation formulation of skin effect problems in multiconductor transmission lines," *IEEE Trans. Magn.*, vol. 25, no. 4, pp. 3013–3015, July 1989.

[19] R. Faraji-Dana and Y. Chow, "The current distribution and ac resistance of a microstrip structure," *IEEE Trans. Microw. Theory Tech.*, vol. 38, no. 9, pp. 1268–1277, Sept. 1990.

[20] A. Ruehli, "Inductance calculations in a complex integrated circuit environment," *IBM J. Res. Develop*, pp. 470–481, Sept. 1972.

[21] C. Gordon, T. Blazeck, and R. Mittra, "Time-domain simulation of multiconductor transmission lines with frequency-dependent losses," *IEEE Trans. Comput.-Aided Design Integr. Circuits Syst.*, vol. 11, no. 11, pp. 1372–1387, Nov. 1992.

[22] C.-S. Yen, Z. Fazarinc, and R. Wheeler, "Time-domain skin-effect model for transient analysis of lossy transmission lines," *Proc. IEEE*, vol. 70, no. 7, pp. 750–757, July 1982.

[23] S. Grivet-Talocia, H.-M. Huang, A. Ruehli, F. Canavero, and I. Elfadel, "Transient analysis of lossy transmission lines: an efficient approach based on the method of characteristics," *IEEE Trans. Adv. Packag.*, vol. 27, no. 1, pp. 45–56, Feb. 2004.

[24] A. Ruehli, G. Antonini, and L. J. Jiang, "Skin-effect loss models for time- and frequency-domain PEEC solver," *Proc. IEEE*, vol. 101, no. 2, pp. 451–472, Feb. 2013.

[25] D. De Zutter and L. Knockaert, "Skin effect modeling based on a differential surface admittance operator," *IEEE Trans. Microw. Theory Tech.*, vol. 53, no. 8, pp. 2526–2538, Aug. 2005.

[26] K. S. Oh, "Accurate transient simulation of transmission lines with the skin effect," *IEEE Trans. Comput.-Aided Design Integr. Circuits Syst.*, vol. 19, no. 3, pp. 389–396, Mar. 2000.

[27] M. A. Leontovich, *Investigation of Propagation of Radio Waves.* Moscow: Academy of Sciences of USSR, 1948.

[28] J. Maloney and G. Smith, "The use of surface impedance concepts in the finite-difference time-domain method," *IEEE Trans. Antennas Propag.*, vol. 40, no. 1, pp. 38–48, Jan. 1992.

[29] K. S. Oh and J. Schutt-Aine, "An efficient implementation of surface impedance boundary conditions for the finite-difference time-domain method," *IEEE Trans. Antennas Propag.*, vol. 43, no. 7, pp. 660–666, July 1995.

[30] S. Yuferev and N. Ida, "Time domain surface impedance boundary conditions of high order of approximation," *IEEE Trans. Magn.*, vol. 34, no. 5, pp. 2605–2608, Sept. 1998.

[31] N. Farahat, S. Yuferev, and N. Ida, "High order surface impedance boundary conditions for the fdtd method," *IEEE Trans. Magn.*, vol. 37, no. 5, pp. 3242–3245, Sept. 2001.

[32] R. Makinen and M. Kivikoski, "Incorporation of conductor loss in the unconditionally stable ADI-FDTD method," *IEEE Trans. Antennas Propag.*, vol. 56, no. 7, pp. 2023–2030, July 2008.

[33] B. Smith, P. Bjorstad, and W. Gropp, *Domain Decomposition Parallel Multilevel Methods for Elliptic Partial Differential Equations.* UK: Cambridge University Press, 1996.

[34] B. Despres, P. Joly, and J. E. Roberts, *A Domain Decomposition Method for the Harmonic Maxwell Equations in Iterative Methods in Linear Algebra.* Amsterdam: North Holland, 1992.

[35] P. Collino, G. Delbue, P. Joly, and A. Piacentini, "A new interface condition in the non-overlapping domain decomposition method for the Maxwell equations," *Comput. Methods Appl. Mech. Eng.*, vol. 148, no. 1C2, pp. 195 – 207, Aug. 1997.

[36] C. Farhat and F.-X. Roux, "A method of finite element tearing and interconnecting and its parallel solution algorithm," *International Journal for Numerical Methods in Engineering*, vol. 32, no. 6, pp. 1205–1227, Oct. 1991.

[37] Y. Li and J.-M. Jin, "A vector dual-primal finite element tearing and interconnecting method for solving 3-D large-scale electromagnetic problems," *IEEE Trans. Antennas Propag.*, vol. 54, no. 10, pp. 3000–3009, Oct. 2006.

[38] S.-C. Lee, M. N. Vouvakis, and J.-F. Lee, "A non-overlapping domain decomposition method with non-matching grids for modeling large finite antenna arrays," *J. Comput. Phys.*, vol. 203, no. 1, pp. 1 – 21, Feb. 2005.

[39] A. Das and D. Gope, "Adaptive mesh refinement for fast convergence of EFIE-Based 3-D extraction," *IEEE Trans. Compon. Packag. Manuf. Techn.*, vol. 5, no. 3, pp. 404–414, March 2015.

[40] C. Bernardi, Y. Maday, and A. Patera, *Nonlinear Partial Differential Equations and Their Applications*. Paris: Longman Publishing Group, 1994.

[41] F. Bouillault, A. Buffa, Y. Maday, and F. Rapetti, "The mortar edge element method in three dimensions: Application to magnetostatics," *SIAM Journal on Scientific Computing*, vol. 24, no. 4, pp. 1303–1327, Feb. 2003.

[42] F. Rapetti, "The mortar edge element method on non-matching grids for eddy current calculations in moving structures," *Inter. J. Numerical Modeling: Electronic Networks, Devices and Fields*, vol. 14, no. 6, Nov. 2001.

[43] T. Arbogast and I. Yotov, "A non-mortar mixed finite element method for elliptic problems on non-matching multiblock grids," *Comp. Meth. in Appl. Mech. and Eng.*, vol. 149, pp. 255–265, Jan. 1997.

[44] M. N. Vouvakis, Z. Cendes, and J. F. Lee, "A FEM domain decomposition method for photonic and electromagnetic band gap structures," *IEEE Trans. Antennas Propag.*, vol. 54, no. 2, pp. 721–733, Feb. 2006.

[45] Z. Peng and J. F. Lee, "Non-conformal domain decomposition method with mixed true second order transmission condition for solving large finite antenna arrays," *IEEE Trans. Antennas Propag.*, vol. 59, no. 5, pp. 1638–1651, May 2011.

[46] M.-F. Xue and J.-M. Jin, "Nonconformal FETI-DP methods for large-scale electromagnetic simulation," *IEEE Trans. Antennas Propag.*, vol. 60, no. 9, pp. 4291–4305, Sept. 2012.

[47] Z. Lou and J.-M. Jin, "A novel dual-field time-domain finite-element domain-decomposition method for computational electromagnetics," *IEEE Trans. Antennas Propag.*, vol. 54, no. 6, pp. 1850–1862, June 2006.

[48] Z. Ye and C.-F. Wang, "Discontinuous Galerkin implementation of domain decomposition time-domain finite-element method," in *Antennas and Propagation (APS/URSI), 2011 IEEE International Symposium on*, 2011, pp. 2338–2341.

[49] Y. Lu and C. Y. Shen, "A domain decomposition finite-difference method for parallel numerical implementation of time-dependent maxwell's equations," *IEEE Trans. Antennas Propag.*, vol. 45, no. 3, pp. 556–562, Mar. 1997.

[50] S. Morgan, "Effect of surface roughness on eddy current losses at microwave frequencies," *J. Applied Physics*, vol. 20, pp. 352–362, Oct. 1949.

[51] E. Hammerstad and O. Jensen, "Accurate models for microstrip computer-aided design," in *Microwave symposium Digest, 1980 IEEE MTT-S International*, May 1980, pp. 407–409.

[52] M. Lukic and D. Filipovic, "Modeling of 3-D surface roughness effects with application to u-coaxial lines," *IEEE Trans. Microw. Theory Tech.*, vol. 55, no. 3, pp. 518–525, Mar. 2007.

[53] X. Guo, D. Jackson, M. Koledintseva, S. Hinaga, J. Drewniak, and J. Chen, "An analysis of conductor surface roughness effects on signal propagation for stripline interconnects," *IEEE Trans. Electromagn. Compat.*, vol. 56, no. 3, pp. 707–714, Jun. 2014.

[54] P. Huray, S. Hall, S. Pytel, F. Oluwafemi, R. Mellitz, D. Hua, and P. Ye, "Fundamentals of a 3-D snowball model for surface roughness power losses," in *Signal Propagation on Interconnects, 2007. SPI 2007. IEEE Workshop on*, May 2007, pp. 121–124.

[55] X. Ma, J. Ochoa, and A. Cangellaris, "A method for modeling the impact of conductor surface roughness on waveguiding properties of interconnects," in *Electrical Performance of Electronic Packaging and Systems (EPEPS), 2013 IEEE 22nd Conference on*, Oct. 2013, pp. 11–14.

[56] A. Sain and K. Melde, "Broadband characterization of coplanar waveguide interconnects with rough conductor surfaces," *IEEE Trans. Compon. Packag. Manuf. Techn.*, vol. 3, no. 6, pp. 1038–1046, Jun. 2013.

[57] Q. Chen, H. W. Choi, and N. Wong, "Robust simulation methodology for surface-roughness loss in interconnect and package modelings," *IEEE Trans. Comput.-Aided Design Integr. Circuits Syst.*, vol. 28, no. 11, pp. 1654–1665, Nov. 2009.

[58] R. Ding, L. Tsang, and H. Braunisch, "Wave propagation in a randomly rough parallel-plate waveguide," *IEEE Trans. Microw. Theory Tech.*, vol. 57, no. 5, pp. 1216–1223, May 2009.

[59] R. Ding, L. Tsang, H. Braunisch, and W. Chang, "Wave propagation in parallel plate metallic waveguide with finite conductivity and three dimensional roughness," *IEEE Trans. Antennas Propag.*, vol. 60, no. 12, pp. 5867–5880, Dec. 2012.

[60] Y.-T. Duan, B. Chen, H.-L. Chen, and D.-G. Fang, "PML absorbing boundary condition for efficient 2-D WLP-FDTD method," *Antennas and Wireless Propagation Letters, IEEE*, vol. 10, pp. 846–849, 2011.

[61] R. Luebbers and H. S. Langdon, "A simple feed model that reduces time steps needed for FDTD antenna and microstrip calculations," *IEEE Trans. Antennas Propag.*, vol. 44, no. 7, pp. 1000–1005, July 1996.

[62] M. Piket-May, A. Taflove, and J. Baron, "FD-TD modeling of digital signal propagation in 3-D circuits with passive and active loads," *IEEE Trans. Microw. Theory Tech.*, vol. 42, no. 8, pp. 1514–1523, Aug. 1994.

[63] G. Kobidze, "Implementation of collocated surface impedance boundary conditions in FDTD," *IEEE Trans. Antennas Propag.*, vol. 58, no. 7, pp. 2394–2403, July 2010.

[64] M. Ha and M. Swaminathan, "A Laguerre-FDTD formulation for frequency-dependent dispersive materials," *IEEE Microw. Wireless Compon. Lett.*, vol. 21, no. 5, pp. 225–227, May 2011.

[65] T. Willke and S. Gearhart, "LIGA micromachined planar transmission lines and filters," *IEEE Trans. Microw. Theory Tech.*, vol. 45, no. 10, pp. 1681–1688, Oct. 1997.

[66] T. Becks and I. Wolff, "Analysis of 3-D metallization structures by a full-wave spectral-domain technique," *IEEE Trans. Microw. Theory Tech.*, vol. 40, no. 12, pp. 2219–2227, Dec. 1992.

[67] N. Venkatarayalu, R. Lee, Y.-B. Gan, and L.-W. Li, "A stable FDTD subgridding method based on finite element formulation with hanging variables," *IEEE Trans. Antennas Propag.*, vol. 55, no. 3, pp. 907–915, Mar. 2007.

[68] J. Xie and M. Swaminathan, "Electrical-thermal cosimulation with nonconformal domain decomposition method for multiscale 3-D integrated systems," *IEEE Trans. Compon. Packag. Manuf. Techn.*, vol. 4, no. 4, pp. 588–601, Apr. 2014.

[69] J. Jin, *The Finite Element Method in Electromagnetics*. New York, USA: John Wiley and Sons, 2002.

[70] M. Yi, M. Ha, Z. Qian, A. Aydiner, and M. Swaminathan, "Skin-effect-incorporated transient simulation using the Laguerre-FDTD scheme," *IEEE Trans. Microw. Theory Tech.*, vol. 61, no. 12, pp. 4029–4039, Dec 2013.

[71] S. Maeda, T. Kashiwa, and I. Fukai, "Full wave analysis of propagation characteristics of a through hole using the finite-difference time-domain method," *IEEE Trans. Microw. Theory Tech.*, vol. 39, no. 12, pp. 2154–2159, Dec 1991.

[72] K. Wu, D. Deslandes, and Y. Cassivi, "The substrate integrated circuits - a new concept for high-frequency electronics and optoelectronics," in *Telecommunications in Modern Satellite, Cable and Broadcasting Service, 2003. TELSIKS 2003. 6th International Conference on*, vol. 1, Oct 2003, pp. P–III–P–X vol.1.

[73] D. Deslandes and K. Wu, "Integrated microstrip and rectangular waveguide in planar form," *IEEE Microw. Wireless Compon. Lett.*, vol. 11, no. 2, pp. 68–70, Feb 2001.

[74] D. Stephens, P. Young, and I. D. Robertson, "Millimeter-wave substrate integrated waveguides and filters in photoimageable thick-film technology," *IEEE Trans. Microw. Theory Tech.*, vol. 53, no. 12, pp. 3832–3838, Dec 2005.

[75] K. Samanta, D. Stephens, and I. Robertson, "Design and performance of a 60-GHz multi-chip module receiver employing substrate integrated waveguides," *IET Microwaves, Antennas Propagation*, vol. 1, no. 5, pp. 961–967, Oct. 2007.

[76] X. Chen, "EM modeling of microstrip conductor losses including surface roughness effect," *IEEE Microw. Wireless Compon. Lett.*, vol. 17, no. 2, pp. 94–96, Feb 2007.

[77] Y. Cassivi, L. Perregrini, P. Arcioni, M. Bressan, K. Wu, and G. Conciauro, "Dispersion characteristics of substrate integrated rectangular waveguide," *IEEE Microw. Wireless Compon. Lett.*, vol. 12, no. 9, pp. 333–335, Sept 2002.

[78] K. S. Yang, S. Pinel, I. K. Kim, and J. Laskar, "Low-loss integrated-waveguide passive circuits using liquid-crystal polymer system-on-package (SOP) technology for millimeter-wave applications," *IEEE Trans. Microw. Theory Tech.*, vol. 54, no. 12, pp. 4572–4579, Dec 2006.

[79] J. H. Hinken, "Conducting spheres in rectangular waveguides," *IEEE Trans. Microw. Theory Tech.*, vol. 28, no. 7, pp. 711–714, Jul 1980.

[80] S. Hall, *Advance Signal Integrity for High-Speed Digital Designs*. Hoboken, New Jersey: John Wiley and Sons, 2009.

[81] J. Kim, W. Lee, Y. Shim, J. Shim, K. Kim, J. S. Pak, and J. Kim, "Chip-package hierarchical power distribution network modeling and analysis based on a segmentation method," *IEEE Trans. Adv. Packag.*, vol. 33, no. 3, pp. 647–659, Aug 2010.

[82] T. Narayanan and M. Swaminathan, "Preconditioned second-order multi-point passive model reduction for electromagnetic simulations," *IEEE Trans. Microw. Theory Tech.*, vol. 58, no. 11, pp. 2856–2866, Nov 2010.

# VITA

Ming Yi was born in Wuhan, China. He received the B.S. degree from Wuhan University of Technology, Wuhan, China, in 2008, the M.S. degree from Shanghai Jiao Tong University, Shanghai, China, in 2011, and the M.S. degree from Georgia Institute of Technology (Georgia Tech), Atlanta, GA, in 2011, all in Electrical and Computer Engineering. He his currently a Ph.D. candidate in School of Electrical and Computer Engineering at Georgia Tech, Atlanta, GA.

From fall of 2008 to fall of 2011, he was with the Center for Microwave and RF Technologies (CMRFT) in Shanghai Jiao Tong University, where he worked in the area of multi-physics modeling. During the summer of 2013, he worked as an intern in Broadcom Corporation, Irvine, CA, where he was involved in signal/power integrity modeling and analysis of IC packages. He is currently a Graduate Research Assistant in Mixed Signal Design Group in Georgia Tech.

His research interests include multiscale chip-package co-simulation and optimization, signal/power integrity modeling and analysis, electromagnetic modeling of IC packages and full-wave electromagnetic solver development.